UNIVERSITÀ DEGLI STUDI DI PARMA

Dottorato di ricerca in Scienze e Tecnologie dei Materiali Innovativi

Ciclo XXVII (2012-2014)

Hybrid and nanostructured materials for photovoltaic and gas sensing applications: preparation and properties

Coordinatore

Chiar.mo Prof. Enrico Dalcanale

Tutor:

Dott. Roberto Mosca

Dottorando: Paolo Fedeli

2015

Abstract

The world-wide increasing demand for energy is one of the most important issues of the era we are living in. Owing to the limited availability of fossil fuels and the strict necessity to reduce the pollutant emissions, great attention has been devoted towards clean and renewable energy resources. Solar energy conversion, in particular, is considered one of the most promising alternatives to face the energy-related challenges, as sunlight is likely the most abundant clean source of energy capable to satisfy the need for energy on global scale with minimum detrimental impact on the environment. Therefore, the development of efficient, cost effective and reliable photovoltaic devices is one of the key purposes of the scientific research in these years.

In this scenario, in the last two decades great interest has been addressed to hybrid and dye-sensitized solar cells, that can be manufactured more inexpensively with respect the traditional photovoltaic devices based on silicon and compound semiconductors. A couple of year ago, the emerging of hybrid metal halide perovskites $MAPbX_3$ (X = I, Br, Cl) as sensitizers in nanostructured solar cells has represented a breakthrough in this field, leading to the achievement of impressive energy conversion efficiencies and opening the way to the realization of novel device architectures. Anyway, despite the huge interest instantaneously arisen about this new class of materials and its application in more and more efficient photovoltaic devices, the origin of the observed outstanding performances has still to be identified and, more generally, a broad spectrum of hybrid perovskite properties is not accurately understood yet.

The first part of the thesis reports the activity concerning hybrid perovskites. $MAPbI_3$ perovskite films on glass substrates were obtained following either a single step solution process, but using different solvents (N,N-Dimethylformamide or γ-butyrolactone), or a two-step dipping procedure. The structural, morphological and optical analysis highlighted that the preparation route mainly affects the morphology, while the crystalline structure and the bandgap are substantially unchanged. The influence of baking time was investigated in $MAPbI_3$ films prepared in different atmospheres from both stoichiometric and MAI-rich precursor solutions, pointing out that the highest light absorbance is achieved by preparing the films in inert atmosphere from stoichiometric precursor solution. Preliminary experiments were performed aiming at sensitizing by $MAPbI_3$ mesoporous ZnO nanosheets to be used for photoanode fabrication, showing that sensitization was likely achieved, even if the process must still be optimized.

Mixed $MAPbI_{3-x}Br_x$ films with Br content varying in the whole $0 \leq x \leq 3$ range were synthesized by properly mixing $MAPbI_3$ and $MAPbBr_3$ precursor solution. Structural analysis confirmed that a solid solution can be formed in the whole $0 \leq x \leq 3$ range. The optical characterization confirmed the possibility to tune the bandgap by varying the Br molar fraction and pointed out that the samples were characterized by a low composition disorder, with a maximum Urbach energy of ≈ 85 meV for $x = 1.89$. The effect of baking parameters was investigated in $MAPbI_2Br$ samples prepared from single precursor solutions having different stoichiometries, finding that only nearly-stoichiometric solutions result in perovskites whose composition depends to a minor extent on the annealing procedures, which makes the synthetic process more reproducible and more promising for large scale solar cell production.

The structural and optical characterizations of mixed $MAPbI_{3-x}Cl_x$ perovskites demonstrated that, regardless of the components ratio in the precursor solution, Cl incorporation in an iodide-based structure is possible only at relatively low concentration levels. However, even if the material band gap remains substantially unchanged, the Cl doping dramatically improves the charge transport within the perovskite layer, explaining the outstanding performances of meso-superstructured solar cells based on this material.

The second part of the thesis describes the activity concerning zinc oxide (ZnO) nanostructures. Single-crystal highly porous ZnO nanobelts were prepared by thermally decomposing $ZnS(en)_{0.5}$ hybrid parent nanostructures synthesized through a solvothermal route on Zn substrates. The investigation at the nanoscale of the $ZnS(en)_{0.5} \rightarrow ZnS \rightarrow ZnO$ conversion pointed out that hybrid decomposition of $ZnS(en)_{0.5}$ results in porous ZnS nanobelts, that are gradually transformed into ZnO by an exchange reaction between oxygen and sulfur. Pores form in the whole nanostructures due to the strong lattice contraction associated with the $ZnS \rightarrow ZnO$ transformation. Control of the ZnO nanobelts distributions was achieved by patterning the Zn metallization on alumina substrates, allowing the fabrication of two contacts structures used for the electrical characterization. The comparison between cathodoluminescence spectra and electrical measurements suggested the presence of a residual sulfur doping that was confirmed by means of EDX analysis.

ZnO mesoporous nanosheets and nanotetrapods were used as active layer in gas sensing devices, that were characterized in different atmospheres by means of impedance spectroscopy. The impedance spectra of both nanostructures in the presence of ethanol (CH_3CH_2OH) and carbon monoxide (CO) at different temperatures and gas concentrations were described by the same equivalent circuit. The different behavior of the sensors response observed for dry carbon monoxide and ethanol suggested a relevant influence of the absorbed water molecules on the conduction in these systems.

Keywords: photovoltaics, hybrid perovskites, gas sensing, mesoporous ZnO nanostructures.

Riassunto

La crescente domanda di energia a livello mondiale costituisce una delle problematiche più rilevanti dell'epoca in cui viviamo. A causa della limitata disponibilità di combustibili fossili e della stringente necessità di ridurre le emissioni inquinanti, una grande attenzione è stata rivolta verso nuove risorse di energia pulite e rinnovabili. Lo sfruttamento dell'energia solare, in particolare, è considerata una delle alternative più promettenti per fronteggiare le questioni legate all'energia, in quanto la luce del sole è verosimilmente la più abbondante risorsa pulita in grado di soddisfare la richiesta di energia su scala globale minimizzando l'impatto negativo sull'ambiente. Pertanto, lo sviluppo di dispositivi fotovoltaici efficienti, poco costosi ed affidabili costituisce uno degli obiettivi chiave della ricerca scientifica in questi anni.

In questo scenario, negli ultimi vent'anni grande interesse è stato indirizzato verso le celle solari ibride e dye-sensitized, che possono essere processate e realizzate con costi significativamente minori rispetto ai tradizionali dispositivi fotovoltaici basati su silicio e su semiconduttori composti. Un paio di anni fa, l'avvento delle perovskiti ibride alogenometalliche $MAPbX_3$ (X = I, Br, Cl) come materiale funzionalizzante in celle nanostrutturate ha rappresentato un vero e proprio breakthrough in questo settore, permettendo il raggiungimento di ragguardevoli efficienze e aprendo la strada alla realizzazione di dispositivi basati su nuove architetture. Ciò nonostante, benché un grande interesse sia istantaneamente emerso nei confronti di questa nuova classe di materiali e della sua applicazione in celle solari via via sempre più efficienti, l'origine di queste eccellenti prestazioni non è ancora stata identificata e, più in generale, una vasta gamma di proprietà di queste perovskiti ibride non è ancora stata accuratamente compresa.

La prima parte di questa tesi descrive l'attività che ha riguardato le perovskiti ibride. Film di perovskite $MAPbI_3$ sono stati sintetizzati su vetro sia mediante deposizione di soluzione precursore utilizzando diversi solventi (N,N-dimetilformammide o γ-butirrolattone) sia mediante una procedura di immersione a due stadi. L'analisi strutturale, morfologica e ottica ha evidenziato che la procedura di preparazione influenza principalmente la morfologia, mentre la struttura cristallina e il bandgap sono sostanzialmente inalterati. L'influenza del tempo di baking è stata investigata in film di $MAPbI_3$ preparati in differenti atmosfere sia da una soluzione stechiometrica che da una soluzione arricchita in MAI. L'analisi ha mostrato che la più alta assorbanza è ottenuta preparando il materiale in atmosfera inerte dalla soluzione stechiometrica. Sono stati condotti esperimenti preliminari di funzionalizzazione con $MAPbI_3$ di nanosheet mesoporosi di ZnO per la fabbricazione di fotoanodi. I risultati suggeriscono che un'effettiva funzionalizzazione è raggiunta, anche se il processo necessita di ottimizzazione.

Sono stati sintetizzati film di perovskite mista $MAPbI_{3-x}Br_x$ al variare del contenuto di bromo nell'intero intervallo $0 \leq x \leq 3$ attraverso opportune miscele delle soluzioni precursore di $MAPbI_3$ e $MAPbBr_3$. L'analisi strutturale ha confermato la possibilità di formare una soluzione solida in tutto l'intervallo $0 \leq x \leq 3$. La caratterizzazione ottica ha confermato la possibilità di variare il bandgap modificando la frazione molare di Br e ha mostrato che i campioni erano caratterizzati da un basso disordine composizionale, con un'energia di Urbach massima di ≈ 85 meV per $x = 1.89$. L'effetto dei parametri di baking è stato investigato su campioni di $MAPbI_2Br$ preparati da singole soluzioni aventi stechiometrie diverse. È stato osservato che solo partendo da soluzioni quasi-stechiometriche è

possibile ottenere una perovskite la cui composizione non dipenda significativamente dai parametri di annealing, evidenziando come procedura di sintesi sia la più riproducibile e promettente per la produzione di celle solari su larga scala.

La caratterizzazione ottica e strutturale della perovskite mista $MAPbI_{3-x}Cl_x$ ha dimostrato che, a prescindere dal rapporto tra le componenti presenti nella soluzione utilizzata come precursore, l'inclusione di cloro nella struttura a base di iodio è possibile solo a livelli di concentrazione relativamente. Tuttavia, anche se il bandgap del materiale rimane sostanzialmente invariato, il drogaggio con cloro migliora sostanzialmente il trasporto di carica nel layer di perovskite, rendendo possibili le notevoli prestazioni delle celle solari "meso-superstructured" basate su questo materiale.

La seconda parte della tesi descrive l'attività che ha riguardato le nanostrutture di ossido di zinco (ZnO). Sono stati ottenuti nanobelt monocristallini mesoporosi di ZnO mediante decomposizione termica di analoghe nanostrutture del composto ibrido $ZnS(en)_{0.5}$ sintetizzate per via solvotermale. Lo studio su scala nanoscopica della trasformazione $ZnS(en)_{0.5} \rightarrow ZnS \rightarrow ZnO$ ha mostrato che la decomposizione del composto ibrido $ZnS(en)_{0.5}$ comporta la formazione di nanobelt porosi di ZnS, che sono gradualmente trasformati in ZnO da una reazione di scambio tra ossigeno e zolfo. La forte contrazione reticolare associata alla trasformazione $ZnS \rightarrow ZnO$ porta all'apertura di pori in tutta la nanostruttura. Grazie alla possibilità di controllare la distribuzione spaziale dei nanobelt di ZnO mediante patterning della metallizzazione di Zn su substrati di allumina, è stato possibile realizzare strutture a due contatti utilizzate per la caratterizzazione elettrica. Il confronto tra spettri di catodoluminescenza e misure elettriche ha suggerito la presenza di un drogaggio residuale di zolfo, che è stato confermato dall'analisi EDX.

Nanosheet mesoporosi e nanotetrapod di ZnO sono stati impiegati come elementi attivi in sensori di gas, che sono stati caratterizzati in differenti atmosfere tramite spettroscopia di impedenza. Gli spettri di impedenza di entrambe le nanostrutture in presenza di etanolo (CH_3CH_2OH) e monossido di carbonio (CO) a differenti temperature sono stati descritti mediante il medesimo circuito equivalente. Il differente comportamento della risposta dei sensori osservato per monossido di carbonio secco e etanolo suggerisce un'influenza rilevante delle molecole d'acqua assorbite sulla conduzione in questi sistemi.

Contents

CHAPTER 1
INTRODUCTION

Finding innovative materials suitable for the fabrication of durable and efficient photovoltaics devices is one of the most relevant purposes of the research on materials science in these years. During the last three decades, the attention of the scientific community has been devoted not only to the improvement of the solar cell performances, but also to the development of easy processable and cost effective devices, as these are two strict requirement to determine the desirable success of the photovoltaic energy generation. Therefore, great interest has arisen towards the so-called 3rd generation solar cells, that candidate themselves as reliable, inexpensive and performing alternatives to traditional devices based on silicon or compound semiconductors. These emerging technologies are considered very attractive due to the possibility to process the devices in mild conditions, resulting in low-cost cells and reduced energy payback times. Nevertheless, their large scale diffusion is being severely hampered by several drawbacks, such as low efficiency, low reproducibility and poor long-time stability.

In this scenario, hybrid metal halide perovskites have recently emerged as one of the most promising materials for a new generation of photovoltaic devices, as perovskite solar cells have shown outstanding performances combined with low-cost processability. In the first part of this thesis, the synthesis and the characterization of methylammonium lead halide perovskites $MAPbX_3$ (X = I, Br, Cl) are presented and discussed. The $MAPbI_3$ compound has been initially proposed by Kim et al[1] as the sensitizer in all-solid-state DSSCs, leading to a power conversion efficiency (PCE) exceeding 9%. The massive research efforts on this material and its application in solar cells have led to a rapid improvement of the efficiencies, and now the PCE has reached the impressive value of 20.1%[2]. Remarkably high efficiencies have been achieved also using mixed $MAPbI_{3-x}Cl_x$ and $MAPbI_{3-x}Br_x$ perovskites. A large number of papers dealing with the device PV performances has been published, where the use different perovskite materials and synthetic procedures has been proposed and investigated. However, few works dealt with the possible relations existing between the perovskite properties and the processes followed to prepare the material. During the activity reported in this thesis, $MAPbI_3$, $MAPbI_{3-x}Br_x$ and $MAPbI_{3-x}Cl_x$ compounds have been synthesized by different preparation procedures and their structural, morphological and optical properties have been investigated, aiming at a deeper understanding of the influence of the synthesis procedures on the

obtained material. The possibility to relate the perovskite properties to the synthetic procedures appears a crucial point to the further development of hybrid perovskite-based solar cells.

The second part of the thesis describes the activity on mesoporous zinc oxide (ZnO) nanosheets and nanobelts obtained by calcination of the hybrid $ZnS(en)_{0.5}$ (en=ethylenediamine) compound prepared by solvothermal route. Hybrid $ZnS(en)_{0.5}$ nanosheets were synthesized for the first time by Jang et al[3], that also demonstrated the possibility to convert them into monocrystalline mesoporous ZnO nanosheets by proper thermal annealing. The same $ZnS(en)_{0.5}$ was synthesized by Zhang et al[4] in form of nanobelts, that were subsequently converted by thermal treatment in elongated ZnS nanoribbons. In this thesis it will be shown that is it possible to obtain single-crystal mesoporous ZnO nanobelts by calcinating parent $ZnS(en)_{0.5}$ hybrid nanobelts grown on conventional Zn foils or insulating substrates. The high surface-to-volume ratio makes both nanosheets and nanobelts promising for gas sensing and photovoltaics applications. Mesoporous ZnO nanosheets were used by Liu et al[5] as active layer in gas sensors. Some studies have been carried out to identify which mechanisms related to the gas absorption are involved in the electrical transport, but many aspects still have to be understood and a general model of the conduction in these systems is still missing. To investigate this aspect, gas sensing devices have been prepared using ZnO nanosheets and nanotetrapod as active layer and characterized in different atmospheres by means of impedance spectroscopy. The possibility to achieve high performances in innovative devices is strictly correlated with a deep understanding of the charge transport mechanisms in these systems.

1.1 Perovskites: structure and most relevant properties

The term “perovskite” refers to a wide class of materials that share the same crystalline structure of calcium titanate, $CaTiO_3$. The general formula of these materials, whose name originates from the Russian mineralogist Lev Aleksevich von Perovski (1792-1856), is ABX_3, where A is a cation, B a metal cation smaller than A and X an oxide or a halide anion. The ideal perovskite structure is characterized by a cubic symmetry where the B cation is 6-fold coordinated by X in an octahedral configuration. Similarly, the A cation is 12-fold coordinated by X in a cuboctahedral configuration and is situated in the center of a cube formed by corner-sharing BX_6 octahedra (figure 1.1). The resulting compound extends as a three-dimensional network formed by the regular repetition of the BX_6 octahedral, intercalated by the A cations.

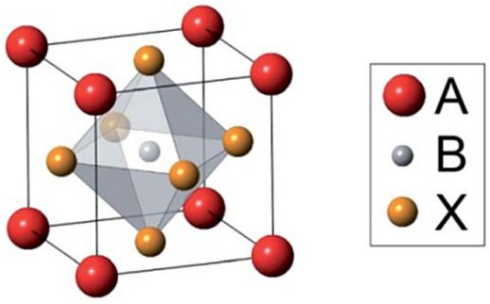

Figure 1.1 Three-dimensional representation of the perovskite crystalline structure. A and B are cations, while X is an oxide or a halide anion.

The perovskite structure is shared by hundreds of different materials endowed with a multitude of different properties, including piezoelectric, ferromagnetic, thermoelectric, semiconducting,

superconducting, photocatalytic and gas sensing[6–13]. Among this broad variety of materials, a special class is composed by those perovskites where A is an organic cation, typically a small and monovalent one such as methylammonium ($CH_3NH_3^+$)[14], ethylammonium ($CH_3CH_2NH_3^+$)[15], tetramethylammonium ($N(CH_3)_4^+$)[16], formamidinium ($NH_2CHNH_2^+$)[17] or guanidinium ($C(NH_2)_3^+$)[18]. This hybrid compounds, that are referred to as organic-inorganic perovskites, are characterized by an impressive versatility, thanks to the possibility to obtain them with different structures depending on the dimensions of the cations. In particular, it has been observed that the three-dimensional ideally cubic structure having the general formula ABX_3 is obtained for small A cations, while for bigger organic groups a layered two-dimensional structure is observed, whose general formula is A_2BX_4.The 2D layered perovskite structure is composed of layers of corner-sharing BX_6 octahedra that are separated by a double layer of organic cations. A projected view of the two different structures is reported in figure 1.2. Organic cations larger than the ones mentioned before exclusively form the 2D layered perovskite structure, that basically does not limit the size of the organic cation and also allows the two monovalent organic cations to be replaced by a divalent one.

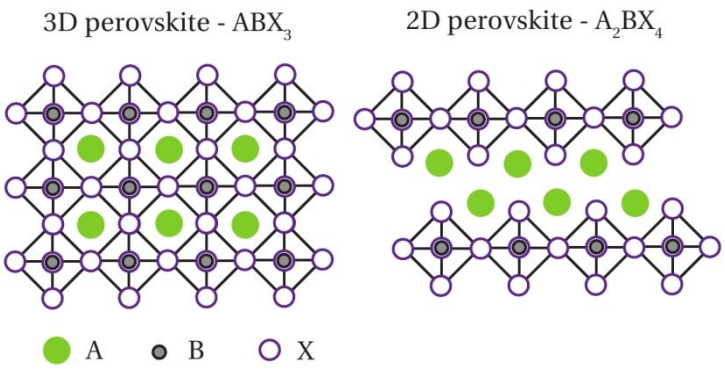

Figure 1.2 Projected representation of the 3D perovskite (ABX_3) and the 2D layered perovskite (A_2BX_4).

Hybrid organic-inorganic perovskites have attracted great attention in the last two decades, thanks to their peculiar properties, the possibility to prepare them via cost effective wet-chemical synthesis routes at mild temperature and pressure conditions and their suitability for solution-processed electronics. The 2D hybrid perovskites have been widely investigated starting from the early 1990s by the Mitzi group[19] and are considered very promising, thanks to their unique optoelectronic properties deriving from the layered structure. The most relevant achievement of the research carried out by Mitzi and coworkers was to point out the strong excitonic features of these layered perovskites and their successful application in transistor and light-emitting diodes[17,20–23].

More recently, the interest towards 3D compounds has been considerably renewed by the applications in solar cells of three-dimensional methylammonium lead halide perovskites, where A = $CH_3NH_3^+$ (CH_3NH_3 = MA), B = Pb^{2+} and X = I^-, Br^- and Cl^- (figure 1.3). The outstanding performances observed, as well as the possibility to synthetize these materials by self-assembling processes from solution in mild conditions, make this class of hybrid perovskites one of the most important material families for high-efficiency and low-cost photovoltaic devices.

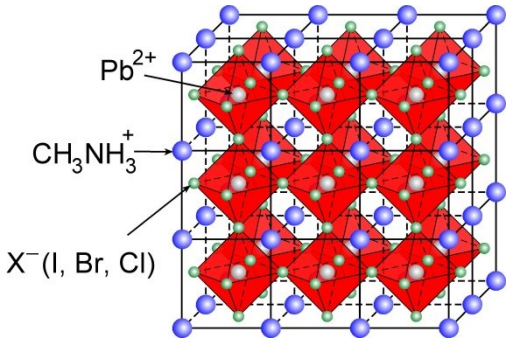

Figure 1.3 Schematic representation of the three-dimensional methyl ammonium lead halide perovskite structure.

The electrical and optical properties of methylammonium lead halide perovskites make these materials particularly suitable for photovoltaics applications. Indeed, they are direct semiconductor materials, whose bandgap depends on composition. The pure tri-iodide perovskite $MAPbI_3$ has the lowest bandgap among the $MAPbX_3$ compounds: in literature, values ranging from 1.50 eV[24,25] and 1.63 eV[26] are reported, corresponding to an absorption onset located at ca. 800 nm and thus suitable for visible light harvesting. Thanks to their high absorption coefficient, which is typically one order of magnitude higher than those of the conventional Ru dyes[1,27], hybrid perovskites have shown remarkable performances when used as sensitizer in dye-sensitized solar cells. Owing to the intensive investigation activity on these materials, several interesting properties have been highlighted in the last two years, leading not only to the increase of the efficiencies of the devices, but also to the fabrication of perovskite-based solar cells having novel architectures, such as meso-superstructured[28] and planar heterojunction[29] solar cells.

1.2 Dye-sensitized solar cells (DSSCs)

The emerging of hybrid perovskites as a new class of materials for photovoltaic applications has been initially driven by the idea of using these materials to replace traditional Ru-based dyes in dye-sensitized solar cells (DSSCs). DSSCs are one of the most representative members of the so called 3rd generation photovoltaic devices, a large family of different typologies of organic and hybrid solar cells that have been proposed during the last two decades as cost effective and easy processable alternatives to the traditional cells based on inorganic materials, such as silicon and compound semiconductors. The first demonstration of energy conversion using a DSSC was reported in 1991 by O'Regan and Grätzel[30], that reported a 7.1-7.9% PCE under solar simulator and a 12% PCE under diffuse daylight. A typical DSSC device is schematized in figure 1.4.

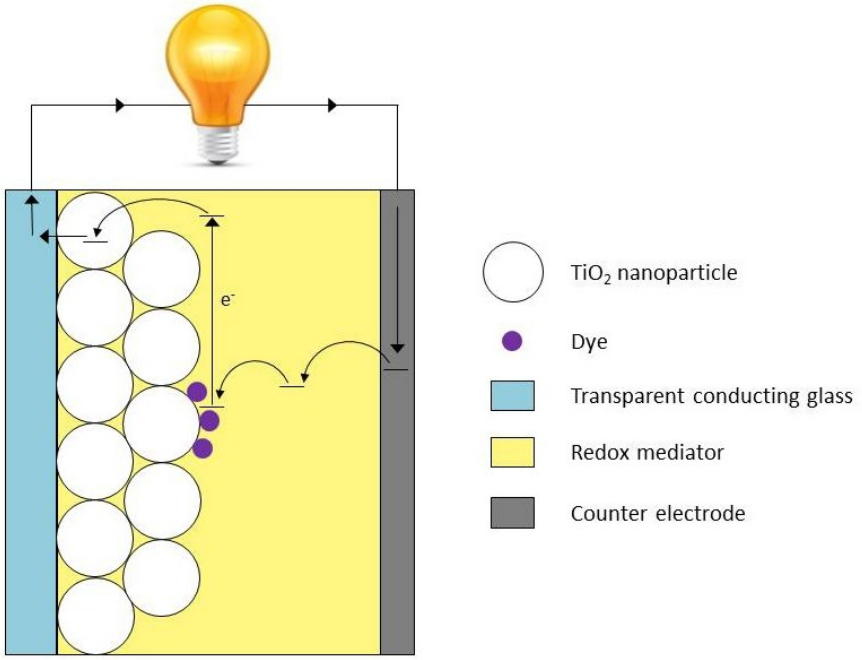

Figure 1.4 Schematic representation of a typical DSSC (not to scale).

When the cell is illuminated, the light is absorbed by the dye molecules, that act as light harvester similarly to chlorophyll in green plants. The light absorption by the dye is responsible for the color of the devices, so that the dye is often referred to as "chromophore". Due to the energy transferred from the absorbed photon to the dye molecule, an electron – hole couple is formed. The dye is chemically anchored to a mesostructured wide-bandgap *n*-type metal oxide semiconductor (typically mesoporous TiO_2) that acts both as a scaffold for the sensitizer and as a transport channel for the photogenerated electrons. Upon illumination, the dye injects photogenerated electrons in the semiconductor conduction band. The charge neutrality of the dye is regenerated by electron donation from a redox couple in the redox mediator electrolyte that infiltrates the mesoporous structure and is in contact with the sensitized junction. After the injection in the porous semiconductive layer, the photogenerated electrons move through the semiconductor network until they are collected by the transparent conducting glass; the whole system composed by the semiconducting porous layer and the conductive glass acts therefore as front electrode (photoanode). At the same time, the initial redox state of the electrolyte is restored by interfacial electron transfer at the back electrode (counter electrode). The circuit is closed by charge migration through an external load (figure 1.4).

In the DSSC originally proposed by O'Regan and Grätzel[30], a mesoporous TiO_2 nanoparticles layer was used as photoanode and a ruthenium-polypyridine-complex was used as dye. As redox mediator, a liquid electrolyte based on I^-/I_3^- redox couples was employed. Thanks to the good conversion efficiency and the cost effectiveness, this device architecture soon became a standard for this kind of solar cells. Nonetheless, in the following 25 years countless variations from this original configuration have been proposed, aiming to further enhance the efficiencies and to achieve an improved long-term stability. Currently, the record PCE achieved under solar simulator by a conventional DSSC is 12%[31].

As for the perovskite-based DSSCs, the interest is focalized upon a particular subset of this wide family of devices, the so-called all-solid-state DSSCs (ss-DSSCs). In these cells, the liquid electrolyte

responsible for the chromophore regeneration is replaced by a solid-state hole transporting material (HTM). Typical HTMs are polymers, such as Poly(3-hexylthiophene) (P3HT), or transparent molecular semiconductors, such as 2,2',7,7'-Tetrakis-(N,N-di-4-methoxyphenylamino)-9,9'-spirobifluorene (spiro-OMeTAD). In particular, the latter has emerged as the largely most used HTM for perovskite-based devices, where the replacement of the liquid I^-/I_3^- electrolyte is necessary because of the rapid degradation of the performances due to the fast dissolution of perovskite dyes in the liquid redox mediator. The replacement of the liquid component by a solid materials involves some technical advantages. Compared to a traditional DSSC, a ss-DSSC can be fabricate following a monolithic approach, while liquid cells are usually constructed by assembling two separate electrodes together with the liquid electrolyte filling the space in between them. Besides, the solid architecture allows circumventing the problems related to the corrosion of the electrodes caused by the liquid redox mediator. Last but not least, ss-DSSCs don't require the expensive sealing that is needed in their liquid counterparts to prevent electrolyte leakage and evaporation, that are two of the most important issues concerning the long term durability of these devices.

It is worth noting that a deep research activity in these years has been carried out also on the optimization of the photoanode, by proposing both new nanostructure morphologies and new materials for photoanode fabrication, where ZnO is one of the most interesting alternatives to TiO_2. Indeed, ZnO is characterized by energy band structure an physical properties similar to those of TiO_2, with improved electrical properties (such as mobility). Moreover, it can be easily synthesized as nanostructures with different size and shape, thus allowing the optimization of the photoanode morphology.

1.3 Hybrid perovskites in photovoltaic devices

The first demonstration of a conversion efficiency in a perovskite-sensitized DSSC was given by Kojima et al in 2009[14], 31 years after the discovery of hybrid perovskites[32]. In that work, a PCE of 3.13% and 3.81% was obtained by sensitizing nanocrystalline TiO_2 with $MAPbBr_3$ and $MAPbI_3$, respectively, and using Br^-/Br_3^- or I^-/I_3^- liquid electrolytes as the redox mediators. Remarkably, a high open-circuit voltage (V_{OC}) of 1.0 V was achieved using $MAPbBr_3$ perovskite, but a photocurrent decay for an open cell exposed to air under continuous irradiation was observed, which limited the device durability. A couple of years later, Im et al[27] reported an efficiency of ≈ 6.5% using $MAPbI_3$ as sensitizer on TiO_2 and a conventional or I^-/I_3^- liquid electrolyte. Interestingly, the dye was present on the semiconducting scaffold in form of quantum dots having a diameter of ca. 2.5 nm. They compared the performances of a perovskite-based cell with those of an analogous device using the commercially available Ru-based N719 dye sensitizer, that resulted in an efficiency of ≈ 3.9%. The higher efficiency of the perovskite cell was attributed to the higher absorption coefficient of $MAPbI_3$ with respect to N719: from transmittance data, the absorption coefficient of the perovskite at 550 nm was estimated to be $1.5 \cdot 10^4$ cm^{-1}, while those obtained for N719 at the same wavelength was $1.5 \cdot 10^3$ cm^{-1}. Nevertheless, nearly 80% degradation of PCE within 10 minutes under continuous irradiation was observed when using $MAPbI_3$ as dye, and this was ascribed to the gradual dissolution of the perovskite into the redox electrolyte.

The perovskite solvation problem was solved by replacing liquid electrolytes by a solid hole transporting material (HTM) in August 2012, when the remarkable PCE value of 9.7% was achieved by a solid-state perovskite solar cell using $MAPbI_3$ as the sensitizer and spiro-MeOTAD as the hole

transporter[1]. The introduction of spiro-MeOTAD as HTM combined with hybrid perovskites as chromophore was a real breakthrough in the field of dye-sensitized cells. For solid-state sensitized solar cells, this represented a step change in performance compared with the best-reported ss-DSSCs, which exhibit about 7% efficiency[33]. Before the introduction of the perovskite dyes, the improvement of ss-DSSCs efficiencies had been hampered by the necessity to limit the thickness of the porous layer to 2 µm, in order to achieve a good HTM infiltration in the pores[34]; using traditional dyes an effective light absorption couldn't be achieved with such thin layers, as a complete sunlight harvesting would have required films as thick as 10 µm[35]. The high absorption coefficient of perovskites dyes led to the possibility to combine good HTM pore filling and strong light absorption even using porous layers few µm thick. The use of perovskite dyes combined with solid HTM was also favored by the facile processability of the devices, methylammonium trihalogen plumbates being almost insoluble in the organic solvents required to deposit spiro-MeOTAD, typically chlorobenzene.

The high performances observed in solid-state perovskite cells were confirmed few months later by Lee et al[28], who obtained a PCE close to 8% using the mixed I/Cl perovskite $MAPbI_{3-x}Cl_x$. Besides, they observed that replacing the conventional TiO_2 porous layer with an insulating Al_2O_3 scaffold led to an open-circuit voltage increase and an improvement of the overall conversion efficiency up to almost 11%. These findings opened the question whether the mixed $MAPbI_{3-x}Cl_x$ perovskite could act both as light absorber and electron transport, as the only possibility for the photogenerated electrons to be collected by the anode was to travel through the perovskite layer, being Al_2O_3 an highly insulating material at room temperature. This consideration pointed out that the cell obtained by Lee et al was characterized by a substantially different architecture from those of the traditional ss-DSSCs, where distinct components are responsible for light harvesting and electron transport. This new configuration was termed "meso-superstructured solar cell" (MSSC), due to the presence of the mesoporous scaffold acting as a superstructure, upon which the photoactive layer is coated. The structure of this cell is showed in figure 1.5, compared with a conventional DSSC.

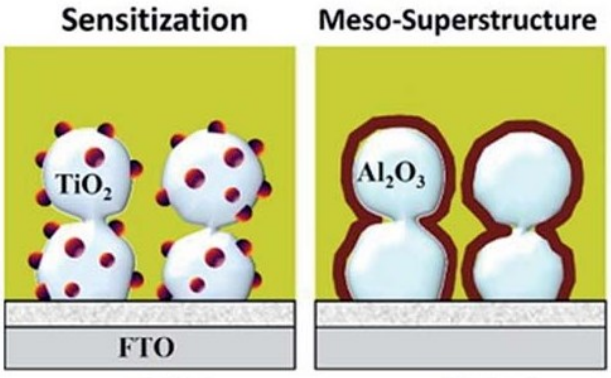

Figure 1.5 Schematic representation of a typical DSSC, where the perovskite is applied as sensitizer, and a MSSC, where the perovskite is deposed on an insulating scaffold as a capping layer acting both as light absorber and charge transporter. From [187].

Soon after, Etgar et al[36] obtained a PCE of 5.5% in a hole conductor-free mesoscopic $MAPbI_3$ perovskite/TiO_2 heterojunction solar cell, where no spiro-MeOTAD was present and the photogenerated holes were transferred to the counter electrode by the perovskite itself. This result pointed out the capability of $MAPbI_3$ crystals to act both as an efficient light harvester and as a hole transporter, highlighting the versatility of this amazing class of materials.

These seminal results triggered intensive research on hybrid perovskite solar cells. In March 2013 Noh et al[37] demonstrated the possibility to tune the bandgap of the perovskite to cover almost the whole visible spectra by varying the Br molar fraction *x* in the mixed I/Br perovskite $MAPbI_{3-x}Br_x$. They achieved the best PCE of 12.3% and, most notably, pointed out the possibility to improve the device durability while keeping efficiency by properly choosing the Br molar fraction. It is worth noting that the material stability is an extremely important aspect concerning the perovskite-based solar cells, since methylammonium metal halides suffer a degradation process when they are exposed to humid air, due to the presence of the hygroscopic $CH_3NH_3^+$ cations.

The perovskite films obtained by one-step deposition of precursor solution were characterized by poor uniformity. Aiming at a better control of the perovskite morphology, in July 2013 Burschka et al[38] proposed a two-step dipping strategy to obtain $MAPbI_3$ on mesoporous TiO_2. Compared to the synthesis by self-assembling from precursor solution, this method resulted in a more uniform and reproducible morphology and in the remarkable PCE of ≈ 15%, which is significantly higher than the record efficiency of 11.9% recorded for traditional DSSCs (figure 1.6).

The work reported by Burschka et al[38] opened the way to the realization of perovskite-based planar heterojunction solar cells. In this configuration, schematized in figure 1.7, a thin film of perovskite is sandwiched between *p*- and *n*-type charge-extracting contacts; a *p-i-n* structure is therefore created, where the perovskite acts as the intrinsic layer and assume all of the principal roles of PV operation, that is light absorption, charge generation, and transport of both electrons and holes. The carrier extraction is achieved through an underlying compact TiO_2 layer for the electrons and a top spiro-MeOTAD layer for the holes (figure 1.7).

Figure 1.7 Schematic representation of a *p-i-n* planar heterojunction solar cell using a perovskite thin film both as light absorber and charge transporter. From [35].

The possibility to obtain planar heterojunction devices in very interesting because of their simpler planar architecture and potential in the reduction of process temperatures with respect to the mesoporous geometries. Besides, a planar configuration is suitable for realizing “all-perovskite” multijunction solar cells. Taking advantage from of possibility to tune the perovskite bandgap, it would be possible to stack perovskite layers with different bandgaps. This is expected to result in a reduced photon energy dissipation and therefore in higher photovoltaic performances[35]. From this point of view, it is worth noting that, besides the tuning of the bandgap by varying the halogen composition[37], it has been recently reported the possibility to reduce the $MAPbI_3$ bandgap by

replacing the methylammonium organic cation by formamidinium (FA)[39]. The resulting $FAPbI_3$ perovskite shows a bandgap value of 1.47 eV, which is very favorable for sunlight harvesting and extends towards lower values the range of achievable bandgaps in hybrid lead halide perovskites.

One of the most important challenges concerning the fabrication of planar heterojunction solar cells is the possibility to obtain flat and uniform perovskite films. Chen et al[29] reported the achievement of a flat $MAPbI_3$ film with a thickness of 350 nm, obtained by a vapor-assisted solution process. When applying this method to fabricate a planar heterojunction solar cell, a PCE of 12.1% was achieved; the same group, few months later, reported a planar heterojunction cell with an efficiency of 19.3%[40]. A dual-source thermal evaporation system was used by Liu et al[41] to deposit on a compact TiO_2 layer a flat $MAPbI_{3-x}Cl_x$ film with a thickness of ≈ 330 nm, resulting in a PCE of 15.4%. Very recently, it was published that the use of $MAPbI_{2.4}Br_{0.6}$ perovskite films allows the fabrication of planar heterojunction solar cells with efficiencies up to 13.1%[42] that make I/Br perovskites very interesting even for planar devices.

The 20% efficiency threshold for hybrid perovskite solar cells has been broken in November 2014, when a new record certified nonstabilized efficiency of 20.1% was achieved by Korea Research Institute of Chemical Technology (KRICT); the details of the device, however, have not been published yet. The exponential growth of the efficiency achieved in the last two years is clearly shown by the NREL efficiency chart (January 2015) (figure 1.6). Owing to exciting efficiency trend and to the cost effectiveness, hybrid perovskite cells are considered, among the several emerging solar technologies, one of the most promising for a large scale diffusion.

From the point of view of the industrial scale-up of such photovoltaic devices, some concerns are present regarding the use of Pb, whose toxicity can represent a severe limitation to the mass production. The requirement for environmental friendly materials has recently addressed the research towards the promising tin-based $MASnI_3$ perovskites, but their extreme sensitivity to the air atmosphere still represents a challenging question for the applicability[43]. However, a recent review pointed out that, assuming to replace the whole cumulative PV power installed in the world (approximatively 1 TW) with lead halide perovskite devices, less than 10^4 tons of Pb would be needed. As a comparison, $4 \cdot 10^6$ tons per year of Pb are used for lead-acid batteries[44]. Therefore, it seems that Pb presence in perovskite could not be such an issue.

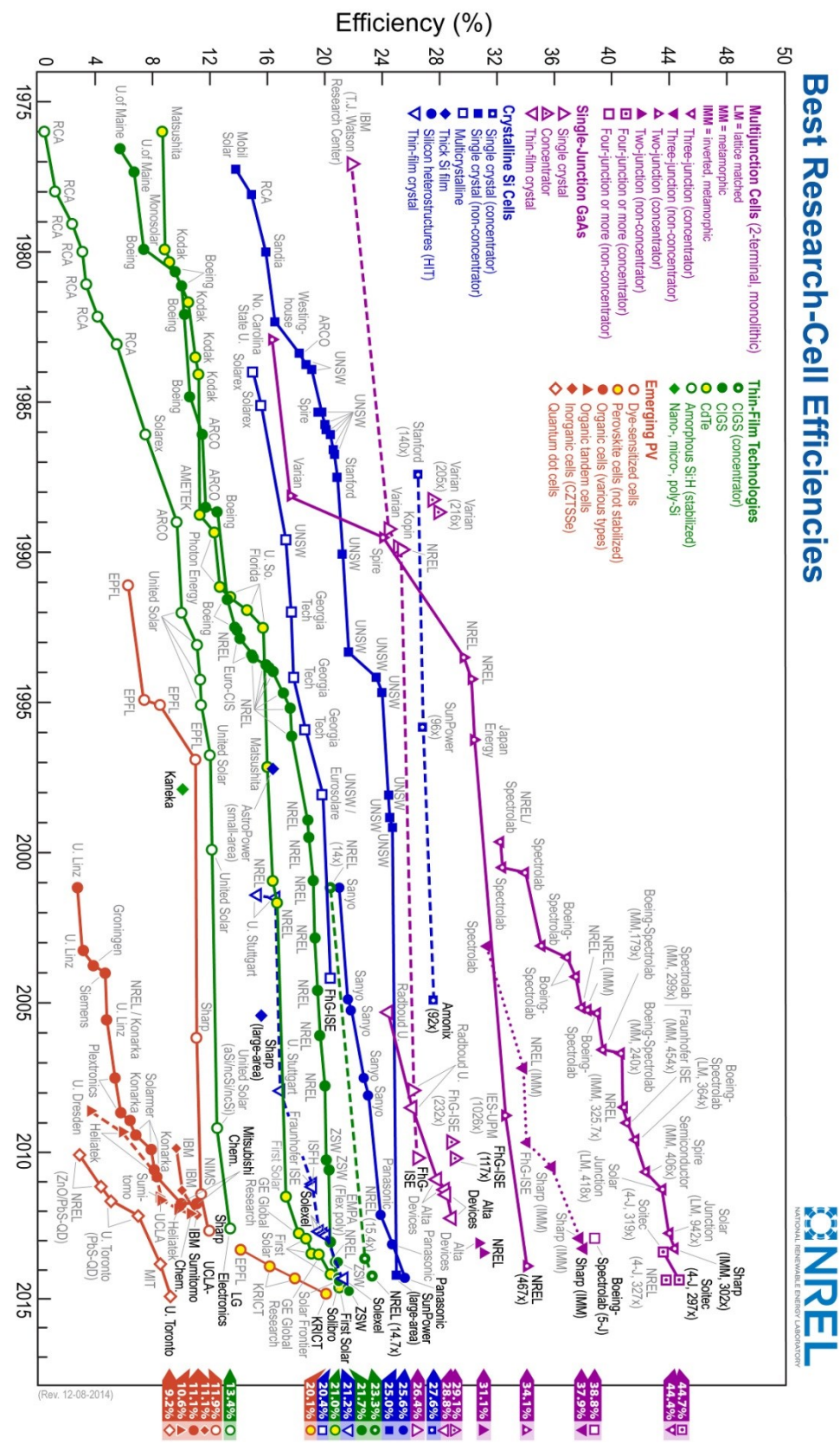

Figure 1.6 Best research-cell efficiencies chart. This plot is courtesy of the National Renewable Energy Laboratory, Golden, CO.

1.3.1 Hybrid perovskites preparation

Up to now the most efficient nanostructured perovskite solar cells exploit $MAPbI_3$ as the light absorber mainly due to the high absorption coefficient of this material. Kim et al[1] reported the preparation of this perovskite by single-step spin coating of precursor solution, using γ-butyrolactone (GBL) as the solvent . In the following months, several variations to this preparation route were proposed. Burschka et al[38] demonstrated the possibility to achieve a good morphology by using a two-step sequential deposition. A similar synthesis route was recently used by Liu et al[45] to prepare planar heterojunction cells on flexible PET substrate, achieving an efficiency of ≈ 10%. Planar devices were achieved also by Chen et al[29] by a vapor-assisted solution process formation of the perovskite, showing an efficiency of ≈ 12%. A similar PCE value was achieved also by Mei et al[46] , that infiltrated a double layer of mesoporous TiO_2 and ZrO_2 by $MAPbI_3$ prepared by drop-casting of a proper precursor solution. An higher efficiency value of ≈ 17% was recently reported by Im et al[47], that obtained a peculiar cuboid morphology by preparing $MAPbI_3$ by a two-step spin-coating procedure. It is worth noting that $MAPbI_3$ has been proposed also for the realization of meso-superstructured cells (figure 1.5), showing an efficiency of ≈ 1% when prepared from stoichiometric solutions and an higher value of ≈ 8 % when prepared using a methylammonium excess.

As anticipated in the previous section, meso-superstructured cells were successfully fabricated using $MAPbI_{3-x}Cl_x$ mixed halide perovskite applied to a non-electron injecting, mesoporous Al_2O_3 scaffold layer[28]. The initial ≈ 8 % efficiency value has recently improved to 15.4% by substituting the mesoporous photoanode by a compact layer of n-typeTiO_2[41]. The preparation of this mixed I/Cl perovskite is usually carried out by single-step spin coating of a precursor solution using N,N-Dymethilformamide (DMF) as the solvent[28,48]. However, the highest efficiencies for this compounds were achieved in planar cells where a flat $MAPbI_{3-x}Cl_x$ was obtained by vapor deposition[41].

A further degree of flexibility has been achieved by the use of perovskites incorporating both iodide and bromide halides ($MAPbI_{3-x}Br_x$) since adjusting the component I/Br ratio allows the bandgap to be tuned to cover almost the whole visible spectrum[37,49,50]. The 12.3% efficiency initially achieved has been recently enhanced to 16.2% by modifying the perovskite synthetic procedure[49], which confirms that optimizing the perovskite preparation is a key tool to improve the photovoltaic performances of these devices. Besides, it was just published that the use of CH3NH3PbI2.4Br0.6 perovskite films allows the fabrication of planar heterojunction solar cells with efficiencies up to 13.1% [§Bi_AEM§] that make I/Br perovskites very interesting even for planar devices.

In this rapidly evolving scenario, many papers have been published dealing with the device photovoltaic performances as determined by the use of different perovskite materials and synthetic procedures, hole transporting materials, photoanodes and solar cell structures. At the same time, few works dealt with the possible relations existing between the perovskite properties and the processes followed to prepare the material, and several different procedures have been proposed for the same material. This situation is well exemplified by the I-Br perovskites synthesized by one-step solution processes. Qiu et al, who were the first to use this material[51], achieved a maximum efficiency of 4.87% from nanostructured solar cells based on TiO_2 nanowire arrays in conjunction with a $MAPbI_2Br$ light harvester obtained using a precursor solution made of MABr and PbI_2 in DMF and annealing at 100 °C for 30 min in ambient air. Noh et al[37] obtained a ≈ 8% efficiency by nanostructured solar cells based on the $MAPbI_2Br$ dye synthesized by processing and baking the samples in inert atmosphere, using a baking at 100°C for 5 min. Recently a lower efficiency of

6.64%[52] was achieved by a $MAPbI_2Br$ perovskite synthesized by using the same approach reported by Noh et al, but varying the solution composition, spin coating the perovskite in air, and using a different hole transport material and a different fabrication of the mesoporous TiO_2 layer. Finally, the same precursors solutions of Noh et al with different thermal treatment (at 100 °C for 10 min in glove box followed by heating in furnace at 100 °C under air stream), TiO_2 paste and hole transport material were used by Suarez et al[53]. In these nanostructured solar cells the maximum efficiency of 2.9% was achieved for a bromide content $x = 1.5$, while Noh et al found the maximum efficiency of 12.3% for $x \approx 0.6$.

In such an intricate context, it is difficult to clarify the relations between preparation procedures and resulting material properties. In most cases the choice of the perovskite synthetic procedures is guided by the optimization of the solar cell performances, which however depend on the synergism of the different component layers, so that it is often difficult to single out the effect of the perovskite layer properties. Therefore, a deep investigation of the influence of the synthetic procedures on the perovskites is needed, since the understanding of this point appears as basic to the further development of hybrid perovskite-based solar cells.

1.4 General properties and applications of zinc oxide

Zinc oxide (ZnO) is a II-VI semiconductor materials that has recently attracted great attention, as proved by the huge amount of publications concerning it that have been published in these years.

Several aspects have been contributing to the increasing interest towards this materials, and among them it is worth mentioning some optical properties such as the large bandgap ($E_g \approx 3.3$ eV at 300 K), the wide room temperature exciton binding energy (≈ 60 meV) and the transparency, as well as other peculiarities such as the piezoelectricity, the biocompatibility and the capability to present significant effects of chemical sensing and catalysis. Last but not least, the attractiveness of this materials has been further enhanced by the emerging in the last 20 years of the possibility to obtain ZnO not only as a bulk, but also as nanocrystals with sizes and shapes; several synthesis routes have been recently developed to obtain ZnO nanostructures, some of which require mild growth conditions and thus are suitable to avoid the high expensiveness issues related to the traditional high temperature synthesis processes.

Thanks to all of these aspects, ZnO is regarded as one of the most promising semiconductor for a new generation of high performances and low cost devices. In this section, a brief overview on the most important properties of this materials will be given, as well as a short review of the state-of-art about the application in the fields of interest for this work, that is the employment as active layer in gas sensors and as photoanode in dye-sensitized solar cells.

The crystalline structure of ZnO has been widely studied from the beginning of the research on this materials, and the first reports on the structural properties date back to the 1930s[54,55]. As most of the II-IV binary compound semiconductors, the crystalline structure of the material is strongly influenced by the growth conditions. In particular, this class of compounds typically crystallize either in the cubic zinc-blende structure or hexagonal wurtzite structure, where each anion is surrounded by four cations at the corners of a tetrahedron, and vice versa. Although this tetrahedral coordination is typical of the sp^3 covalent bonding, these materials present also a substantial ionic character, that results in an increase of the bandgap value with respect to the one that would be

expected from a pure covalent bonding[56]. The ionicity of ZnO resides at the borderline between covalent and ionic semiconductors.

At ambient conditions, the thermodynamically stable phase is the wurtzite (figure 1.8). The wurtzite structure has an hexagonal unit cell with lattice parameters a = 0.3296 and c = 0.52065 nm, with a ratio c/a = 1.633[57]. The structure, that belongs to the spatial groups of C^4_{6v} or $P6_3mc$, consist in two interpenetrating hexagonal-close-packed (*hcp*) sublattices, each of which consists of only one type of atom displaced with respect to each other along the *c*-axis. The tetrahedral coordination results in non-central symmetric structure that is responsible for the piezoelectricity and pyroelectricity observed in this material.

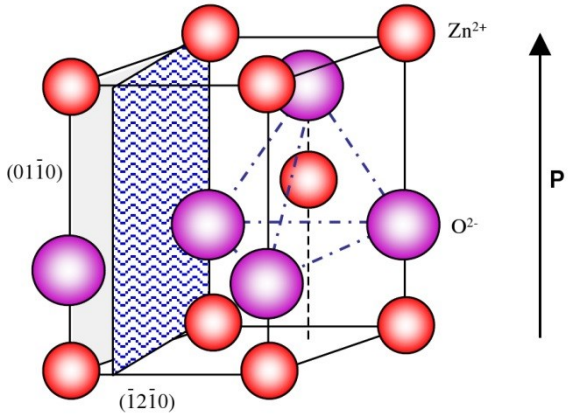

Figure 1.8 The wurtzite structure model of ZnO. The tetrahedral coordination of Zn–O is shown. From [57].

Among the different ZnO properties, transparency has attracted great attention for the realization of devices. This feature, combined with the possibility to improve the electrical properties by introducing in the structure proper dopant species, makes ZnO a very suitable material for the realization of transparent conductive oxides (TCOs), that are widely used in a great number of different applications. Indeed, in most optoelectronic devices such as flat panel displays, light-emitting diodes (LEDs), photodetectors (PDs) and solar cells, it is essential to use a transparent electrode such as a thin-film transparent conducting oxide. Despite indium tin oxide (ITO) films deposited by magnetron sputtering are widely used today for most transparent electrode applications, a significant interest has recently grown towards other TCO semiconductor such as Al-doped ZnO (AZO), Ga-doped ZnO (GZO) and Sn-doped ZnO (TZO), because of the expected worldwide shortage of In. The growing demand for TCO thin film is the driving force for looking at alternative materials since a stable supply of ITO may be difficult to achieve for the expanding market because of the cost and, as mentioned, limited amount of indium available. In this contest, ZnO-based TCO are good candidates thanks to their high optical transparency (in the 90% range), good conductivity, nontoxicity, excellent surface smoothness and convenient processability (low temperature deposition and good etchability for patterning). Up to now, the best results have been obtained by Al-doping (AZO), and Ga-doping (GZO), achieving low resistivity (less than $2\cdot10^{-4}$ Ω·cm) and high carrier concentrations (higher than 10^{21} cm^{-3})[58].

The fine control of the electrical properties of ZnO is a key challenge for the purpose of the realization of novel devices characterized by high performances and reliability. It is well known that unintentionally doped ZnO shows a residual *n*-type conductivity but, although a great number of

papers have been published in the years concerning this topic, the origin of this conductivity is still controversial and the mechanisms responsible for it are intensely debated. However, it is diffusely accepted that this conductivity is correlated with deviation from stoichiometry due to the presence of intrinsic defects such as oxygen vacancies (V_O) and zinc interstitials (Zn_i). Nonetheless, it has also been suggested that the *n*-type conductivity of unintentionally doped ZnO films is only due to hydrogen (H) which acts as a shallow donor with an ionization energy about 30 meV. This assumption is valid since hydrogen is always present in many growth methods and can easily diffuse into ZnO in large amounts due to its large mobility[59].

The electron density of unintentionally doped ZnO samples strongly depends on the preparation methods. Indeed, the carrier density of 10^{21} cm^{-3} usually observed for undoped ZnO can be reduced to about 10^{17} cm^{-3} for samples grown by molecular beam epitaxy (MBE)[60] and below 10^{14} cm^{-3} for samples grown by hydrothermal route[61].

n-type doping of ZnO is technologically very easy to be achieved, if compared with *p*-type doping. High-quality *n*-type doping ZnO films are successfully employed in several devices as *n*-type layers, as well as transparent electrodes in optoelectronic devices. Typical donors used are group III elements (B, Al, Ga, In), rare earth metals (Sc, Y), group IV elements (Si, Ge, Sn) and group VII elements (F, Cl, I). The production of highly conductive ZnO films has been achieved by various deposition methods such as MBE, sputtering, PLD and chemical vapor deposition[56].

As in most of wide-bandgap semiconductors (GaN, ZnS, ZnSe, CdS), it is difficult to obtain *p*-type doping in ZnO. The limitations for the realization of such a doping can be various, such as the acceptor compensation by native intrinsic defects (V_O and Zn_i) or background impurities (H); the poor solubility of most *p*-type dopants in the ZnO structure represents another challenge. Known acceptors in ZnO include group I elements (Li, Na, K), Cu, Ag, Zn vacancies and group V elements (N, P, As); nevertheless, many of these species form deep acceptors and thus don't contribute significantly to the hole density in the material. Nowadays, the group V elements are regarded as the most promising to reach *p*-doped ZnO, even if theory suggests some difficulty in achieving shallow acceptor level[59].

1.4.1 ZnO nanostructures

In the last years an intense research activity has been focused on ZnO nanostructured systems. One-dimensional nanostructures (nanowires, nanorods) have attracted increasing attention thanks to their peculiar physical properties deriving from quantum confinement, such as electronic quantum transport and enhanced radiative recombination of carriers. ZnO nanowires are considered very promising in applications such as short-wavelength nanolasers, field-effect transistors, ultrasensitive nanosized gas sensors, nanoresonators, transducer, actuators, nanocantilevers and field emitters (FEs)[59]. Moreover, 1D nanostructures offer the opportunity to investigate experimentally the effects of the quantum confinement, so are also very important for the understanding of the fundamental phenomena in low-dimensional systems. It is worth to highlight the possibility to obtain patterned and vertically aligned ZnO nanowires and nanorods (figure 1.9), usually achieved via the vapor-liquid-solid (VLS) process with the use of metal catalysts, which initiate and guide the growth[62]. Other techniques have been employed to obtain aligned one-dimensional structures, such as metalorganic vapor-phase epitaxy (MOVPE)[63] and homoepitaxial electrodeposition[64], and in general a significant interest is devoted to this kind of nanostructures and their application in several fields, such as nano-

optoelectronics, nanosensing[65] and photovoltaics[66,67]. Nanowires, nanorods and nanobelts have been proposed the realization of field effect transistors (FETs). Some prototypal devices have been already tested showing very interesting features, such as higher electron mobility with respect to analogous devices based on thin films and the possibility to modulate the transport properties using illumination or chemical passivation of surfaces[56].

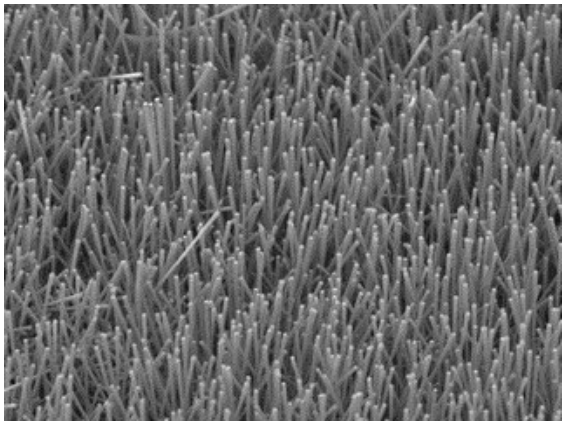

Figure 1.9 SEM image of vertically aligned ZnO nanorods.

The appealing of ZnO nanostructures is not limited to one-dimensional geometries. In the last decade various nanocrystals have been obtained with an impressive variability in size and shape; figure 1.10 shows some examples of such different structures. Well known geometries include nanotetrapods[68], nanocombs[62], nanoflakes[69] and various hierarchical structures[70]. Moreover, it has been demonstrated the possibility to obtain also crystals having a planar aspect, such as nanoribbons, nanobelts[71] and nanoplates[72]. The possibility to combine the ZnO properties with the reduced dimensions makes these materials highly suitable for the fabrication of novel devices, both for strictly nanosized structures and for mesoscopic crystals, where an actual quantum confinement of the carrier is not reached.

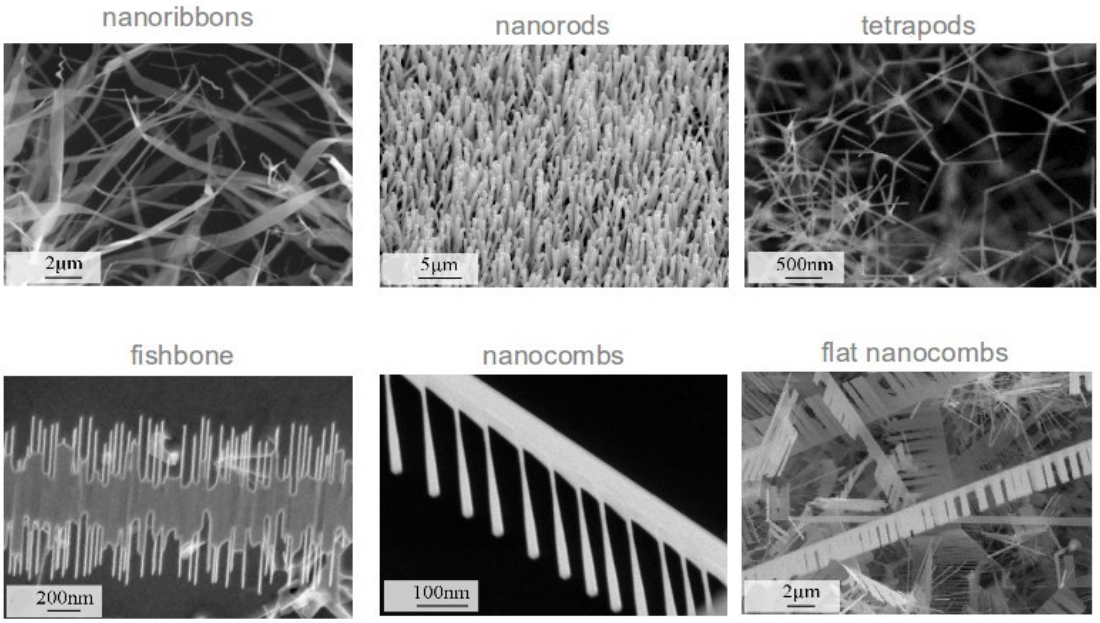

Figure 1.10 Exemplifying SEM images of some ZnO nanostructures having different sizes and shapes.

Some papers have recently reported the synthesis of ZnO nanostructures characterized by a diffuse mesoporous morphology[3,5,71,72], opening the way to a dramatic enhancement of the surface-to-volume ratio, that is one of the most attractive peculiarities of the nanosized system in general. An example of application that could take great advantage from the mesoporous structure is the gas detection, where the surface-to-volume ratio is considered to have a strong impact on the performance of the devices. Indeed, the huge amount of surface should provide a very large number of chemisorption sites for the gas molecules compared to a bulk system, and thus result in improved sensitivity and fast-response. The same reason makes these mesoporous nanostructures very promising for the fabrication of photoanodes in DSSCs, where the large area should result in a high number of sensitization sites for the chromophore molecules responsible for the light absorption, leading to a better light harvesting and so at the end to an improvement in the solar energy conversion efficiency.

The applications described in this paragraph represent only few examples of the almost countless possible applications of ZnO nanostructures. The reach of a large scale diffusion of such innovative systems requires the possibility to obtain a massive production of reliable and reproducible devices and so the understanding of the charge transport mechanism is a key challenge, since they have strong repercussions on the performances. In the same way, the design of novel devices that allow to effectively exploit the peculiarities of ZnO nanostructures remains a technological issue that will have to be faced in the next years.

1.5 Zinc oxide nanostructures in DSSC

Since the first demonstration of solar energy conversion by a dye-sensitized solar cell reported by O'Regan and Grätzel in 1991[30], TiO_2 has been considered the most suitable material for the realization of the nanoporous layer (see the scheme of DSSC reported in figure 1.4). In the following years great efforts have been dedicated to improve the initial power conversion efficiency of 7.1% and nowadays an efficiency of 11.9% has been achieved by Yella et al in a mesoscopic solar cell that incorporate a $Co^{(II/III)}$tris(bipyridyl)-based redox electrolyte in conjunction with a custom synthesized donor-π-bridge-acceptor zinc porphyrin dye as the np-TiO_2 sensitizer[31]. The possibility to obtain nanoporous TiO_2 films by low-cost processes such as spin-coating of commercially available TiO_2 nanoparticles dispersions has encouraged the employment of this material, as the nanostructured morphology is a crucial point for the large area available for dye molecules absorption as well as for providing effective light scattering in the visible wavelength range, thus extending the optical pathway of the incident light and enhancing the probability of absorption by the sensitizer. Besides, the suitable relative positions of energy levels at the semiconductor–sensitizer interface (i.e., the position of the conduction-band edge of TiO_2 at a lower energy than the excited-state energy level of the dye) allow for the effective injection of electrons from the dye molecules to the semiconductor (figure 1.11).

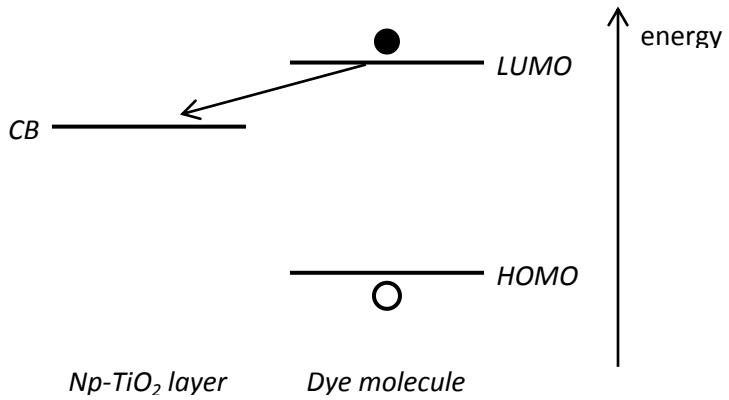

Figure 1.11 Schematization of the band alignment at the dye-TiO_2 interface.

Despite DSSCs have attracted great attention in the last two decades, thanks to their cost effectiveness, it was not possible to reach efficiency values comparable with the ones that could be achieved by other novel promising solar cells realized with other approaches (such as thin-film or crystalline Si solar cells), as pointed out by the NREL efficiency chart reported in figure 1.6. The reasons for this difficulty in enhancing the conversion efficiency in dye-sensitized solar cells are connected with several aspects, but it is generally accepted that one of the major limitation is the energy loss due to recombination between electrons and either the oxidized dye molecules or electron-accepting species in the electrolyte during the charge transport process[73]. Such a recombination is mostly derived from the lack of a depletion layer on the surface of the nanostructured TiO_2.

ZnO has been proposed as an alternative material for the preparation of nanostructured layers to be employed in DSSCs. The energy band structure and the physical properties of ZnO are similar to those of TiO_2 (table 1.1), while the electron mobility is generally higher than in TiO_2, and this could be favorable for the transport of the electron with reduced recombination loss when used as photoanode. Besides, it is well known that the band profiles in ZnO nanostructures present a bending in the regions close the surface, due to the presence of defect-related acceptor states localized on the surface. The barrier height resulting from this band bending is typically higher than 0.25 eV[74] and results in a superficial depletion layer whose dimension is 50 nm or more for an unintentionally doped sample presenting the typical value for the residual donor concentration of 10^{17} cm^{-3} [56]. This depletion layer at the nanocrystal surface acts as a shield since the built-in electric field associated with the band bending has the effect to keep the carriers confined in the inner parts of the nanostructures, spatially separated from the superficial regions where the semiconductor is in contact with the oxidized dye and the electrode, and thus preventing recombination phenomena that are detrimental for the overall efficiency.

	ZnO	TiO_2
Crystal structure	wurtzite, zinc-blende, rocksalt	rutile, anatase
Energy bandgap (eV)	3.2-3.3	3.0-3.2
Electron mobility (cm^2Vs^{-1})	205-300 (bulk)	0.1-4 (bulk)
Refractive index	2.0	2.5
Electron effective mass (m_e)	0.26	9
Relative dielectric constant	8.5	170
Electron diffusion coefficient (cm^2s^{-1})	5.2 (bulk), $1.7 \cdot 10^{-4}$ (nanoparticles film)	0.5 (bulk), $\approx 10^{-8}$-10^{-4} (nanoparticles film)

Table 1.1 Most relevant physical properties of ZnO and TiO_2. The values are taken from [73].

Although the highest efficiency of 6.6% achieved with the ZnO-based DSSC using nanoporous nanosheets of iodine-doped ZnO (ZnO:I)[75] is still significantly lower than the limit reached using TiO_2, the interest for this material is still remarkable. The appealing of ZnO for this application is raised also by the possibility to grow a wide variety nanostructures different in size and shape, thanks to its ease of crystallization and anisotropic growth.

The use of ZnO nanoparticulate films as photoanode has been widely studied, thanks to the direct availability of porous structures with assembled nanoparticles and the simplicity of synthesis of nanoparticles via chemically based solution methods. Chemical routes to obtain nanoparticles with dimensions ranging from ten to several tens of nanometers include sol-gel[76] and doctor-blade[77] methods. The reported conversion efficiencies for this kind of structures are fairly low, with values in the range 0.4-2.22%[73]. An higher efficiency of 3.4% was reported using a ZnO nanoparticulate film prepared by electrostatic spray deposition (EDS); in this case, the nanoparticle-containing precursor solution was mixed with polyvinyl alcohol (PVA) in order to avoid the agglomeration of the nanoparticles and so to control the porosity and the specific surface area of the film[78].

Preparation of ZnO-based DSSCs has been reported also using nanosheets[79], nanobelts[80] and nanotetrapod[81]. ZnO nanosheets obtained by hydrothermal growth process of previously hydrothermally grown ZnO nanoparticles have demonstrated a relatively low efficiency of 1.55%, likely due to an insufficient internal surface area[79]. ZnO films with nanobelt arrays prepared through an electrodeposition method were also studied for DSSCs applications, yielding to a PCE of 2.6%[80]. Porous networks obtained by multiple depositions of nanotetrapods having dimension in the range 1-20 µm have been also employed in DSSCs resulting in overall PCEs of 1.20-3.27%[73].

One of the major issues related to employment of ZnO in DSSCs in combination with the widely-used commercial Ru-based dyes, such as N719 and N3, is that the surface of the crystal is deteriorated when nanostructured are soaked in an acidic dye solution containing the Ru complex for an extended period of time, that is necessary to provide a sufficient load of dye on the nanostructures. In particular, it has been observed the formation on the surface of a Zn^{2+}/dye complex that, for long soaking times, can agglomerate to form a thick covering inactive for electron injection and obviously detrimental for the overall efficiency of the solar cell. This means that the sensitization time of ZnO in

acidic dyes is limited by its stability, resulting in insufficient dye adsorption and electron injection and thus poor performance of DSSCs[73].

An possible way to overcome this severe limitation is the use of different dyes from those commercially available and most used in this devices. From this point of view, the emerging of the hybrid methylammonium metal halide perovskites as sensitizers in DSSCs a couple of years ago has renewed the interest in the application of ZnO nanostructures for energy conversion, thanks to their high light-absorption coefficient and the outstanding performances they have demonstrated in traditional TiO_2-based solar cells. Recently, Son et al reported a PCE of 11.3% using 1 µm long ZnO nanorods sensitized with $CH_3NH_3PbI_3$[82]; this value might be improved by tailoring the nanorod dimensions, since it has been estimated that the best trade-off between effective light scattering and absorption and reduced recombination phenomena should be reached by 800 nm long nanorods[83]. A 5-nm-diameter ZnO nanoparticle layer of 25 nm thickness on ITO glass resulted in an overall efficiency of 15.7% for perovskite cells and 10.2% on a flexible substrate, with no high-temperature sintering required[45]. As a final remark, it is worth to stress that no stability issues concerning ZnO stability when put in contact with perovskites precursor solutions have been reported so far.

1.6 Zinc oxide nanostructures for gas sensing applications

Gas sensors play an essential role for a several applications in widely different fields. Indeed, the detection and monitoring of gaseous species is a crucial aspect for many purposes, varying from the environmental protection (pollutants monitoring, air-quality control in weather stations) to applications in automotive (car ventilation control, gasoline vapor detection), security (leaks detection, toxic/flammable/explosive gas detection), food quality control, industrial production (monitoring of fermentation or other processes) and, last but not least, human health control (breath analysis, early-stage diseased diagnosis).

In this scenario, solid-state semiconductor-based gas sensors are regarded as one of the most interesting devices, thanks to their operation simplicity, good sensitivity to ambient condition and cost effectiveness for a large mass diffusion[84–86]. The gas detection is realized by a chemical reaction that takes place at the surface of the sensor active layer, where the monitored gas molecules are chemisorbed. The semiconductor interaction with the gas molecules results in a change in the conductivity of the active layer material, so ideally the state of the atmosphere surrounding the gas sensor can be monitored by measuring the variation of the current that flows in the active layer when a constant dc bias is applied. Semiconducting metal oxides, such as SnO_2, ZnO, WO_3, TiO_2, Ga_2O_3 or NiO have been widely investigated in the last years due to their good properties including high sensitivity, rapid response, and fast recovery, even if, depending on the material properties and the chemical species to be detected, operating temperatures of some hundreds of centigrades are typically needed to have an efficient response[87–91]. As the availability of a large area for gas chemisorption is essential to achieve high sensing performances, the research has soon been focalized on nanostructured materials, owing to the dramatic increase in surface-to-volume ratio with respect to thin films or bulk. Therefore, the interest nowadays is mainly oriented towards those oxides that can be easily grown as nanocrystals, SnO_2 being the most used material in the field[68].

In this scenario, ZnO is one of the earliest discovered and most widely applied metal oxides for gas detection applications, and the first report of its employment for gas sensing purposes dates back to 1962, when a ZnO thin film prepared by vacuum evaporation of metallic Zn and subsequent oxidation

was used to detect traces of several gaseous species, such as toluene (C_7H_8), benzene (C_6H_6), ethanol (CH_2CH_3OH), propane (C_3H_8) and carbon dioxide (CO_2)[92]. Ever since, the interest in ZnO-based gas sensing has maintained high and a huge number of papers have been published about this topic, where ZnO has demonstrated high electrochemical stability, non-toxicity, suitability to doping, low cost and sensitivity to many sort of gases. The recent development of nanotechnology has further increased the interest on ZnO, thanks to the possibility to obtain a wide variety of nanocrystals with different shapes and size and enhanced properties with respect their bulk counterparts. In particular, most of the attention has been devoted to one-dimensional or quasi-one-dimensional nanostructures (as nanowires, nanorods, nanopillars or similar structures)[86,87,89], but also other morphologies, such as nanoparticles[93,94], nanoplatelets[95], nanotetrapods[68] and hierarchical structures[89] have been tested, showing promising results.

The improvement of the performances (sensitivity, fast response) is a crucial point for these devices. Similarly, the lowering of the operating temperature is required for energy saving purposes as well as for a satisfactory long-term device reliability. Moreover, another very important issue still open is the selectivity of the response of the devices to one, or a limited class of, gaseous species: most the applications of interest need the sensor to accurately monitor just one particular gas, giving a response that is not modified by the interaction with other pollutants that are generally present in a wide variety in the surrounding atmosphere, and whose influence on the sensor response would make completely meaningless any indication returned by the sensor itself. Aiming to all of these improvements, that would boost the large-scale diffusion of such devices, the understanding of the charge transport phenomena in the active layer is a key point, as well as the identification of the mechanisms related to gas absorption that are involved with the electrical transport. This kind of investigation is not trivial, since a lot of different aspects must be taken into account, related to the film morphology (presence of barriers at the point contact between two adjacent nanocrystals) and to the material itself (surface depletion, presence of high-density surface defects), and this is confirmed by the fact that, although some studies have been carried out[96–99], many aspects still have to be understood and a general model of the conduction in these systems is still missing. In the next paragraph, some general aspects concerning the electrical transport in a nanostructured semiconductive film will be described.

1.6.1 Electrical transport in a nanostructured metal oxide film

Generally, the charge transport phenomena in nanostructured metal oxide films is described assuming that a potential barrier is present at the surface of the nanocrystals[98,99].

According to the model proposed by Barsan et al.[98], that concern the transport in SnO_2 nanoparticles, the conduction in such a layer is strongly influenced by the size and the morphology of the nanocrystals. If a compact layer is considered (figure 1.12a), two different situations can present, depending on the ratio between the thickness of the layer and the Debye length λ_D, that for a *n*-type semiconductor is defined as

$$\lambda_D = \sqrt{\frac{\varepsilon k_B T}{e^2 N_D}} \tag{1.1}$$

where e is the elementar charge, k_B the Boltzmann constant, N_D the donor concentration and ε the dielectric constant of the material.

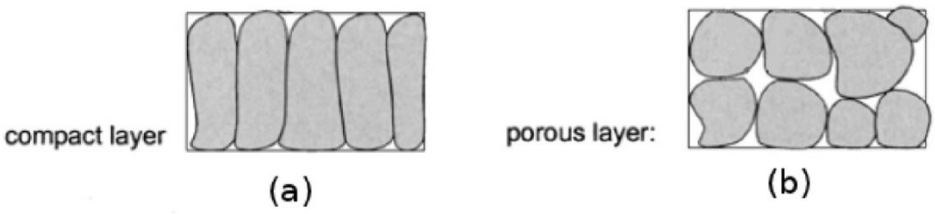

Figure 1.12 Schematization of a compact nanostructured layer (a) and a porous nanostructured layer (b). From [98].

Due to the presence of a surface potential barrier, a region depleted of charge carriers is formed close to the surface of the material (depletion layer). If the depletion layer width is smaller than the physical dimension of the layer ($z_0 < z_g$ in figure 1.13) the conduction takes place in the non-depleted region that is not depleted, whose thickness is $z_g - z_0$, characterized by a much higher conductivity with respect to the superficial depleted layer. A potential barrier eV_S is located at the surface of the nanocrystals[100]

$$eV_S = \frac{e^2 N_D}{2\varepsilon} z_0^2 \tag{1.2}$$

The depleted region present a very high resistivity and is substantially unavailable for the charge transport.

In the opposite case $z_0 > z_g$, the layer is completely depleted and highly resistive. Since the whole band bending eV_S should be located into a spatial region z_0 that is bigger than the physical thickness of the layer, the actual barrier height at the surface is $e\Delta V_S < eV_S$.

Every effect that is able to modify the charge state of the surface, such as the chemisorption of an oxidizing or reducing gas species on the surface of the nanostructures, can turn the situation of partially depleted layer into a completely depleted layer, and vice versa. Indeed, in the depletion approximation the condition of charge neutrality requires that between the charge located at the surface Q_s and the thickness z_o of the depletion layer the following relation is satisfied

$$Q_S = -eN_D z_o \tag{1.3}$$

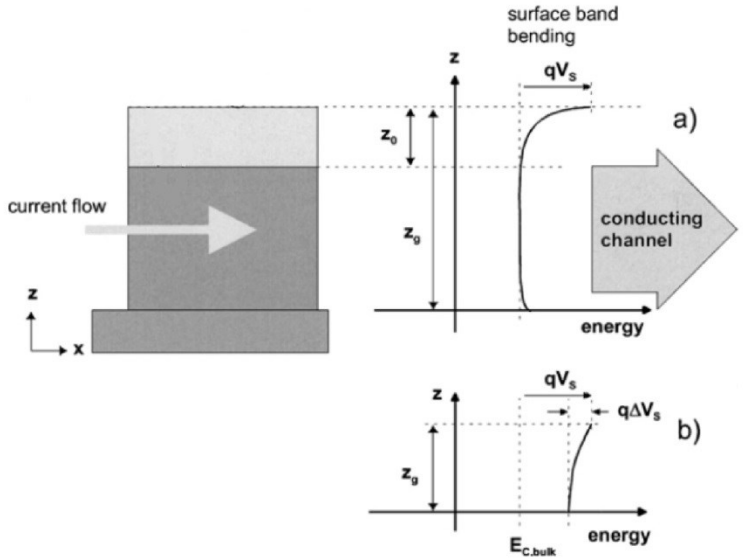

Figure 1.13 Band profiles for a partially depleted compact layer (a) and a completely depleted compact layer (b). From [98].

Similarly to the case of the compact layer, also in the case of a porous layer (figure 1.12b) the formation of superficial barriers is connected with the nanocrystals size and two different situations, represented in figure 1.14, can occur. If the size x_g of the nanostructure is bigger than two times the

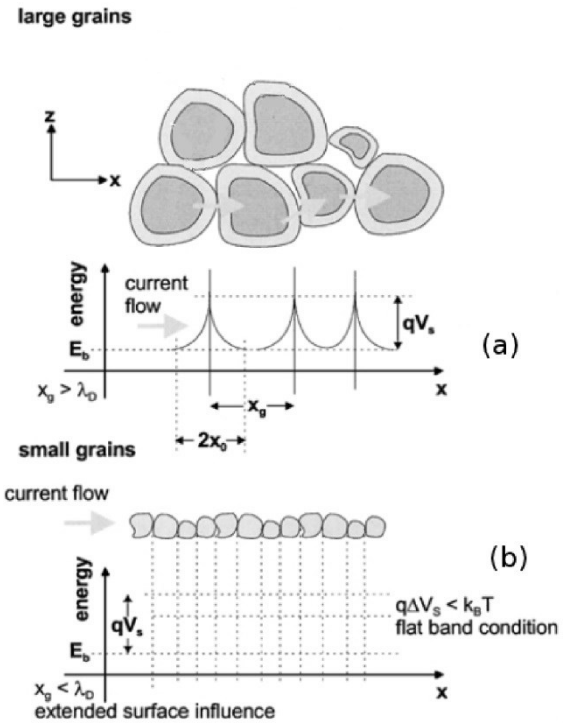

Figure 1.14 Band profiles for (a) a partially depleted porous layer and (b) a completely depleted porous layer. From [98].

thickness x_0 of the superficial depletion layer, the carrier has to pass a barrier eV_S when flowing from a nanostructure to the adjacent one (figure 1.14a). If $x_g < 2x_0$, instead, the barrier height is reduced to $e\Delta V_S < eV_S$. In this latter case, if the nanocrystal are so small that the condition $x_g < \lambda_D$ is satisfied, for the barrier height we have that $e\Delta V_S < k_BT$ and the band bending is so reduced that the conduction can be effectively approximated as the transport in flat-bands condition in a carrier depleted semiconductor (figure 1.14b)[98,99].

The description of the transport mechanisms in a porous layer is not significantly changed in the presence of a layer composed by nanocrystals interconnected by necks (figure 1.15); this is a common situation when the nanostructures, after the deposition, are sinterized by an high temperature annealing.

If the necks size is bigger than the depletion layer thickness ($z_n > z_0$ in figure 1.15a), the conduction takes place in the bulk regions that are not depleted, similarly to the case of a partially depleted compact layer. The opposite case ($z_n < z_0$, that physically corresponds to completely depleted necks) is analogous to the case of not interconnected grains (figure 1.14a); indeed, the carrier has to pass potential barriers while flowing into the layer.

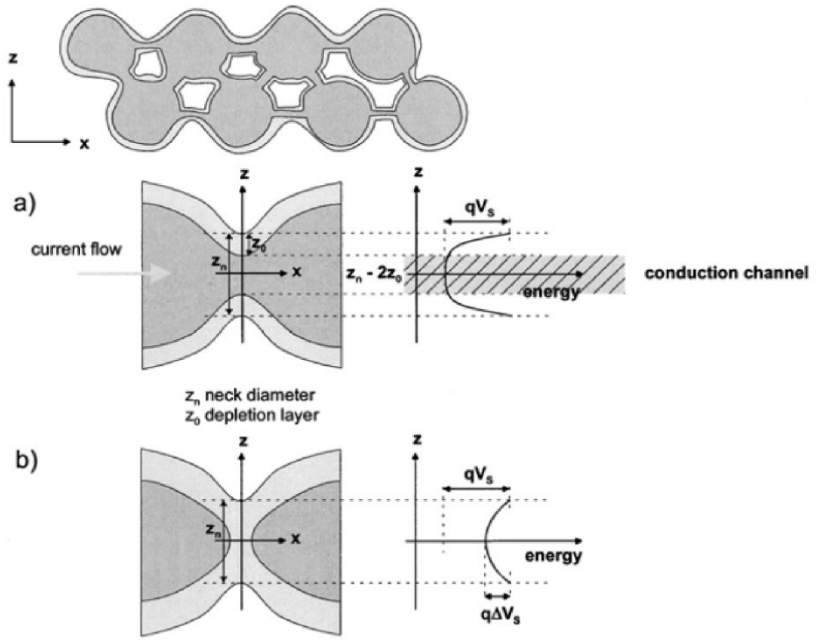

Figure 1.15 Schematic representation of a porous layer composed by nanocrystals with interconnections, for partially depleted necks (a) and fully depleted necks (b). From [98].

To summarize, the electrical conduction in a porous layer can be described by the three mechanisms represented in figure 1.16: transport in the not depleted bulk region (figure 1.16a), transport in presence of potential barriers (figures 1.16a and 1.16b) and transport in flat-band conditions in fully depleted nanostructures (figure 1.16c).

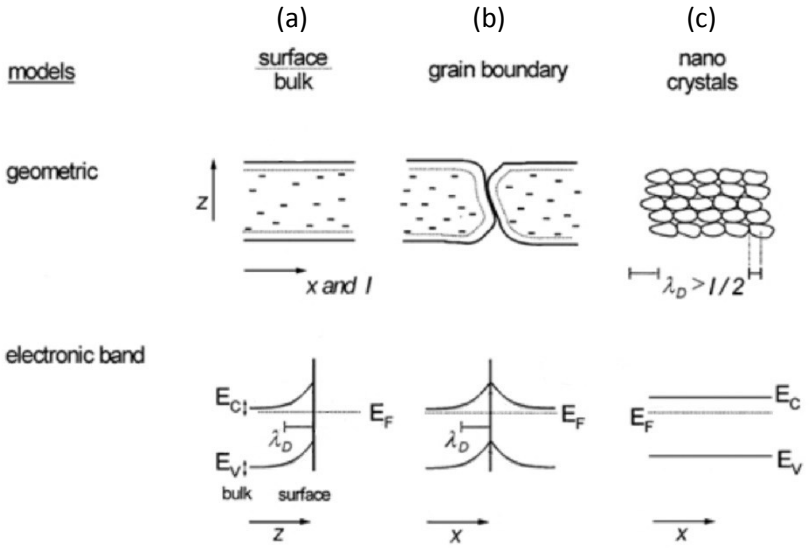

Figure 1.16 Different charge transport mechanisms in a porous nanostructured layer. From [98].

The morphology of the ZnO nanostructures studied in this work, that is mesoporous nanosheets and mesoporous nanobelts, is characterized by a diffuse porosity throughout the material, as discussed in detail in chapter 4 (see figures 4.8c and 4.27). The SEM and TEM images point out that it is not possible to identify a “bulk” region in these structures, since the pores spread in the whole crystals

that are thus composed by a sort of "network" of ZnO channels, whose diameter is typical smaller than 50 - 70 nm. In such a situation, the nanostructures can be considered as completely depleted: in fact, a typical donor concentration of unintentionally doped ZnO samples N_D = 10^{17} cm^{-3} [56] and a superficial barrier height of 0.25 eV[74], result in a depletion layer width of 50 nm, that is comparable with the size of the material channels. Therefore, it can be reasonably assumed that the conduction takes place in flat-band conditions, as schematically represented in figure 1.14b for a layer composed of completely depleted grains.

According to Many et al[101], the transport mechanisms in such a situation are determined by the ratio between the electronic mean free path λ and the diameter $2r$ of the grain, that is assumed spherical. The scattering phenomena at the surface strongly influence the mobility μ, that for this simple geometry can be expressed as

$$\mu = \frac{\mu_B}{1 + W \cdot \lambda/2r} \tag{1.4}$$

where μ_B is the bulk mobility and W the anelastic surface scattering probability. If the nanocrystals are very small, the factor $\lambda/2r$ is not negligible and the influence of the surface scattering must be taken into account. The probability W is related to the deviation of the surface structure from a simple projection of the bulk structure; more specifically, this deviation represents the difference between the scattering center concentration experienced by the carriers when they move in the proximity of the surface and scattering center concentration experienced by the carriers into the bulk. This difference in the scattering center concentration can be due to chemisorbed chemical species at the surface of the nanostructures, and so the conductivity of the porous layer is significantly influenced by the surrounding atmosphere.

In the case that the size of the grains is significantly bigger than the electronic mean free path ($2r >> \lambda$) the influence of the surface scattering becomes less important, and the state of the surface influences the conductivity mainly through the concentration of the carriers that contribute to the transport. Since the inner region of the grains are depleted, the transport takes place essentially on the surface of the nanocrystals and the conductivity is proportional to the superficial carrier concentration n_S[98]. It is worth noting that, if the negative charge localized at the surface in the acceptor states is modified (for example by the interaction with gas molecules), also the barrier height eV_S and the carrier concentration n_S are changed as well, thus resulting in a variation in the conductivity of the whole layer.

As a final consideration, it must be stressed that the nanostructures considered in this work possess a huge surface-to-volume ratio, due to their mesoporous morphology. This suggest that they can be very suitable for the fabrication of gas sensing devices, since the conduction in such systems, as discussed before, is strongly influenced by the state of the surface and so can be taken as an accurate indicator of the ambient conditions experienced by the material.

1.7 Mesoporous ZnO nanostructures from $ZnS(en)_{0.5}$ hybrid precursor

In 2008 Jang et al[3] demonstrated the possibility to obtain single-crystal mesoporous ZnO nanosheets by calcination of the hybrid $ZnS(en)_{0.5}$ precursor, prepared as powder by solvothermal route. The synthesis of the hybrid $ZnS(en)_{0.5}$ compound was reported also by Mosca et al[102], that demonstrated the possibility to obtain platelets with different sizes by changing the Zn source used in the solvothermal process. The $ZnS(en)_{0.5}$ complex belongs to the $MQ(L)_{0.5}$ [M=Zn or Cd; Q=S, Se, or Te;

and L=en (ethylenediamine, $C_2H_8N_2$) or pda (1,3-propanediamine, $C_3H_{10}N_2$) class of organic-inorganic hybrids that can be synthesized as nanocrystals by the solvothermal method, as demonstrated by Huang et al using ZnTe[103] as the inorganic component. This material is characterized by the lamellar structure schematized in fig. 1.1, where alternating planes of ZnS and ethylendiamine are stacked along the *a*-axis. The Zn atoms in the material are tetrahedrally coordinated by three sulfur atoms and one nitrogen of the ethylenediamine molecule. The alternation of Zn and S atoms forms six-membered rings that share edges to form layers that are perpendicular to the *a*-axis. These layers are then connected to each other through bonding of the nitrogen atoms, as shown in the schematic representation of the structure reported in figure 1.17.

The paper published by Jang et al[3] reported the possibility convert to $ZnS(en)_{0.5}$ nanoplatelets into mesoporous ZnS or ZnO nanosheets by proper thermal treatments. In particular, single-crystal mesoporous ZnS and ZnO nanosheets were obtained by calcination in air at 400 and 600 °C, respectively. In the same paper, the so-obtained ZnS and ZnO nanocrystals showed good photocatalytic activity. The preparation of porous ZnO nanosheets from $ZnS(en)_{0.5}$ was reported also by Nasi et al[72], that ascribed the good photocatalytic properties observed to high surface-to-volume ratio. Owing to their large specific area, these porous nanocrystals showed also good gas monitoring performances, as reported by Liu et al[5].

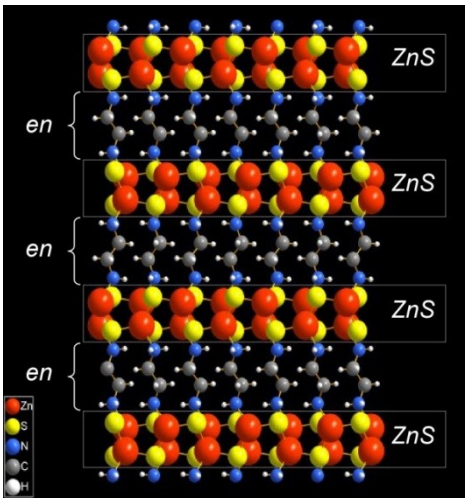

Figure 1.17 Structure of the $ZnS(en)_{0.5}$ compound along the *a*-axis.

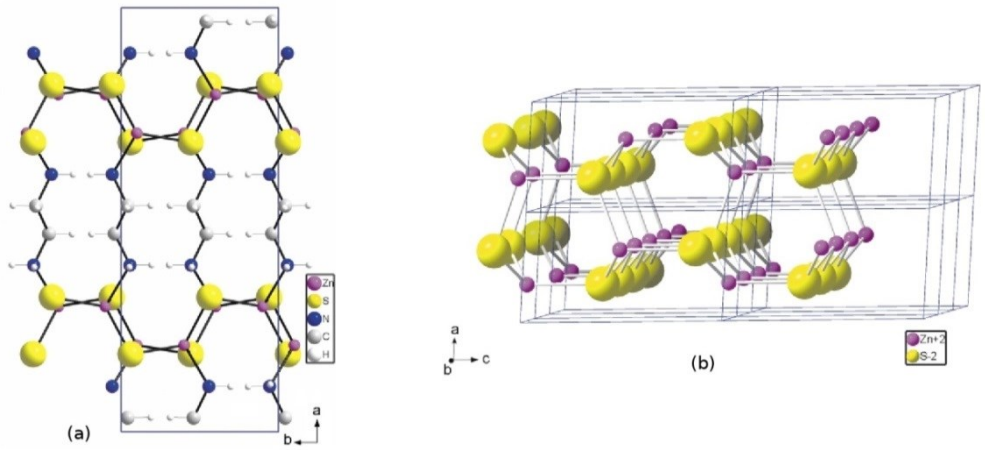

Figure 1.18 (a) View of the $ZnS(en)_{0.5}$ structure down the *c*-axis showing the ethylenediamine groups linking the layers together and (b) view of the structure of the ZnS plane down the *b*-axis showing the Zn-S rings. From [167].

The same $ZnS(en)_{0.5}$ compound was obtained in form of nanobelts supported on a Zn foil by Zhang et al[4], by adding in the solvothermal system a capping ligand agent, specifically KBH_4. In their paper, Zhang et al[4] hypothesized that tetrahydroborate ion, BH_4^-, served as a ligand to Zn and bound selectively onto particular facets of the seed particles, thus favoring a strong anisotropic growth resulting in the observed elongated structures. The as-grown hybrid nanobelts were subsequentely annealed at 300 °C in Ar atmosphere, obtaining ZnS nanobelt supported on metallic Zn foils.

CHAPTER 2
EXPERIMENTAL

2.1 Reagents and precursors

Unless stated otherwise, all the reagents and materials used in all synthesis procedures were purchased from Sigma-Aldrich and used as received, without further purifications.

2.2 Synthesis of methylammonium lead halide perovskites

In the next paragraphs the synthesis procedures followed to obtain the HOI methylammonium lead halide perovskite samples are described. Since one of the aim of this work was to study the influence of the synthesis conditions on the properties of the resulting perovskites, different synthesis parameters were used. In this section, the procedures identified as "standard" for each material are presented; all the variations to these routes and their effects on the materials will be described and discussed in detail in chapter 3.

2.2.1 Spin-coating

Typically, the perovskite samples were synthesized as a film supported on a flat 1 inch x 1 inch microscope glass slide. The deposition was made by spin coating on the substrate the proper precursor solution. During the spin coating process, schematized in figure 2.1, the precursor solution is ideally distributed upon the whole rotating substrate by the action of the centrifugal force and, at the same time, the evaporation of the solvent begins.

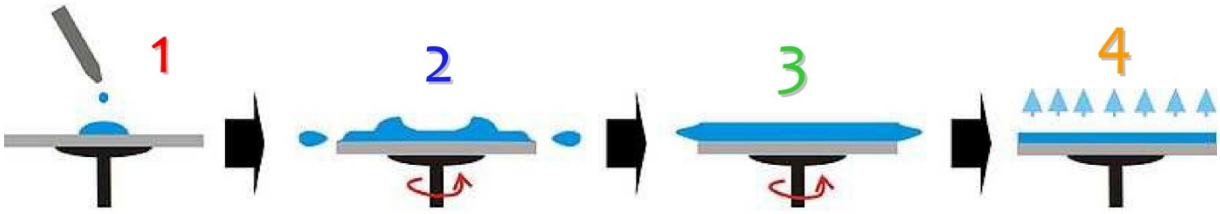

Figure 2.1 Spin coating process.

However, it has been observed that, using the glass substrates after usual solvent cleaning, it wasn't possible to reach a complete coverage of the substrate and the distribution of the material resulting from the spin coating process was very poor. This is mainly due to the low wettability of the glass substrates, that prevents an effective spreading of the solution on the rotating slide. To achieve a good uniformity of the material it is thus necessary to perform a pre-treatment on the glass slides in order to improve the hydrophilicity of their surface, since the solvents used in the precursor solutions are polar solvents. Two different treatments on the glass slides were used:

"Piranha" solution The substrates were immersed in a becker containing the so-called "Piranha" solution (H_2SO_4 and H_2O_2, 2:1 volume ratio) at a temperature of 60 °C for 15 min; then, they were rinsed for 10 times in distilled water and finally dried in blowing nitrogen.

Reactive Ion Etching The substrates were previously washed with acetone and with 10% HCl, rinsed with distilled water and absolute ethanol and dried with nitrogen. Then, they were treated with an O_2 plasma in a Reactive Ion Etching (RIE) system Plasmafab 340 for 12 min, with a pressure of 200 mTorr and a power of 300 W.

Both treatments results in an excellent coverage. In figure 2.2 the comparison between the distribution of the material with or without pre-treatment is shown.

For the scanning electron microscopy (SEM) analysis, some deposition were performed on conductive Si substrates. In this case, no pre-treatment was needed to achieve a good coverage.

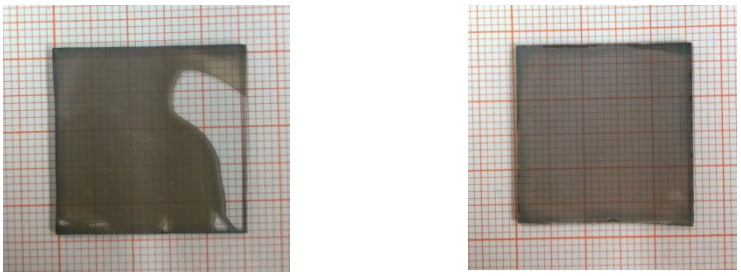

Figure 2.2 Sample without pre-treatment (left) and with RIE pre-treatment (right).

2.2.2 Preparation of MAI, MABr and MACl

Methylammonium iodide (MAI) was prepared following the procedure reported by Kim et al[1]. Hydroiodic acid (30 mL, 0.227 mol, 57 wt% in water) and methylamine (33.79 mL, 0.273 mol, 33 wt% in absolute ethanol) were stirred in ice bath for 2 h. After stirring at 0 °C for 2 h, the resulting solution was evaporated at 50 °C. The resulting powder was then washed 5 times with diethyl ether, dried in an oven at 65 °C for 20 min and finally dried overnight under vacuum.

Methylammonium bromide (MABr) was prepared following the procedure reported by Noh et al[37]. Hydrobromic acid (13.45 mL, 0.119 mol, 48 wt% in water) and methylamine (10 mL, 0,116 mol, 41 wt% in water) were stirred in ice bath for 2 h. The precipitates were recovered by evaporation at 50 °C, washed 5 times with diethyl ether and dried in an oven at 65 °C overnight. The resulting powders were dissolved in absolute ethanol, recrystallized from diethyl ether and dried in an oven at 65 °C overnight. Finally, the powders were dried under vacuum for 24 h.

Methylammonium chloride (MACl) was purchased from Fluka and used as received.

2.2.3 Synthesis of $MAPbI_3$

Three different approaches were followed to prepare methylammonium lead iodide perovskite samples:

γ-butyrolactone precursor solution The approach reported by Kim et al[1] was followed. The precursor solution (40 wt%) was obtained by dissolving MAI and PbI_2 (1:1 molar ratio) in γ-butyrolactone (99+%, Acros Organics) (GBL); typical quantities were 2 mL GBL, 383 mg MAI and 1110 mg PbI_2. The solution was maintained at a temperature of 60 °C in a silicone oil bath while stirring overnight and then spin coated on the substrate for 60 s at 1500 rpm. Samples were finally baked on a hot plate at 100 °C for 15 min under nitrogen flux. As described in section 3.1, some samples were prepared by performing this procedure in ambient air, while some other samples were prepared by performing this procedure in a Ar-filled glove box.

Dimethylformamide precursor solution The precursor solution (40 wt%) was obtained by dissolving MAI and PbI_2 (1:1 molar ratio) in anhydrous N,N-dimethylformamide (DMF); typical quantities were 0.5 mL DMF, 80.65 mg MAI and 234 mg PbI_2. The solution was maintained at a temperature of 60 °C in a silicone oil bath, was stirred overnight and then spin coated on the substrate for 60 s at 1500 rpm. Samples were finally baked on a hot plate at 100 °C for 15 min under nitrogen flux.

Two-step sequential deposition The $MAPbI_3$ film was obtained following a two-step sequential deposition by dipping a PbI_2 film into a MAI solution in 2-propanol (10 mg mL^{-1}). The PbI_2 film was formed by spin coating a 462 mg mL^{-1} PbI_2 solution in DMF; typical quantities were 1 mL DMF and 462 mg PbI_2. The solution was maintained at a temperature of 60 °C in a silicone oil bath, was stirred overnight and then was spin coated on the substrate for 90 s at 6500 rpm. After spinning, the samples were baked on a hot plate at 70 °C for 30 min under nitrogen flux. Following the procedure reported by Burschka et al[38], the so-obtained PbI_2 films were dipped in the MAI solution for 20 s, rinsed with 2-propanol and baked on a hot plate at 70 °C for 30 minutes. As discussed in section 3.1.3, this procedure didn't result in a satisfactory material formation. Therefore, we used the following different dipping procedure. The PbI_2 films were dipped in the MAI solution for 20 s, rinsed with 2-propanol and dichloromethane and baked on a hot plate at 70 °C for 5 minutes. Afterwards, the films were allowed to cool naturally and dipped again in the MAI solution for 20 min, rinsed with 2-propanol and dichloromethane and finally baked on a hot plate at 70 °C for 30 minutes.

2.2.4 Synthesis of $MAPbI_{3-x}Br_x$

Methylammonium lead I/Br mixed perovskite samples were prepared following an approach derived from Noh et al[37]. The $MAPbI_3$ solution (30 wt%, 0.785M) was prepared by dissolving MAI and PbI_2 (1:1 molar ratio) in GBL at room temperature; typical quantities were 3 mL GBL, 374.2 mg MAI and 1085.7 mg PbI_2. The $MAPbBr_3$ solution (28.5 wt%, 0.785M) was prepared by dissolving MABr and $PbBr_2$ (1:1 molar ratio) in DMF at room temperature; typical quantities were 3 mL DMF, 263.8 mg MAI and 864.9 mg PbI_2. The $MAPbI_{3-x}Br_x$ solution, with the desired *x* value, was obtained by mixing of the $MAPbI_3$ and $MAPbBr_3$ solutions in the (3-x):x volume ratio. The obtained solution was stirred for 5 min and then spin coated on the substrate for 60 s at 1500 rpm. Finally, samples were baked on a hot plate at 100 °C for 5 min under nitrogen flux.

Some samples having $x = 1$ ($MAPbI_2Br$) were also prepared following two different procedures. The first one was those reported by Qiu et al[51], using a $MAPbI_2Br$ precursor solution (20 wt%) obtained by dissolving MABr and PbI_2 (1:1 molar ratio) in DMF at room temperature; typical quantities were

1.5 mL DMF, 69 mg MABr and 284 mg PbI_2. After stirring for 1 h, the solution was spin-coated on the substrate for 60 s at 1500 rpm. Finally, the samples were baked on a hot plate under nitrogen flux for various times and temperatures that will be described in detail in section 3.3.2.

In the second approach, the $MAPbI_2Br$ precursor solution (22 wt%) was obtained by dissolving MAI and $PbBr_2$ (Fluka) (3:1 molar ratio) in DMF at room temperature; typical quantities were 2 mL DMF, 300 mg MAI and 230 mg $PbBr_2$. After stirring for 2 h, the solution was spin-coated on the substrate for 60 s at 1500 rpm. Finally, the samples were baked on a hot plate under nitrogen flux for various times and temperatures that will be described in detail in section 3.3.2.

2.2.5 Synthesis of $MAPbI_{3-x}Cl_x$

Methylammonium lead I/Cl mixed perovskite samples were prepared following two different approaches, in order to change the I:Cl ratio in the resulting material[48].

In the first approach[28], the precursor solution (20 wt%) was obtained by dissolving MAI and $PbCl_2$ (3:1 molar ratio) in DMF at room temperature; typical quantities were 2 mL DMF, 300 mg MAI and 175 mg $PbCl_2$. The solution was stirred at room temperature overnight, centrifugated and then spin-coated on the substrate for 60 s at 1500 rpm. Samples were finally baked on a hot plate at 100 °C for 1 h under nitrogen flux.

In the second approach, the precursor solution (20 wt%) was obtained by dissolving PbI_2 and MACl (1:1 molar ratio) in DMF at room temperature; typical quantities were 3 mL DMF, 618 mg PbI_2 and 90.5 mg MACl. The as obtained solution was spin-coated on the substrate for 60 s at 1500 rpm. Finally, the samples were baked on a hot plate at 100 °C for 10 min under nitrogen flux.

2.3 Preparation of functionalized ZnO nanosheets

2.3.1 Preparation of mesoporous ZnO films

Mesoporous ZnO nanosheets films were obtained by centrifugation of suspensions on flat glass substrates. Before the deposition, the surface of the glass substrates was prepared by using the "piranha" solution described in section 2.2.1; the whole cleaning procedure was the same reported in section 1.4.1. A 64 mg/L suspension of nanosheets in water was prepared, magnetically stirred for 5 min and sonicated for 1 min. Then, the substrates and the suspension were loaded into a centrifuge test tube and centrifuge cycle was applied as follows: acceleration 400 rpm s^{-1}, 4000 rpm for 5 min, deceleration 400 rpm s^{-1}. After the deposition, the samples were extracted from the test tube and dried in a vacuum oven at 65 °C overnight. Finally, a sintering treatment in oven in air was applied to the samples, according to the following ramps: first ramp 300 °C/h until reaching 400 °C; 6 minutes stop at 400 °C; second ramp 200 °C/h until reaching 450 °C; 1h stop at 450 °C; natural cooling.

2.3.2 Deposition of $MAPbI_3$ perovskite

The $MAPbI_3$ perovskite was deposited on the obtained ZnO nanosheets films by spin-coating the DMF precursor solution reported in section 2.2.3. The spin coating was performed at 1500 rpm for 60 s. After spinning, the samples were baked on a hot plate at 100 °C for 15 min under nitrogen flux.

2.4 Preparation of the ZnO nanostructures

2.4.1 Synthesis of the $ZnS(en)_{0.5}$ precursor

Two different synthesis routes were followed to obtain the $ZnS(en)_{0.5}$ in form of nanosheets and nanobelts, following the procedures reported in [102] and [71], respectively. In a standard synthesis of nanosheets, sulfur powders (3.8 mmol) were loaded into a commercial Teflon-lined autoclave (Parr 4744 digestion bomb) having 45 mL capacity together with $ZnCl_2$ (1.9 mmol), that acts as zinc source for the formation of the material. Then the autoclave was filled with ethylenediamine (30 mL), sealed and placed at room temperature into a programmable oven where the process temperature of 180 °C was reached by heating at 60 K/h and kept constant for 12 h. The oven was finally allowed to cool naturally to room temperature. The product was filtered and washed with absolute ethanol and deionized water to remove the residual impurities and the organic solvent. The resulting white powders were thoroughly washed with ethanol, deionized water and ethyl ether, and dried overnight in an oven at 65 °C.

The $ZnS(en)_{0.5}$ nanobelts were obtained as supported on 99.99% Zn foils or properly Zn metalized alumina or glass substrates. The alumina substrates were cleaned by rinsing in hot acetone and isopropyl alcohol, and dried in blowing nitrogen. Zn foils were cleaned by rinsing in hot acetone and 10% HCl. Substrate metallization was achieved by evaporating first Au contacts in a Auto 306 BOC Edwards electron beam system using a Cr adhesion layer and then covering Au by evaporating 5 µm thick Zn layers in a tailor made single source thermal ablation system. Metal patterns were defined by standard photolithography and lift-off procedures so that the Zn area was maintained at 1.5 cm^2. The syntheses were performed by adding S powder (0.25 mmol), KBH_4 (0.75 mmol), and ethylenediamine (20 mL) in the Teflon-lined autoclave. The mixture was stirred vigorously on a magnetic stir plate for 5min and then the metallized alumina substrate or the Zn foil was inserted into the liner. The autoclave was sealed, put in an oven, maintained at 200 °C for 24 h and finally allowed to cool naturally to room temperature. The substrate with synthesis products was removed from the solution, washed by rinsing in ethanol and de-ionized water and dried overnight in an oven at 65 °C.

2.4.2 $ZnS(en)_{0.5}$ precursor calcination

The as-synthesized $ZnS(en)_{0.5}$ nanocrystals were converted in mesoporous ZnO by a proper thermal annealing; the details of the decomposition of the hybrid organic-inorganic compound and the formation of the porous structure will be discussed in Section 4.1. The hybrid nanostructures were initially put in an oven at room temperature, in air atmosphere. The temperature was raised at 400 °C by heating at 100 K/h and then maintained at this value for 50 h. Then the oven was allowed to cool naturally at room temperature and heated again up to a temperature of 600 °C and maintained at this temperature for 2 h. Finally, the oven was allowed to cool down to room temperature. As a reference, some $ZnS(en)_{0.5}$ nanobelt samples were annealed at 400 °C in nitrogen flux with the same temperature ramps used for the annealing in air.

2.5 Preparation and characterization of gas sensing devices

2.5.1 Substrate preparation and active layer deposition

Mesoporous ZnO nanosheets prepared as described in section 2.4 were used as nanostructured active layer in prototypal gas sensing devices. The devices were realized on 3 mm x 3 mm alumina substrates. On the substrate, a Pt heating elements and patterned Au contacts with Cr adhesion layer were evaporated in a Auto 306 BOC Edwards electron beam system; parallel geometry on the same side of the substrate was designed for these two elements and their patterning was obtained by means of simple mechanical masks. Even if Pt heater is often put on the back side of the alumina substrate, the described parallel geometry was chosen in order to simplify bonding operations (an important detail when a cost-effective device has to be realized). A schematization of the substrate before the nanosheets deposition is shown in figure 2.3.

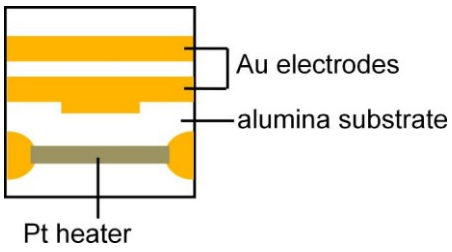

Figure 2.3 Schematization of the alumina substrate prepared with Au contacts and Pt heater.

On the prepared substrates, the active layer was created by depositing the nanosheets between the two Au contacts. To do this, nanosheets were accurately dispersed in a water suspension that was centrifugated onto the substrate with contacts, resulting in a film covering the whole area. Afterwards, the film was mechanically removed from the entire substrate except the region between the electrodes; as a result, a highly porous film of entangled ZnO nanosheets was obtained between the Au contacts (figure 2.4a). Finally, the device was ultrasonically bonded on a TO8 sample holder by using a Hybond 626 wire bonder. A floating geometry was used (figure 2.4b) so that it is possible to maintain the sensor operating temperature without heating the whole sample holder; this is an important aspect to achieve low power consumption devices suitable for portable applications.

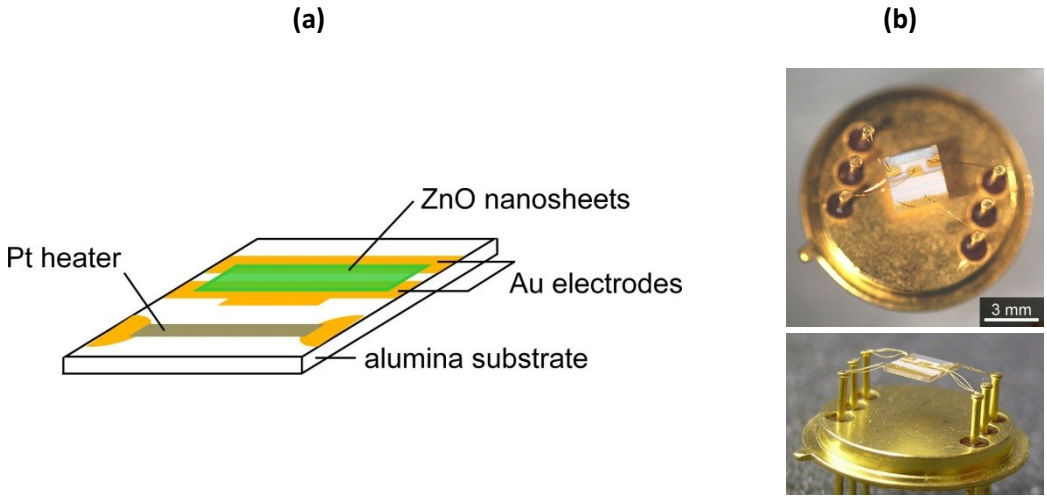

Figure 2.4 (a) Schematization of the gas sensor and (b) floating geometry bonding of the sensor on TO8 sample holder.

2.5.2 Gas sensors characterization

Gas sensing properties were evaluated using the flow-through technique under a constant 500 mL min^{-1} flow. The temperature of the sensor was controlled by setting the Pt heater resistance to the value predicted by the usual relation that correlates the resistance *R* of a Pt element and its temperature *T*

$$R(T) = R_{amb} \cdot [1 + \alpha_{Pt}(T - T_{amb})] \quad (2.1)$$

where T_{amb} and R_{amb} are respectively the room temperature and the resistance at room temperature and α_{Pt} is the temperature coefficient of Pt. For α_{Pt} the tabulated value of $3.93 \cdot 10^{-3}$ $°C^{-1}$ was assumed. The desired resistance was set by applying to the Pt heater a proper AC bias using a controller realized in the Wheatstone bridge configuration. The use of AC supply instead of the usual DC one allows avoiding the electromigration phenomena that arise when a DC bias is maintained for a long time on a Pt resistance, leading after several hours of bias application to the destruction of the resistance itself.

Electrical resistance of the sensor structure was measured by applying a stabilized 5V DC bias and measuring the current by using a Keithley 6485 Picoammeter. The measurements were performed in a home-made gas test apparatus composed by Bronkhorst El-Flow thermal mass flow-controllers, instrument-grade stainless steel lines and a 150 cm^3 test cell, where temperature and relative humidity (RH) were continuously monitored by a Pt1000 temperature sensor and a Honeywell calibrated humidity sensor, respectively. The desired relative humidity and gas concentration in the 500 mL min^{-1} flow were generated by mixing proper flows of synthetic dry air, water vapor saturated air and certified mixtures of diluted testing gas in air.

2.6 Characterization methods

2.6.1 SEM analysis

Scanning Electron Microscopy (SEM) characterization was carried out in a Jeol JSM-6400F system, using an acceleration voltage of 15 kV.

The morphological and light emission spectroscopic characterizations of the ZnO NBs were carried out using a S360 Cambridge SEM equipped with a commercial Gatan mono CL system for cathodoluminescence spectroscopic studies. The system is equipped with a grating and a multi-alkali photomultiplier sensitive in the range 350–830 nm (3.6 eV to 1.5 eV). The spectra were collected with an accelerating voltage of 10 keV and a beam current of 15 nA.

2.6.2 TEM analysis

High-Angle Annular-Dark-Field (HAADF) scanning transmission electron microscope and High-Resolution Transmission Electron Microscopy (HRTEM) were performed in a Jeol 2200FS system with an acceleration voltage of 200 keV. The same instrument was used to perform Selected Area Electron Diffraction (SAED).

2.6.3 XRD analysis

X-Ray Diffraction (XRD) on the ZnO nanosheeets and nanobelts samples was performed by using a D500 Siemens system. XRD on perovskites samples obtained as film on flat substrates were carried out in the D500 Siemens system. Some perovskites films on glass were carefully scratched from their

substrates by an edged glass slide to obtain powders; on these powders, XRD characterization was performed with a Thermo X'tra powder diffractometer equipped with Cu Kα radiation and a Thermo Electron Si(Li) solid state detector. Diffraction pattern were collected by 0.05° 2θ steps and counting times ranging from 2 to 10 s per step. These XRD patterns on powders were used to perform a Le Bail profile refinement using the program GSAS, in order to obtain the lattice parameters of the compounds that will be discussed in chapter 3.

2.6.4 Electrical characterization

The conductivity of the ZnO nanobelts were studied by current-voltage (I-V) measurements carried out in a two-probe configuration using a Keithley 2635 system. The electrical contact with the NB film on the substrate was obtained connecting two copper wires on two adjacent Zn pads, with silver paint. To investigate the temperature dependence of the conductivity, the samples were put in a tubular furnace, that allowed us to explore the temperature range 20 °C – 400 °C, in air atmosphere.

The impedance spectroscopy (IS) measurements on the ZnO nanosheets were carried out with an HP4192 impedance analyzer. The impedance was measured in the range 5 Hz – 13 MHz, using a perturbation sinusoidal signal with an amplitude of 250 mV.

2.6.5 Impedance spectroscopy

Impedance spectroscopy is a technique that allows investigating most of the electric properties of the materials. It can be used to study the dynamics of free or bonded charges in bulk or interface regions in almost every sort of liquid or solid material: ionic materials, semiconductors and dielectrics[104].

The technique is based on the measurement of the impedance of the examined sample, as a complex function of the frequency, in the desired frequency range. The measurements are performed by applying an electrical stimulus (a known voltage or current) to the sample and observing the response (the resulting current or voltage). It is assumed that the properties of the electrodes-material system are time-invariant, and one of the basic purposes of impedance spectroscopy is to determine these properties, their interrelations, and their dependences on different controllable variables as, for example, temperature, composition of the atmosphere, applied hydrostatic pressure, and applied static voltage or current bias.

The most used procedure to determine the impedance spectrum is to apply to the electrodes a sinusoidal voltage signal at a fixed frequency and measure the amplitude and the phase of the resulting current, using a proper analog circuit or a digital FFT analyzer. The frequency analyzed can range from few mHz to tens of MHz.

2.6.5.1 Impedance data analysis

As schematically represented in the diagram of figure 2.5, the interpretation of the acquired spectrum can be done following two different approaches, depending on whether or not preliminary detailed information concerning the sample are available.

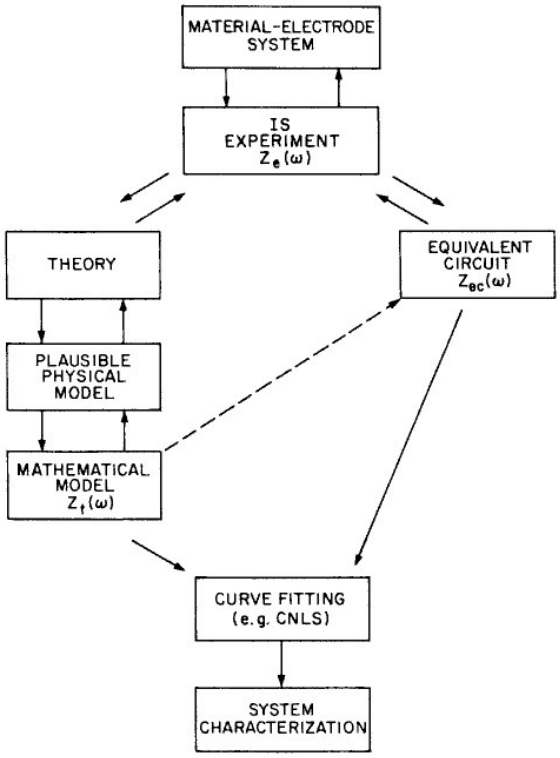

Figure 2.5 Schematization of the procedures followed for IS data.

The first approach is to create an exact mathematical model based on plausible physical considerations about the studied system, whose theoretical impedance $Z_t(\omega)$ can provide a good fitting of the data. The second approach is to find an empirical electrical circuit (the so-called equivalent circuit) whose impedance $Z_{ec}(\omega)$ describes the measured values. In both cases, $Z_t(\omega)$ and $Z_{ec}(\omega)$ depends on several parameters that can be calculated through the fitting procedure, that is usually CNLS (complex nonlinear least-squares fitting). This last choice is in general the best one, since the attempt to develop a theoretical model $Z_t(\omega)$ from lacking information could not only result in an incomplete description of the sample, but also lead to incorrect conclusions.

In this work all the impedance spectra acquired have been fitted with an empirical equivalent circuit, owing to the lack of enough details about the charge transport mechanisms in the systems in exam.

There are some limitations about the analysis of impedance spectra through an equivalent circuit. Jonscher showed that the achievement of a satisfactory best fitting of the experimental points doesn't in any way justify a juxtaposition of circuital elements and physical phenomena[105]. Sometimes it can be possible to assign a defined physical meaning to a circuital element, when this evidence is supported and confirmed by repeated measurements performed on different samples or on the same sample in different conditions.

In many cases the fitting of the impedance spectrum does not allow us to identify a unique equivalent circuit, but leads to different circuital configurations that all give a good description of the data. Indeed, in a circuit having three or more elements, it is usually possible to rearrange the interconnections, the values of the elements and their typology to still obtain the same impedance $Z_{ec}(\omega)$; an example is given in figure 2.6, where three different circuits have the same impedance value for every frequency, assuming that their elements are correlated by proper algebraic relations. However, this ambiguity doesn't compromise the possibility to identify a unique equivalent circuit to

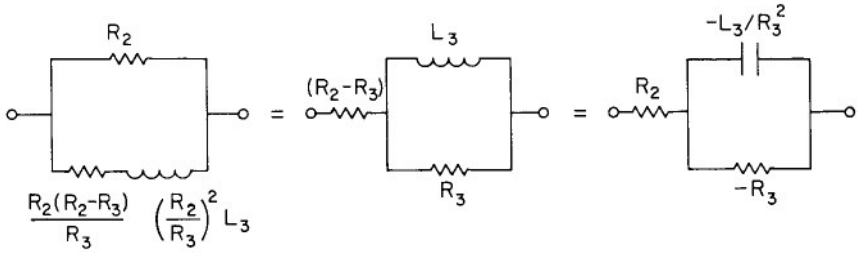

Figure 2.6 Example of three different circuits having the same impedance for every value of the frequency. The circuit elements are correlated by the equations reported in the figure. From [104].

describe the empirical data. The choice can be properly made by the comparison of different data sets $Z_{ex}(\omega)$, acquired in different experimental conditions. Otherwise, the simplicity criterion should be followed, and therefore the circuit having less elements should be assumed as the equivalent circuit of the system.

It has been observed that in several systems the experimental impedance $Z_{ex}(\omega)$ can't be effectively described by an equivalent circuit composed by a finite number of resistors, capacitances and inductances. In this case, a satisfactory best fit can be achieved by introducing a semi-empirical element, the constant phase element (CPE), whose impedance depends on two parameters A and n and is expressed by the relation

$$Z_{CPE} = \frac{1}{A(i\omega)^n} = \frac{1}{A(i\omega)}\left[\cos\left(\frac{n\pi}{2}\right) - i\sin\left(\frac{n\pi}{2}\right)\right] \tag{2.2}$$

In the expression of Z_{CPE}, only the modulus $1/A\omega^n$ depends on the frequency, while the phase $n\pi/2$ is constant and independent from the frequency. The parameter n can vary from 0 to 1; if $n = 0$, the CPE impedance can be simplified and reduces to

$$Z_{CPE} = \frac{1}{A} \tag{2.3}$$

that is the expression of the impedance of a resistor whose value is $1/A$. In the case $n = 1$, instead, the impedance of CPE is written as

$$Z_{CPE} = \frac{1}{i\omega A} \tag{2.4}$$

that is just the impedance of a capacitance A.

The physical interpretation of the CPE is related to the response of the materials to the application of external electric fields. In particular, it has been shown that the impedance expression (2.2) describes non-local relaxation processes in those systems whose dielectric response is characterized by a distribution of relaxation times instead of one single relaxation time τ, as in the simple model of the Debye relaxation[104]. Without introducing this circuital element, the description of such system would require an equivalent circuit composed by an infinite number of resistors and capacitors.

It has been proposed that such a distribution of relaxation times arises from microscopic roughness due to scratches and wells localized on solid surfaces, ion absorption processes and chemical inhomogeneities in the surfaces[106], porosity of the electrodes and in general spatially distributed properties in systems presenting inhomogeneities on the microscopic scale[107]. Although some theoretical aspects concerning the physical interpretation of the CPE are still to be clarified, this circuital elements is widely used in literature to describe the impedance of a great variety of

materials in different experimental conditions. For the purposes of this work, it is worth noting that equivalent circuits including one or more CPEs have been proposed as model for nanostructured metal oxide layers employed as active element in gas sensing devices[108–110].

2.6.6 Photoluminescence measurements

Photoluminescence (PL) spectra were collected using a Edinburgh Instruments CD900 single photon counting spectrometer. When performing PL measurements, this instrument works as a simple spectrofluorimeter: the light emitted by the light source is monochromatized and then impinges on the sample, which is excited and thus emits light in all directions. The emitted light is collected by a detector and directly analyzed by a CPU interface. Photoluminescence signals are plotted as intensity of emitted light vs. emission wavelength.

2.6.7 Absorbance measurements

The absorption spectra were collected in transmission mode using a single beam Jasco UV-vis V-530 spectrometer. In this configuration, schematized in fig. 2.7, the light beam is emitted by a proper source (in the case of Jasco V-530, a deuterium lamp in the range 190 – 350 nm and a halogen lamp in the range 350 – 1100 nm), passes through a diffraction grating monochromator and then impinges on the sample. The transmitted light is detected by a Si photodiode.

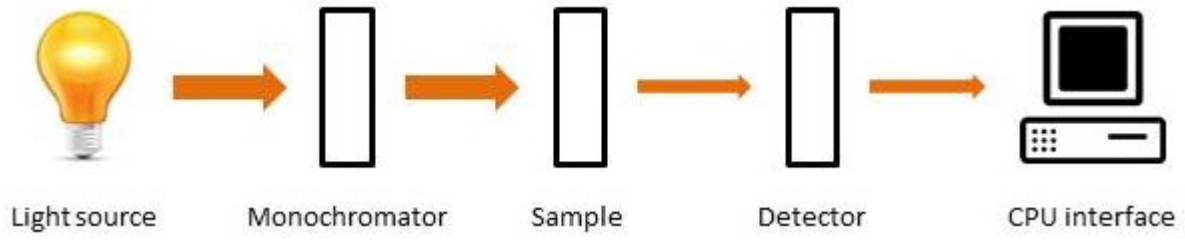

Figure 2.7 Schematization of a single-beam spectrometer working in transmission mode.

The absorbance *A* is defined as

$$A = \ln\left(\frac{I_0}{I}\right) \tag{2.5}$$

where *I* is the light transmitted through the sample and I_0 is the light transmitted through a blank sample. So, before any spectrum collection, a baseline measurement is required on a blank to determine I_0 at every wavelength.

Owing to the light scattering caused by non-flat surfaces, the transmission configuration is not the optimal one for an accurate investigation of nanostructured or rough materials, such as the ZnO nanostructures and the hybrid perovskites studied in this thesis. The light absorption in these materials can be more accurately investigated by means of diffuse reflectance measurements.

2.6.8 Diffuse reflectance measurements

The diffuse reflectance spectra were collected at the “Giacomo Ciamician” Chemistry department at University of Bologna. The measurements were performed in a double beam spectrophotometer Perkin-Elmer Lambda 45 equipped with a RSA-PE-20 integrating sphere accessory (LabSphere), whose geometry is schematized in fig. 2.8. Even if the instrument is set for double beam measurements, only one light beam is used when working with the integrating sphere, that has its

own detector (a Si photodiode) communicating directly with the CPU interface bypassing the detector of the spectrometer.

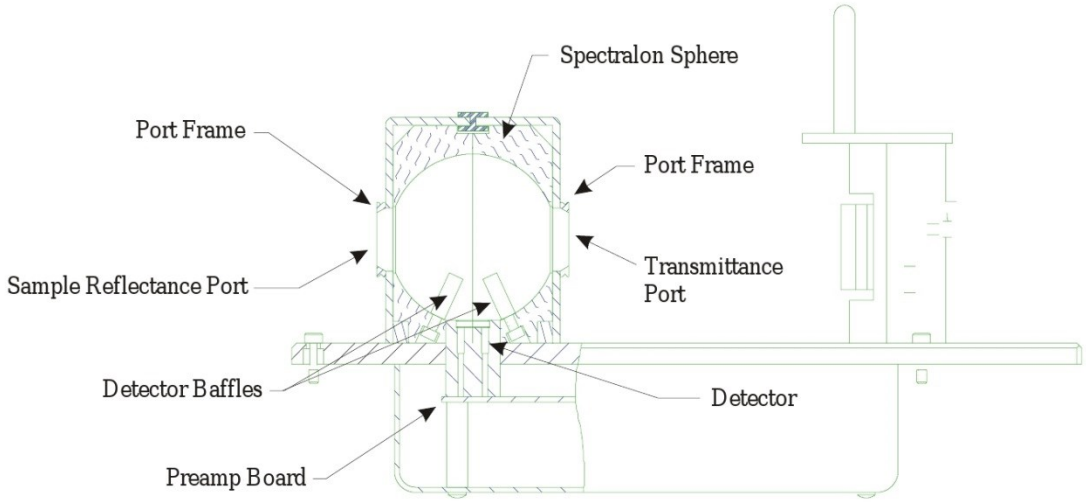

Figure 2.8 Schematization of the LabSphere RSA-PE-20 integrating sphere.

The internal surface of the sphere is completely coated by a fully fluorinated polymer named Spectralon, characterized by an absolute reflectance value very close to 1 in the whole UV-vis range. The sample is mounted on a Spectralon coated sample holder and then inserted on the surface of the sphere. The light beam, after being monochromatized, enters from the transmittance port and impinges on the sample; then the reflected light, after multiple reflections on the inner surface of the sphere, is collected by the detector which is protected by two baffles made of Spectralon, in order to avoid blinding due to the direct beam.

Before the collection of the spectra, a blank sample spectrum has to be recorded in the explored wavelength range in order to set the reference signal. Then, the CPU interface records the sample data as percentage of reflectance compared with the blank. The so-obtained diffuse reflectance spectra are then elaborated and transformed in absorbance-like spectra by using the Kubelka-Munk model, which is described in detail in the following paragraph.

2.6.8.1 The Kubelka-Munk model

The electromagnetic response of a particle assembly can be usually described from radiative transfer models that consider the stationary distribution of intensity in space resulting from the incoherent interaction of radiation with matter, in which the geometry, the radiation source distribution and the boundary conditions are well known. These models take into account the energy conservation principle, as well as the principles of electrodynamics, thermodynamics and geometric optic.

The application of radiative transfer requires assuming that the phases of the scattered light are statistically distributed and the radiation fields are independent. Under these hypotheses, it is possible the addition of the field intensities rather than the amplitudes[111]. Therefore, the model can be applied only to diluted systems or to systems where the particles are larger than the wavelength, while its applicability to submicron and nanometer sized particles must be considered as critical.

However, various many-flux models have been successfully proposed, which assume certain numbers of photons fluxes in the (+z) direction and in (-z) direction as an approach to radiative transfer

through a particle assembly. Among them, the two-flux model of Kubelka and Munk[112] is the most popular and applied, owing to its simplicity and accuracy of its predictions.

The Kubeka-Munk model is a simplified analysis of the interaction of incoming light with a layer of material (such as a layer of paint) proposed by P. Kubelka and F. Munk in 1931[112] and widely used for several typologies of materials (for example semiconductors, but even materials of industrial interest such as paper or paints[113,114]). The Kubelka-Munk theory describes the reflection, the absorption and the transmission of light through a layer of material that both scatters and absorbs light. Since it is a two-flux model, only diffuse light is considered. This simplification is appropriate in the case that strong scattering occurs, the incident light is diffuse or the surfaces considered are optically rough. The model introduces the macroscopical coefficients S (Kubelka-Munk scattering coefficient) and K (Kubelka-Munk absorption coefficient, that indicate the efficiency of the material in scattering and absorbing light, respectively. The effective scattering coefficient is related to the usual scattering coefficient s by $S = 2(1 - \zeta)s$, where the forward scattering ratio ζ is defined as the ratio of the energy scattered by a particle in the forward hemisphere to the total scattered energy. For Rayleigh scattering (light wavelength >> size of the scattering particle), $\zeta = 1/2$, while for Mie scattering (light wavelength ≈ size of the scattering particle), $1/2 \leq \zeta \leq 1$. The effective absorption coefficient is related to the usual absorption coefficient α by $K = \varepsilon\alpha$, where the average crossing parameter ε is defined such that the average path length travelled by diffuse light crossing a length dz is εdz[115]. For collimated light, $\varepsilon = 1$, while for diffuse light, $\varepsilon = 2$. It is usual in applying the Kubelka-Munk model to write $\zeta = 1/2$ and $\varepsilon = 2$, so that $S = s$ and $K = 2\alpha$.

Consider two fluxes across the x-direction through a thin layer of thickness dx in a sample of total thickness d (see figure 2.9), assuming a diffuse illumination of the sample. The flux $I(x)$ in the positive x-direction is decreased by absorption and backscattering inside the layer and is increased by backscattering of the flux $J(x)$ in the negative x-direction, therefore

$$\mathrm{d}I(x) = -(K+S)I(x)\mathrm{d}x + SJ\mathrm{d}x \tag{2.6}$$

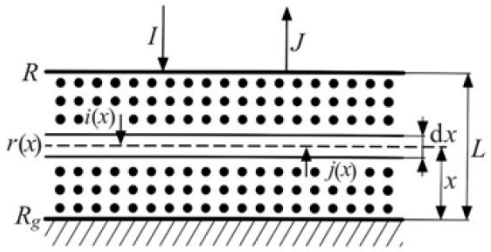

Figure 2.9 Two-fluxes Kubelka-Munk model schematization.

Vice versa, the flux $J(x)$ in the negative x-direction is decreased by absorption and backscattering inside the layer and is increased by backscattering of the flux $I(x)$ in the positive x-direction:

$$-\mathrm{d}J(x) = -(K+S)J(x)\mathrm{d}x + SI\mathrm{d}x \tag{2.7}$$

It is worth noting that the minus sign on the left-hand side of equation 2.7 is due to the convention that $J(x)$ is counted in the negative x-direction.

Equations 2.6 and 2.7 are two differential equations with two flux terms, $I(x)$ and $J(x)$; these equations can be solved only for the ratio $J(x)/I(x)$. The solutions calculated in x = 0 (front side of the

sample) and x = *d* (rear side of the sample) are of special interest. In particular, the ratio *J*(0)/*I*(0) at x = 0 defines the diffuse reflectance R_{KM} of the sample[111]

$$R_{\mathrm{KM}} = \frac{(1-\gamma)(1+\gamma)[\exp(Ad) - \exp(-\mathrm{Ad})]}{(1+\gamma)^2 \exp(Ad) - (1-\gamma)^2 \exp(-Ad)} \tag{2.8}$$

Similarly, the ratio *J*(*d*)/*I*(*d*) defines the diffuse transmittance T_{KM} of the sample

$$T_{\mathrm{KM}} = \frac{4\gamma}{(1+\gamma)^2 \exp(Ad) - (1-\gamma)^2 \exp(-Ad)} \tag{2.9}$$

In equations 2.8 and 2.9 the two parameters *γ* and *A* have been introduced. These quantities are related to *K* and *S* by the simple relations

$$\gamma = \sqrt{\frac{K}{K+2S}} \tag{2.10}$$

$$A = \sqrt{K(K+2S)} \tag{2.11}$$

Let us now consider the situation in which $Ad \rightarrow \infty$. In this situation, the transmittance defined by the equation 2.9 becomes zero. The reflectance is then the reflectance of an opaque layer; equation 2.8 becomes

$$R_\infty = 1 + \frac{K}{S} - \sqrt{\frac{K^2}{S^2} + 2\frac{K}{S}} \tag{2.12}$$

From the experimental point of view, it is not possible to estimate *K* from measurements. Instead, R_∞ and *S* are measured for opaque systems and equation 2.12 is resolved for *K*:

$$\frac{K}{S} = \frac{(1-R_\infty)^2}{2R_\infty} = F(R_\infty) \tag{2.13}$$

where $F(R_\infty)$ is the so-called Kubelka-Munk remission function.

When inhomogeneous materials are considered, probably the weakest assumption of the Kubelka-Munk theory is that a sample may be treated as continuous medium, and so reflectance properties can be described through the use of differential equations. Nonetheless, such theory is conveniently applied and by far the most widely used of the reflectance theories. One of its important applications is connected with the assumption that the Kubelka-Munk remission function $F(R_\infty)$

$$F(R_\infty) = \frac{(1-R_\infty)^2}{2R_\infty} \tag{2.14}$$

is proportional to the absorption coefficient *α*. This assumption was shown to be approximately valid for weakly absorbing powdered samples[116]. In the case of powdered or rough layers, based on this assumption the semiconductor bandgap is generally determined through diffuse reflectance measurements, as discussed in the next section. It is worth noting that the sample should be thick enough that incident light is absorbed or scattered before reaching the substrate. However, in many cases of interest the semiconductor coating may be too thin to completely absorb or scatter the incident radiation. Generally, in these cases the bandgap energy is however determined by assuming that absorbance is proportional to the K-M remission function *F*(*R*) obtained from the measured

reflectance *R*. Even if a strict theoretical justification for this procedure is still lacking, obtained bandgaps are in fair agreement with those achieved by measuring light transmission, temperature dependence of the electrical conductivity and photoconductivity[117].

2.6.8.2 Determination of the bandgap from optical properties

The value of the bandgap (E_g) for a semiconductor can be calculated from the absorption coefficient $\alpha(\omega)$. The theoretical treatment of the inter-band transitions from a microscopic point of view results in a general expression for $\alpha(\omega)$ and shows that the behavior of the absorption coefficient in the energy range of the fundamental absorption edge, for a direct bandgap material, is described by the law[118]

$$\alpha(\omega) = A\sqrt{\hbar\omega - E_g} \tag{2.15}$$

where *A* is a constant. According to the equation 2.15, the plot of $[\alpha(\omega)*\hbar\omega]^2$ as a function of the incident photons energy $\hbar\omega$ (the so-called *Tauc plot*) is a straight line, and the value of E_g is given by the intercept of this line with the energy axis. An example of such a plot is reported in fig. 1.6. This kind of elaboration is widely used in the literature for deriving the bandgap value of a vast series of semiconductors, including some materials of interest for photovoltaic applications, such as III-V compounds and copper-based chalcopyrites (CGS, CIGS); some examples are given in refs.[119–122]. An example of Tauc plot is reported in figure 2.10.

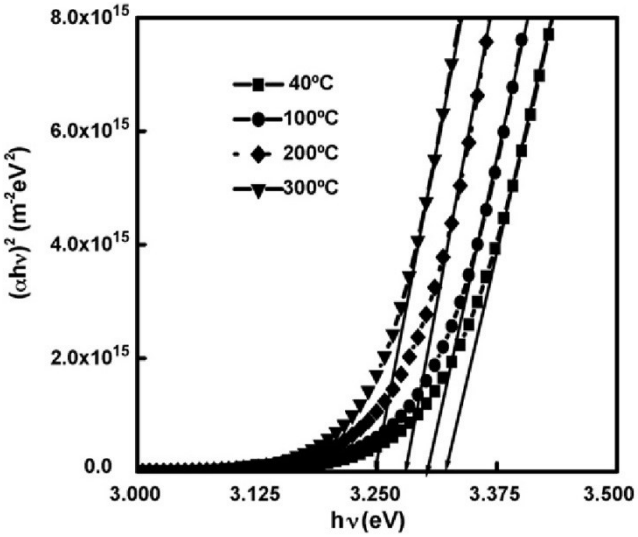

Figure 2.10 Determination of the bandgap by using Tauc plot for different ZnO samples. From [188].

From an experimental point of view, in the case of a smooth uniform film the absorption coefficient can be easily derived from an absorbance spectrum measurement on the sample, since the absorbance *A* and the coefficient α are related by the simple relation

$$\alpha(\omega) = \frac{A(\omega)}{\delta} \tag{2.16}$$

where δ is the thickness of the film. This was not the case of the materials studied in this work, that were characterized by a significant roughness of the surface, as described in section 3.1.1. Because of

this roughness, typically the absorbance spectra collected in transmission mode following the procedure described in paragraph 2.6.7 were affected by an ineliminable background in the sub-bandgap energy range, due to the scattering of the light by the irregularities of the surface of the samples. As an example, in fig. 2.11 the typical absorbance spectrum of a $MAPbI_3$ sample is reported.

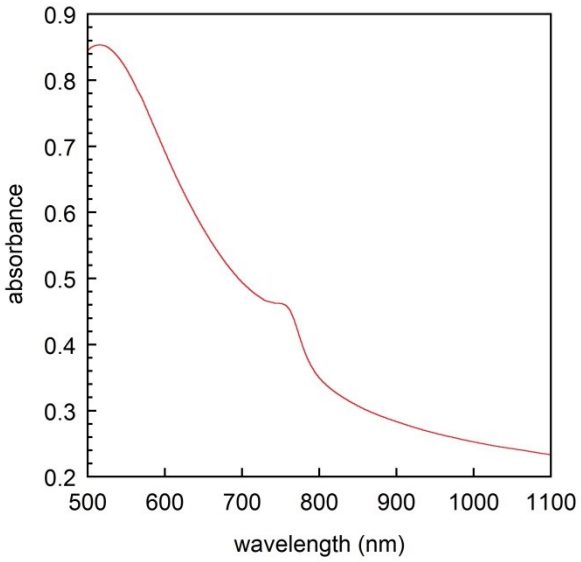

Figure 2.11 Typical absorbance spectrum of $MAPbI_3$ collected in transmission mode.

An accurate description of the absorption properties of materials having such an irregular morphology is possible only if the experimental set-up is able to detect the light that, after interacting with the sample, propagates in every direction. Diffuse reflectance performed with the configuration described in paragraph 2.7.2 is a more indicated technique to investigate the optical properties of these materials from a quantitative point of view, since the integrating sphere makes it possible to detect the light diffused in the whole solid angle[123].

2.6.9 Urbach absorption edge

The behavior of the absorption coefficient $\alpha(\omega)$ in proximity of the fundamental absorption edge was investigated for the first time by Franz Urbach. In 1953, studying light absorption in silver bromide (AgBr) crystals, he was the first to observe experimentally an exponential increase of α with the photon energy[124]. The same exponential trend, initially observed in indirect bandgap materials such as silver halides, was found by Werner Martienssen to be followed also by alkali halides with direct bandgap, for energies ranging over more than 1 eV and for absorption coefficients ranging over several decades[125].

In the subsequent decades, an Urbach-like absorption edge was observed in an impressive variety of crystalline and amorphous materials, including layered, chained and nanodimensional structures, ferroics, superionic conductors and organic molecular crystals[126,127]. So, the exponential region of α began to be referred to as the Urbach-Martienssen (or more frequently only Urbach) tail.

In the case of the Urbach behavior of the absorption edge, the temperature and spectral dependence of absorption coefficient are described by the equation

$$\alpha(\hbar\omega) = \alpha_0 \exp\left[\frac{\sigma(\hbar\omega - E_0)}{k_B T}\right] = \alpha_0 \exp\left[\frac{\hbar\omega - E_0}{E_U(T)}\right] \quad (2.17)$$

where σ is the steepness parameter of the absorption edge, E_0 and $\alpha_0 = \alpha(E_0)$ are the coordinates of the "bundle" point of convergence of the different absorption edges and $E_U(T)$ is the so-called Urbach energy, which is equal to the inverse of the slope of the edge $\Delta\ln(\alpha)/\Delta(\hbar\omega)$. An example of typical spectral dependence of absorption edges for different temperatures is reported in figure 2.12, illustrating the Urbach absorption edge for a superionic conductor material such as Cu_7GeSe_5I.

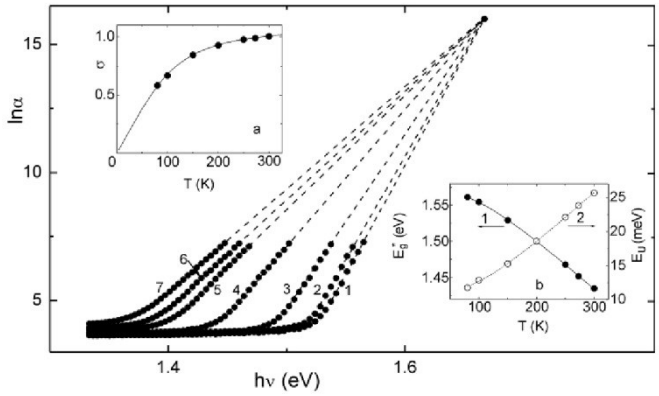

Figure 2.12 Spectral dependence of the Urbach absorption edge for Cu_7GeSe_5I crystal at various temperatures *T*: 80 K (1), 100 K (2), 150 K (3), 200 K (4), 250 K (5), 273 K (6), 300 K (7). The insets show the temperature dependences of the steepness parameter σ (a), optical bandgap E_g (1b) and the Urbach energy E_U (2b) (from[126]).

From a theoretical point of view, the understanding of the fundamental basis of the Urbach edge phenomena is still to be achieved. However, it is generally accepted that the exponential increase of the absorption coefficient below the absorption edge results from the electronic transitions between the tail of density-of-states at the top of the valence band and the one at the bottom of the conduction band[126]. It is known that the Urbach energy E_U is related to the crystalline lattice disordering caused by structural peculiarities as well as induced by external factors. According to Skumamch et al, E_U can be generally expressed as the sum of three different contributions[128]

$$E_U = (E_U)_T + (E_U)_X + (E_U)_C \quad (2.18)$$

where $(E_U)_T$, $(E_U)_X$ and $(E_U)_C$ are respectively the energy contributions of the temperature disordering, structural disordering, and compositional disordering. The nature of the temperature contribution $(E_U)_T$ is essentially phononic, since this sort of disorder is mainly caused by the lattice thermal vibrations. The structural disordering $(E_U)_X$ can be intrinsic (caused by intrinsic defects of structure, e.g. vacancies or dislocations) or induced by external factors (deviation from stoichiometry, doping, ion implantation, hydrogenation, etc.), while the compositional disordering $(E_U)_C$ is caused by atomic substitution in mixed crystals, such as alloys.

In literature, there are a lot of papers reporting the analysis of the Urbach energy to investigate the lattice disorder of a great variety of materials, both crystalline and amorphous; some examples are given in refs.[129–131]. Recently, indications about structural and compositional disorder on perovskites films have been derived from the Urbach absorption edge, as reported by DeWolf et al for $MAPbI_3$ samples[131] and by Sadhanala et al for mixed $MAPbI_{3-x}Br_x$ samples[50].

CHAPTER 3
HYBRID LEAD HALIDE PEROVSKITES

3.1 $MAPbI_3$ perovskites

3.1.1 $MAPbI_3$ perovskites from γ-butyrolactone precursor solution

$MAPbI_3$ perovskite were initially synthesized from GBL precursor solution. The bright yellow precursor solution was deposited on glass substrates, obtaining a milky yellowish layer at the end of the spin-coating processes. When performing the subsequent baking, a color change from yellowish to dark brown occurred, indicating the beginning of the perovskite formation process.

In the early stages of the activity, the precursor solution preparation and the spin-coating process were performed in ambient air, with a humidity typically ranging from 30% to 50%. The XRD pattern of the film obtained, for a baking at 100 °C for 15 min, is reported in figure 3.1. The synthesized $MAPbI_3$ has a perovskite tetragonal structures, in agreement with experimental and theoretical data reported in literature [37,51,132,133]. The film obtained on flat glass substrate is poorly oriented.

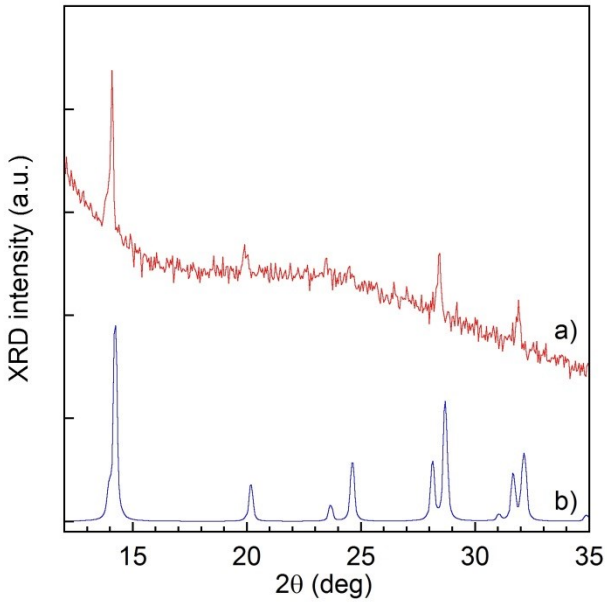

Figure 3.1 XRD pattern of (a) $MAPbI_3$ film obtained from GBL precursor solution, compared with (b) those calculated by Poglitsch et al[133].

To allow a more accurate XRD characterization, $MAPbI_3$ fine powders were obtained by carefully scratching the films using an edged glass slide and analyzed (figure 3.2). The powder XRD pattern was used to perform a LeBail refinement with the program GSAS[134], that confirms that the obtained $MAPbI_3$ has a tetragonal structure with lattice parameters a = 8.8755(5) Å and c = 12.6735 Å and a total cell volume of 998.35 $Å^3$. These values are in good agreement with those reported in literature[132,133,135].

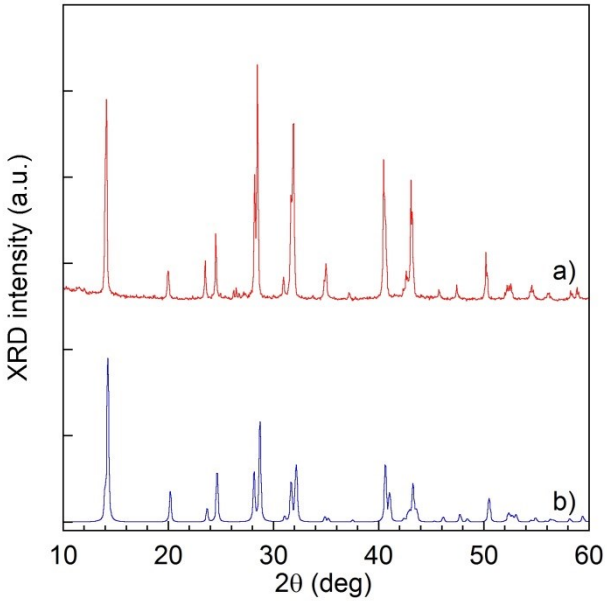

Figure 3.2 XRD patterns of (a) $MAPbI_3$ powders obtained by scratching the film obtained on glass substrate compared with (b) the calculated $MAPbI_3$ pattern[133].

SEM images of the sample (figure 3.3) point out that the films obtained by this method are characterized by a highly inhomogeneous morphology. For the standard thermal treatment (100 °C for 15 min), the resulting $MAPbI_3$ film is composed by structures having a circular shape with diameters ranging from 0.5 µm to 10 µm (figure 3.3), in good agreement with what is reported by Burschka et al for films prepared following this procedure[38]. The uncovered glass substrate can be observed in between these circular structures, indicating that the film does not provide a complete coverage of the substrate.

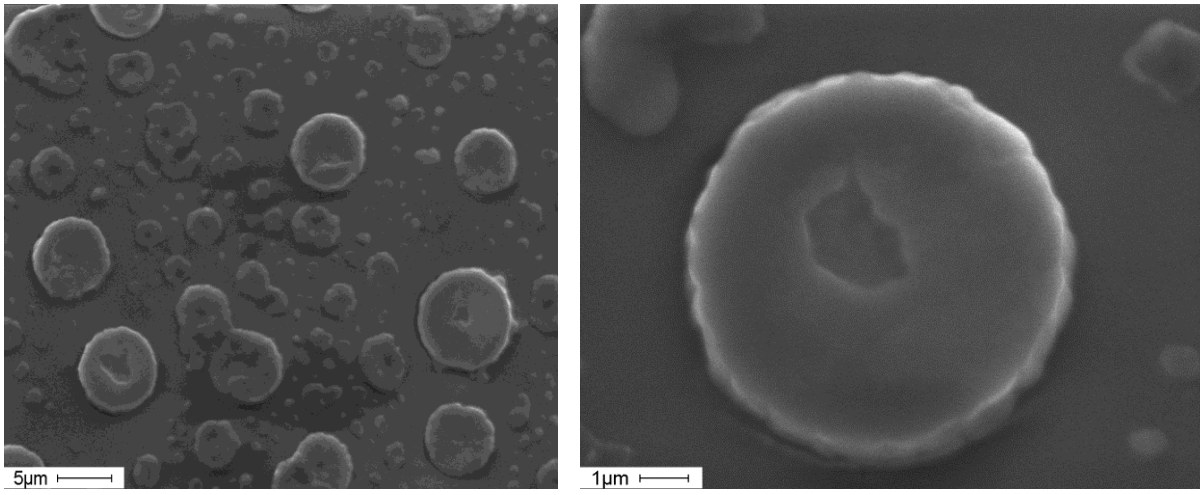

Figure 3.3 SEM images of a $MAPbI_3$ film obtained from GBL precursor solution.

This strongly inhomogeneous morphology has a great influence on the flatness of the films, that was investigated by means of step profiler measurements. In figure 3.4 the profile of a typical sample is reported. It can be observed that the surface is characterized by a pronounced roughness, that is comparable with the thickness itself of the film. To quantify the film roughness, the root mean square roughness (R_{RMS}) was calculated, defined by

$$R_{RMS} = \sqrt{\frac{1}{N}\sum_{i=1}^{N}(y_i - y_M)^2} \tag{3.1}$$

where y_i is the height of the i-esim point on the surface and y_M is the mean thickness of the film. The R_{RMS} value obtained for the profile reported in figure 2.5 is 390 nm, that is comparable with the film mean thickness itself, estimated to be 595 nm. The very irregular morphology is also confirmed by optical microscopy observations, where a great number of small holes spreading throughout the samples can be detected.

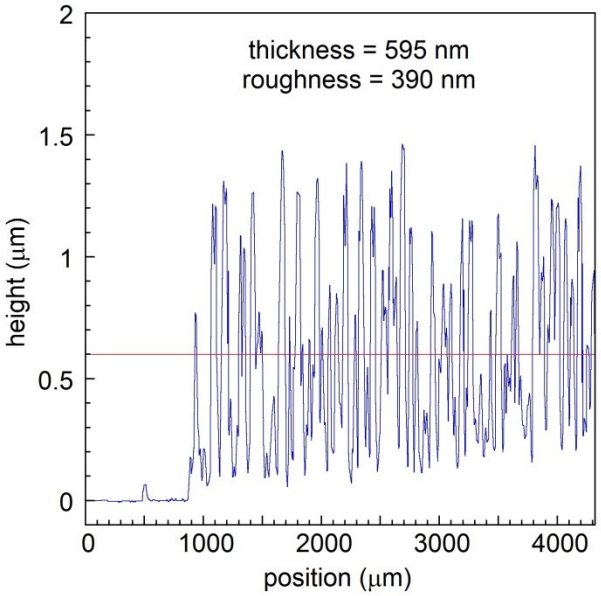

Figure 3.4 Step profiler analysis of a $MAPbI_3$ film obtained from GBL precursor solution. The red line indicates the mean thickness (595 nm). The estimated R_{RMS} is 390 nm.

This surface roughness results in light-scattering, that gives a significant background in the absorbance measurements carried out in transmission mode (figure 3.5). Therefore, an accurate analysis of the optical properties on these samples is possible only by means of diffuse reflectance measurements carried out with the integrating sphere setup (see section 2.6.8). Light-scattering is observed also for samples prepared from DMF precursor solution and by two-step sequential deposition (figure 3.5), whose morphology will be discussed later.

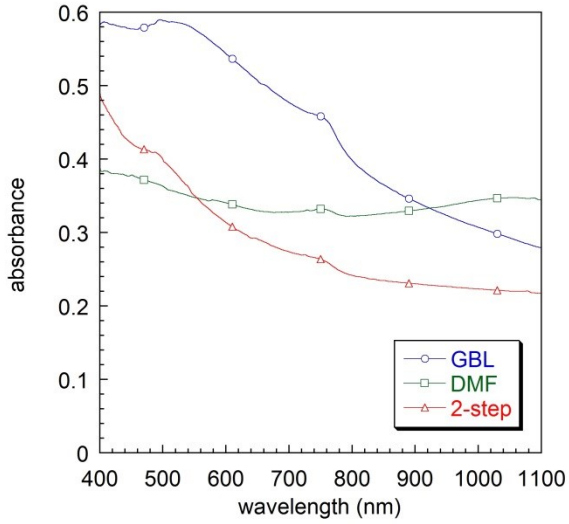

Figure 3.5 Absorption spectra of $MAPbI_3$ films acquired in transmission mode.

In figure 3.6 a typical diffuse reflectance spectrum of $MAPbI_3$ film prepared from GBL precursor solution is reported. The diffuse reflectance presents a strong drop located approximatively at 780 nm. For wavelengths shorter than this value, no other significant features of the spectra can be observed. Similar diffuse reflectance spectra were observed for $MAPbI_3$-sensitized TiO_2 films by Kim et al[1].

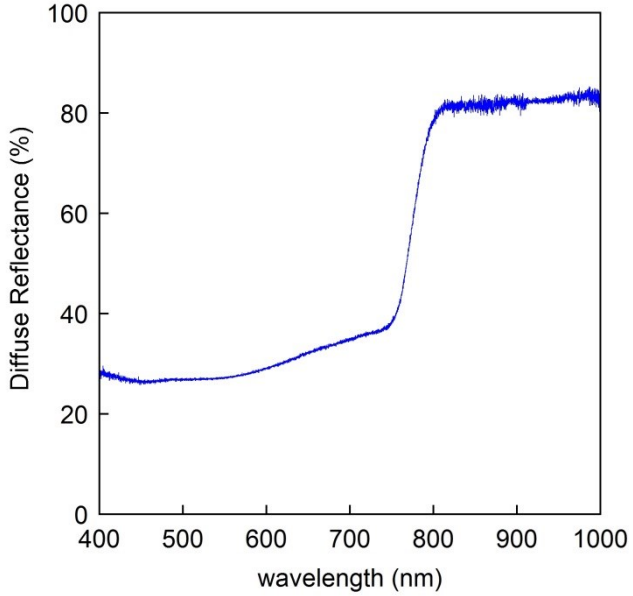

Figure 3.6 Diffuse reflectance spectra of $MAPbI_3$ sample prepared from GBL precursor solution.

The Kubelka-Munk model described in section 2.6.8.1 was used to transform the diffuse reflectance data in absorbance-like spectra. Figure 3.7 shows that no significant absorption is observed in the infrared wavelength range, while for $\lambda \approx 780$ nm the absorbance of the samples has a sharp increase corresponding to the fundamental absorption edge[37,82,136]. The dark grey/black color that

characterizes the samples is a direct consequence of this absorbance behavior, as the light absorption of the material covers all the visible range.

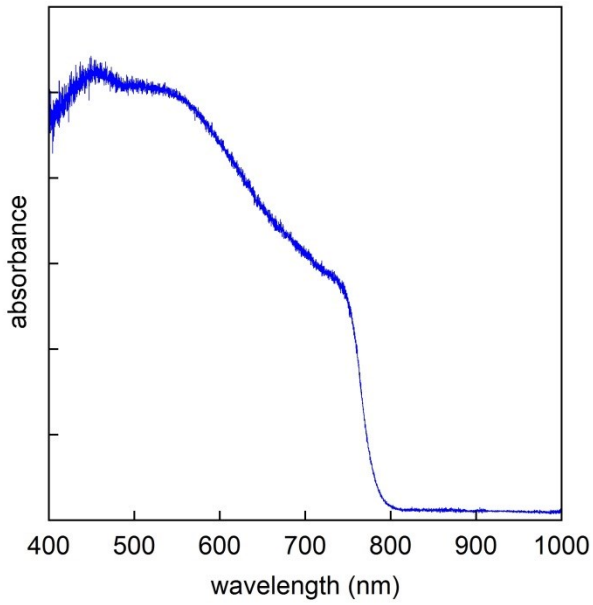

Figure 3.7 Absorbance spectrum for $MAPbI_3$ sample prepared from GBL precursor solution.

The corresponding Tauc plot (see section 2.6.8.2) is reported in figure 3.8. The estimated optical bandgap E_g is 1.60 eV, in good agreement with both experimentally measured data ranging from 1.50[24,25] to 1.63 eV[26] and results from density functional theory (DFT) calculations (E_g = 1.63 eV)[137]. It is worth noting that this value is close to the 1.0-1.5 eV E_g range indicated as the optimal bandgap range for a direct semiconductor to be employed in solar applications, yielding the maximum theoretical conversion efficiency[138].

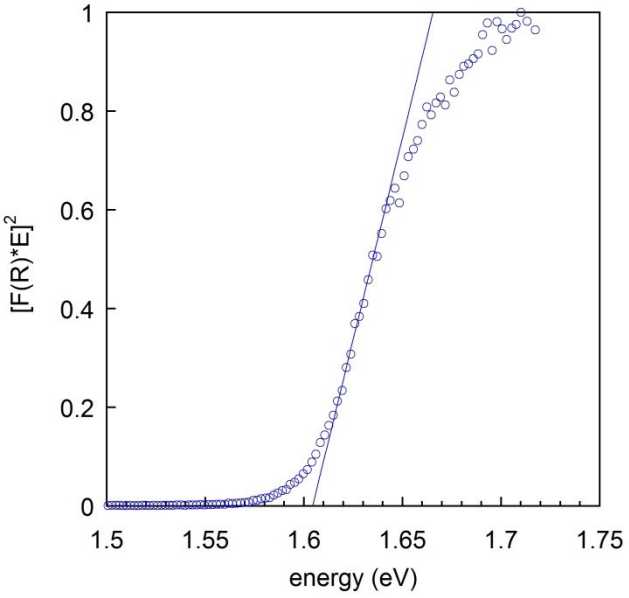

Figure 3.8 Determination of the optical bandgap via Tauc plot for $MAPbI_3$ sample prepared from GBL precursor solution.

3.1.2 $MAPbI_3$ perovskites from dimethylformamide precursor solution

Figure 3.9 shows the typical XRD pattern obtained for $MAPbI_3$ films synthesized from DMF precursor solution. The comparison with the XRD pattern calculated by Poglitsch et al[133] points out that $MAPbI_3$ perovskite is achieved when DMF is used, with the predicted tetragonal structure. Only two diffraction peaks can be observed in the pattern; since in the Bragg-Brentano geometry only the reflection sequence related to the row of the reciprocal lattice normal to the film plane is observed, this indicates that the obtained films are highly oriented. As a consequence, the diffraction peaks of the samples prepared from DMF-based solution are significantly higher than XRD peaks of the samples prepared from GBL-based solution. These observations suggest that the use of DMF instead of GBL results in more oriented films.

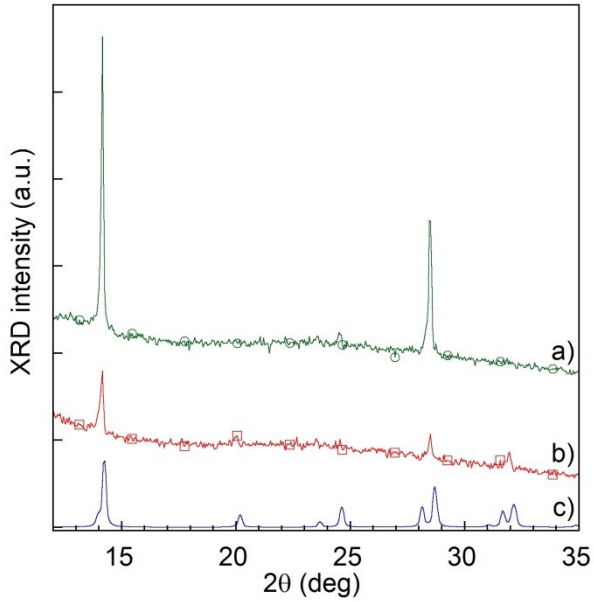

Figure 3.9 XRD patterns of (a) $MAPbI_3$ film obtained from DMF precursor solution and (b) $MAPbI_3$ film obtained from GBL precursor solution compared with (c) those calculated by Poglitsch et al[133].

The solvent used in the precursor solution heavily affects also the morphology of the obtained $MAPbI_3$ film. In figure 3.10 the SEM images of the perovskite film obtained by spin coating of DMF precursor solution are shown for a sample annealed with the standard thermal treatment (100 °C for 15 min). As in the case of GBL-based solution, it is not possible to obtain a spatially continuous film, and the morphology of the sample is highly inhomogeneous; in this case the film is composed by needle-like structures several tens of microns long, instead of the circular structures observed in the films obtained using GBL (see figure 3.3). The uncovered glass substrate can be observed in between these acicular structures (figure 3.10b), indicating that the film does not provide a complete coverage of the substrate.

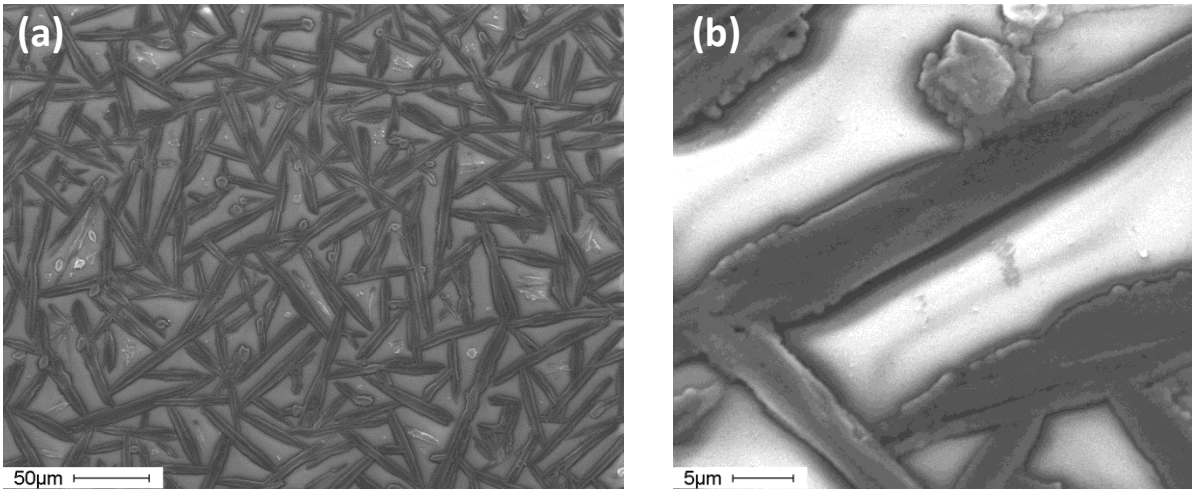

Figure 3.10 SEM images of a $MAPbI_3$ film obtained from DMF precursor solution.

In figure 3.11 a magnification of these needle-like structures is showed. It can be observed that these structures are aggregates composed by small grains having dimensions ranging from 100 nm to few microns. These results are in good agreement with the results reported by Burschka et al[38].

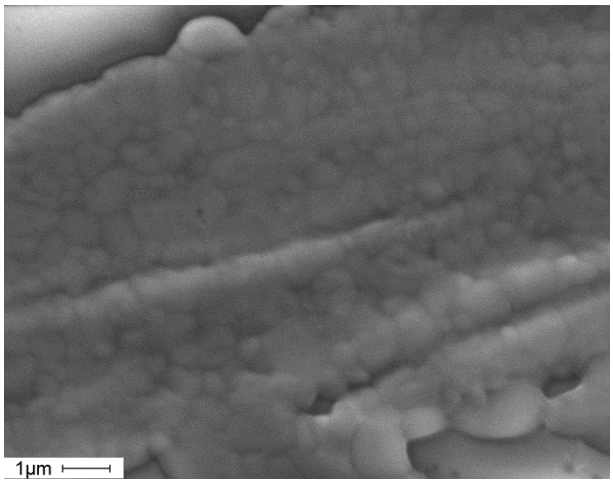

Figure 3.11 SEM image of a needle-like structure in $MAPbI_3$ film obtained from DMF precursor solution.

The different morphology highlighted by SEM images reported in figure 3.3 and 3.11 and the different film orientation degree indicate that the solvent plays a key role in the crystallization process that leads to the hybrid perovskite formation. As GBL and DMF have different vapor pressures, 1.5 mmHg and 2.7 mmHg respectively at room temperature (Sigma-Aldrich), the velocity of the evaporation during the spin-coating and the baking processes is expected to be significantly higher for DMF than GBL. Since the self-assembling process is triggered by the solvent evaporation, the formation of the perovskite crystals is expected to take place in a shorter time interval when DMF is used, resulting in different morphological properties of the obtained material.

The diffuse reflectance (figure 3.12a) and absorbance (figure 3.12b) spectra show that the fundamental absorption edge is located at approximatively the same wavelength both for $MAPbI_3$ from GBL solution and DMF solution. The optical bandgap value E_g achieved via Tauc plot for films

obtained from DMF solution is 1.60 eV (figure 3.13), in agreement with those observed in films obtained from GBL solution.

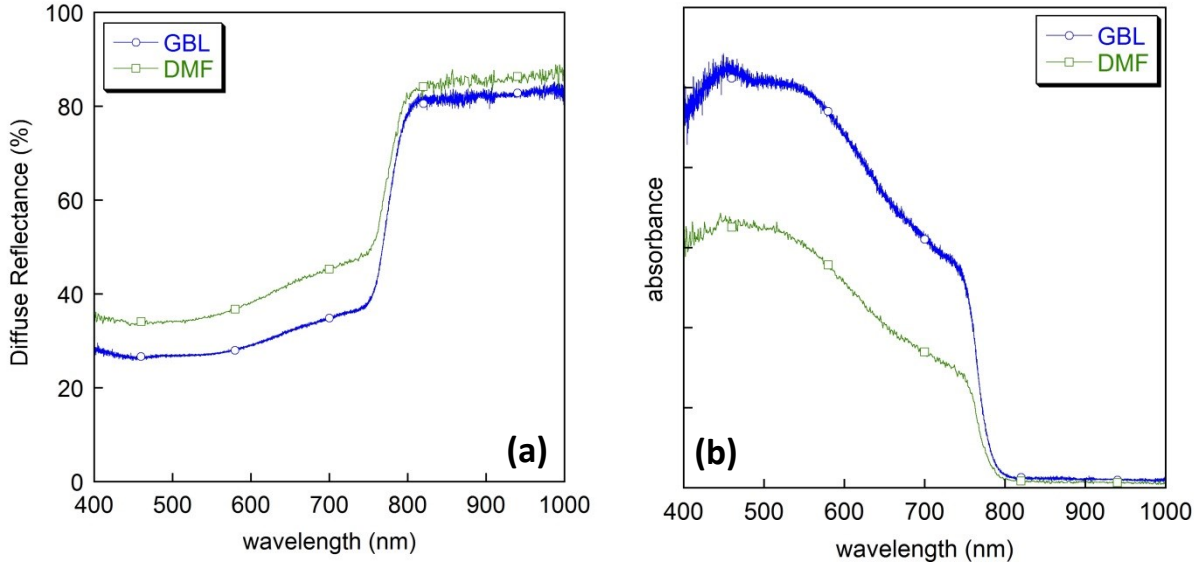

Figure 3.12 (a) Diffuse reflectance and (b) absorbance spectra for $MAPbI_3$ samples prepared from GBL and DMF precursor solutions, respectively.

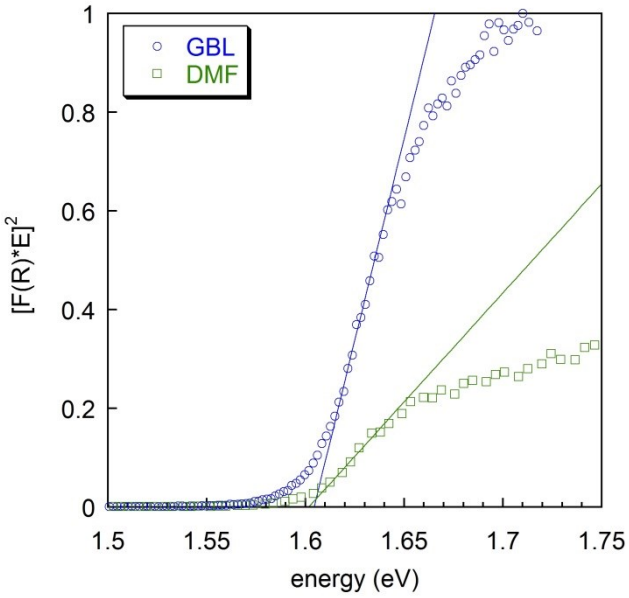

Figure 3.13 Tauc plot for $MAPbI_3$ samples prepared from GBL and DMF precursor solutions, respectively.

3.1.3 $MAPbI_3$ perovskites from two-step sequential deposition

This large variability in the $MAPbI_3$ films obtained from precursor solutions prepared with different solvents has been observed in literature and is claimed to be one of the reason of the wide spread in the photovoltaic performances of the resulting devices[38]. Aiming to higher performances, a more uniform and controllable morphology of the perovskite layer would be desirable.

In July 2013 Burschka et al demonstrated that, by following a two-steps sequential deposition route, it was possible to obtain a $MAPbI_3$ film having a good uniformity without spurious residual phases in it[38]. Basically, their technique consisted in the conversion into $MAPbI_3$ perovskite of a previously deposited PbI_2 film, by dipping it in a proper MAI solution. When applied to the fabrication of solid-state mesoscopic solar cells, this deposition procedure resulted in an overall efficiency of approximately 15% with an impressive reproducibility of the devices performances. In their paper, the authors pointed out that the conversion of PbI_2 into perovskite was greatly facilitated in the case PbI_2 had been deposited on a nanostructured TiO_2 network; indeed, in this circumstance the nanoporous geometry of the scaffold forces PbI_2 to form nanometric-sized crystals that show an high conversion rate. On the other hand, in the case PbI_2 had been deposited on a flat substrate, the authors reported the incomplete perovskite formation, with a great amount of unreacted PbI_2 in the final film even for dipping times longer than 45 min.

The attention towards hybrid perovskite films deposited on flat substrates has strongly increased in the last year, as some prototypal perovskite-based solar cells having a planar heterojunction geometry have shown promising performances[41,45,139], so that some researchers believe that the thin-film planar setup is one of the future directions for the perovskite technology that could further increase the efficiency values towards the 20% and 25% thresholds[35]. Therefore, the application of a two-step, or multi-step deposition to achieve well-formed $MAPbI_3$layers on planar substrates, such as glass or transparent conductive oxides, is a deal of great interest, despite the technological difficulties reported concerning the long times required to convert the PbI_2 crystal structure by infiltrating MAI[140] and the dissolution of the perovskite material that occurs when it is put in contact for a long time with the solvents typically used to prepare the MAI solution.

Following this idea, we investigated the possibility to obtain a well formed $MAPbI_3$ layer on flat glass substrates with a two-step deposition technique. As described in paragraph 2.2.3, the general approach that we followed was to spin-coat a uniform PbI_2 film on the substrates and then to dip them in a proper MAI solution. Before the dipping, the PbI_2 films were characterized by a good uniformity and a bright yellow color. We observed that, as soon as the film was put in contact with the MAI solution, the color turned to brown, indicating the beginning of the perovskite formation. Nonetheless, the possibility to obtain a complete conversion of PbI_2 into perovskite, as well as a satisfying uniformity of the finally obtained films, were found to strongly depend on the followed dipping procedure.

As a first attempt, the PbI_2 film was dipped in the MAI solution for 20 s, rinsed with 2-propanol and finally dried on a hot plate at 70 °C for 30 min to remove the excess solvent, as reported for the conversion of PbI_2 into $MAPbI_3$ on mesoporous scaffolds by Burschka et al[38]. At the end of the process, a dark brown film on glass substrate was obtained, characterize by a poor uniformity. However, the XRD pattern (figure 3.14a) shows the presence of the peaks related to the perovskite tetragonal phase together with a peak located at $2\theta = 12.7°$ that was identified as a reflection of the hexagonal PbI_2 phase (JCPDS n. 73-1754), indicating a non-complete conversion of the PbI_2 film. The remarkable height of the PbI_2 peak with respect to the perovskite peaks indicates that in the sample a huge amount of unconverted PbI_2 is still present, suggesting that the dipping time must be significantly increased to achieve a complete conversion. However, the increasing of dipping time up to 20 minutes didn't result in a complete PbI_2 conversion (figure 3.14b); besides, after 20 min dipping the obtained films showed a light grey color, indicating a partial dissolution of the perovskite. The

dissolution of $MAPbI_3$ in 2-propanol for long times has been reported by Burschka et al[38] and could hamper the possibility to obtain good films on flat substrates by using this method, as the polar solvents required to dissolve MAI are expected to dissolve the perovskite as well.

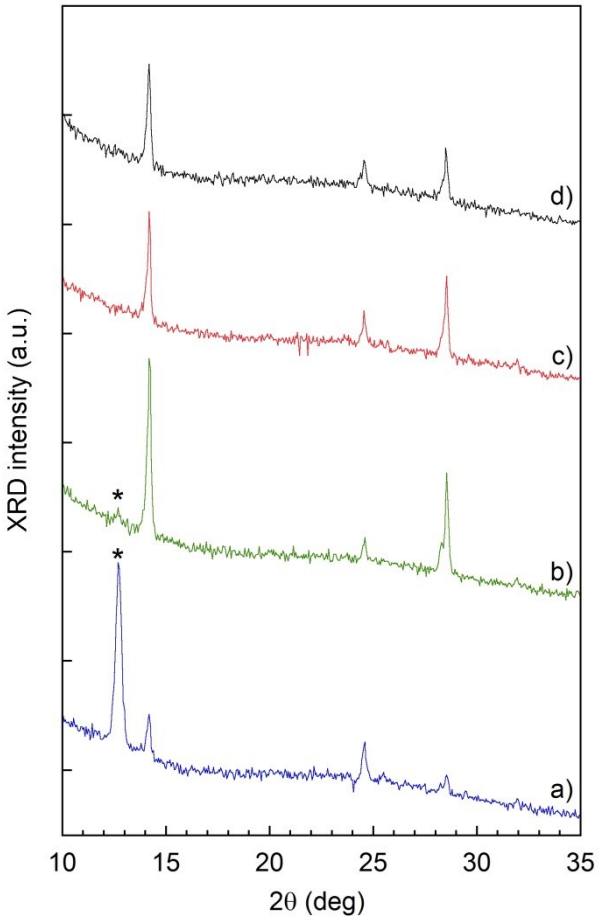

Figure 3.14 XRD patterns of $MAPbI_3$ film obtained for different dipping times in a 10 mg mL^{-1} MAI solution in 2-propanol: (a) 20 s, (b) 20 min, (c) 20 s + 20 min and (d) 20 s + 20 min with reduced baking time (see text). Asterisks indicate the PbI_2 diffraction peak.

In order to check the possibility to complete the PbI_2 conversion, the film obtained after 20 s dipping was dipped for a second time in the MAI solution, for a time of 20 min. The resulting sample has the expected dark brown color, indicating no massive perovskite dissolution. The XRD pattern (figure 3.14c) shows only the peaks of the perovskite and no residual PbI_2 phases can be detected, indicating the complete conversion of the original PbI_2 film. These results indicate that the dipping strategy followed for this sample is a good trade-off between the achievement of a complete PbI_2 conversion and the need to avoid a massive dissolution of the material finally obtained. Nevertheless, the obtained film still exhibited a very poor morphology characterized by the presence of some stripes on the surface of the film. To explain this lack of uniformity, it must be considered that, when the sample is extracted from the MAI solution and rinsed in 2-propanol, a thin film of residual alcohol remains on the surface. Therefore, a small amount on $MAPbI_3$ is expected to dissolve in this 2-propanol layer and when the sample is put on the hot plate, as the evaporation of the solvent slowly proceeds, the perovskite precipitates giving origin to the observed not uniform morphology.

To achieve a better morphology we rinsed the sample in dichloromethane (CH_2Cl) after each rinsing in 2-propanol. As CH_2Cl has been proposed in literature as antisolvent for $MAPbI_3$[141], the effect of further rinsing the film with this reagent is to force the instantaneous precipitation of the perovskite dissolved in 2-propanol, thus preventing the non-uniform precipitation during the drying. This additional rinsing resulted in films showing an impressive uniformity on the whole substrate area. In order to optimize the whole two-dipping process, we checked the possibility to reduce the baking time after the first dipping. We found that well-formed samples could be obtained when this baking time is reduced to 5 min (figure 3.14d), and so this process was assumed as standard, that is 20 s dipping followed by 5 min baking, further 20 min dipping and finally 30 min baking.

SEM images of the PbI_2 film before the dipping and the $MAPbI_3$ film finally obtained are reported in figure 3.15 and 3.16, respectively. The film morphology on the microscale is completely modified when the PbI_2 is converted in the perovskite. The PbI_2 film (figure 3.15) is composed by needle-like structures, whose length is few micrometers. After the dipping a very uniform and continuous film is obtained (figure 3.16a); further magnification (figure 3.16b) shows that the film is composed by adjacent perovskite crystallites having dimension of 100-200 nm. It is worth noting that this morphology is significantly more uniform that the one achieved by preparing $MAPbI_3$ from both GBL and DMF precursor solutions (figures 3.3 and 3.10), therefore this synthesis route is most promising for the application of $MAPbI_3$ in planar heterojunction solar cells.

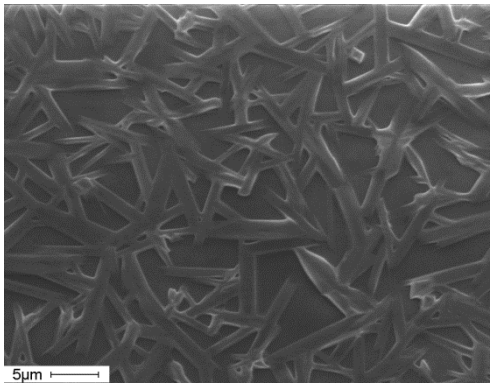

Figure 3.15 SEM image of a typical PbI_2 film.

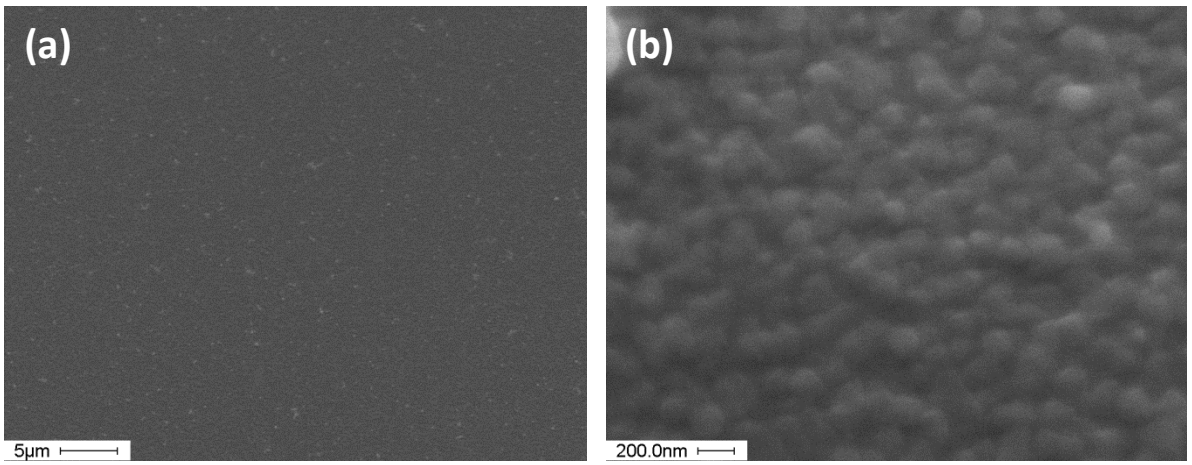

Figure 3.16 SEM image of $MAPbI_3$ film obtained by multi-step sequential deposition for a magnification of (a) 2500X and (b) 40000X.

The diffuse reflectance (figure 3.17a) and absorbance (figure 3.17b) spectra of $MAPbI_3$ samples prepared by two-step dipping strategy are in good agreement with those observed for films prepared from precursor solution. The same bandgap value E_g = 1.60 ± 0.01 eV is found for the samples resulting from the three different synthesis routes (figure 3.18), where the uncertainty refers to the spread of the calculated E_g for several films of the compound.

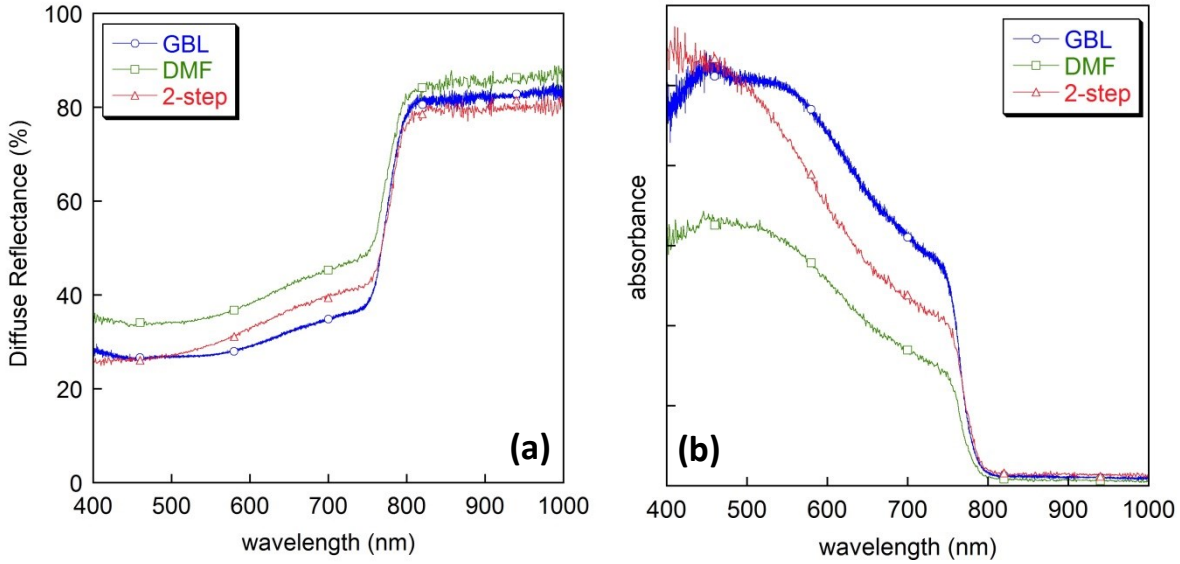

Figure 3.17 (a) Diffuse reflectance and (b) absorbance spectra for $MAPbI_3$ samples prepared from GBL precursor solution, DMF precursor solution and two-step dipping strategy, respectively.

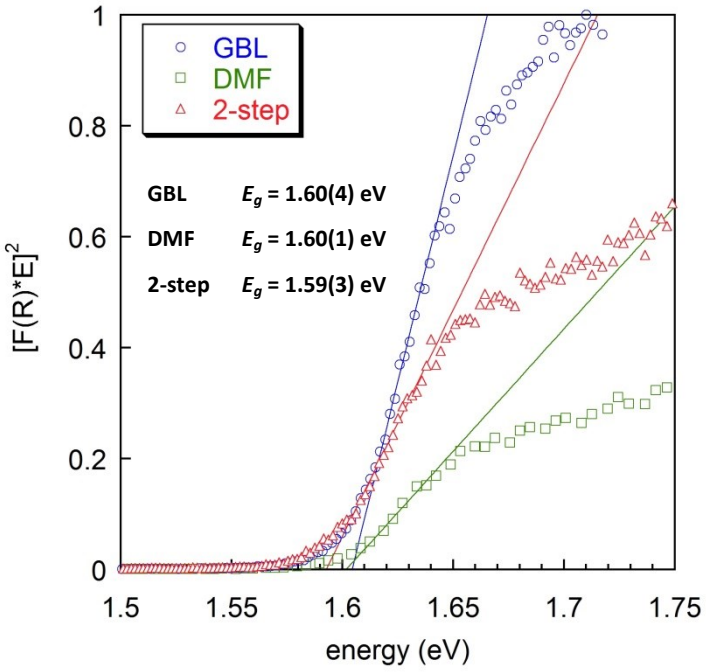

Figure 3.18 Tauc plot for $MAPbI_3$ samples prepared from GBL precursor solution, DMF precursor solution and two-step dipping strategy, respectively.

It is worth noting that the same bandgap value E_g = 1.60 ± 0.01 eV was found for a wide variety of $MAPbI_3$ samples obtained by different synthesis parameters, such as different solvents or different baking time and temperature (figure 3.19), indicating that E_g is only slightly influenced by the preparation route.

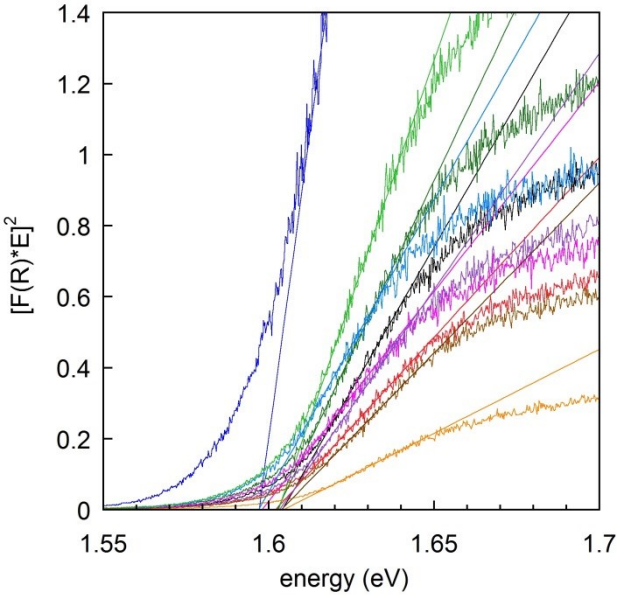

Figure 3.19 Tauc plot for $MAPbI_3$ samples obtained by different synthesis parameters.

3.1.4 Presence of PbI_2 in $MAPbI_3$ films

XRD spectra of $MAPbI_3$ films prepared in ambient air sometimes pointed out the presence of the PbI_2 diffraction peak at 2θ = 12.7° (figure 3.20a), with an intensity classifiable as an impurity phase. The presence of PbI_2 is generally considered as a telltale of perovskite degradation and as a detrimental factor for the solar cells performances. Since no PbI_2 is observed when $MAPbI_3$ films are prepared when the same synthesis route is completely performed in an inert atmosphere in glove box[37], we repeated the film preparation performing all the steps in an Ar-filled glove box. The XRD pattern of the so obtained sample shows no presence of any PbI_2 residual phase (figure 3.20b). This result suggest that the presence of the PbI_2 residual phase is related to the degradation of the MAI salt with the ambient moisture, since hygroscopic nature has been reported for methylammonium halides[142]; in such a case, since MAI and PbI_2 are present in stoichiometric ratio in the precursor solution, the lack of the decomposed MAI is expected entail the impossibility of a complete reaction of the whole PbI_2 quantity, thus resulting in a leftover PbI_2 amount in the film finally obtained.

This hypothesis suggested us the possibility to prepare $MAPbI_3$ films in air avoiding the presence of PbI_2 by slightly modifying the stoichiometry in the precursor solution, that is using 20% molar excess of methylammonium. Therefore, we prepared precursor solutions having a 1.2:1 MAI:PbI_2 molar ratio instead of the conventional 1:1. The XRD patterns of the samples obtained in air from 1.2:1 precursor solutions (figure 3.20c) systematically didn't show any diffraction peak related to PbI_2. The use of a 20% molar excess of methylammonium leads to the formation of the conventional tetragonal $MAPbI_3$ structure (figure 3.20c), suggesting that the excess of the methylammonium salt is eliminated during the baking process[143,144]. Therefore, the use of a MAI-rich precursor solution can

be considered as a suitable route to obtain $MAPbI_3$ films with no PbI_2 inclusion, without the necessity to process the material in inert atmosphere.

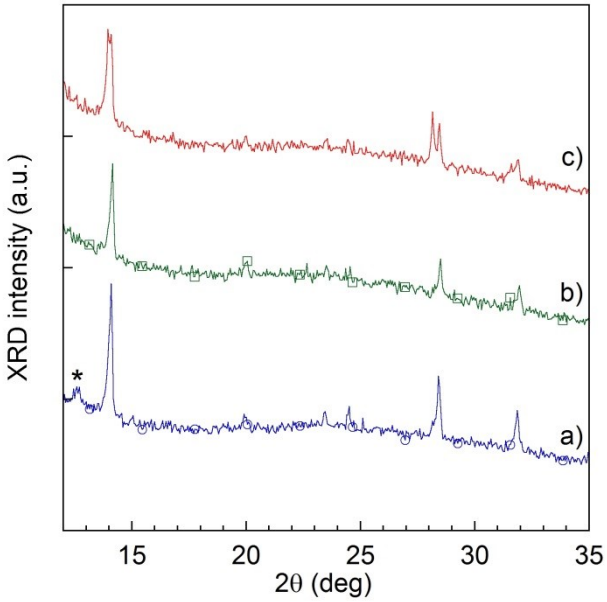

Figure 3.20 XRD patterns of $MAPbI_3$ film obtained from a) 1:1 MAI:PbI_2 solution in air, b) 1:1 solution in Ar-filled glove box, and c) 1.2:1 solution in air. Asterisks indicate the PbI_2 diffraction peak.

3.1.5 Influence of the baking time

The influence of the thermal treatment on structural and optical properties was investigated for $MAPbI_3$ films obtained from GBL precursor solution and baked for different times, ranging from 5 to 60 min, at the standard temperature of 100 °C. In figure 3.21 XRD patterns are reported for samples prepared in ambient air from 1:1 precursor solution and annealed with different baking times, ranging from 5 min to 60 min. In the XRD pattern of the sample annealed for 5 min only the peaks of the tetragonal perovskite structure are present, indicating that this short baking is enough to correctly form the material. For treatments longer than 15 min, the perovskite is still present without additional phases, indicating that the material doesn't suffer decomposition due to lengthened baking. It is worth noting that the height of the XRD peaks is comparable in all the conditions explored, suggesting that not the crystallinity nor the orientation degree of the film are significantly affected by the baking time in the investigated range.

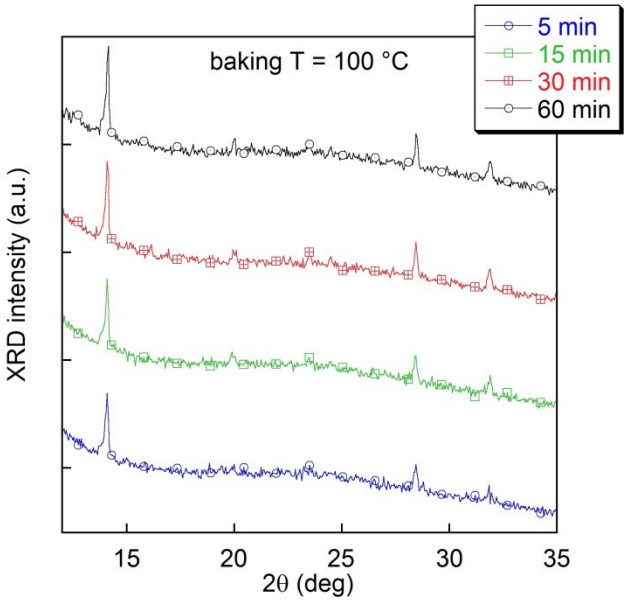

Figure 3.21 XRD patterns of $MAPbI_3$ films obtained in ambient air from 1:1 precursor solution and baked for different times at T = 100 °C.

Diffuse reflectance measurements were performed on these samples. From these measurements, E_g values were achieved via Tauc plot (figure 3.22) while Urbach energies E_U (table 3.1) were obtained by fitting the linear region of the ln[$F(R)$] vs E plot (figure 3.23), as described in paragraph 2.6.9. The obtained bandgap value is 1.60 eV for all the different treatments.

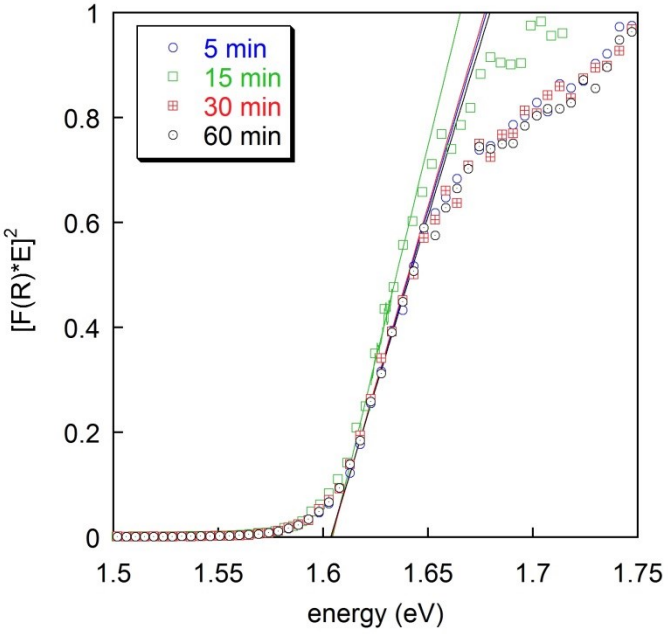

Figure 3.22 Tauc plot for $MAPbI_3$ films obtained in ambient air from 1:1 precursor solution and baked for different times at T = 100 °C.

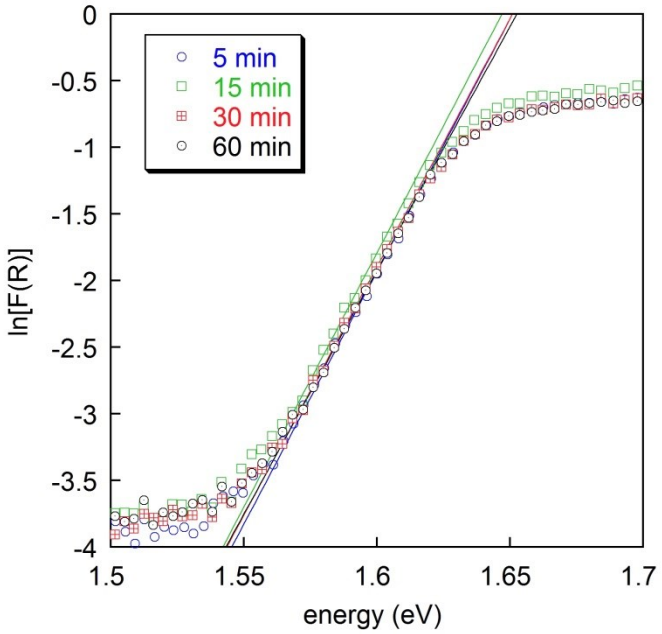

Figure 3.23 Linear regions of ln[$F(R)$] function used to calculate Urbach energies for $MAPbI_3$ films obtained in ambient air from 1:1 precursor solution and baked for different times at T = 100 °C.

Baking time	E_U (meV)
5 min	26
15 min	26
30 min	27
60 min	27

Table 3.1 Urbach energy values calculated for $MAPbI_3$ films obtained in ambient air from 1:1 precursor solution and baked for different times at T = 100 °C.

The E_U values reported in table 3.1 show that for these samples the Urbach energy depends on a minor extent on the baking time. Since the Urbach energy value is related to crystalline lattice disorder, this result suggests that the crystalline order in the films is not heavily affected by the duration of the thermal treatment, for the time region explored.

The same analysis was carried out on $MAPbI_3$ films prepared in air using the 1.2:1 precursor solution, containing the 20% molar excess of methylammonium. Comparable XRD patterns are obtained for different baking times (figure 3.24) and nearly the same bandgap value of 1.60 eV was found for all the samples (figure 3.25), comparable with those calculated for samples prepared from 1:1 precursor solution in air (figure 3.22). Also Urbach energy values were found to be marginally affected by the

baking time and comparable to those obtained for samples synthesized from stoichiometric solution (table 3.2).

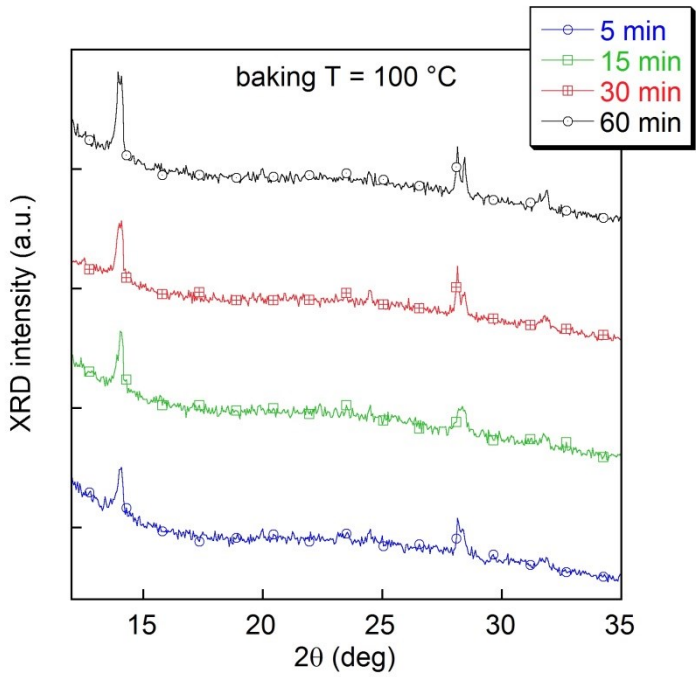

Figure 3.24 XRD patterns of $MAPbI_3$ films obtained in ambient air from 1.2:1 precursor solution and baked for different times at T = 100 °C.

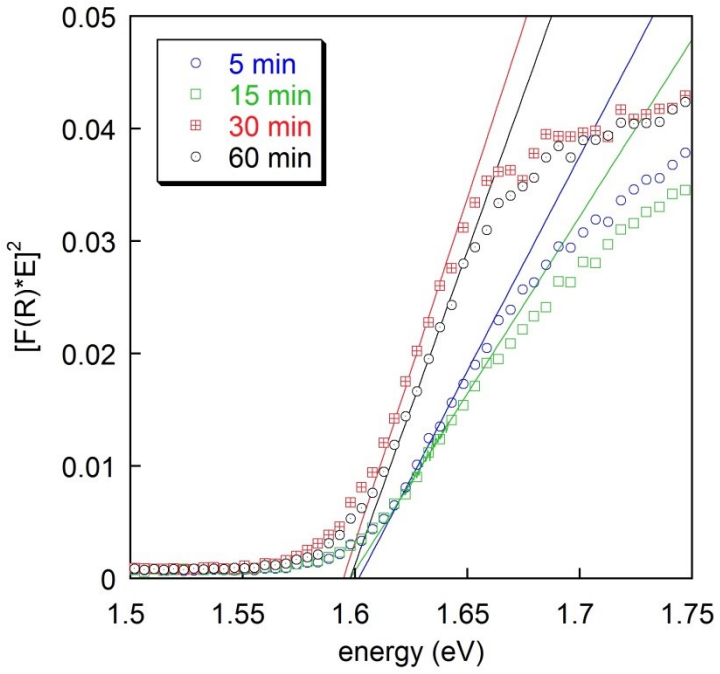

Figure 3.25 Tauc plot for $MAPbI_3$ films obtained in ambient air from 1.2:1 precursor solution and baked for different times at T = 100 °C.

	1:1	1.2:1
Baking time	E_U (meV)	E_U (meV)
5 min	26	33
15 min	26	33
30 min	27	31
60 min	27	32

Table 3.2 Urbach energy values calculated for $MAPbI_3$ films obtained in ambient air from 1:1 and 1.2:1 precursor solution, respectively, and baked for different times at T = 100 °C.

These results indicates that the material properties are almost unchanged when a methylammoniun excess is used; however, the comparison between the Tauc plots obtained for the 1:1 and 1.2:1 solutions (figures 3.23 and 3.25, respectively) suggests that an improved absorbance is increased when the stoichiometric solution is used, as it will be discussed in section 3.1.6.

Similarly to what observed in samples prepared in air, the structural and optical properties are not significantly affected by baking time when films from 1.2:1 solution are prepared in inert atmosphere in an Ar-filled glove box. Indeed, the XRD patterns corresponding to different times (figure 3.26) are comparable to each other, and the bandgap value is ≈ 1.60 eV for all samples (figure 3.27). Urbach energies (table 3.3) are comparable to those found for samples prepared in air.

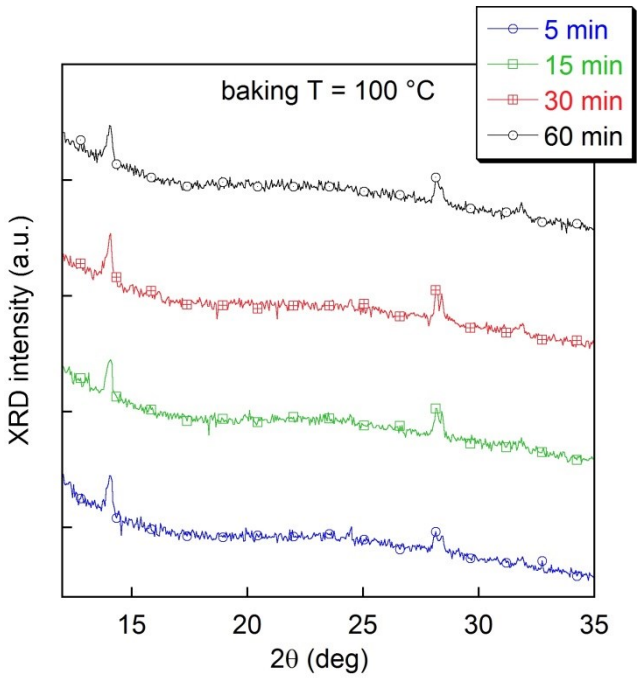

Figure 3.26 XRD patterns of $MAPbI_3$ films obtained in glove box from 1.2:1 precursor solution and baked for different times at T = 100 °C.

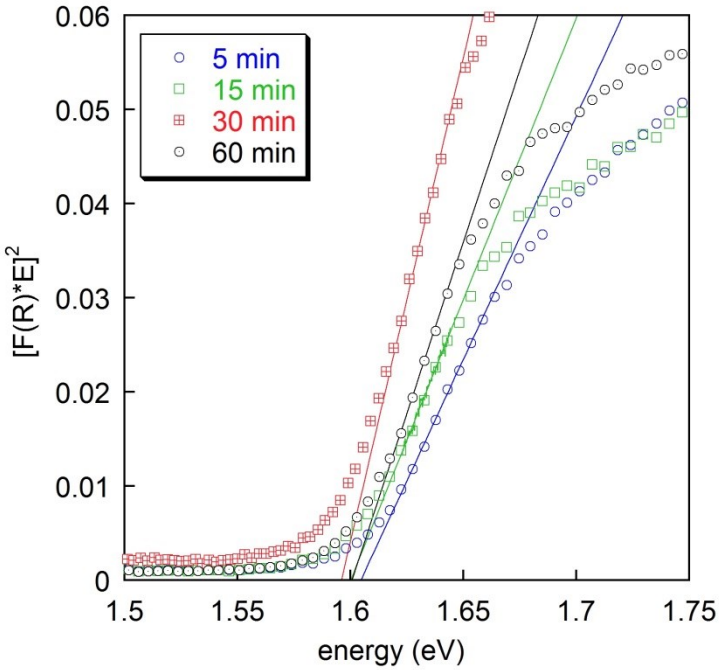

Figure 3.27 Tauc plot for $MAPbI_3$ films obtained in glove box from 1.2:1 precursor solution and baked for different times at T = 100 °C.

	Ambient air	Glove box
Baking time	E_U (meV)	E_U (meV)
5 min	33	27
15 min	33	32
30 min	31	30
60 min	32	31

Table 3.3 Urbach energy values calculated for $MAPbI_3$ films obtained in ambient air and in inert atmosphere, respectively, from 1.2:1 precursor solution, and baked for different times at T = 100 °C.

Comparable results were found when the samples are prepared in glove box from the stoichiometric precursor solutions. XRD patterns corresponding to different times (figure 3.28) are comparable to each other, and nearly the same bandgap value of 1.60 eV is found for all samples (figure 3.29). In table 3.4, the Urbach energy values found for these samples are summarized, together with those achieved for samples prepared from 1.2:1 solution and for samples synthesized in ambient air.

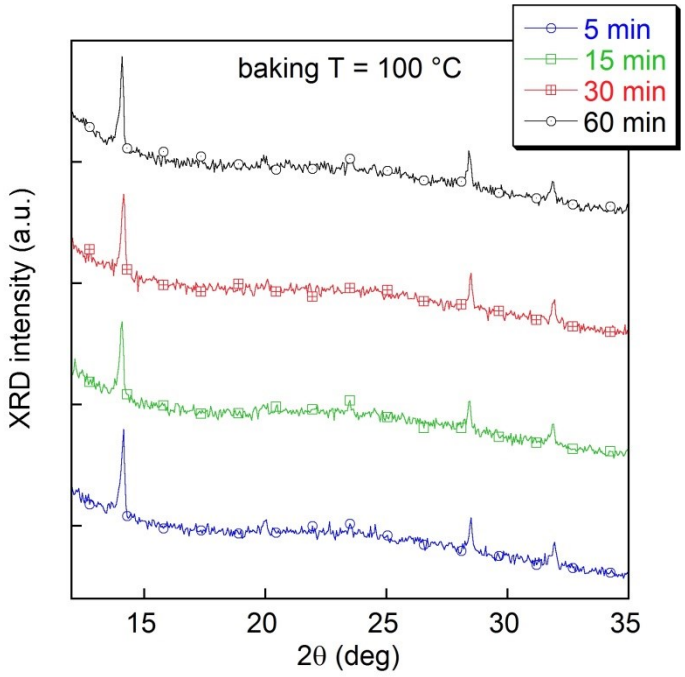

Figure 3.28 XRD patterns of $MAPbI_3$ films obtained in glove box from 1:1 precursor solution and baked for different times at T = 100 °C.

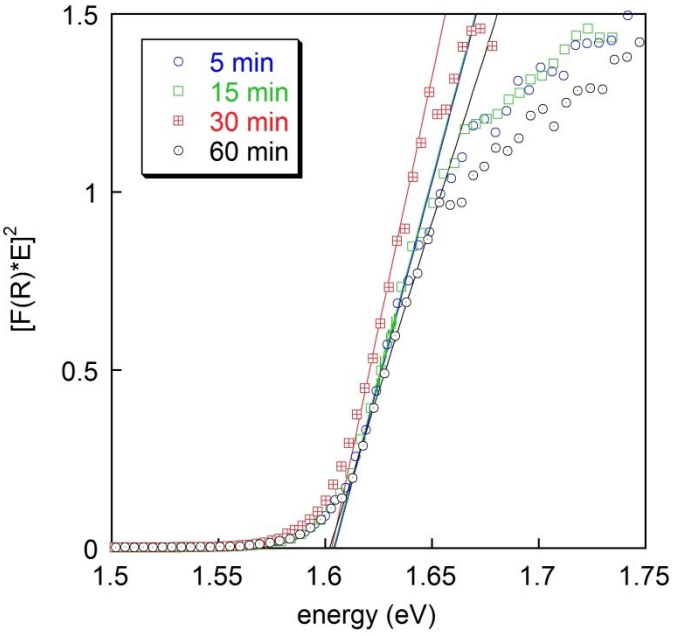

Figure 3.29 Tauc plot for $MAPbI_3$ films obtained in glove box from 1:1 precursor solution and baked for different times at T = 100 °C.

	Ambient air		Glove box	
	1:1	1.2:1	1.1	1.2:1
Baking time	E_U (meV)	E_U (meV)	E_U (meV)	E_U (meV)
5 min	26	33	28	27
15 min	26	33	24	32
30 min	27	31	26	30
60 min	27	32	29	31

Table 3.4 Urbach energy values calculated for $MAPbI_3$ films obtained in different conditions and baked for different times at T = 100 °C.

The E_U values reported in table 3.4 suggest that, for each synthesis route considered, the crystalline order in the films is not heavily affected by the duration of the thermal treatment, for the time region explored. In literature, a E_U value of 15 meV for $MAPbI_3$ was found by Sadhanala et al[50], who used a single step solution process similar those used here, and by De Wolf et al[131] on films prepared by a two-steps synthesis procedure.

It is worth noting that the Urbach energies of the samples prepared in air are comparable with those found for the samples prepared in glove box. This may indicate that the obtained material is characterized by similar crystalline lattice disorder degree whether it is prepared in a well controllable inert atmosphere or in ambient air, where humidity is present and the atmosphere conditions are globally less controlled. To the best of our knowledge, up to now there are no indications in literature about the influence of the preparation atmosphere on the crystalline order of $MAPbI_3$, as both papers by Sadhanala group and De Wolf group reported only about samples prepared in inert atmosphere[50,131].

3.1.6 Absorbance of $MAPbI_3$ films synthesized in different conditions

Absorbance spectra of $MAPbI_3$ samples prepared from 1:1 and 1.2:1 solutions in ambient air and in glove box (baking time = 15 min) are compared in figure 3.30.

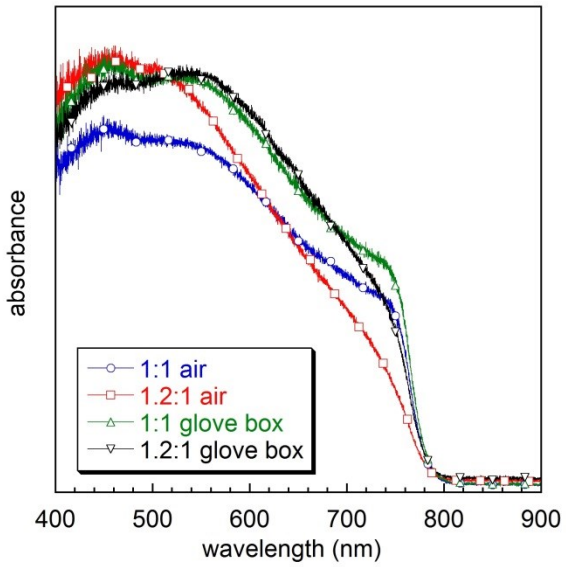

Figure 3.30 Absorbance spectra of $MAPbI_3$ films obtained in different conditions and baked for different times at T = 100 °C.

The comparison between the absorbance points out that perovskite prepared in glove box shows improved light-harvesting properties with respect to films prepared in ambient air. It is worth noting that the sample prepared in air from 1.2:1 precursor solution shows a less efficient light absorption with respect to the stoichiometric sample prepared in glove box. This result is not in agreement with what reported by Wehrenfennig et al[145], that however used a significantly higher methylammonium excess (3:1 MAI:PbI_2 molar ratio). Anyway, absorbance spectra reported in figure 3.30 suggest that the most suitable route to achieve PbI_2-free $MAPbI_3$ perovskite with high light absorption efficiency is the synthesis from stoichiometric solution in inert atmosphere.

3.2 Sensitization of ZnO nanosheets by $MAPbI_3$ perovskites

Mesoporous ZnO nanosheets discussed in section 4.2 can be considered very promising for photovoltaic applications, thanks to their peculiar morphology and their monocristallinity. As reported in section 4.2, where their preparation and properties are described in detail, these nanosheets are characterized by a highly porous morphology and therefore by a huge surface-to-volume ratio that is a key feature to achieve a large number of possible sensitization sites. It is worth noting that these nanosheets were preliminary employed in traditional liquid Ru-based DSSCs, fabricated by the IIT institute in Lecce, Italy, Without any kind of optimization, the devices showed an average PCE of 3.3%; this value is not far from the record of 6.6% for a ZnO-based DSSC[75], thus demonstrating the suitability of these nanostructures for this application.

We performed preliminary sensitization of ZnO nanosheets films with $MAPbI_3$ perovskites, following the experimental procedure reported in section 2.3. Figure 3.31 shows SEM images of the ZnO nanosheets film obtained by centrifugation. It can be observed that this deposition method results in a good coverage of the whole substrate (figure 3.31a) and that a thickness of ≈ 10 μm is achieved (figure 3.31b).

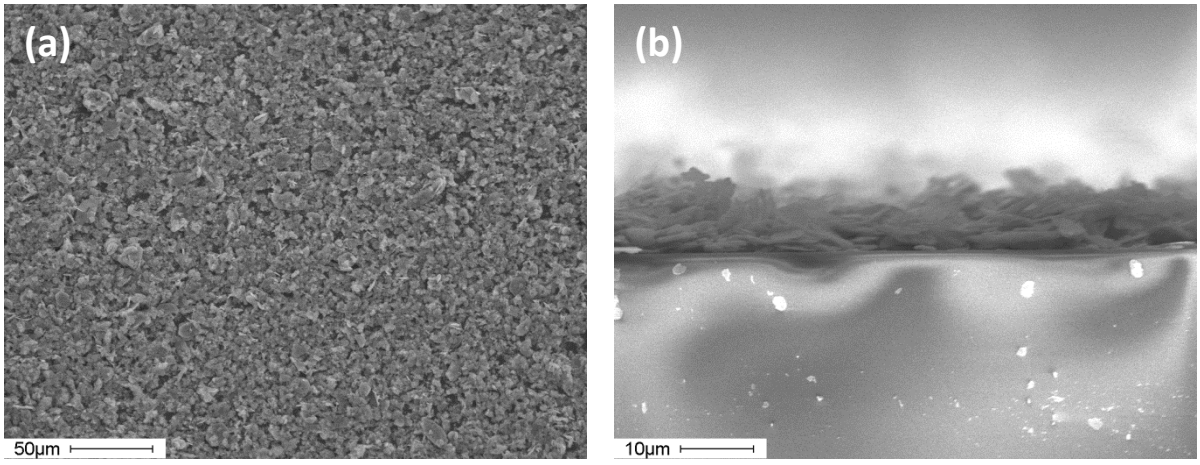

Figure 3.31 (a) SEM image of the ZnO nanosheets film obtained by centrifugation and (b) cross section of the image (a).

The color of the nanosheets film, that initially was white, turned to black after perovskite precursor solution spin-coating and annealing.

The XRD pattern of a typical nanosheets film sensitized by $MAPbI_3$ perovskite (figure 3.32) points out the presence of diffraction peaks that can be ascribed to both ZnO and $MAPbI_3$ perovskite. The additional peak of PbI_2 at $2\theta = 12.7°$ is also present, as sometimes observed in literature on nanostructured substrates[28].

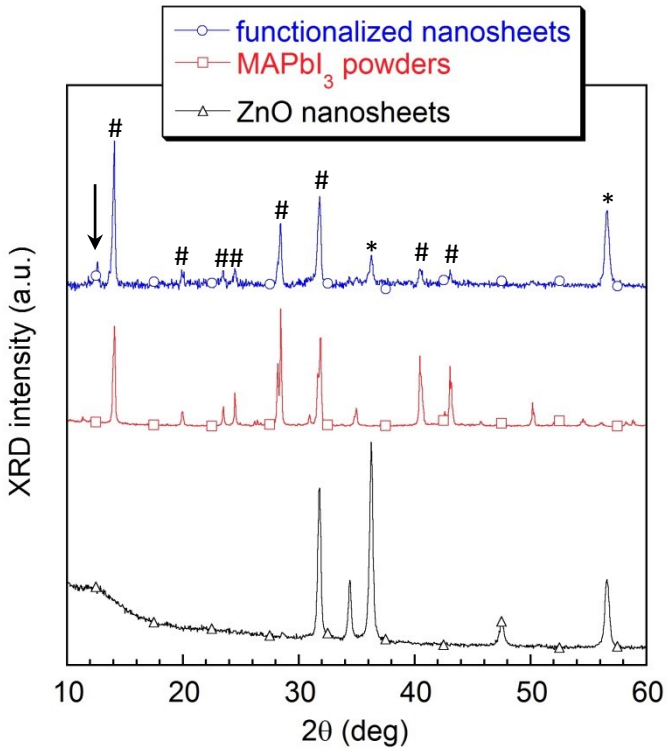

Figure 3.32 XRD pattern of a ZnO nanosheets film sensitized by $MAPbI_3$ perovskites. Hashes indicates diffraction peaks related to $MAPbI_3$, while asterisks indicates ZnO ones. The arrow indicate the peak related to PbI_2.

In figure 3.33 the SEM image of a sensitized ZnO nanosheets film is reported, compared with a non-functionalized one. No evidence of the perovskite presence can be observed on the nanocrystals, pointing out that a thin perovskite film is enough to confer the evident dark color.

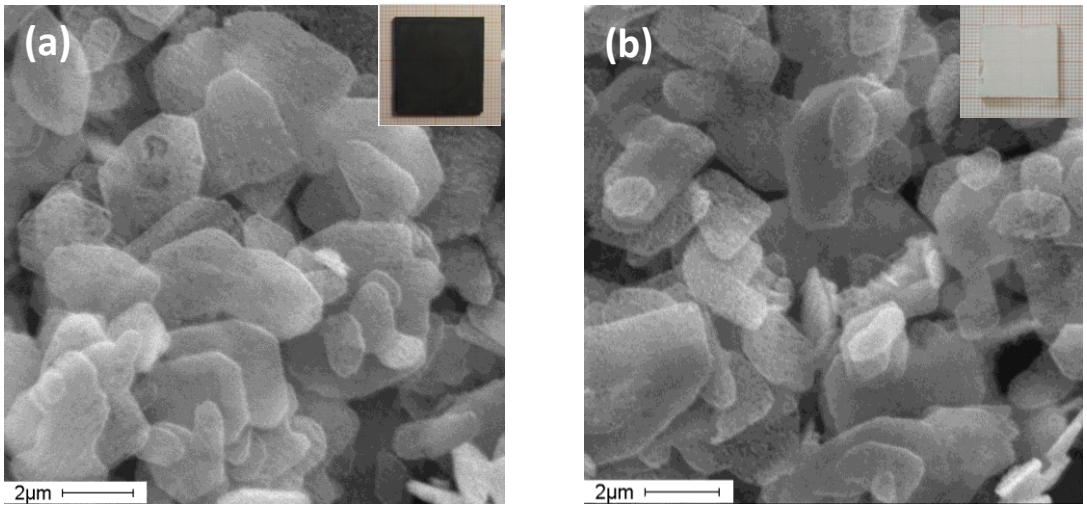

Figure 3.33 (a) SEM image of sensitized ZnO nanosheets film compared with (b) a similar bare nanosheets film. The inset shows the color of the samples.

The presence of perovskite in the film was investigated by TEM analysis, showing that perovskite tends to form clusters on the ZnO nanostructures, whose dimension is ca. 20 nm (figure 3.34). The formation of perovskite clusters is in good agreement with what was reported in literature for TiO_2 nanostructures functionalized by $MAPbI_3$ obtained from GBL precursor solution[27,146]. The EDX analysis (figure 3.35) indicates that the perovskite dye is well dispersed on the nanostructured film. It is worth noting that while performing TEM analysis a degradation process of the perovskite was observed; as a result, at the end of the measurement $MAPbI_3$ was completely converted in PbI_2.

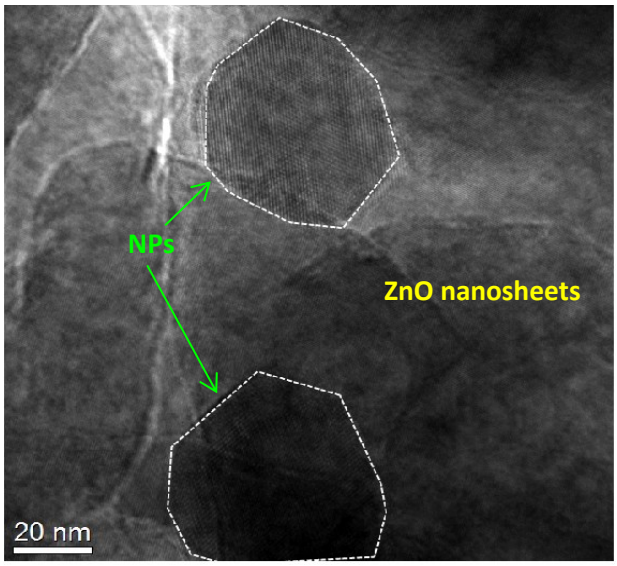

Figure 3.34 TEM image of a ZnO nanosheets film sensitized by $MAPbI_3$ perovskite.

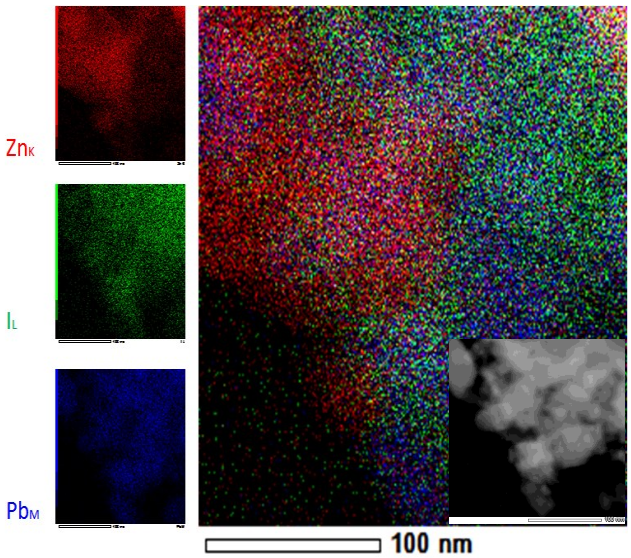

Figure 3.35 EDX map on a ZnO nanosheets film sensitized by $MAPbI_3$ perovskite. The Zn, I and Pb distributions are indicated respectively in red, green and blue. The inset shows the HAADF image used to derive the EDX map.

In figure 3.36, diffuse reflectance spectra for bare ZnO nanosheets, bare $MAPbI_3$ perovskite and a typical sensitized sample are reported. The diffuse reflectance of the functionalized film points out the contributions of both nanosheets and perovskites: a first reflectance loss located at ca. 780 nm is due to the perovskite band-to-band absorption, and a further small absorption at ca. 400 nm can be detected, due to ZnO nanostructures.

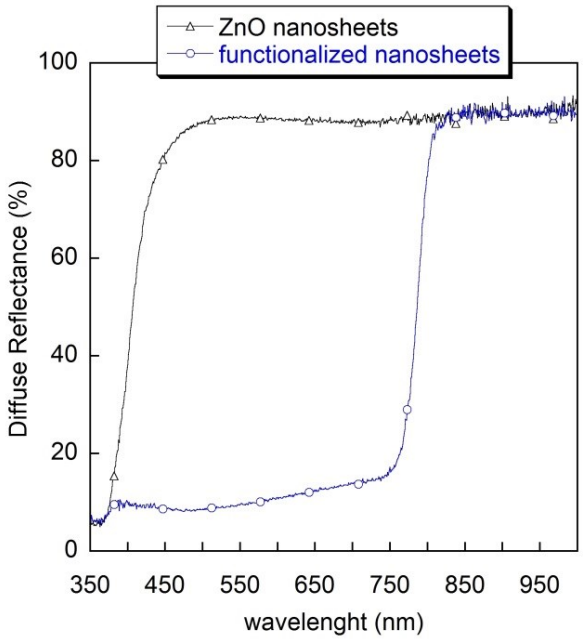

Figure 3.36 Diffuse reflectance spectrum of a ZnO nanosheets film sensitized by $MAPbI_3$ perovskite compared with a similar bare ZnO nanosheets film spectrum.

To investigate the mutual interaction between ZnO nanosheets and $MAPbI_3$ perovskites, we performed photoluminescence measurements on both functionalized nanostructures and bare perovskites. The spectra were collected using an excitation wavelength of 395 nm.

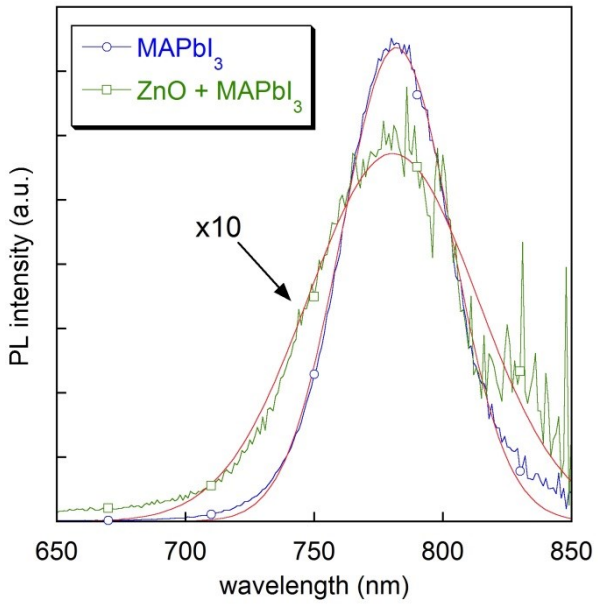

Figure 3.37 Photoluminescence spectra of $MAPbI_3$ perovskite and ZnO nanosheets film sensitized by $MAPbI_3$. Blue and green lines are the collected spectra, red lines the Gaussian best fits.

Both emission spectra (figure 3.37) show a peak at ≈ 780 nm (≈ 1.59 eV). The PL signal observed for the nanosheets is very noisy but still distinguishable. It is worth noting that the peak amplitude observed for the functionalized nanosheets is approximatively ten times smaller than those observed for the bare perovskite, thus suggesting that there is a charge transfer from the perovskite to the ZnO nanostructures. However, the presence of a residual PL signal related to $MAPbI_3$ points out that the perovskite infiltration process is not optimized, as shown also by TEM analysis (figure 3.38), showing that the perovskite is present on the edges of the pores, but not inside the pores themselves.

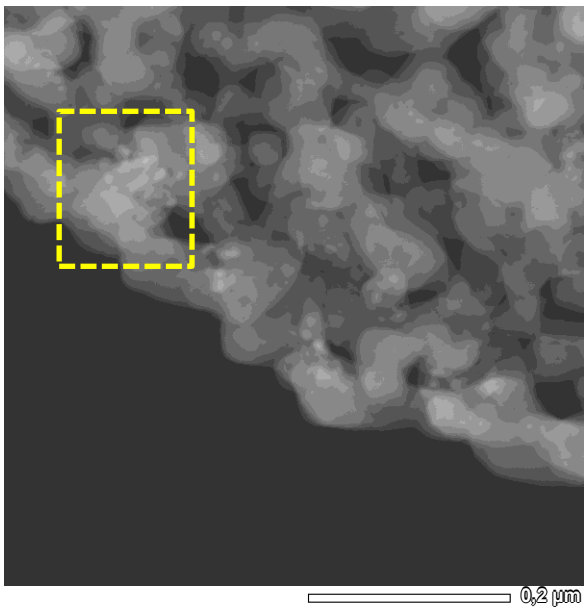

Figure 3.38 TEM image of a ZnO nanosheet sensitized by $MAPbI_3$. The yellow square highlights the perovskite dots.

Therefore, these preliminary investigations suggest that actually it is possible to sensitize porous ZnO nanosheets by $MAPbI_3$. Currently, work is in progress to optimize the sensitization procedure, in order to achieve a better permeation of the perovskite dye.

3.3 $MAPbI_{3-x}Br_x$ perovskites

3.3.1 $MAPbI_{3-x}Br_x$ perovskites by mixing $MAPbI_3$ and $MAPbBr_3$ precursors

Noh et al demonstrated the possibility to obtain $MAPbI_{3-x}Br_x$ in the whole range $0 \leq x \leq 3$ by properly mixing $MAPbI_3$ and $MAPbBr_3$ precursor solutions[37]. In this work it was highlighted as there is a univocal relation between the bromide molar fraction x and the perovskite bandgap E_g, that can be therefore considered as a function $E_g(x)$ of the bromide content. As a consequence, any compositional variation in the mixed I/Br perovskite determined by the modification of the synthesis process can be monitored by analyzing the value of $E_g(x)$. As an example, Kulkarni et al[147] used different volume and molar ratio of MAI and MABr and the composition of the resulting $MAPbI_{3-x}Br_x$ compound was estimated through the dependence on x of the bandgap energy $E_g(x)$ given by Noh et al. Following this approach, we prepared $MAPbI_{3-x}Br_x$ samples by mixing $MAPbI_3$ and $MAPbBr_3$ precursor solutions, according to the procedure described in section 2.2.4.

The XRD patterns of the obtained samples are shown in figure 3.39. The results show that a complete solid solution is formed in the whole range $0 \leq x \leq 3$. As the bromide content is increased, the diffraction peaks are shifted towards higher angles, because of the decrease of lattice spacings due to the gradual substitution of the larger I atoms with the smaller Br atoms[37,147]. The LeBail refinement, performed on the spectra with the software GSAS, shows that the tetragonal perovskite structure of $MAPbI_3$ (corresponding to $x = 0$) is maintained while increasing the bromide content up to $x = 0.57$; starting from this point, the crystal symmetry becomes cubic. This observed transition is in good agreement with the behavior observed by Noh et al[37].

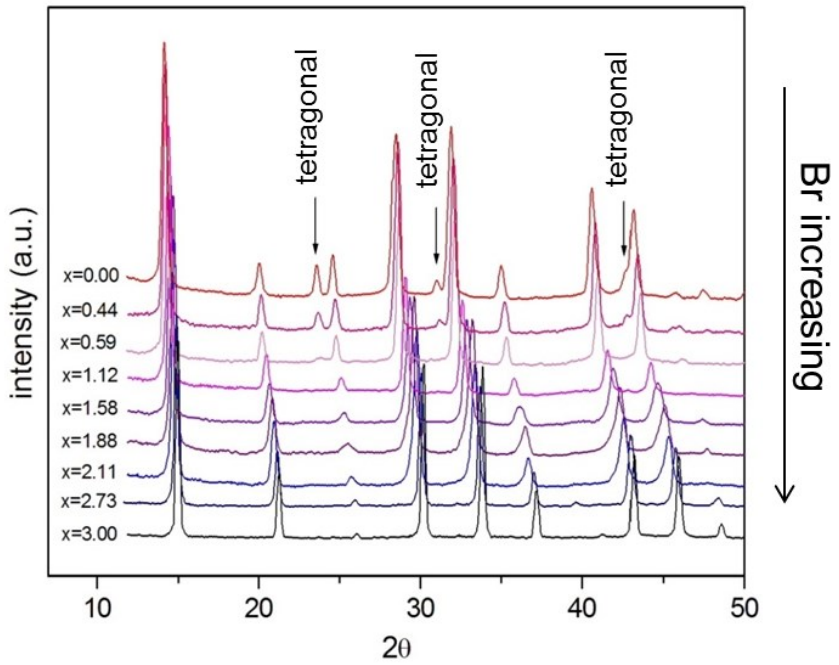

Figure 3.39 Composition dependent evolution of the powder XRD pattern for the $MAPbI_{3-x}Br_x$ perovskites; the characteristic diffraction peaks of the tetragonal phase are indicated by the arrows.

From the XRD patterns, the lattice parameters were also calculated (figure 3.40). The lattice volume is strongly influenced by the composition, and in the cubic region decreases monotonically with *x*. In this region, the lattice parameter is expected to follow the simple Vegard law, an approximate empirical rule which correlates, at constant temperature, the crystal lattice parameter of an alloy and the concentrations of the constituent elements[148]. For the stoichiometry $MAPbI_{3-x}Br_x$, the Vegard law has the form

$$a(x) = \frac{x}{3} a_{\mathrm{Br}} + \frac{3-x}{x} a_{\mathrm{I}} \tag{3.2}$$

where a_{Br} and a_I are respectively the lattice parameters of $MAPbBr_3$ and $MAPbI_3$. A slight negative deviation from the Vegard prediction is observed; a small deviation was reported also by Kulkarni et al[147] and related with a possible small miscibility gap, a site preference for the bromide in the perovskite octahedra, or further variations in symmetry as Br substitutes I.

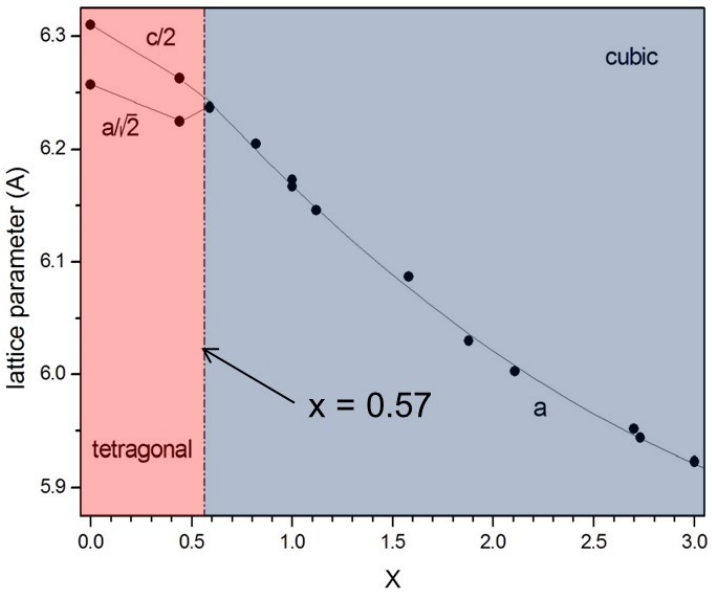

Figure 3.40 Composition dependent evolution of the lattice parameters for the $MAPbI_{3-x}Br_x$ perovskites.

The absorbance spectra corresponding to different *x* molar fractions are reported in figure 3.41. The absorbance onset is blue-shifted as *x* increases, consistently with previous literature data[37,50,147] and for all the compositions spectra are featureless above the excitonic structure and bandgap. The different position of the absorption edge is responsible for the colorful aspect of the films, that exhibit different colors depending on the bromide content (figure 3.42).

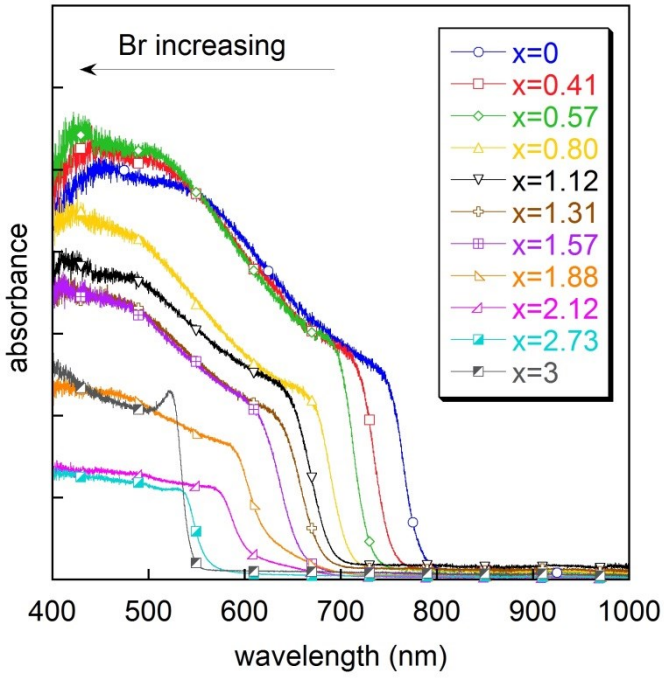

Figure 3.41 Composition dependent evolution of absorbance spectra for the $MAPbI_{3-x}Br_x$ perovskites. For the sake of clarity, only most significant spectra are shown.

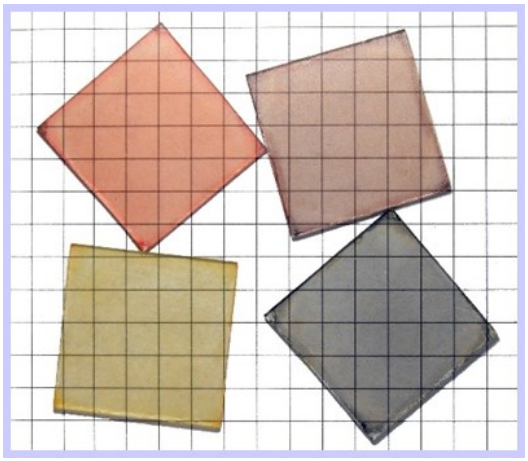

Figure 3.42 $MAPbI_{3-x}Br_x$ colorful films having different *x*. By increasing the Br^- content, the color turns from black (*x* = 0) to brown, orange and finally dark yellow (*x* = 3).

The above absorbance spectra were used to calculate the optical bandgap of the samples through the Tauc plot (figure 3.43), following the same procedure described in section 2.6.8.2 and already applied on $MAPbI_3$ samples (section 3.1).

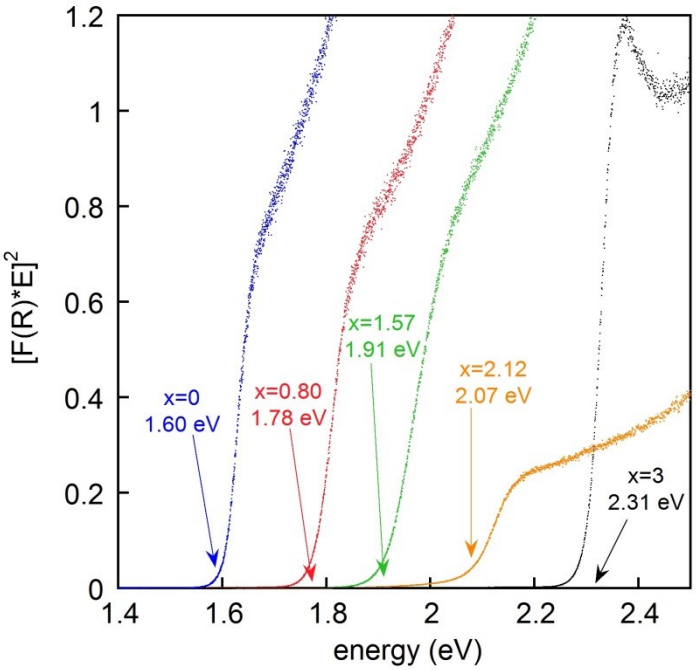

Figure 3.43 Tauc plot for the $MAPbI_{3-x}Br_x$ perovskites. For the sake of clarity, only most significant spectra are shown. The relevant sample compositions and the corresponding bandgap energies obtained by the Tauc analysis are also indicated.

The obtained E_g values are reported in figure 3.44 as a function of *x*, together with those reported by Noh et al[37]. It can be observed as the values resulting from our analysis are slightly larger than those found by Noh et al, and this is likely due to the different methods used to determine the optical

bandgap. Indeed, in their work Noh et al used the onset of the absorbance to derive E_g instead of the Tauc plot. To verify this hypothesis, we calculated the optical bandgap of our samples also from the absorption onset; the obtained values were few meV tens smaller than those derived by the Tauc analysis and not far from the curve given in [37]. This is not surprising since it is well known that the bandgap energy determined from the absorbance onset may depend, for example, on film thickness[113], while absorption by defect and impurity states causes a smearing of the absorption edge that makes the estimation of the optical band gap less precise[149].

The dependence on the Br^- molar fraction x of the obtained E_g can be well described by a parabolic expression in x (equation 3.3), in analogy with the behavior reported by Noh et al[37].

$$E_{\mathrm{G}}(x) = E_{\mathrm{I3}} + (E_{\mathrm{Br3}} - E_{\mathrm{I3}} - b)\,\frac{x}{3} + b\,\left(\frac{x}{3}\right)^2 \tag{3.3}$$

In this expression, E_{I3} and E_{Br3} are respectively the $MAPbI_3$ and $MAPbBr_3$ bandgaps and b the so-called bowing parameter, that accounts for the effects of composition disorder on the conduction and valence band edges[150]. The best fitting of the experimental E_g values with equation 3.3 results in E_{I3} = 1.604 eV, E_{Br3} = 2.307 eV and b = 0.176 eV. The found $MAPbI_3$ bandgap is in good agreement with the values reported in literature[48,151], as well as the bandgap found for $MAPbBr_3$[152]. The value found for the bowing parameter is significantly lower than b = 0.33 eV reported by Noh et al[37], suggesting that the composition disorder in our samples is low, despite we performed the synthesis in ambient air while the samples investigated in ref. [37] were processed in inert atmosphere.

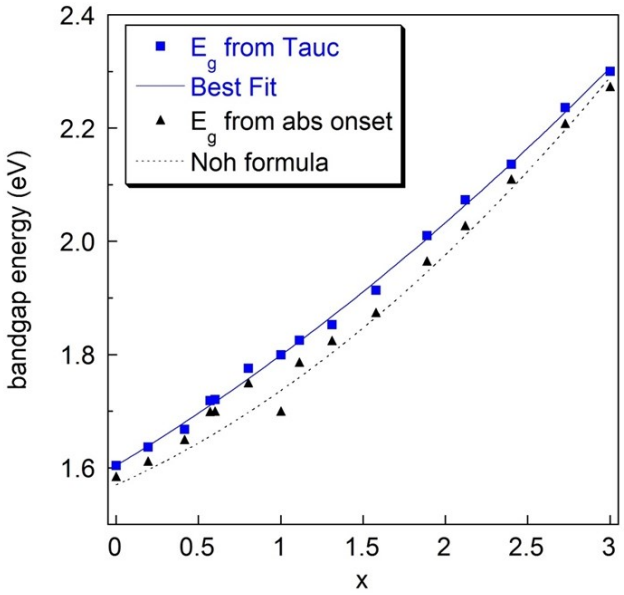

Figure 3.44 Bandgap energy for the $MAPbI_{3-x}Br_x$ perovskites as a function of the Br content x. Blue squares are the E_g values calculated from the Tauc analysis, whose parabolic best fitting is represented by the full line. Triangles are the E_g values obtained from the absorbance onsets. Dashed line represents the E_g dependence on x reported in ref. [37].

Aiming at a deeper insight about the correlation between the bromide content and the crystalline disorder in the perovskite films, we analyzed the behavior of the Urbach energy E_U when varying x (figure 3.45).

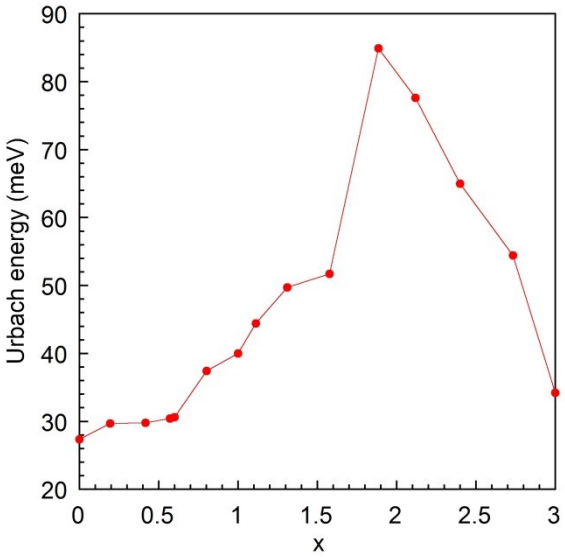

Figure 3.45 Urbach energies E_U calculated for $MAPbI_{3-x}Br_x$ perovskites with different compositions.

For the pure tri-iodide perovskite (x = 0) E_U is 27 meV, which is consistent with the results reported in section 3.1.5. The Urbach energy increases slightly with x up to $x \approx 0.6$, where the crystal structure transforms from tetragonal to cubic. For larger x values the Urbach energy increases more rapidly until it reaches a maximum of ≈ 85 meV at x = 1.89; then E_U decreases down to 34 meV for the pure tri-bromide compound. A similar behavior was recently shown by Sadhanala et al[50], who used a single step solution process similar to the one used here and found that the maximum E_U value of 90 meV was located at x = 2.4. As discussed in section 3.1.5, for $MAPbI_3$ they achieved E_U = 15 meV, that is the same value reported previously by DeWolf et al[131] on films prepared by a two-steps synthesis procedure. It is worth noting that both results were obtained by photothermal deflection spectroscopy (PDS) on samples prepared in inert atmosphere, while our perovskite films were synthesized in ambient air. However, the comparison between E_U values for two different sets of $MAPbI_3$ films prepared respectively in Ar-filled glove box and in ambient air reported in section 3.1.5 confirms that the Urbach energy is comparable for both the atmospheres. This finding seems to rule out that the higher E_U we found result from the sample preparation in air. The origin of the difference between E_U values found for our $MAPbI_3$ samples and those reported by DeWolf et al and Sadhanala et al is still under investigation.

It is worth noting that in our films the Full Width at Half Maximum (FWHM) of the XRD pattern obtained on the powdered samples in the cubic phase points out a behavior similar to those of the Urbach energy, reaching its maximum just at x = 1.89 where E_U is maximum (figure 3.46) . According to the Scherrer law, the peak FWHM is related to the average crystallite/grain size d by the relation

$$d \propto \frac{1}{\mathrm{FWHM}} \tag{3.4}$$

The very different morphologies observed at the various Br^- concentrations (figure 3.47) suggest that also the average grains size could be strongly influenced by the film composition. The correspondence between the trends observed for FWHM and E_U points out that the defect content as measured by the Urbach energy increases when the grain size decreases, thus indicating that sub-bandgap absorption is likely related to defect states at the grain boundaries, which is consistent with the observation that solar cell efficiency increases with grain size[153].

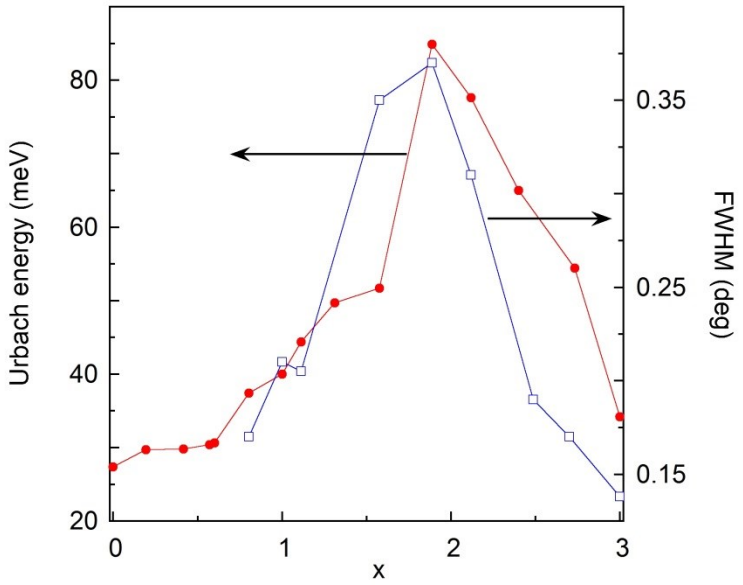

Figure 3.46 Urbach energies E_U and FWHM calculated for $MAPbI_{3-x}Br_x$ perovskites with different compositions.

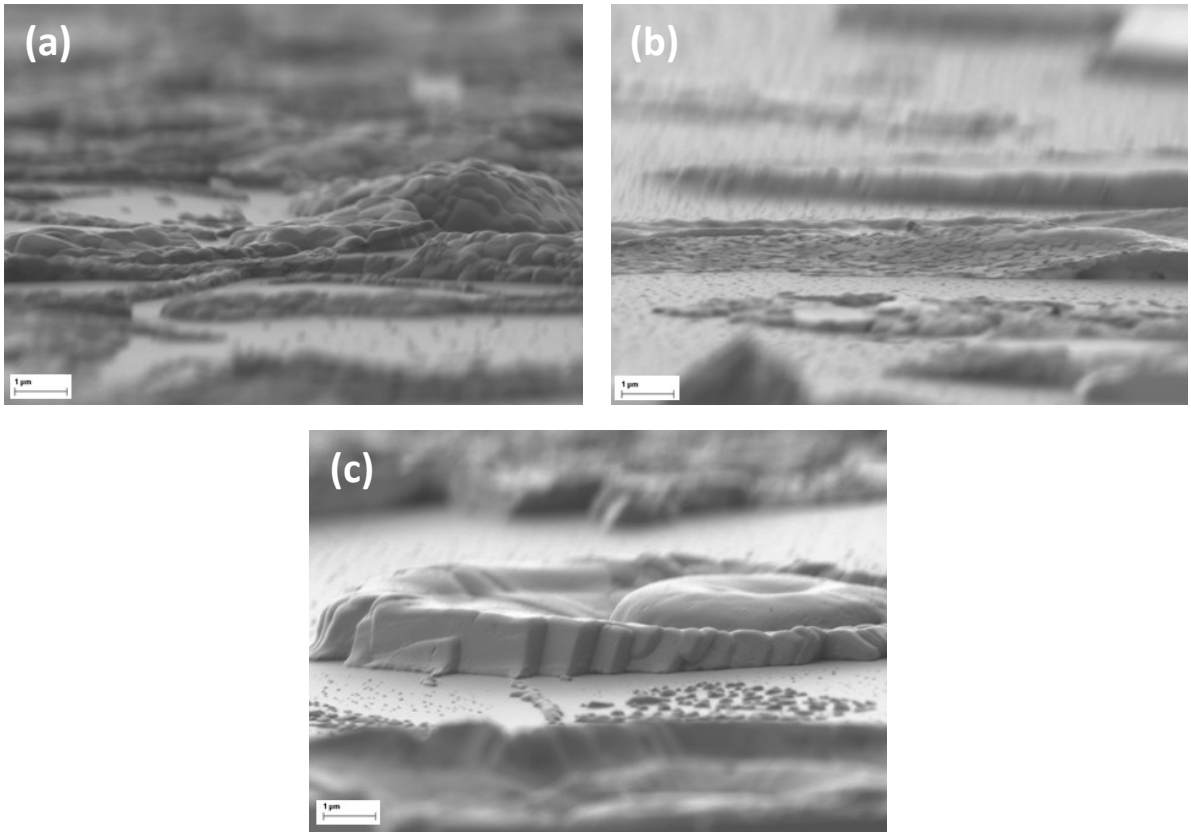

Figure 3.47 SEM images of $MAPbI_{3-x}Br_x$ samples with Br content of (a) 0.80, (b) 1.89 and (c) 3.00.

3.3.1.1 Influence of the preparation process

To assume the equation 3.3 as a reliable relation to derive the composition of a generic $MAPbI_{3-x}Br_x$ film from its bandgap value, it must be verified that the optical and structural properties of the samples analyzed to derive it are not affected by the baking conditions.

A baking temperature of 100 °C is often used for single step synthesis from solution of lead halide perovskites, while the baking time usually ranges from 15 to 45 min[36,48,51,152,154]. Therefore, we tested the stability of the prepared $MAPbI_{3-x}Br_x$ films for thermal treatments performed at 100 °C for various time. As reference compositions, we chose x = 0 ($MAPbI_3$) and x = 1 ($MAPbI_2Br$). For $MAPbI_3$ both absorption spectra and XRD patterns are nearly independent of the annealing time up to 60 min (figure 3.48).

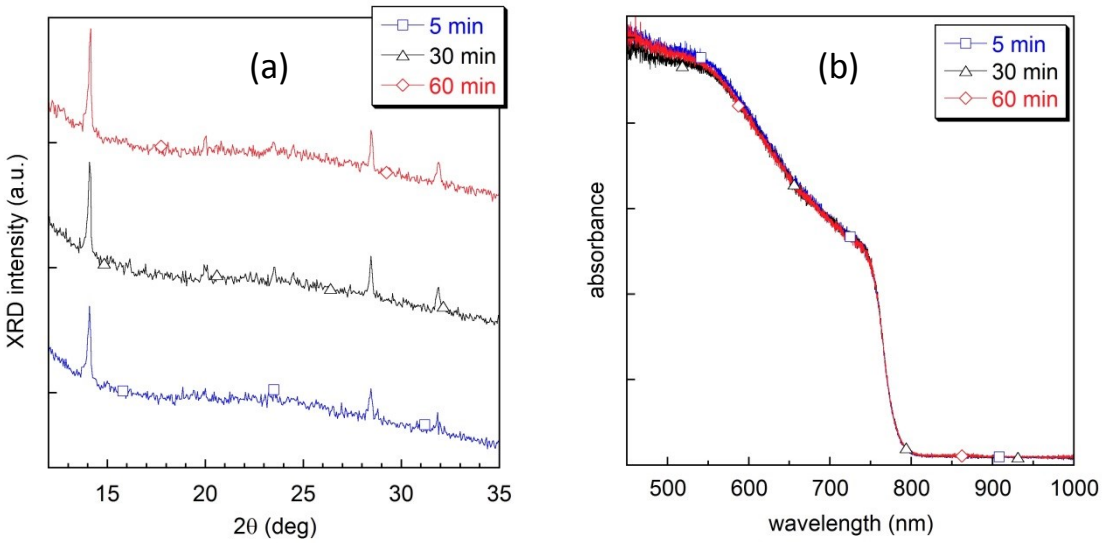

Figure 3.48 (a) XRD patterns and (b) absorption spectra of $MAPbI_3$ films baked at 100 °C for times ranging from 5 to 60 min.

A different behavior is observed when considering $MAPbI_2Br$ films. The samples treated for 5 and 10 min show comparable XRD patterns and absorption spectra (figure 3.49), while those annealed for 20 min point out the emergence of the diffraction peak of PbI_2 at 2θ = 12.7° in the XRD pattern as well as a slight blue-shift of the absorption onset. This indicates that the perovskite starts decomposing by the formation of PbI_2 and the increase of the Br/I ratio in the perovskite when the annealing is prolonged, as also confirmed by the PbI_2 XRD peak observed by Sadhanala et al in their 45 min annealed films[50]. These results point out also that the formation process of the perovskite is already complete after 5 min baking, and so that a thermal treatment at 100 °C for 5 min has to be considered a suitable annealing to correctly form $MAPbI_{3-x}Br_x$ perovskites when using a mixture of $MAPbI_3$ and $MAPbBr_3$ solutions. Therefore, the E_g values measured for the samples described in section 2.2 are not affected by thermal annealing,

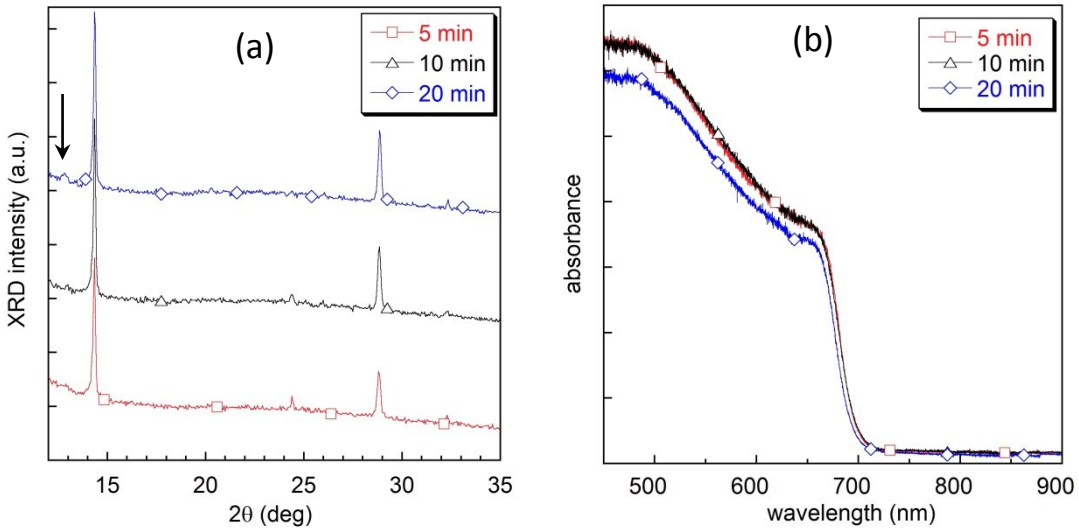

Figure 3.49 (a) XRD patterns and (b) absorbance spectra of $MAPbI_2Br$ films baked at 100 °C for times ranging from 5 to 60 min. The arrow in XRD pattern indicates the PbI_2 peak.

3.3.2 $MAPbI_{3-x}Br_x$ perovskites from single precursor solution

3.3.2.1 $MAPbI_{3-x}Br_x$ from 1.2:1 precursor solution

The first precursor solution we considered is those proposed by Qiu et al[51] to obtain $MAPbI_2Br$ perovskites. As described in section 2.2.4, this solution is obtained by dissolving in DMF equimolar amounts of PbI_2 and MABr. Similarly to what was observed for $MAPbI_3$ samples (see section 3.1.4), the XRD patterns of the $MAPbI_2Br$ films prepared following the Qiu method in ambient air often pointed out the presence of a peak at $2\theta = 12.7°$, related to the hexagonal PbI_2 phase (figure 3.50). On the contrary, we didn't observe any evidence of PbI_2 formation when the whole synthesis process was performed in an Ar-filled glove box. Similarly to $MAPbI_3$, we hypothesize that the presence of a residual PbI_2 phase was related to the decomposition of MABr salt caused by the ambient moisture[142]. We thus $MAPbI_2Br$ films in air enhancing the MABr content in the precursor solution, i.e. by using a 1.2:1 MABr:PbI_2 molar ratio instead of the conventional 1:1. Indeed, the XRD analysis on the samples prepared using the 1.2:1 solution in ambient air systematically didn't show any diffraction peak related to PbI_2, and the obtained spectra were comparable to those of samples prepared from 1:1 solution in inert atmosphere (figure 3.50).

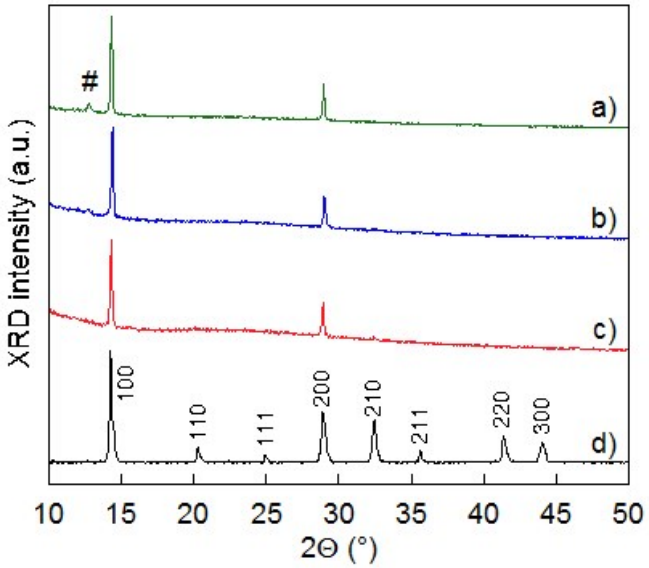

Figure 3.50 XRD patterns of $MAPbI_2Br$ films prepared by (a) 1:1 $MABr:PbI_2$ solution in air, (b) 1:1 solution in Ar-filled glove box, and (c) 1.2:1 solution in air. Pattern d) refers to the powdered sample obtained by the 1.2:1 solution in air. The hash indicates the PbI_2 peak.

In figure 3.51 the Tauc plot of samples prepared with the three different procedures, i.e. 1:1 solution in air, 1:1 solution in glove box and 1.2:1 solution in air, are reported.

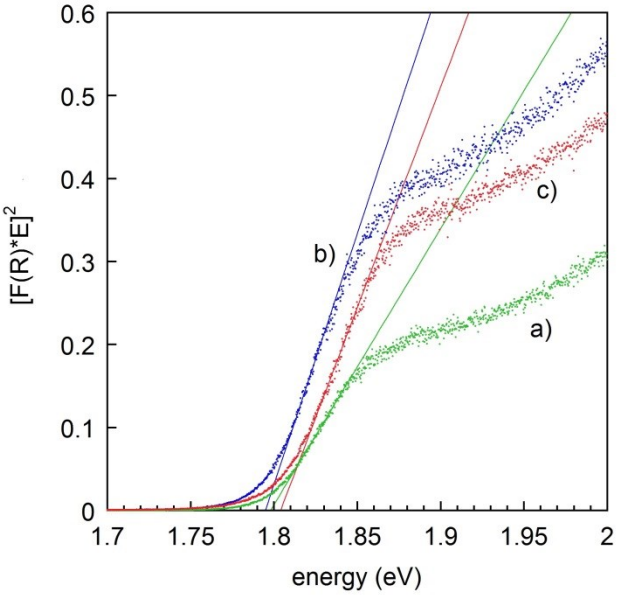

Figure 3.51 Tauc plot for $MAPbI_2Br$ films prepared by a) 1:1 $MABr:PbI_2$ solution in air, b) 1:1 solution in Ar-filled glove box, and c) 1.2:1 solution in air.

The obtained bandgap values depend on a minor extent on both atmosphere and presence of the MABr excess. The value of E_g = 1.80 eV that we found is in good agreement with the 1.81 eV bandgap energy reported for $MAPbI_2Br$ nanosheets layers[155] and with the 1.78 eV value reported for $MAPbI_2Br$ films[51]. According to the equation 3.3, the E_g value corresponds to a Br^- content $x \approx 1$.

XRD measurements performed on powdered samples show that in all the cases the samples are crystallized in the cubic perovskite structure, consistently with the results found for samples with *x* = 1 prepared by mixing $MAPbI_3$ and $MAPbBr_3$ precursor solutions (figure 3.39 and 3.40). Anyway, it must be pointed out that a tetragonal structure is reported by Qiu et al for $MAPbI_2Br$[51]. Nevertheless, our XRD patterns on these samples systematically pointed out the lack of the (211) and (213) reflections typical of the tetragonal perovskite symmetry, located respectively at 2θ = 23.55° and 2θ = 31.40°.

The influence of the baking conditions on the $MAPbI_2Br$ perovskite obtained from precursor solution with 1.2:1 MABr:PbI_2 molar ratio was then investigated. The XRD patterns obtained for samples baked for different time and temperatures are comparable and show no presence of PbI_2 in the film (figure 3.52), thus pointing out that the structure is very stable and not significantly influenced by variations both of time and temperature, for the baking conditions explored.

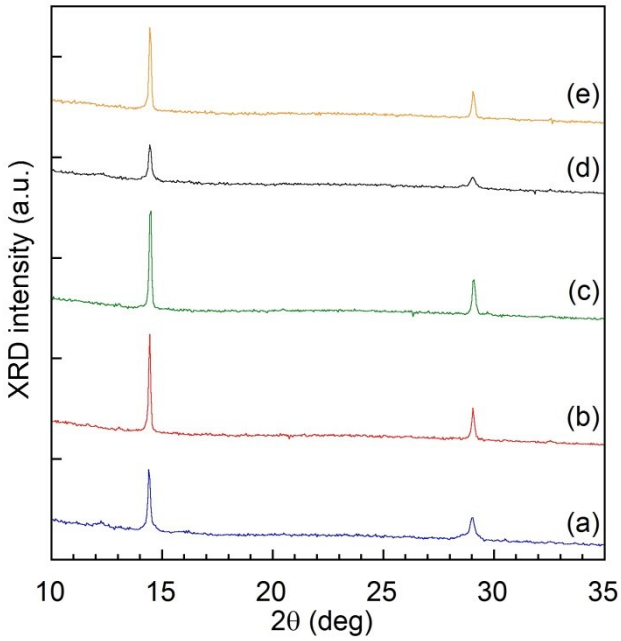

Figure 3.52 XRD patterns of $MAPbI_2Br$ films obtained from the 1.2:1 solution by annealing at 100 °C for (a) 5 min, (b) 20 min and (c) 60 min, and for 20 min at (d) 120 °C and (e) 80 °C.

On the contrary, the absorbance spectra of the samples (figure 3.53) are modified by changing the baking parameters. In particular, absorbance progressively decreases when the annealing time is increased from 5 to 60 min at 100 °C (figure 3.53a). The influence of the temperature is shown in figure 3.53b, for a fixed baking time of 20 min. Slightly higher absorbance steps at the band edge are obtained at 100 and 110 °C compared to those observed for lower temperatures, while at 120 °C an overall decrease of the absorbance is observed.

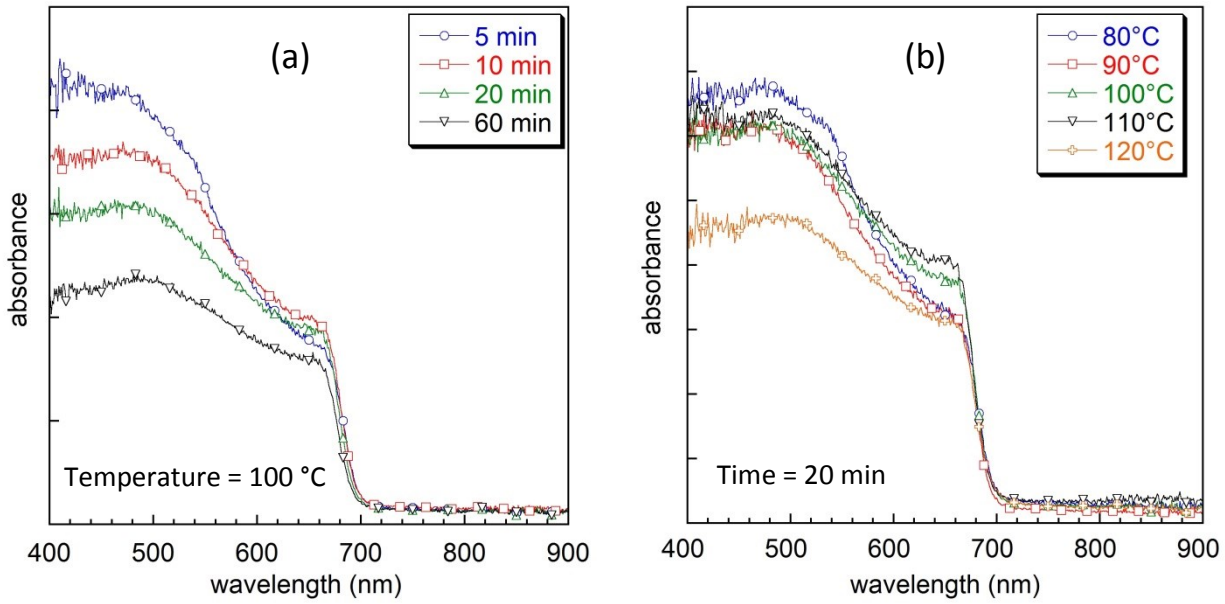

Figure 3.53 Absorbance spectra of $MAPbI_2Br$ films obtained from the 1.2:1 solution by annealing for (a) different times and (b) temperatures, as indicated.

The values of the bandgap E_g and the Urbach energies E_U derived from the measurements shown in figure 3.53 are reported in table 3.5, together with the corresponding x molar fractions calculated by equation 3.3 from the relevant E_g values.

Fixed annealing time = 60 min			
Temperature(°C)	E_g(eV)	x	E_U(meV)
80	1.79	0.96	39
90	1.80	1.00	34
100	1.80	1.00	32
110	1.81	1.05	31
120	1.80	1.00	36
Fixed annealing temperature = 100 °C			
Time (min)	E_g(eV)	x	E_U(meV)
5	1.79	0.96	36
10	1.80	1.00	36
20	1.80	1.00	32
60	1.81	1.05	32

Table 3.5 E_g, E_U and x values calculated from the absorbance spectra of figure 3.53.

For all the baking parameters explored the bandgap energies measured are around the 1.80 eV value expected for $MAPbI_2Br$, thus indicating that the composition of the obtained material is well preserved, especially for intermediate times and temperatures. Similarly, a minor influence of the annealing conditions is found on the Urbach energy. These results show that the $MAPbI_2Br$ perovskite made using the 1.2:1 solution is compositionally rather stable, likely due to the presence of the MABr excess that compensates losses of the organic material during the annealing process. In

conclusion, both structural and optical analysis indicate that the composition of the obtained material is substantially independent from the baking procedure.

3.3.2.2 $MAPbI_{3-x}Br_x$ from 3:1 precursor solution

We synthesized the mixed I/Br perovskite also using another single precursor solution having a different molar ratio between its components. As described in section 2.2.4, this solution was obtained by dissolving in DMF MAI and $PbBr_2$ with a molar ratio of 3:1. This solution, which was recently used also by Yang et al[156], is analogous to those used by Lee et al[28] to synthetize the mixed $MAPbI_{3-x}Cl_x$ perovskite, as described in section 3.4.1. In their pioneering work, Lee et al addressed the stoichiometry of the compound as $MAPbI_2Cl$, while nowadays, after the work described in the following sections of this thesis and published in ref. [48], it is generally accepted that the formation of this compound is prevented by the large difference in the ionic radii of Cl^- and I^- anions. In the case of mixed Br/I perovskite, where the formation of an extended solid solution is allowed we observed that the composition of the resulting material is strongly influenced by the synthesis procedures, and more specifically by the annealing parameters.

Figure 3.54 shows the XRD patterns measured on films obtained by different thermal treatments. The spectra of films annealed at 120 °C for 45 min (figure 3.54a) show broad perovskite peaks at 2θ = 14.3° and 28.7° corresponding to the (100) and (200) perovskite Bragg reflections. The two additional peaks observed at 2θ = 12.3° and 16° are similar to those reported for $MAPbI_{3-x}Br_x$ films prepared by the same 3:1 precursor solution, but annealed at 105 °C[156]. In close analogy with what suggested for $MAPbI_{3-x}Cl_x$ films, they are considered to originate from products such as lead oxyhalides resulting from the slow drying process in humid air[157] and to the incorporation of methylammonium halides and their variations[158]. These peaks and the one at 2θ = 29.7°, that is related to PbI_2, point out that 45 min treatments are too short to allow the films to form properly at 120 °C. On the contrary, annealing for 60 and 120 min results in XRD patterns where only the presence of highly oriented perovskite films is pointed out, while treatments as long as 150 min cause the PbI_2 peak to appear with a significant reduction of the perovskite peaks amplitude, which means that perovskite decomposition is relevant. When considering samples annealed for 60 min at different temperatures, the XRD patterns (figure 3.54b) show that only for a temperature of 120 °C the perovskite is well formed without any other undesired phases. For lower temperatures, the peaks at 2θ = 12.3° and 16° are observed, while at 130 °C the PbI_2 peak at 2θ = 12.7° appears and at 140 °C it becomes dominant, with a significant reduction of the perovskite peaks, indicating that the compound decomposes at this temperature.

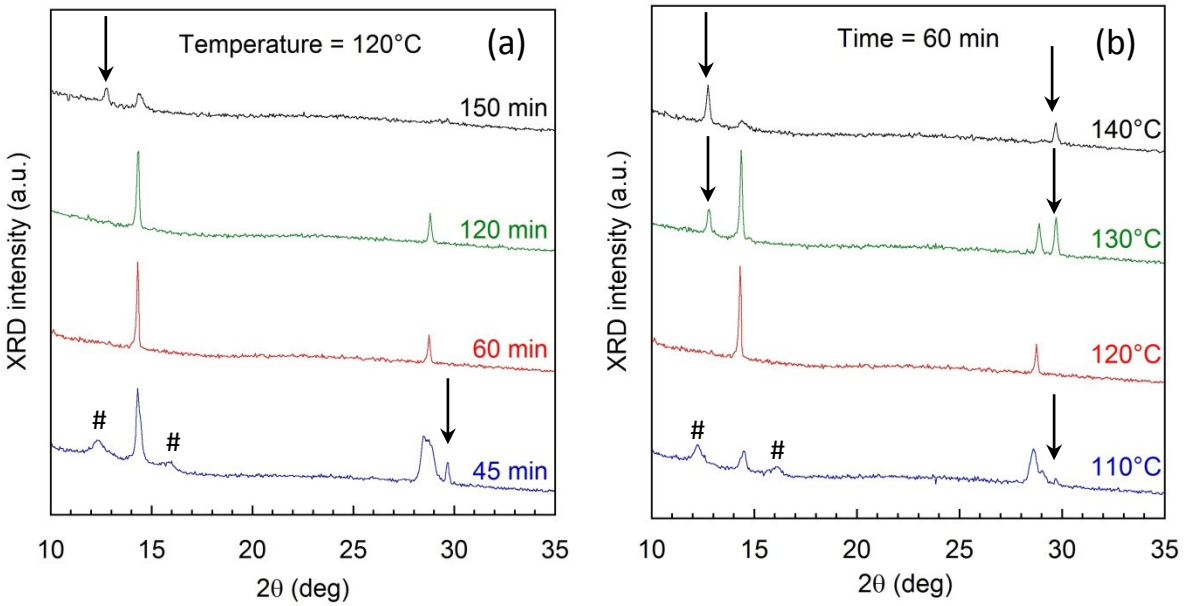

Figure 3.54 XRD patterns of $MAPbI_2Br$ films obtained from the 3:1 solution by annealing for (a) different times and (b) temperatures, as indicated. The arrows indicate the PbI_2 diffraction peaks, while the hashes indicate peaks originating from oxyhalides and incorporation of methylammonium halides and their variations (see text).

The strong influence of the baking procedure on the properties of the obtained perovskite is confirmed by the analysis of the absorbance spectra (figure 3.55).

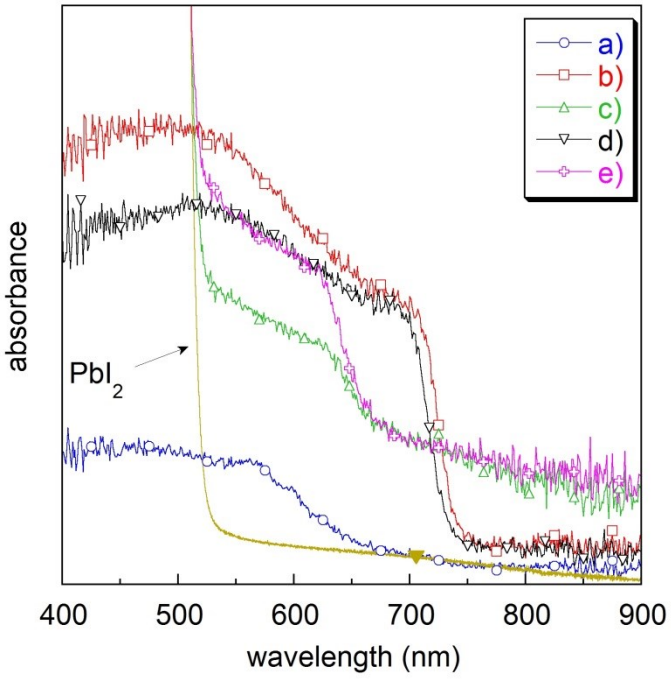

Figure 3.55 Absorbance spectra of $MAPbI_2Br$ films obtained from the 3:1 solution by annealing for 60 min at a) 110°C, b) 120°C and c) 130°C and at 120°C for d) 120 min, and e) 150 min. A typical absorbance spectrum of a PbI_2 film is also shown.

The samples show an absorbance spectrum typical of a pure phase perovskite film only for an annealing temperature of 120 °C. For a lower temperature (110 °C) a low absorbing compound is achieved, while for a temperature of 130 °C the spectrum shows the perovskite absorbance onset together with a second step at about 515 nm, whose spectral position corresponds to the bandgap of PbI_2. The absorbance contribution of PbI_2 is observed also in films annealed at 120 °C for 150 min, where the XRD pattern (figure 3.54) demonstrated that perovskite decomposes for long-lasting treatments. It is worth noting that the observable PbI_2 contribution to absorbance indicates that PbI_2 is present in a higher amount than those that would compete to an impurity phase, while in the $MAPbI_3$ films the PbI_2 is always detected only from XRD patterns with intensity classifiable as an impurity phase (section 3.1.4).

The above results indicate that annealing conditions affect the position of the perovskite absorbance onset, and thus the value of the bandgap E_g. According to the relation 3.3, this implies that the perovskite composition depends on thermal treatment. This is clearly pointed out in table 3.6, where the bandgap, Urbach energy and composition values obtained for the different baking procedures used are summarized. In particular, it can be observed that Br^- content increases with annealing time and temperature, ranging from x = 0.478 for the well-formed films annealed at 120 °C for 60 min to x = 1.44 for the poorly formed films treated at 110 °C. This composition variation is consistent with results recently obtained by Yang et al.[156], who used the 3:1 solution as well and showed that annealing at 155 °C instead of 105 °C shifts the absorption edge from 758 to 640 nm, which indicates that x changes from 1.86 to 0.45, according to eq.(2) in ref.[37].

Fixed annealing time = 60 min			
Temperature(°C)	E_g(eV)	x	E_U(meV)
110	1.96	1.70	300
120	1.69	0.47	38
130	1.75	0.76	84
140	1.82	1.10	265
Fixed annealing temperature = 120 °C			
Time (min)	E_g(eV)	x	E_U(meV)
30	1.68	0.41	58
45	1.66	0.31	66
60	1.69	0.47	38
120	1.71	0.57	45
150	1.86	1.28	173

Table 3.6 E_g, E_U and x values calculated from the absorbance spectra of figure 3.55.

Table 3.6 points out that also Urbach energy depends strongly by the annealing conditions. The lowest E_U value (38 meV) is found for the well-formed perovskite obtained after a baking at 120 °C for 60 min, while the maximum is observed for the poor-formed compound obtained after a 60 min baking at 110 °C. These values confirm that not only the bromide content, but also the film disorder depends on the annealing procedure on a much larger extent with respect the $MAPbI_{3-x}Br_x$ obtained from 1.2:1 precursor solution. This is likely due to the highly non-stoichiometric nature of the precursor solution, since perovskite formation implies that the large halides and methylammonium

ions excess is lost by mechanisms that can be made more complex due to the presence of humid air. Therefore, thermal treatment must be very accurate to guarantee an acceptable reproducibility of the synthesis process, which makes this last solution the less promising for large scale solar cell production.

3.4 $MAPbI_{3-x}Cl_x$ perovskites

In October 2012 Lee et al reported the possibility to use mixed $MAPbI_2Cl$ hybrid perovskite as light harvester in all-solid-state solar cells[28]. Few months later the same group improved the cell efficiency by using a low-temperature deposition process for the Al_2O_3 scaffold and the same material as light harvester[159], but in this latter work, the stoichiometry of perovskite was addressed as $MAPbI_{3-x}Cl_x$ instead on $MAPbI_2Cl$, without giving any other detail concerning the incorporation of Cl in the structure. This pointed out that the chlorine amount in the compound was not well defined and the perovskite formation process was still not completely understood. Since in both papers the chlorine role was not discussed, we investigated the chlorine inclusion in mixed I/Cl perovskites synthesized by different routes and its effect on the perovskite properties. The results of this activity have been reported in ref. [48].

Following the synthesis route proposed by Lee et al[28], we prepared $MAPbI_{3-x}Cl_x$ perovskite films by spin-coating on flat glass substrates a precursor solution prepared dissolving in DMF a large excess of MAI over $PbCl_2$, with a 3:1 molar ratio; for the sake of brevity, the films obtained from this route will be hereafter referred as "3:1" films. When trying to obtain this solution, we always observed suspended particles that we couldn't avoid. Usually, solution filtering is reported in literature. We centrifuged the suspension aiming to study this particulate, but it was not possible to collect enough powder for any analysis.

After the spin-coating deposition of the precursor solution, a milky yellowish film was observed; the samples were then baked on a hot plate in nitrogen atmosphere at 100 °C for 60 min. Soon after putting the samples on the hot plate, a color change from yellowish to dark brown was observed, similarly to what was observed for $MAPbI_3$ films (see section 3.1).

The XRD pattern of the obtained perovskite film is reported in figure 3.56, together with the one reported by Lee et al[28]. The XRD pattern shows that the film is highly oriented, similarly to what is observed for $MAPbI_3$ films prepared from DMF precursor solution (see section 3.1.2). In agreement with the spectra reported by Lee et al for the same material[28], the diffraction peak of PbI_2 can also be detected with an intensity classifiable as an impurity phase. It is worth noting that, in contrast with was observed for $MAPbI_3$ samples, the presence of the PbI_2 peak in these samples was observed whether the film were prepared in ambient air or in inert atmosphere in glove box. The spectrum reported by Lee et al present also a non-identified phase resulting in a peak located at $2\theta = 15.56°$. This spurious phase is not observed in our samples.

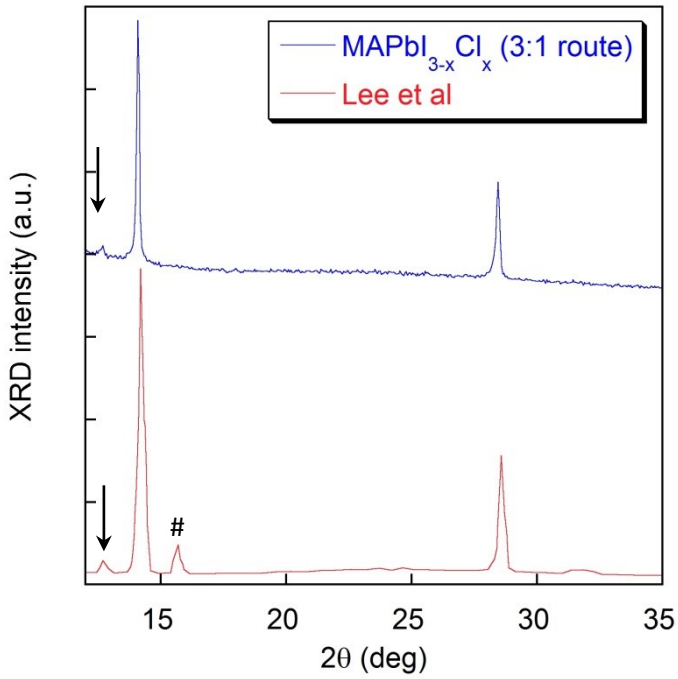

Figure 3.56 XRD pattern of the 3:1 $MAPbI_{3-x}Cl_x$ film, compared with those reported by Lee et al[28]. Arrows indicate the PbI_2 diffraction peak, while the hash indicate the unassigned peak reported in the reference paper.

Analysis of the *d*-spacings related to the perovskite reflection sequence suggests that the obtained perovskite main phase could be strictly related to $MAPbI_3$. To confirm this hypothesis the XRD analysis was repeated on the powders, that were carefully scraped from the glass substrates by the same procedure followed to obtain $MAPbI_3$ powders (see section 3.1.1).

The obtained XRD profile is reported in figure 3.57, compared to those reported in figure 3.2 for $MAPbI_3$ powders. LeBail profile refinement performed with the software GSAS determined that the obtained 3:1 film crystallizes in the tetragonal perovskite structure with lattice parameters a = 8.8535(3) Å and c = 12.6434(4) Å, giving a cell volume of 991.5 $Å^3$. The calculated lattice parameters are quite different from those reported by Lee et al (a = 8.825 Å, b = 8.835 Å and c = 11.24 Å)[28], in particular the c axis, while they are very similar to those calculated by the same refinement for $MAPbI_3$ (a = 8.8755(5) Å, c = 12.6735(8) Å, V = 998.35 $Å^3$).

The calculated lattice parameters indicate a ca. 0.7% reduction of the unit cell volume of the 3:1 $MAPbI_{3-x}Cl_x$ powders with respect to $MAPbI_3$ powders. Although small, this difference is not negligible, as it is well above the instrumental sensitivity, and it could be reasonably explained by hypothesizing the formation of a $MAPbI_3$ structure presenting a certain level of Cl-doping. Thus, these results suggest that $MAPbI_3$ formation is favored when the molar ratio I:Pb in the precursor solution is 3:1; the excess chloride and methylammonium is assumed to evaporate during the drying process.

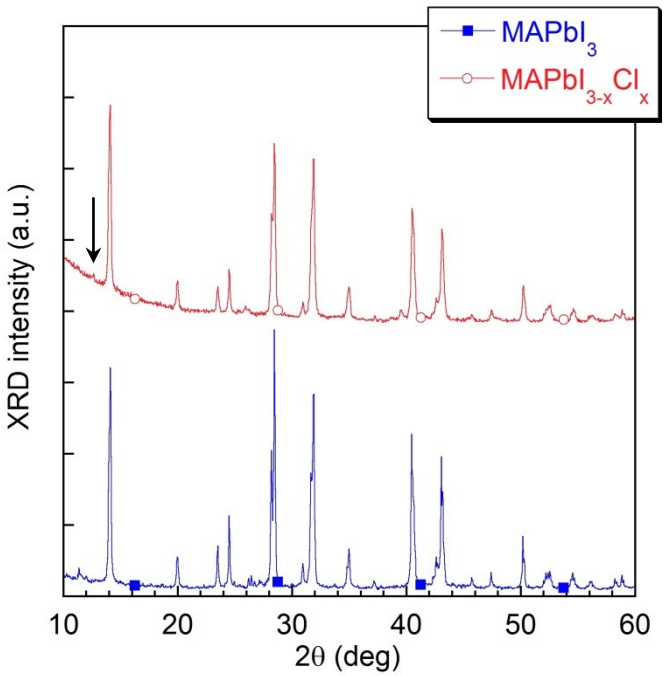

Figure 3.57 XRD pattern of powders scraped from 3:1 $MAPbI_{3-x}Cl_x$ film, compared with $MAPbI_3$ powders. The arrow indicates the PbI_2 diffraction peak.

To promote the Cl incorporation in the perovskite structure, we investigated the formation of the perovskite using a precursor solution characterized by a different stoichiometry. As reported in section 2.2.5, this precursor solution was obtained by dissolving in DMF equimolar amounts of PbI_2 and MACl (1:1 molar ratio). We observed no particulate formation at concentrations similar to those used in 3:1 route (20 wt%), likely due to the PbI_2 solubility in DMF, that is about 2 orders of magnitude higher than those of $PbCl_2$. For the sake of brevity, the films obtained from this route will be hereafter referred as "1:1" films.

The XRD patterns (figure 3.58) show that 1:1 films are highly oriented, systematically pointing out the presence of $MAPbI_3$ and PbI_2 together with a further phase that was present also in the pattern reported by Lee et al for the 3:1 films, but that was not assigned[28]. The XRD analysis on powdered samples (figure 3.59) allowed to identify this additional phase as the cubic $MAPbCl_3$ perovskite, with a = 5.683(2) Å.

The segregation of the cubic $MAPbCl_3$ indicates that the chloride solubility limit in the iodide derivative is quite low, in line with the unfavorable calculated formation energies[137], and that the formation of an extended solid solution is prevented. Similarly to what is observed in Sn-based hybrid halide perovskites[160], the reason that hampers the Cl^- solubility in the $MAPbI_3$ structure can be likely identified in the significant difference in the ionic radii of Cl^- and I^- anions (1.67 and 2.08 Å, respectively[161]). Therefore, from XRD data we can argue that the perovskite composition cannot be tuned by varying the I:Cl molar ratio in the precursor solution[48], contrary to what is observed in Br/I mixed-halide perovskites[37], where the difference in Br^- and I^- anions ionic radii is smaller (1.67 and 1.82 Å, respectively[161]).

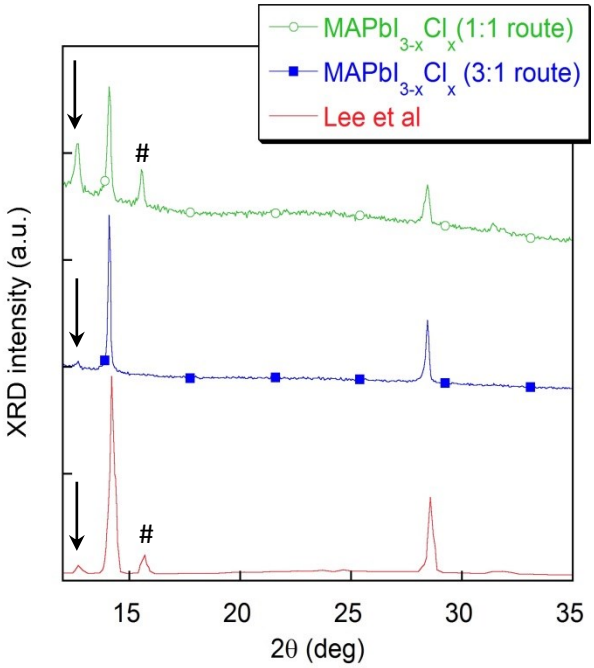

Figure 3.58 XRD pattern of a 1:1 film, compared with a 3:1 film and the pattern reported by Lee et al[28]. Arrows indicate the PbI_2 diffraction peak, while hashes indicates the peak assigned to cubic $MAPbCl_3$.

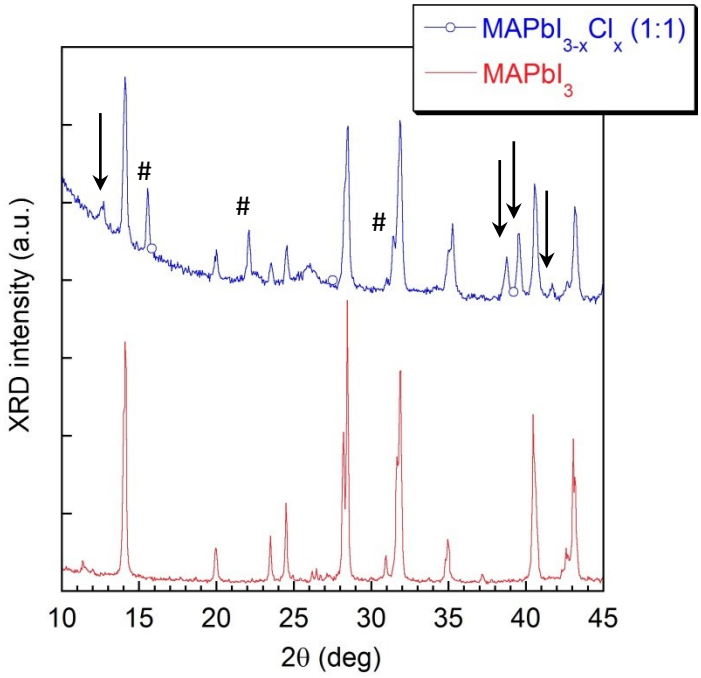

Figure 3.59 XRD pattern of powders scraped from 3:1 $MAPbI_{3-x}Cl_x$ film, compared with $MAPbI_3$ powders. Arrows indicate the PbI_2 diffraction peaks, while hashes the peaks assigned to the cubic $MAPbCl_3$ perovskite.

This deduction was further supported by the optical characterization showing that in all the samples the absorption edge appears at about 780 nm (figure 3.60), that represents a usual feature of $MAPbI_3$[1,27,162].

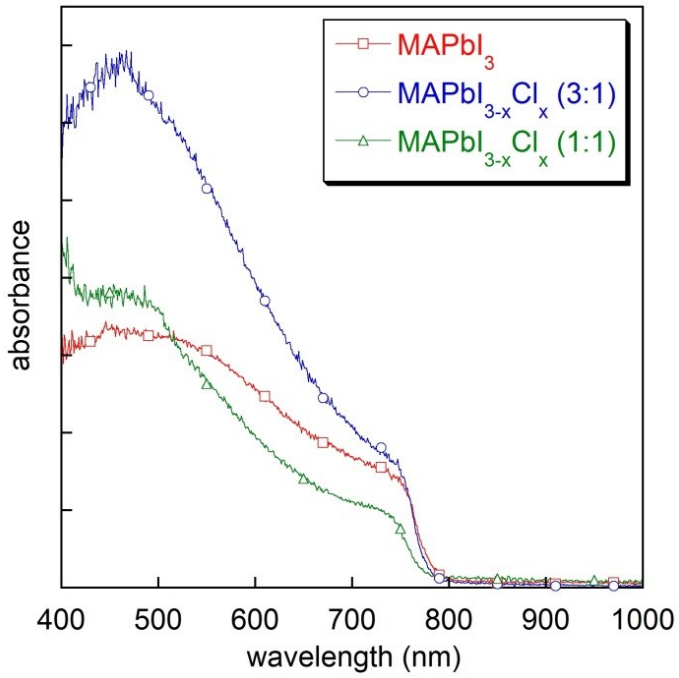

Figure 3.60 Absorption spectra of $MAPbI_3$, 3:1 and 1:1 $MAPbI_{3-x}Cl_x$ films.

The Tauc plot calculated from the diffuse reflectance spectra reveals that the optical bandgap is 1.60 eV for the $MAPbI_3$ film, 1.61 eV for the 3:1 film and 1.62 for the 1:1 film (figure 3.61), pointing out that the bandgap of both $MAPbI_{3-x}Cl_x$ films is comparable with those found for $MAPbI_3$ reported in section 3.1. The value of 1.61 eV calculated for the 3:1 film is different from the value reported by Lee et al, namely 1.55 eV[28], likely because this latter was extracted from the Incident Photon to Current (IPCE) onset measured in a solid-state DSSC using the perovskite as light absorber.

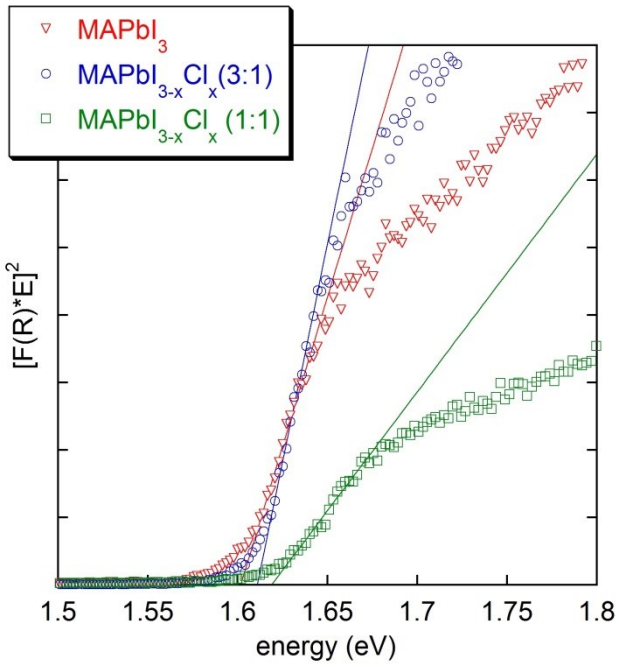

Figure 3.61 Determination of the optical bandgap via Tauc plot for $MAPbI_3$, 3:1 and 1:1 $MAPbI_{3-x}Cl_x$ films.

As for the 3:1 and 1:1 films, based on the results obtained on $MAPbI_{3-x}Br_x$ and $MAPbBr_{3-x}Cl_x$, Papavassiliou et al proposed that even in $MAPbI_{3-x}Cl_x$ the optical absorption bands varied linearly with the Cl molar fraction x[26]. Under this assumption and using for the bandgap of $MAPbCl_3$ an E_g value of 3.11 eV[162], the bandgap values found for 3:1 and 1:1 $MAPbI_{3-x}Cl_x$ (1.61 and 1.62 eV, respectively) would be compatible to x values smaller than 4%, reasonably matching the XRD results. Aiming at a more quantitative evaluation of the Cl^- inclusion in the structure, we performed SEM-EDS on the 3:1 film, but in both films and powdered samples we could not achieve reliable values of the Cl concentration as the amplitude of the Cl-related signal was observed to decrease during the measurement[48].

The indications deriving from both structural and optical characterization were supported also by DFT analysis, that was performed in collaboration with Computational Laboratory for Hybrid/Organics Photovoltaics (CLHTYO, CNR-ISTM, Perugia, Italy) aiming to model the structural and electronic modifications possibly induced by Cl-doping in $MAPbI_3$ structure. A large tetragonal cell initially composed of 32 $MAPbI_3$ units was considered, allowing to explore a Cl doping as small as ca. 1% (1 chloride:95 iodide atoms), considering additional values of 0% (corresponding to the pure MAPbI3 phase), 4%, 8%, and 33% doping (corresponding to $MAPbI_2Cl$ stoichiometry). All the details of this simulation work, that is beyond the aims of this work, are given in ref. [48]. Most notably, for x = 4% a reduction of the cell volume of 0.76/0.91% was found, and a slight or null band gap increase. These results are strongly correlated to the experimental data and confirm a low Cl incorporation of about 3-4% in the I-based perovskite.

3.4.1 Solar cells using $MAPbI_3$ and $MAPbI_{3-x}Cl_x$ as sensitizer

In order to evaluate the impact on the photovoltaic performances of the Cl inclusion in the $MAPbI_3$ perovskite, some conventional all-solid-state DSSCs using $MAPbI_3$ and $MAPbI_{3-x}Cl_x$ as light absorber were prepared at IIT institute in Lecce (Italy). Solar cells were fabricated on semitransparent fluorine doped tin oxide (FTO) coated glass, covered with a compact TiO_2 layer that acts as the anode. After the sensitization with the perovskite of the nanoporous TiO_2 layer, spiro-MeOTAD was spun coated on as hole collecting and transporting layer and finally the Ag cathode was evaporated on the top of the device[48]. Figure 3.62 shows a schematic representation of the complete device.

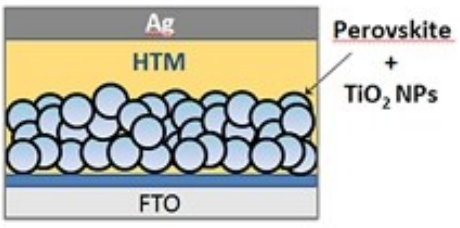

Figure 3.62 Schematization of the all-solid-state DSSCs realized using $MAPbI_3$ and $MAPbI_{3-x}Cl_x$ as sensitizers. From [48].

In figure 3.63 the room temperature current density – voltage (J-V) curves of three representative PS1-3 based devices are reported. The characteristics were acquired under Air Mass 1.5 Global (AM 1.5G) solar simulator with an irradiation intensity of 100 mW cm^{-2}. In table 3.7 the average parameters obtained from measurement on different sets of cells are reported.

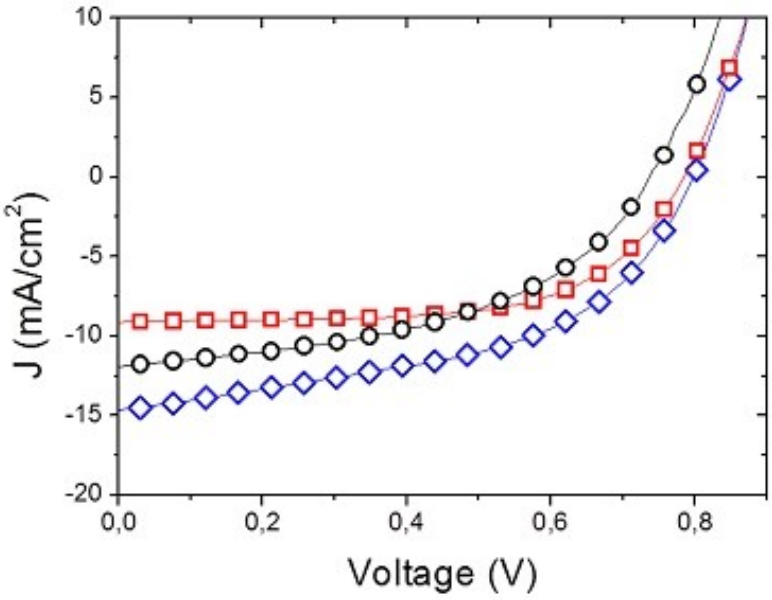

Figure 3.63 J–V curves under illumination for the PS1 –PS3 based hybrid devices. From [48].

	PCE (%)	FF	V_{oc} (V)	J_{SC} (mA/cm^2)
O ($MAPbI_3$)	3.85 ± 0.94	0.45 ± 0.16	0.76 ± 0.02	11.65 ± 2.94
◊ (3:1)	6.15 ± 1.24	0.51 ± 0.09	0.76 ± 0.06	16.36 ± 4.11
□ (1:1)	3.85 ± 0.04	0.56 ± 0.06	0.75 ± 0.02	9.23 ± 1.28

Table 3.7 Photovoltaic parameters of the solar cells.

The differences observed in the device performances, summarized in table 3.7, can be directly ascribed to the active materials, since the device architecture remains substantially unchanged for the three different perovskites. The increasing J_{SC} going from 1:1 to $MAPbI_3$ to 3:1 device can be ascribed to the cooperation of increased light harvesting capabilities and improved charge transport properties. The J_{SC} as high as 16.36 mA/ cm^2 represents the most relevant difference among 3:1 and the other two compounds.

Aiming to deepen the role of the charge transport on the photovoltaic performances of the three perovskites, the series resistance (R_S) was studied for the same set of representative devices reported in figure 3.63 containing the different perovskites as active harvesting component. In particular the reciprocal series resistance, calculated as the slope at $V = V_{OC}$ of the illuminated J–V curves[163], was plotted against the short-circuit current for different light intensities[37]. In this case, the difference in R_S is expected to mainly depend on the light harvester layer and in particular on the intrinsic charge transport properties, as the other factors affecting R_S, such as electrode resistances and the base contact resistances, can reasonably be assumed as comparable, due to the use of same architecture and materials in the cell configuration[164].

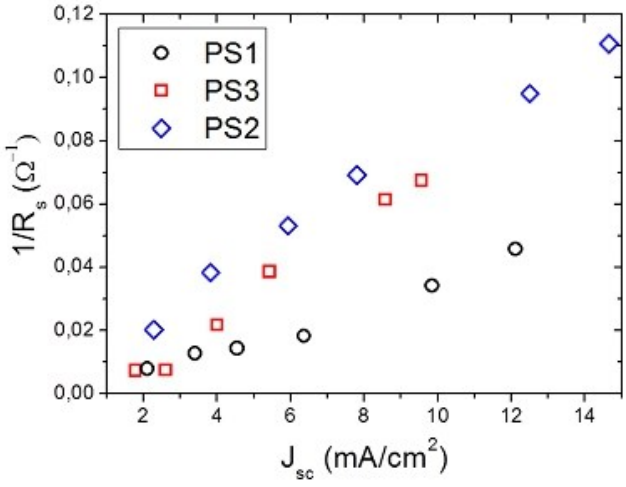

Figure 3.64 The relationship between reciprocal series resistance and short-circuit current density (J_{SC}) for the cells fabricated from PS1−3 as light harvesters. J_{SC} was obtained as a function of light intensity. From [48].

Figure 3.64, that shows the $1/R_S$ trend, highlights a steeper slope for 3:1 and 1:1 based cells compared with the cell containing $MAPbI_3$. This confirms that charge transport properties are substantially improved by the inclusion of a relatively low amount of chloride in $MAPbI_{3-x}Cl_x$ in both 3:1 and 1:1 devices. This is in agreement with the observation that both electron and holes diffusion are significantly higher in $MAPbI_{3-x}Cl_x$ than in $MAPbI_3$. Indeed, Stransk et al reported for $MAPbI_{3-x}Cl_x$ values larger than 1 μm[165], while the electron and holes diffusion lengths observed for $MAPbI_3$ are limited to few hundreds of nm[166].

These results highlight that, although Cl inclusion in $MAPbI_3$ is possible only at low concentrations, Cl doping dramatically improves the charge transport in the perovskite layer, leading to the realization of solar cells with lower series resistances and higher PCE values[48].

CHAPTER 4
ZINC OXIDE NANOSTRUCTURES

4.1 Mesoporous ZnO nanobelts

Hybrid $ZnS(en)_{0.5}$ nanostructures were proposed in literature as precursor for mesoporous ZnO nanocrystals[3,5,72], as described in section 1.7. However, before the work reported in this thesis, the transformation of $ZnS(en)_{0.5}$ into ZnO had been successfully demonstrated only for nanocrystals having a bi-dimensional platelet shape. Aiming at extending this procedure to other kinds of nanostructures, we synthesized $ZnS(en)_{0.5}$ in form of nanobelts by the solvothermal preparation route reported by Zhang et al[4] et described in section 2.4. As reported by Zhang et al[4], we initially performed the synthesis on metallic Zn foils. Figure 4.1 shows the XRD pattern of the as-synthesized nanobelts compared to the XRD pattern calculated for this material by Ouyang et al[167].

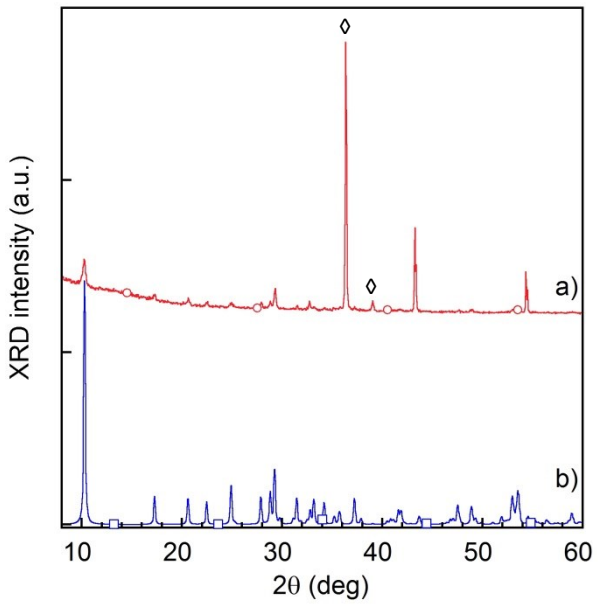

Figure 4.1 XRD patterns of as-synthetized $ZnS(en)_{0.5}$ hybrid nanobelts on Zn foil (a), compared with those calculated for $ZnS(en)_{0.5}$ by Ouyang et al[167] (b). Zn peaks are indicated by ◊.

In the experimental pattern several peaks can be individuated. Those marked with ◊ originate from the metallic Zn substrate, while the other diffraction peaks matches those of the pattern calculated for the $ZnS(en)_{0.5}$ compound, that indicates that $ZnS(en)_{0.5}$ is characterized by an orthorhombic structure.

The morphology of the obtained $ZnS(en)_{0.5}$ nanobelts films was investigated by means of SEM analysis. Figure 4.2 shows that the solvothermal synthesis results in an entanglement of a large quantity of hybrid belt-like structures, characterized by lengths in the range of 10-15 µm and widths of 80-500 nm, in good agreement with what observed by Zhang et al[4].

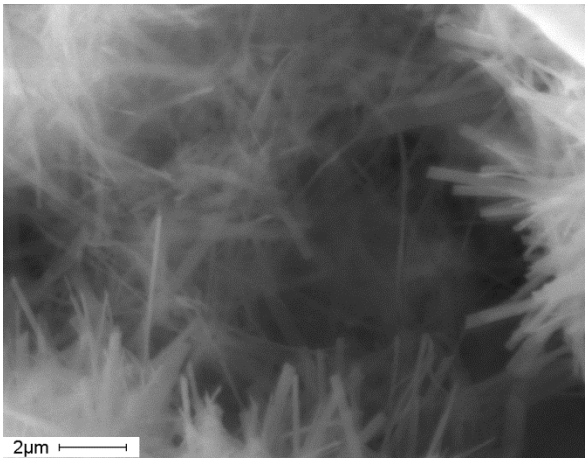

Figure 4.2 SEM image of as-synthetized $ZnS(en)_{0.5}$ hybrid nanobelts on Zn foil.

As described in section 2.4, the as-grown nanobelts were initially annealed at 400 °C for 50 h in air. In the typical XRD pattern of the resulting samples (figure 4.3), the $ZnS(en)_{0.5}$ peaks have completely disappeared, and two sets of diffraction peaks can be observed, corresponding to the hexagonal wurtzite ZnS (♦) phase (JCPDS no. 36-1450, a = 0.382 nm and c = 0.626 nm) and the hexagonal wurtzite ZnO (*) phase (JCPDS no. 36-1451, a = 0.325 nm and c = 0.521 nm), respectively. This indicate the coexistence of these two phases in the material, in agreement with what observed for $ZnS(en)_{0.5}$ nanosheets[3,72]. It is worth noting that Zhang et al reported the conversion of $ZnS(en)_{0.5}$ nanobelts in bare ZnS structures by thermal annealing at 300 °C in Ar atmosphere[4].

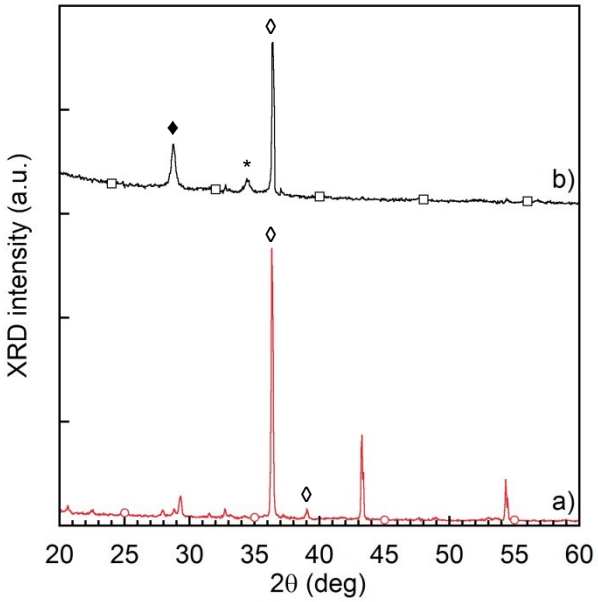

Figure 4.3 XRD patterns of $ZnS(en)_{0.5}$ hybrid nanobelts on Zn foil (a) and sample calcinated at 400 °C (b). ◊, ♦ and * indicates Zn, ZnS and ZnO peaks, respectively.

After a further annealing at 600 °C for 2 h in air, in the XRD pattern (figure 4.4) the peaks corresponding to the wurtzite ZnS phase disappear and only the peaks of wurtzite ZnO can be observed. This indicate that the nanobelts have been thoroughly converted into ZnO, similarly to what observed for $ZnS(en)_{0.5}$ nanosheets[3,5,72].

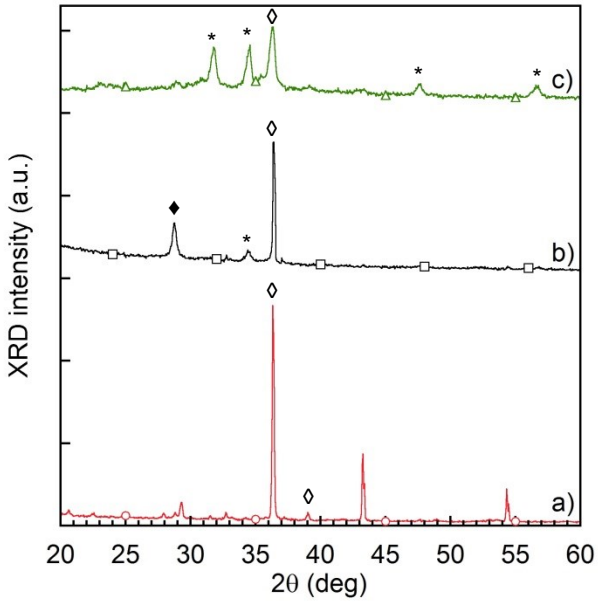

Figure 4.4 XRD patterns of $ZnS(en)_{0.5}$ hybrid nanobelts on Zn foil (a), sample calcinated at 400 °C (b) and sample calcinated at 600 °C. ◊, ♦ and * indicates Zn, ZnS and ZnO peaks, respectively.

Figures 4.5a and 4.5b show typical SEM images of the nanobelts after the annealing at 400 °C and the further calcination at 600 °C, respectively. It is evident that the thermal annealings don't affect the morphology of the entanglement nor the shape of the crystals, that maintain their original belt-like aspect.

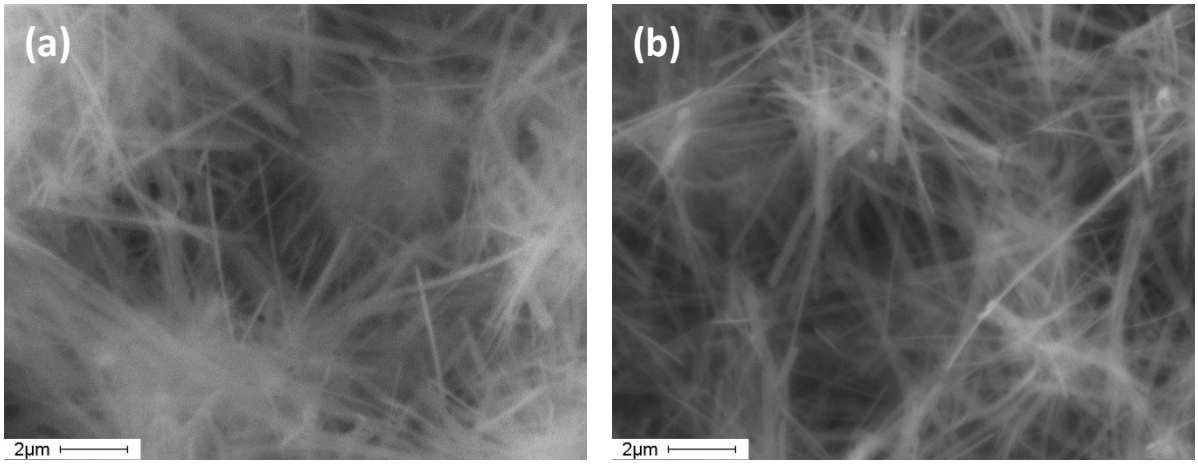

Figure 4.5 SEM image of (a) sample calcinated at 400 °C for 50 h and (b) sample calcinated at 400 °C for 50 h + 600 °C for 2 h.

The possibility to obtain patterned nanobelts distributions on insulating substrates is a strict requirement for the application in microelectronic devices. Therefore, we performed the synthesis of $ZnS(en)_{0.5}$ nanobelts and the subsequent calcination on Zn metalized alumina substrates, whose preparation is described in section 2.4. Some syntheses were carried out also on transparent glass substrates, but the electrical measurements that will be described in section 4.1.4 revealed that glass could not provide the needed electrical insulation at high temperatures. Therefore, alumina was assumed as standard insulating substrate.

Figure 4.6 shows the XRD patterns referred to a sample prepared on alumina before the thermal treatments, after the calcination at 400 °C and after the calcination at 600 °C, respectively. The XRD patterns confirm the results observed when performing the synthesis on a Zn foil. In the XRD pattern of the as-synthesized hybrid nanobelts (fig. 4.6a), several peaks can be individuated. The peaks marked with # and ◊ represent respectively the reflection of the alumina substrate and the metallic Zn pads upon which the growth occurs. The remaining peaks, marked with ▲, closely correspond to the diffraction pattern of $ZnS(en)_{0.5}$[167], indicating that the synthesis of the desired material could be achieved on the metalized substrate. In the pattern of the sample calcinated at 400 °C for 50 h (fig. 4.6b) the $ZnS(en)_{0.5}$ peaks have completely disappeared, while the peaks of the hexagonal wurtzite ZnS (♦) together with the peaks of the hexagonal wurtzite ZnO (*) can be observed; the peaks of the alumina substrate and the Zn pads are still present. In the pattern of the sample calcinated at 400 °C for 50 h and then at 600 °C for 2 h (fig. 2.10c), only the peaks of the wurtzite ZnO, the alumina substrate and the Zn pads can be observed, indicating the complete conversion of nanobelts into ZnO.

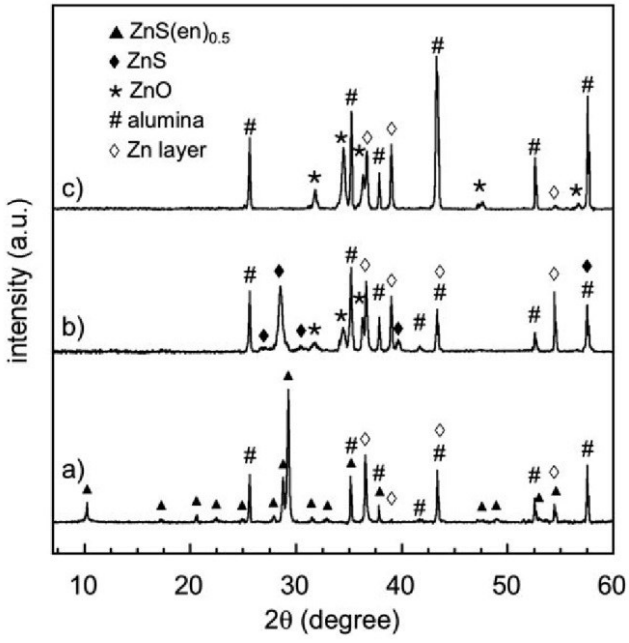

Figure 4.6 XRD patterns of (a) as-synthetized $ZnS(en)_{0.5}$ hybrid precursor, (b) sample calcinated at 400 °C for 50 h and (c) sample calcinated at 400 °C for 50 h + 600 °C for 2h.

Similarly to what observed in the samples grown on Zn substrate, the morphology of the nanobelt entanglement is not significantly affected by the thermal treatments (figure 4.7).

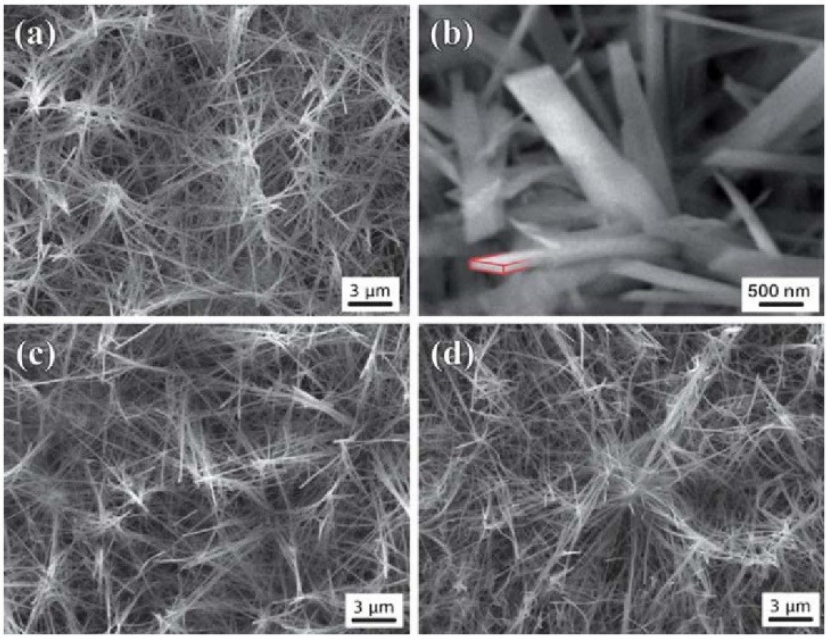

Figure 4.7 SEM images of (a and b) $ZnS(en)_{0.5}$ hybrid precursor, (c) sample calcinated at 400 °C for 50 h and (d) sample calcinated at 400 °C for 50 h + 600 °C for 2h. In (b) the contour of a nanobelt is highlighted in red.

4.1.1 TEM analysis

TEM analysis on the calcined samples was perfomed in order to investigate the changes in the nanoscale morphology of the structures resulting from the different thermal treatments. In figure 4.8a the HAADF image of a nanobelt coming from a sample annealed at 400 °C in nitrogen flux is shown. After the annealing in this atmosphere, the hybrid nanobelts are converted in wurtzite ZnS nanobelts characterized by a sponge-like morphology, with a large quantity of nanoscopic pores diffused in the whole structures. The comparison with the figure 4.8b, that is the HAADF image of a sample heat-treated at 400 °C in air, highlights the radical effect that the annealing atmosphere has a on the resulting belts morphology. In consequence of this annealing, indeed, the nanobelts show a very inhomogeneous structure, with the appearance of a chain of nanometer sized grains around the edges and some similar isolated grains on the flat surfaces. Several holes separate the external chain of grains from the core of the nanobelts, which maintain the same sponge-like morphology of the nanobelts annealed in nitrogen flux. This morphological evolution is in close correlation with those reported for the hybrid $ZnS(en)_{0.5}$ nanosheets[72].

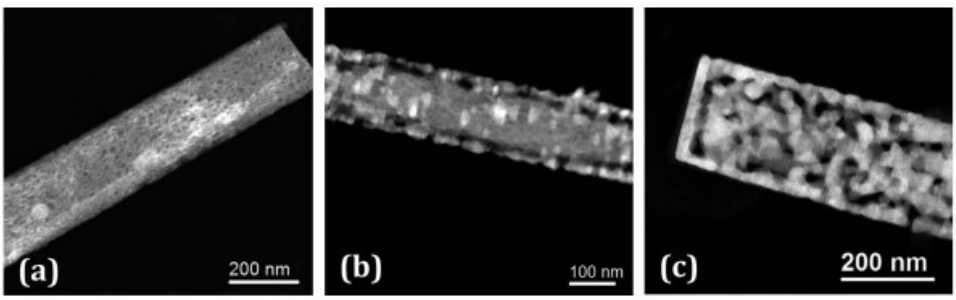

Figure 4.8 HAADF images of (a) sample calcinated at 400 °C for 50 h in N_2 flux, (c) sample calcinated at 400 °C for 50 h in air and (d) sample calcinated at 400 °C for 50 h + 600 °C for 2h in air.

The SAED pattern of this sample (figure 4.9) is composed by two sets of perfectly aligned diffraction spots, corresponding to the ZnS and ZnO wurtzite phases, consistently with the results found for the nanosheets[72]. The well-defined diffraction spots indicate that the nanobelts are single-crystals. In figure 4.10 a HRTEM micrograph of the sample and the corresponding FFT are reported. The FFT shows two sets of spots corresponding to ZnS and ZnO, respectively, thus confirming the coexistence of the two phases.

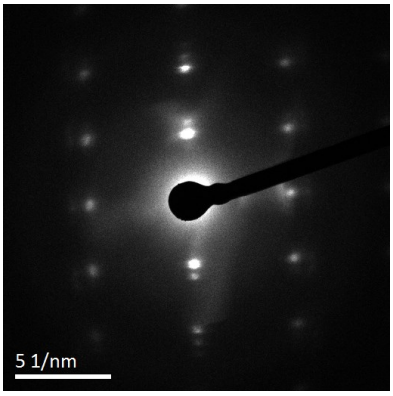

Figure 4.9 SAED pattern of a sample annealed in air at 400 °C.

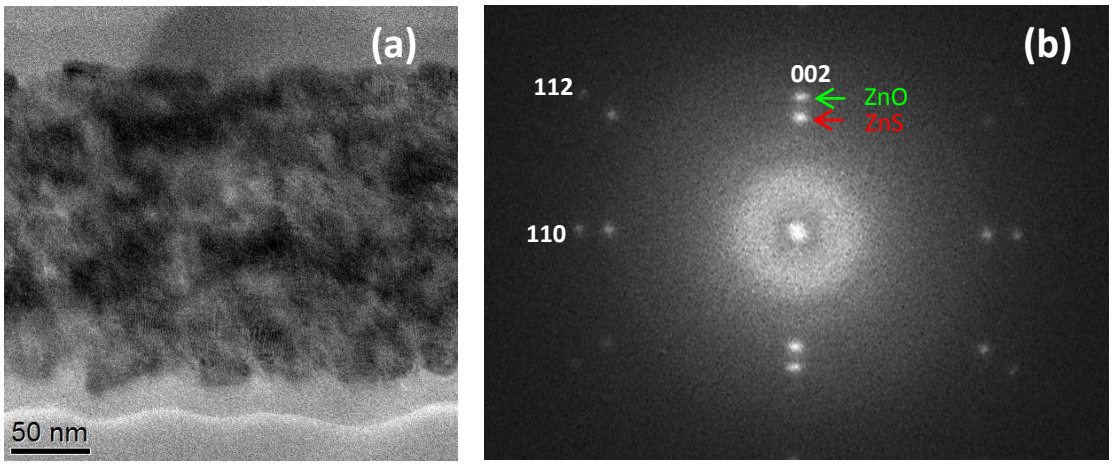

Figure 4.10 (a) HRTEM micrograph and (b) FFT of a sample annealed in air at 400 °C.

The spatial distribution of the elements in the nanobelts can be evaluated from the Energy-Filtered TEM (EFTEM) images reported in figure 4.11: the sulfur and oxygen distributions indicate that the grains correspond to the oxidized regions of the samples. This suggests that the oxidation of the material, in these experimental conditions, begins from the lateral zones of the structures.

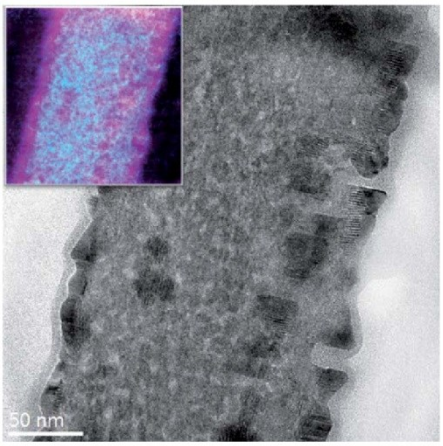

Figure 4.11 Zero loss energy filtered TEM image of sample annealed in air at 400 °C. Inset: oxygen (pink) and sulfur (light blue) composite element map.

Aiming to a deeper understanding of the evolution of structural properties of the nanobelts at the atomic scale, HREM and FFT analyses were performed (figure 4.12). From the HREM images, three different regions can be distinguished into a nanobelt: the inner core (region A), the external grains (region B) and the grains grown in the internal zone (region C). The FFT elaboration confirms the indications given by the EFTEM, since the regions A and B exhibit the structures of ZnS and ZnO, respectively. The calculated lattice spacings of the two phases indicates that the structure of the ZnO grains is completely relaxed[71]. In close analogy with what was observed for the nanosheets[72], misfit dislocations are present at the interface ZnS/ZnO. In the regions of the sample where ZnO grains grew on the ZnS flat facet (region C), the FFT shows the superposition of the two phases and the Moirè fringe pattern occurs in the TEM image due to the overlap of the two mismatched lattices.

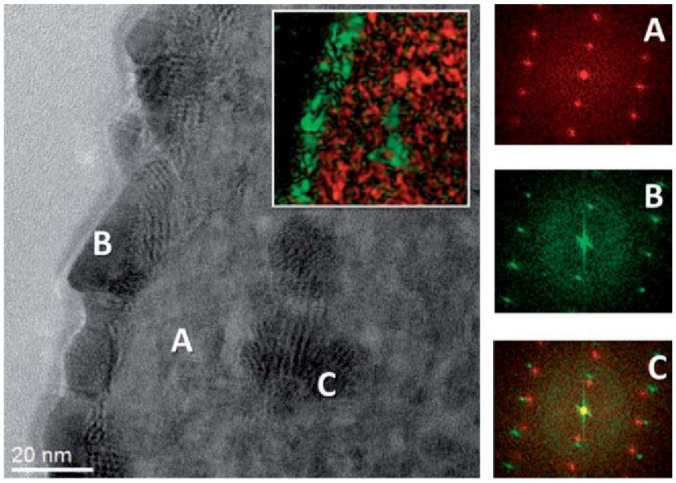

Figure 4.12 HREM image of sample annealed at 400 °C in air and FFTs of the (A) ZnS core, (B) ZnO grain at the nanoplates edge, and (C) ZnO grain superimposed to the ZnS crystal. The color map in the inset displays the inverse FFT generated by selecting the diffraction spots of ZnS (red) and ZnO (green).

The structural and morphological properties of the nanocrystals are completely changed when the sample is processed by a further annealing in air at 600 °C for 2 h. The figure 4.8c shows the HAADF image of a single nanobelt: the sponge-like morphology previously observed has completely disappeared and now the nanostructure is totally composed by grains and exhibit the same strongly

porous aspect reported for the ZnO nanosheets[3,5,72]. A closer insight in the structure of the sample can be reached by the HREM image and the corresponding SAED pattern reported in figure 4.13. Only the wurtzite ZnO phase can be detected, meaning that the original material has been completely oxidized and so that the total conversion of ZnS into ZnO has been achieved, in agreement with the indications deriving from the XRD pattern of the sample (figure 4.6). It is worth noting that mesoporous ZnO nanobelts are single crystals and the orientation of the original ZnS crystals has been maintained. This suggests that the oxidation process doesn't affect significantly the oriented connection among the ZnO grains and so the conversion $ZnS(en)_{0.5} \rightarrow ZnS \rightarrow ZnO$ can as a whole be considered as a topotactic transformation[71], consistently with what was reported for the same conversion of $ZnS(en)_{0.5}$ nanoplatelets[3,72]. During the processes of $ZnS(en)_{0.5}$ decomposition to ZnS and transformation of ZnS to ZnO, the positions of Zn atoms are minimally changed, since ZnS and ZnO show the same hexagonal wurtzite structure derived from the orthorhombic structure of the hybrid precursor. Thus, the definition of topotaxy (from the Greek τόπος, "place", and τάξις, "order") is satisfied. The observed pseudomorphism, i. e. the conservation of the shape of the nanobelts despite the relevant modifications on the nanoscale, is due to the limited displacement of the Zn atoms during the whole two-step transformation[3].

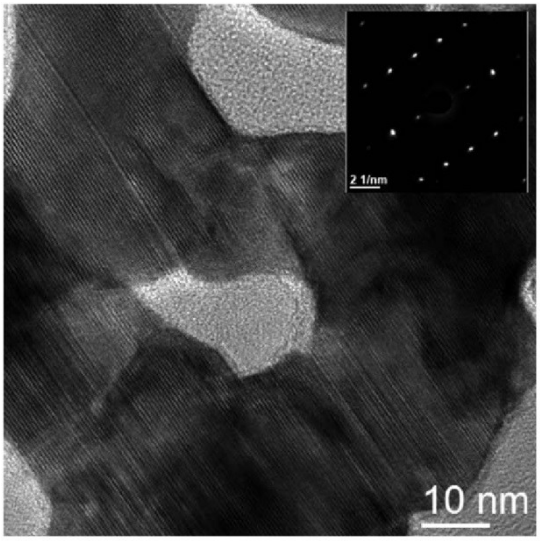

Figure 4.13 HREM image of the sample annealed at 600 °C. The SAED pattern in the inset demonstrates that the ZnO nanobelts are single crystals.

The considerations resulting from the SEM and TEM analyses indicate that the microscopical mechanisms involved in the $ZnS \rightarrow ZnO$ conversion of the nanobelt are analogous to those that occur during the same transformation in the nanosheets[72]. According to Lu et al[168], the oxidation of ZnS occurs with the exchange reaction between oxygen and sulfur:

$$2ZnS + 3O_2 \rightarrow 2ZnO + 2SO_2 \uparrow \quad (4.1)$$

This oxidation process is already active at 400 °C and so in the sample annealed at 400 °C in air the sponge-like ZnS core, resulting from the thermal decomposition of the organic part of the precursor, is surrounded by a chain of ZnO grains, that are perfectly oriented with respect to the original ZnS lattice. The partial conversion of ZnS into ZnO causes a significant lattice contraction, due to the large lattice mismatch between the two phases, and a strong tensile stress is generated inside the

material. This stress is released by the formation of the misfit dislocations observed at the ZnS/ZnO interface as well as by the creation of pores that separate the external ZnO grains from the ZnS core. In consequence of this, the amount of the surface of the material exposed to the air increases during the process and so the formation on new ZnO grains is fostered, and this results in the formation of the lateral chain-like region shown in figure 4.8b.

The further annealing at 600 °C for 2 h completes the oxidation process and leads to the entire conversion ZnS → ZnO. The strong tensile stress field consequent the lattice contraction is relaxed through the formation of the mesoporous structure in all the regions of the nanobelts. This transformation leaves substantially unchanged the geometrical aspect of the nanobelts and the morphology of the nanobelt entanglement, as clearly shown by the comparison among the figures 4.7a, 4.7b and 4.7c. The finally obtained ZnO mesoporous nanobelts are single crystals with the same wurtzite structure and orientation of the original ZnS.

4.1.2 Cathodoluminescence characterization

The optical emission properties of the nanobelts were investigated by means of room-temperature chatodoluminescence (CL) measurements, that were performed on the sample annealed at 400 °C in nitrogen flux, the sample annealed at 400 °C in air and the sample further annealed at 600 °C in air.

The spectra, that are reported in figure 4.14, are dominated by a broad band falling in the energy range 1.7-3 eV for all the three different samples. The different emission bands that contribute to the spectra were individuated by Gaussian deconvolutions.

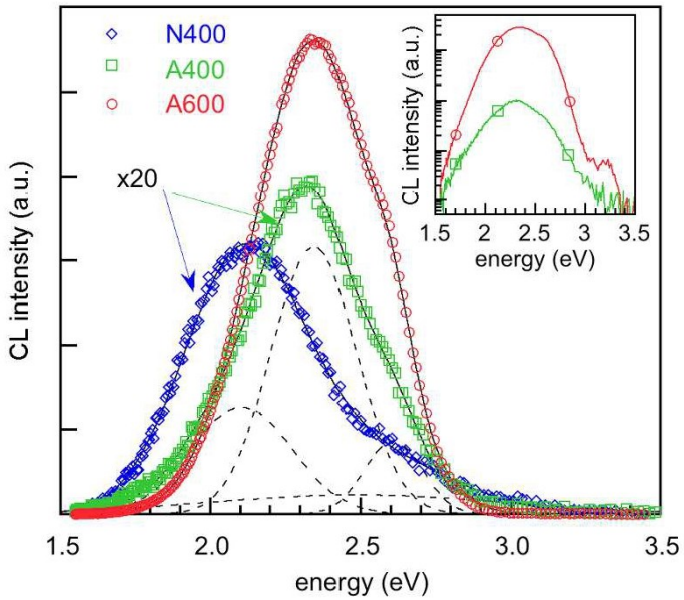

Figure 4.14 CL spectra of sample annealed in nitrogen at 400 °C (◊), in air at 400 °C (□) and in air at 600 °C (○). Full lines are the best fittings achieved by Gaussian deconvolutions, while dotted lines show the four components obtained from the fitting for sample annealed in air at 400 °C. The inset shows the semilog CL spectra of samples annealed in air at 400 °C (□) and at 600 °C (○).

The spectrum of the sample annealed at 600 °C in air consist of two emission bands located respectively at 2.54 eV (488 nm) and 2.36 eV (525 nm). The first band correspond to the green light emission usually observed in the ZnO nanostructures and ascribed to recombinations at deep levels,

presumably caused by oxygen defects[169–171]. The origin of the band at 2.36 eV is not completely clear. Besides these two emissions, a weak UV band can be observed around 3.2 eV (inset in fig. 2.17), which is likely due to the near-band edge emission of the ZnO[172]. The lower intensity of the UV emission compared with the other bands is most likely related to the competing presence of surface recombination processes that are dominant in such a porous material, characterized by a huge surface-to-volume ratio.

The spectrum of the sample annealed at 400 °C in nitrogen, constituted by ZnS nanobelts, consists of two components at 2.10 eV (590 nm) and 2.49 eV (498 nm), respectively. Similar emission bands are often observed in ZnS nanostructures and generally ascribed to defect-related recombinations[173–175].

As for the sample annealed at 400 °C in air, an excellent fitting of the CL spectrum is achieved by using the four emission energies found for ZnO and ZnS, in agreement with XRD, SEM and TEM investigations that show the coexistence of the wurtzite ZnS and ZnO phases in this sample.

As a final remark, it is worth noting that the radiative recombination efficiency of the mesoporous ZnO nanobelts is about 30 times larger than that of the other two samples (in fig. 4.14 the spectra of the samples annealed at 400 °C are multiplied by a factor 20 to be represented on the same scale of the spectrum of the ZnO nanobelts, for an easier comparison).

4.1.3 Patterning of the $ZnS(en)_{0.5}$ nanobelts distribution

In 2008 Zhang et al[4] proposed that the growth of hybrid nanobelts containing zinc calchogenides was controlled by a mechanism of metallic zinc oxidation by elemental calchogen (S or Se) followed by the reaction of zinc with calchogen and ethylenediamine to form the HOI compound. According to this model, the metallic Zn pads on the alumina substrate act both as physical support for the nanobelt entanglement and as zinc source during the growth process of the crystals. Nanobelts are expected to grow preferentially onto the zinc pads, since the zinc needed to the formation of the hybrid complex is not available in the unmetalized regions of the substrate. Thus, patterning the zinc metallization can be used as a tool to define the areas of the substrate where the anchored nanobelts will be obtained.

In order to check the real possibility to effectively pattern the nanobelt distribution, solvothermal synthesis was performed on alumina substrate metalized with a defined geometry, consisting in Zn pads separated by gaps (Δ) ranging from 50 µm to 1 mm (figure 4.15).

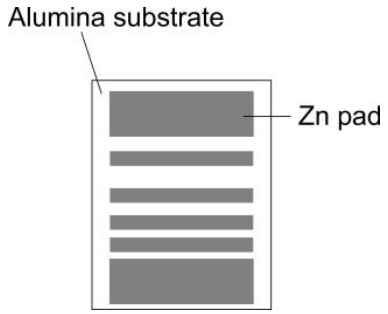

Figure 4.15 Schematization of the alumina substrate with the patterned Zn metallization

The SEM images of the obtained nanobelts confirm that the growth of the nanostructures actually occurs only in correspondence of the Zn pads, while no nanostructures formation can be observed upon the bare alumina in the gap regions (figure 4.16a). However, some nanobelt overgrowth can be observed on the alumina in regions as wide as about 100 µm close to the Zn pads. This behavior can be explained by the consideration that the formation of the hybrid materials is related to the oxidation of metallic Zn by S atoms, and the concentration of the S-oxidized Zn atoms is expected to decrease as the distance from the metallic pad is increased, thus inhibiting the nanobelt growth when the distance becomes higher that a certain threshold.

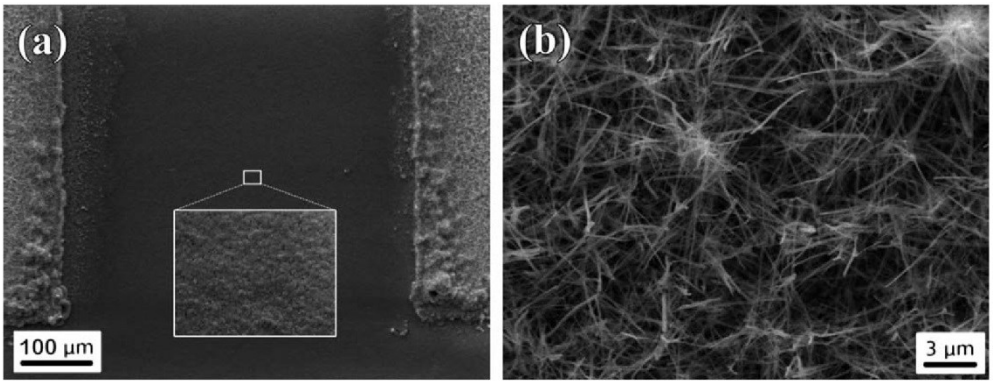

Figure 4.16 SEM image of (a) the patterned nanobelts growth for a gap *Δ* of 500 µm with the overgrowth close to the pads, and (b) the porous ZnO nanobelts distribution obtained after the annealing at 600 °C in the 100 µm region between two adjacent pads. The inset of (a) shows the bare alumina between the pads where no growth is observed.

The overgrowth of the nanobelts outside the metalized regions represent a limitation to the resolution of the growth patterning. On the other hand, this allows having two adjacent pads electrically interconnected by a ZnO nanobelt entanglement, if the gap *Δ* between them is small enough. This is confirmed by the photocurrent measurements reported in figure 4.17, that were performed by contacting two adjacent Zn pads using Au probes. When the pad separation is 500 µm, the illumination of the sample doesn't produce any significant variation in the current level, while a significant photocurrent can be observed when the separation is 100 µm, with a slow response to VIS-UV light and a slow recovery.

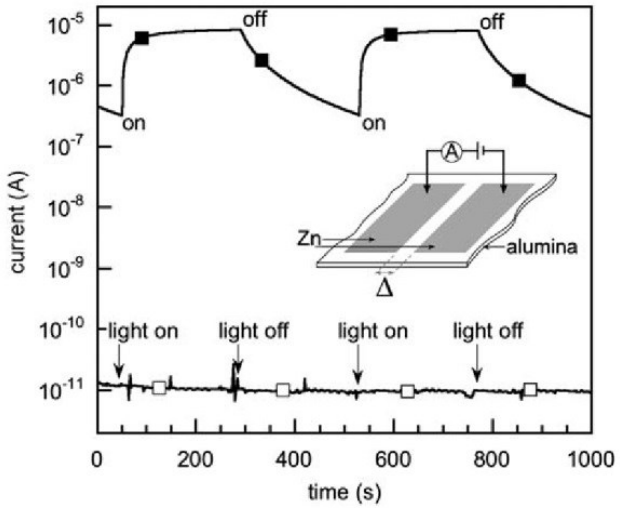

Figure 4.17 Photocurrent response to VIS-UV excitation for pads separated by a gap *Δ* = 100 µm (■) and by a gap *Δ* = 500 µm (□). The inset shows a schematic representation of the measurement setup.

The photoresponse of the nanobelts to VIS-UV excitation shows that the photocurrent presents a slow decay when the light is turned off. Such a behavior, that is often observed in ZnO, may be attributed to the capture of the photo-generated holes in deep trap levels, and subsequent hole emission and e^-/h recombination. In this case, the characteristic time constant of the current recovery is governed by the depth of these trap levels in the forbidden band, and can be very long, up to several thousands of seconds[176]. It is worth noting that the use of an UV filter doesn't affect the time constants and has the only effect to reduce the photocurrent. This confirms that the observed photoresponse does not originate only from photo-induced band-to-band transitions, that require illumination with wavelengths in the UV range or shorter, but is determined also by carrier trapping phenomena associated with defects into the bandgap.

4.1.4 Current-voltage measurements

In order to have an insight on the transport properties of the ZnO mesoporous nanobelts, current-voltage (I-V) measurements were performed on patterned samples. Referring to patterning schematized in figure 4.15, I-V curves were acquired by contacting Zn pads separated by a gap Δ = 100 µm and a gap Δ = 200 µm electrically connected by the overgrowth of nanobelts; the measurements were performed at various temperatures ranging from 100 °C to 250 °C.

Figure 4.18 shows the absolute I-V curves measured using two pads separated by a 100 µm gap. The nanobelts show an ohmic behavior in the whole range of voltages considered (-3V, 3V) and the current is dramatically increased when the temperature is raised above 100 °C, confirming the semiconductive properties of the material.

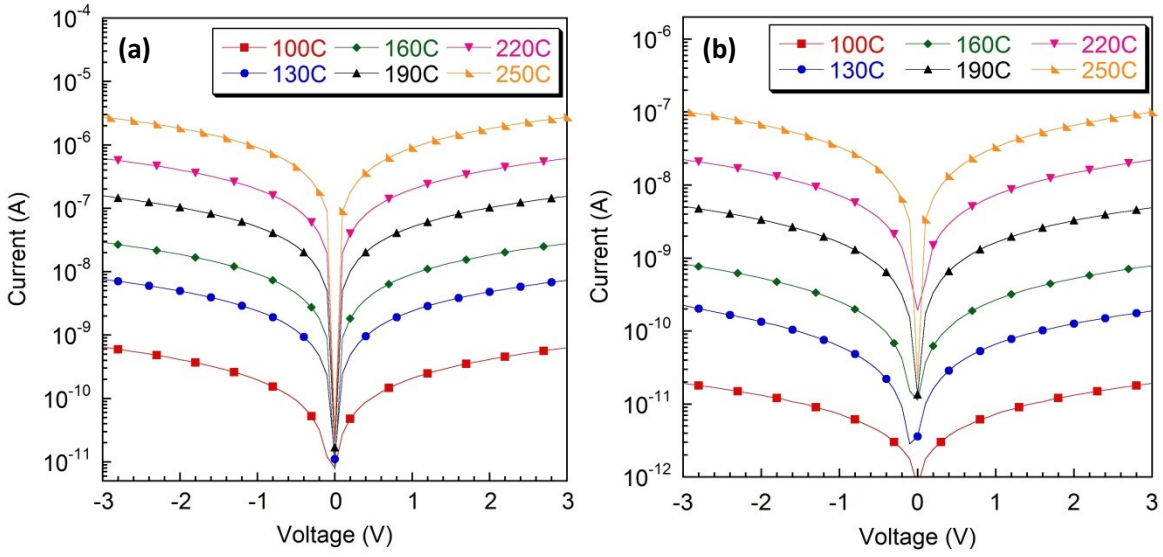

Figure 4.18 I-V curves for pads separated by a gap *Δ* = 100 µm (a) and *Δ* = 200 µm (b).

The conductances calculated from the I-V characteristics are reported in an Arrhenius plot (figure 4.19), both for *Δ* = 100 µm and *Δ* = 200 µm. It can be observed that the values are well described by the law

$$G(T) = G_0 \exp\left(-\frac{E_a}{k_B T}\right) \tag{4.2}$$

that indicates a thermal activated transport in these structures. The values for the activation energy E_a calculated for Δ = 100 µm and Δ = 200 µm are respectively 0.94 eV and 0.93 eV, in excellent agreement to each other.

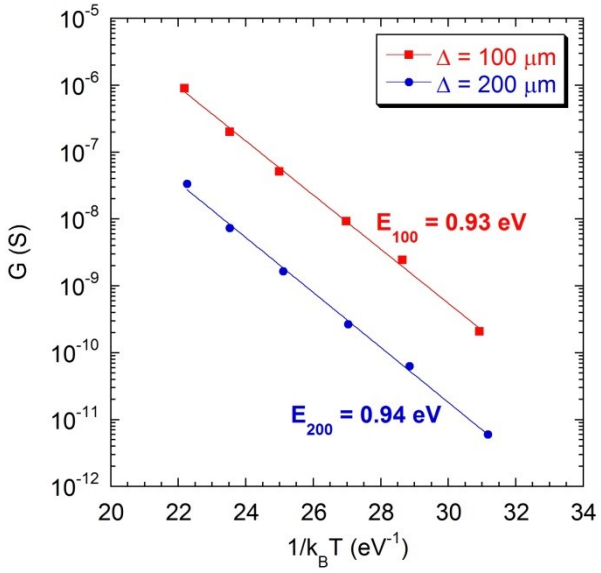

Figure 4.19 Arrhenius plot for pads separated by a gap Δ = 100 µm and Δ = 200 µm.

It is worth noting that the conductance does not scale proportionally with the gap dimension. Indeed, the conductance measured for Δ = 200 µm is more than one order of magnitude smaller than those measured for Δ = 100 µm. This is likely due to strong reduction of the overgrown nanobelts density when the distance from the Zn pad is increased (figure 4.20). Therefore, the thickness of the nanobelt entanglement in the central regions of the 200 µm gap is expected to be significantly smaller than those in the 100 µm gap.

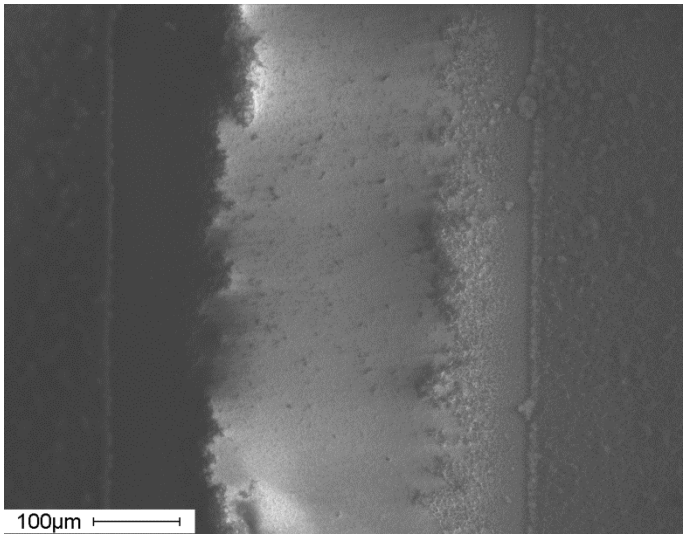

Figure 4.20 SEM image of the patterned nanobelts growth for a gap Δ of 200 µm with the overgrowth close to the pads, whose density is reduced when increasing the distance from the metalized regions.

The comparison between these electrical measurements and the cathodoluminescence characterization (section 4.1.2) points out that the sum of the found E_a values and 2.36 eV, that is the energy of the unassigned emission band observed in the CL spectrum, is approximately 3.3 eV, that is just the room-temperature value of the ZnO bandgap[59]. This suggests that the level responsible for the conduction is likely the same that gives rise to the emission centered at 2.36 eV.

EDX map of a single nanobelts (figure 4.21) shows the presence of a not-negligible sulfur amount in the structure. This result is compatible with the preparation process followed to obtain the nanobelts, that consider the formation of the porous ZnO nanocrystals by substituting the sulfur atoms in the original ZnS lattice with oxygen atoms, during the annealing in air at 600 °C. The presence of S atoms in the finally obtained ZnO nanobelts is likely due to an incomplete sulfur out diffusion during the annealing, and so can be considered as a residual sulfur doping on the ZnO nanobelts. By means of EDX analysis, the amount of residual S in the nanobelts structures was estimated to be 0.7%, corresponding to a S molar fraction $x_S = 0.007$.

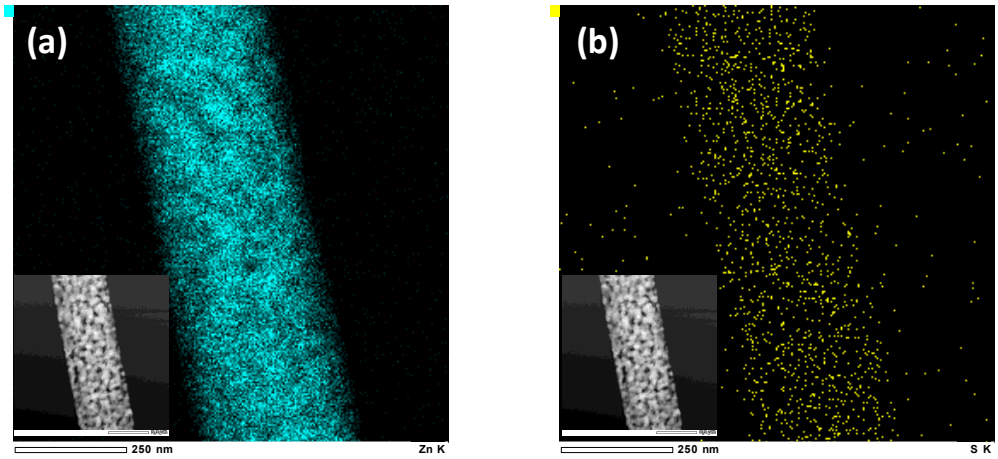

Figure 4.21 EDX maps of a single ZnO nanobelt: (a) zinc map (light blue), (b) sulfur map (yellow). Insets show the HAADF images used to derive the EDX maps.

The evaluation of the impact on the optical and electrical properties of such a S doping is not trivial. Preliminary DFT calculations have been performed, indicating that the sulfur inclusion in the ZnO structure should result in the formation of an energy level located 0.93 eV above the valence band[177]. The position of this theoretically calculated level is consistent both with the CL features and the activation energy of the nanobelts. The Arrhenius plots reported in figure 4.19 indicate that the conduction in this structures is determined by the level that gives rise to the activation energy E_a = 0.93 eV, therefore the position of the level found by DFT could suggest, that is 0.93 eV above the valence band, could suggest a *p*-type conduction in these nanostructures. However, the influence on the electrical properties of ZnO of sulfur doping is deeply debated in literature. Yoo et al reported that, in a S-doped ZnO film, the activation energy strongly depends on the S amount, finding E_a = 0.06 eV for x_S = 0.01 and E_a = 0.26 eV for x_S = 0.03 and a *n*-type conduction[178]. An excess of carriers in conduction band supplied by S impurities was observed also for S-doped ZnO nanowires by Shen et al[169], that reported also a light emission band located at 2.37 eV, consistently with the band observed at 2.36 eV for the nanobelts (see figure 4.14).

These results seem to rule out the hypothesis of a *p*-type conductivity in the nanobelts. Nevertheless, we cannot exclude that in the nanobelts the level responsible for the emission at 2.36 eV and the

conduction is related to sulfur. Currently, the preparation of gas sensors using nanobelts as active layer is ongoing, to check the polarity of the majority carriers. According to the sensing mechanism for ZnO nanostructures described in section 4.3.1, the response of the material to the exposure to a reducing gas, such as ethanol or carbon monoxide, is different depending on the sign of the majority carriers. Indeed, the electron transfer towards the conduction band resulting from gas molecules chemisorption on the surface results in an increased conductivity for a *n*-type material and in a reduced conductivity in a p-type material. Therefore, the investigation of the response to gas exposure of the nanobelts is expected to provide further information about the electrical properties and the influence on them of the observed sulfur doping.

It is worth noting that in the mesoporous ZnO nanosheets described in the following sections the EDX analysis pointed out the inclusion in the ZnO structure of sulfur atoms (figure 4.22), with a concentrations of about 1.3% (x_S = 0.01).

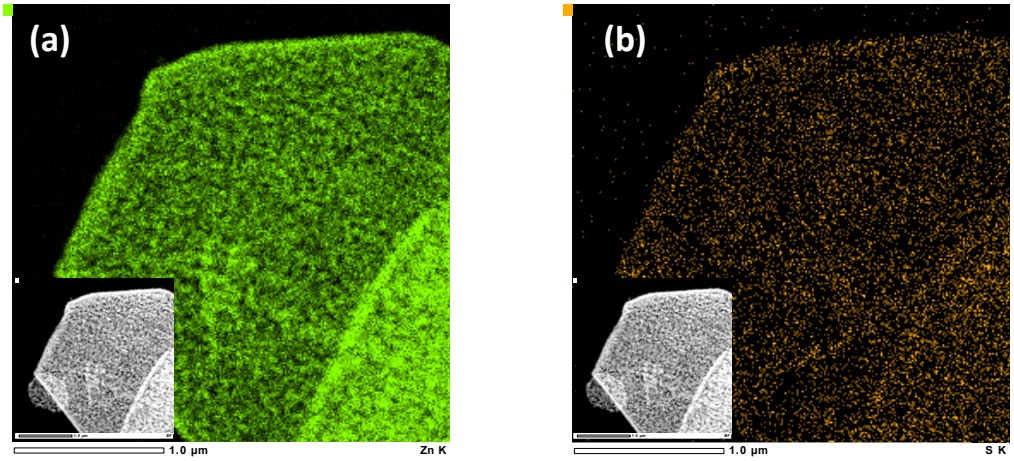

Figure 4.22 EDX maps of a single ZnO nanosheet: (a) zinc map (light green), (b) sulfur map (yellow). The insets show the HAADF images used to derive the EDX maps.

The calculated x_S suggest that the residual S amount in the nanosheets is higher than those observed in the nanobelts, that are characterized by x_S = 0.007. However, the difference between the calculated x_S for nanobelts and nanosheets cannot be considered as meaningless, since it is close to the sensitivity limit of the EDX technique. Therefore, from the EDX analysis it can be concluded that both in nanosheets and in nanobelts a small comparable S doping is present, resulting from the residual sulfur atoms that have not diffused outside the lattice during the final annealing step at 600 °C.

To better clarify the impact of the residual S doping on the electrical properties of the nanosheets, the behavior of the nanosheet conductance when the temperature is varied was investigated. To do that, impedance spectroscopy measurement were performed in air atmosphere for different temperatures ranging from 200 to 400 °C on gas sensors prepared with nanosheets as reported in section 2.5; the value of the real part of the impedance at low frequencies was assumed as the dc resistance of the nanosheets entanglement deposited between the two Au contacts.

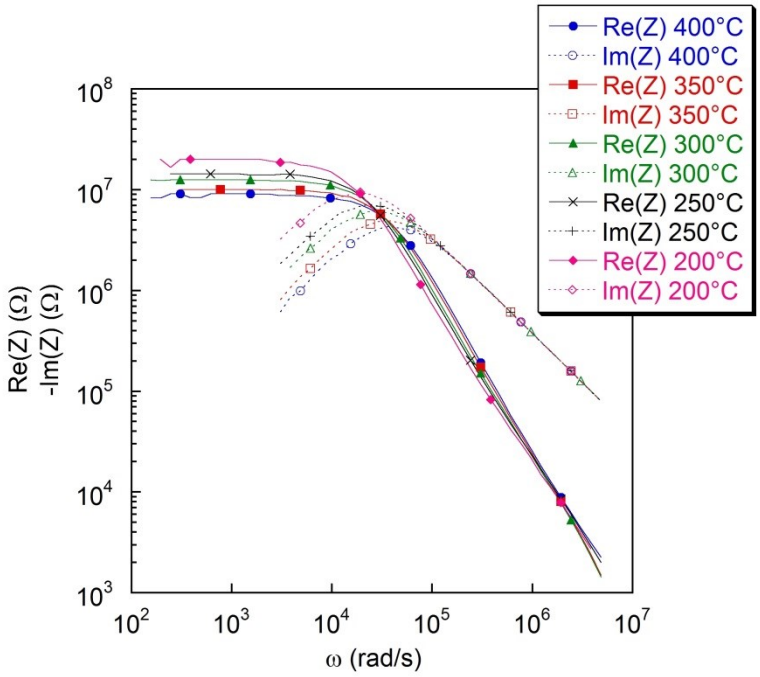

Figure 4.23 Impedance spectroscopy measurements on ZnO nanosheets for temperatures ranging from 200 °C to 400 °C.

The conductance values obtained from the impedance spectra shown in figure 4.23 showed that, similarly to the nanobelts, the transport in the nanosheets is thermally activated with an activation energy E_a = 0.11 eV, significantly lower than those found for nanobelts (E_a = 0.93 eV). This difference indicates that the charge transport mechanisms in the two nanostructures are different, and further investigation is required to understand the origin of the found E_a values. Currently, cathodoluminescence measurements are ongoing on nanosheet to investigate if the light emission spectrum presents one or more bands related with the level responsible for E_a = 0.11 eV. Since EDX maps indicate the presence of S doping in both the nanostructures, it is difficult to assert the idea that the observed E_a values result from S doping in both nanosheets and nanobelts. One possible hypothesis that can be considered is that the different behavior between nanosheet and nanobelt could be related to the presence of residual boron in nanobelts, since the solvothermal process to obtain hybrid $ZnS(en)_{0.5}$ elongated belts uses KBH_4 as a reagent, while KBH_4 is not required when synthesizing $ZnS(en)_{0.5}$ platelets (see section 2.4). Unfortunately, light elements like boron are very challenging to be detected with EDX analysis. In any case, further investigation is needed to understand both the transport mechanisms in nanosheet and nanobelt and the possible role of S in determining the electrical and optical properties of these materials.

4.1.5 Synthesis on $ZnS(en)_{0.5}$ nanobelts on transparent substrates

The application of the obtained mesoporous ZnO nanobelt for photovoltaic applications requires the possibility to synthetize them as supported on transparent substrates. Therefore, we performed solvothermal synthesis on glass substrates coated with a transparent unintentionally doped ZnO (UZO) film, grown by Pulsed Electron Deposition (PED). The thickness of the UZO layer was about 500 nm. SEM analysis of the obtained samples (figure 4.24a) pointed out that the solvolthermal process resulted in nanobelts having a morphology comparable to those obtained on Zn foils or Zn metalized

alumina substrates. However, we observed that the nanobelt entanglement had a poor adhesion to the substrate and it was not possible to obtain a good coverage on a large area (figure 4.24b). This is likely due to the whole consumption of the UZO layer during the nanocrystals growth, since UZO acts both as Zn source and physical support.

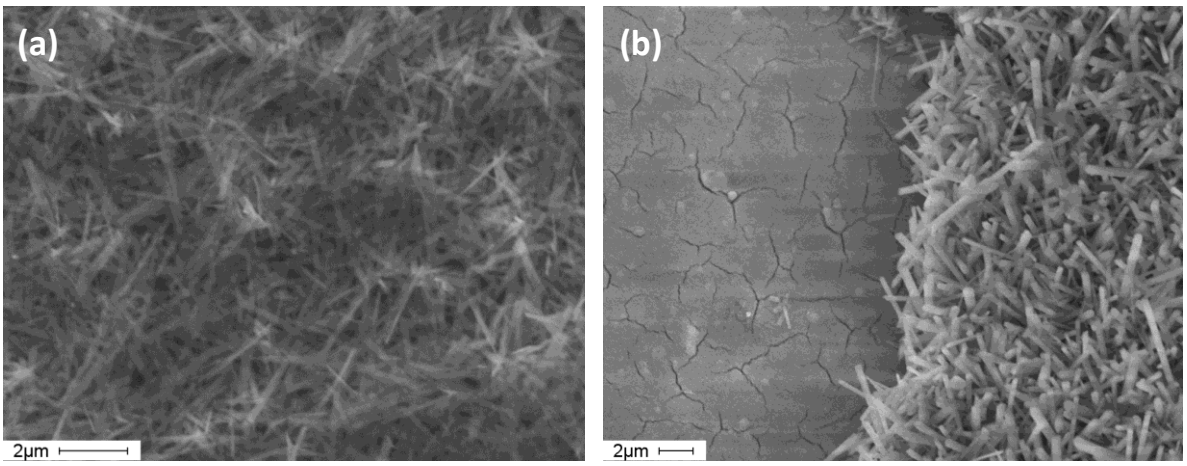

Figure 4.23 (a) $ZnS(en)_{0.5}$ nanobelts grown on UZO transparent substrate and (b) poor adhesion of the obtained nanobelt entanglement.

Currently, activity is ongoing in order to achieve a thicker layer of transparent ZnO to use as the support for the nanobelt synthesis.

4.2 Mesoporous ZnO nanosheets

$ZnS(en)_{0.5}$ hybrid compound was synthesized also in form of nanosheets, that were obtained as powders by following the solvothermal route reported by Mosca et al[102] and described in section 2.4. The XRD pattern of the as-grown nanosheets (figure 4.24) confirms that the formation of the $ZnS(en)_{0.5}$ was achieved.

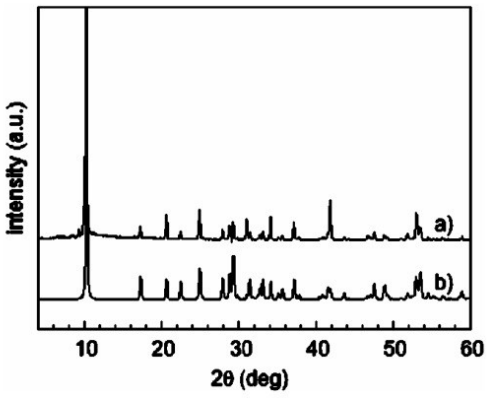

Figure 4.24 Typical XRD pattern of the $ZnS(en)_{0.5}$ nanosheets (a) compared with the pattern calculated by Ouyang et al[167] (b).

As reported in literature[3,5,72,102], the obtained powders consist of plate-like sheets with a lateral dimension of about 1-3 µm and a thickness in the range 100-250 nm (figure 4.25).

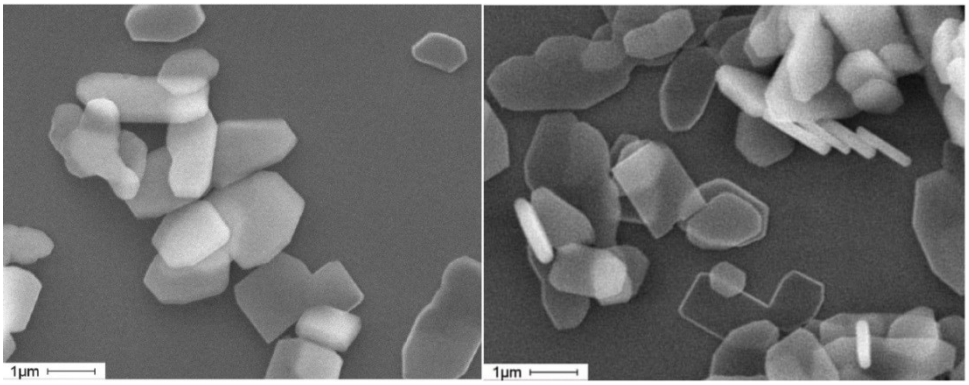

Figure 4.25 Typical SEM images of the as-synthetized $ZnS(en)_{0.5}$ nanosheets.

Similarly to the nanobelts described in section 4.1, we converted the hybrid nanosheets in monocrystalline mesoporous ZnO nanosheets by performing the thermal treatments in air reported by Nasi et al[72], that is 50 h at 450 °C + 2 h at 600 °C. The typical XRD pattern of the annealed samples (figure 4.26) shows that the nanosheets were completely converted into hexagonal wurtzite ZnO.

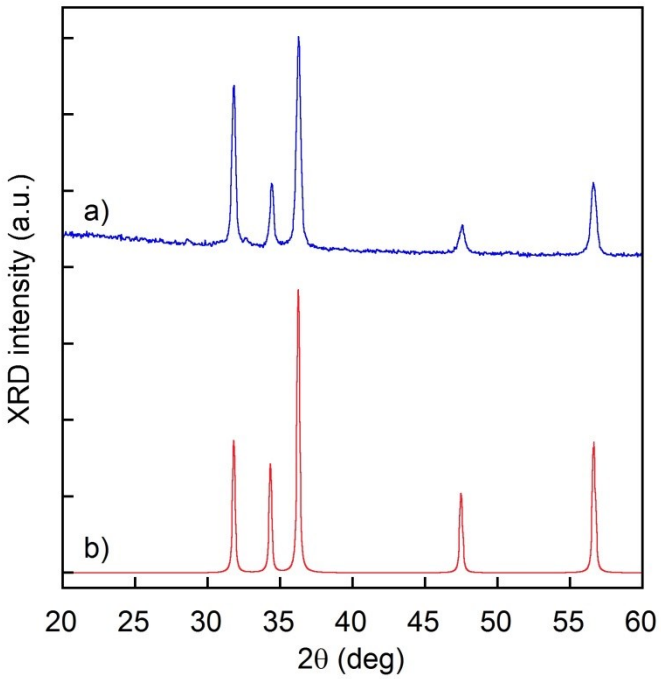

Figure 4.26 Typical XRD pattern of the calcinated samples (a) compared with those calculated for ZnO (b).

SEM analysis (figure 4.27) confirmed that the obtained ZnO nanosheets are characterized by an highly porous sponge-like morphology, as reported in refs. [3], [5] and [72]. It is worth noting that the nanosheet morphology on the nanoscale is comparable with those observed in the nanobelts obtained from the same hybrid precursor (figure 4.8c).

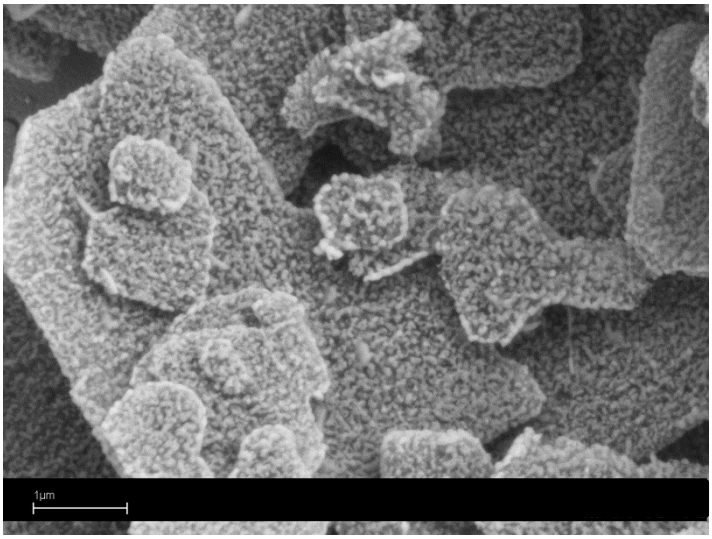

Figure 4.27 Typical SEM image of ZnO nanosheets obtained after the calcination of the hybrid precursor.

4.3 Gas sensor devices based on ZnO mesoporous nanosheets

Mesoporous ZnO nanosheets derived from $ZnS(en)_{0.5}$ precursor were proposed for gas sensing applications by Liu et al[5]. Owing to their porosity and monocrystallinity, these nanostructures are considered very promising for gas monitoring. However, the understanding of the mechanisms related to gas absorption in a key point to achieve high-performance devices. In order to investigate the conduction in these systems and the influence on charge transport of temperature and atmosphere, we prepared gas sensors using as active layer the porous ZnO nanosheets described in section 4.2. The preparation procedure to fabricate the devices is reported in section 2.5.

4.3.1 Nanosheets response to ethanol

The effectiveness of the response of a gas sensing device to a particular gas species is quantified by a parameter *S* called sensitivity, that is defined as

$$S = \frac{G_{gas} - G_0}{G_0} \tag{4.4}$$

where G_{gas} is the active device conductance in presence of the monitored gas and G_0 is the conductance when the gas measured is not present. We studied the response of a gas sensor based on nanosheets to ethanol, that is one of the most used gases to test the performances of this kind of devices. More specifically, we tested the device sensitivity to ethanol by measuring the DC conductance while fluxing dry air containing certified ethanol with concentrations ranging from 5 to 60 ppm (figure 4.28). The sensitivity was determined according to the relation 4.4. The measurement was carried out keeping the sensor at the operating temperature of 400 °C.

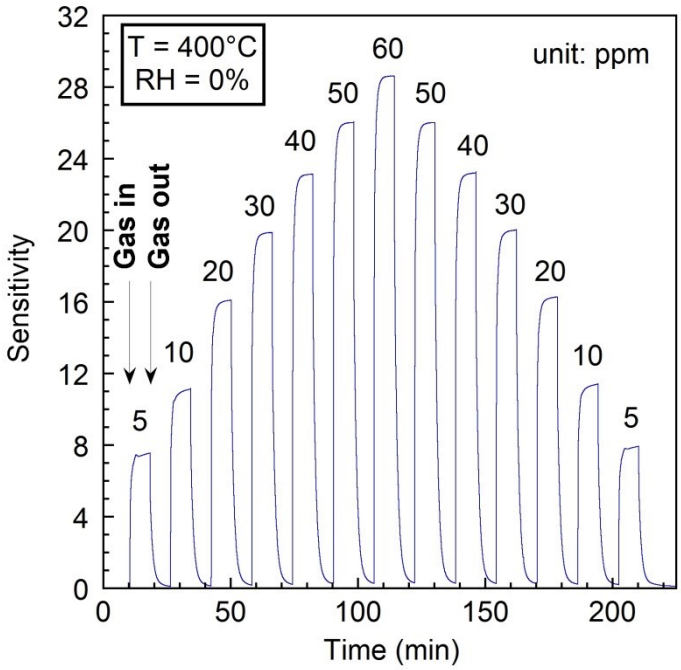

Figure 4.28 Dynamic response to ethanol of ZnO mesoporous nanosheets for *T* = 400 °C and RH = 0%.

Figure 4.28 shows that, as soon as ethanol is introduced in the test cell, the current flowing in the sensor is strongly increased, even for low gas concentrations. As the ethanol concentration is increased, the sensitivity of the sensor increases reaching the maximum value *S* = 28.6. This behavior is always observed for a wide variety of ZnO nanostructures[68,85,86,89,94,179] and it is described considering the interaction between the chemisorbed ethanol molecules and the surface of the nanocrystals. It is well known that oxygen species absorption plays an important role in electrical transport properties of ZnO nanostructures. Depending on the temperature, reactive oxygen species are chemisorbed at the nanocrystals surface; at low temperature, this phenomenon concerns principally O_2^-, while at high temperature O^{2-} and O^- are chemisorbed and O_2^- rapidly disappears[180]. The whole oxygen adsorption process is generally described by the following formulae[89,180]:

$$O_2(\text{gas}) \leftrightarrow O_2(\text{ads}) \tag{4.5}$$

$$O_2(\text{ads}) + e^- \leftrightarrow O_2^-(\text{ads}) \tag{4.6}$$

$$O_2^-(\text{ads}) + e^- \leftrightarrow 2O^-(\text{ads}) \tag{4.7}$$

When the nanostructures are surrounded by air, oxygen molecules are adsorbed on the surface to generate chemisorbed oxygen species (O_2^-, O^{2-}, O^-) by capturing electrons from the conductance band and therefore reducing the conductivity of the material. When the material is exposed to a reducing gas, such as ethanol, at high temperature the chemisorption of ethanol molecules on the surface takes place. By reacting with the ionic oxygen species on the surface, the ethanol reduces their concentration and the corresponding captured electron are released, according to the reaction[180]

$$CH_3CH_2OH(\text{ads}) + 6O^-(\text{ads}) \leftrightarrow 2CO_2 + 3H_2O + 6e^- \tag{4.8}$$

As a result, the conductivity of the nanostructures is increased. This is, basically, the reducing gases sensing mechanism for metal oxides nanostructures. The behavior observed for the mesoporous nanosheets is in qualitative agreement with this model.

It is worth noting that the sensor shows a negligible hysteresis, since the sensitivities corresponding to the various [eth] have approximatively same value whether they are measured while increasing or decreasing the concentration (figure 4.29). The maximum hysteresis of 4.8% is observed for [eth] = 5 ppm. This is a remarkable feature, as a reproducible response is a strict requirement to consider a gas sensing device as reliable.

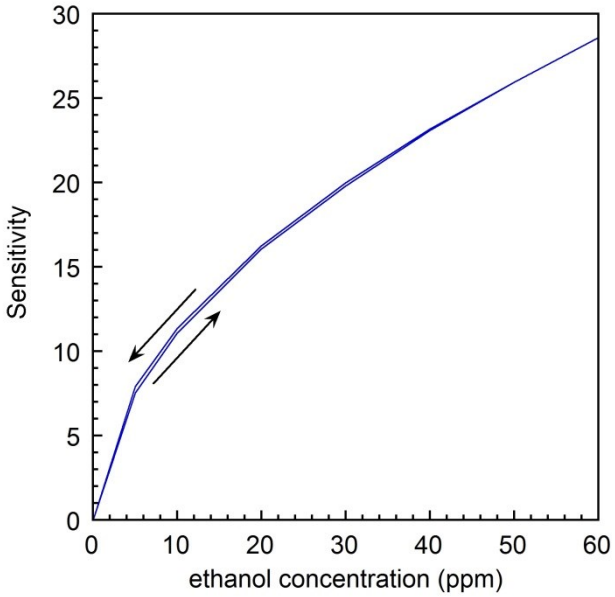

Figure 4.29 Response hysteresis of ZnO mesoporous nanosheets for *T* = 400 °C and RH = 0%. The up and down arrows correspond to sensitivity values measured while increasing and decreasing [eth], respectively.

As a comparison, different gas sensors were prepared following the same procedure described in section 2.5 but using as active layer ZnO nanotetrapods grown from vapor phase, as reported in[68], instead of nanosheets. This nanotetrapods (figure 4.30) are well known in literature to be an excellent candidate material for gas sensing purposes[68,181,182].

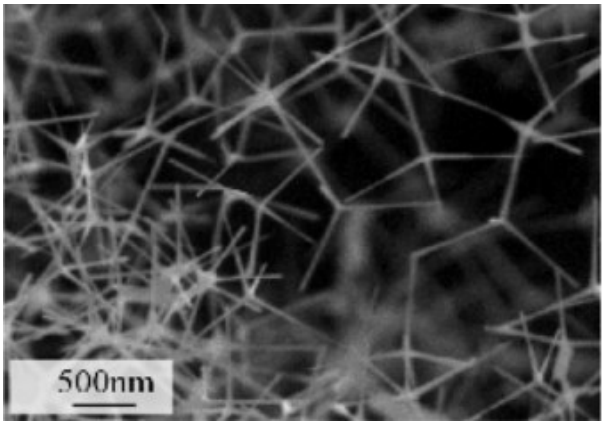

Figure 4.30 SEM image of ZnO nanotetrapods grown from vapor phase according to the procedure reported in[68].

In figure 4.31 the sensitivity of the gas sensors prepared with the two different nanostructures are shown. According to Hongsith et al[183] the sensitivity of the sensor is related to the ethanol concentration by a power-law dependence, that can be expressed by the simple empirical relation

$$S = 1 + a \cdot [\text{eht}]^b \tag{4.9}$$

where *a* and *b* are two parameters. The *S* values found for both devices are in good agreement with the behavior predicted by equation 4.9; the best fitting gives for the exponent *b* the values of 0.56 for nanosheets and 0.51 for nanotetrapods, indicating that the dependence of the response on the ethanol concentration is comparable for the two different nanostructures. Since no optimization processes were carried out on the sensors, the slight difference between the *S* values measured for the nanosheets-based and the tetrapod-based sensors is meaningless. The tailoring of the device properties, such as geometry of the contact or thickness of the active layer, is expected to result in improved sensitivities for both nanostructures[184].

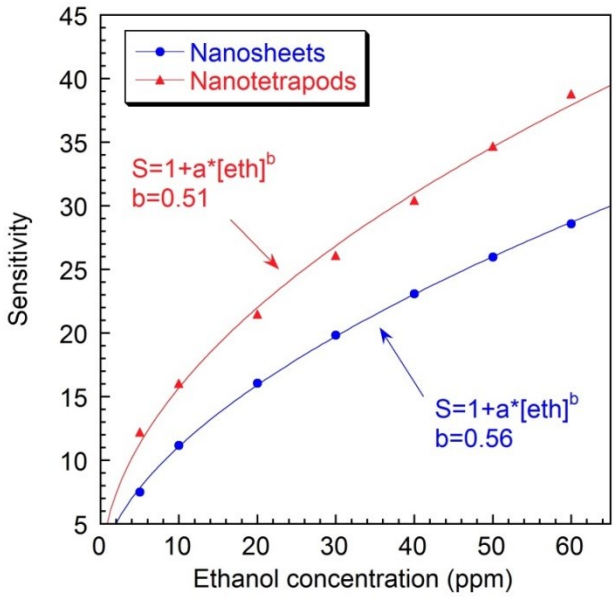

Figure 4.31 Sensitivity values obtained for nanosheets-based and nanotetrapod-based gas sensors for different ethanol concentrations. Red and blue lines correspond to the power-law fitting obtained for nanotetrapods and nanosheets, respectively.

4.3.2 Impedance spectroscopy measurements on gas sensors

Impedance spectroscopy measurements were performed on both nanosheets-based and nanotetrapods-based sensors at different temperatures and in different atmospheres. As an example, in figure 4.32 the typical impedance spectrum for nanosheets at a temperature of 400 °C and an ethanol concentration of 40 ppm is shown.

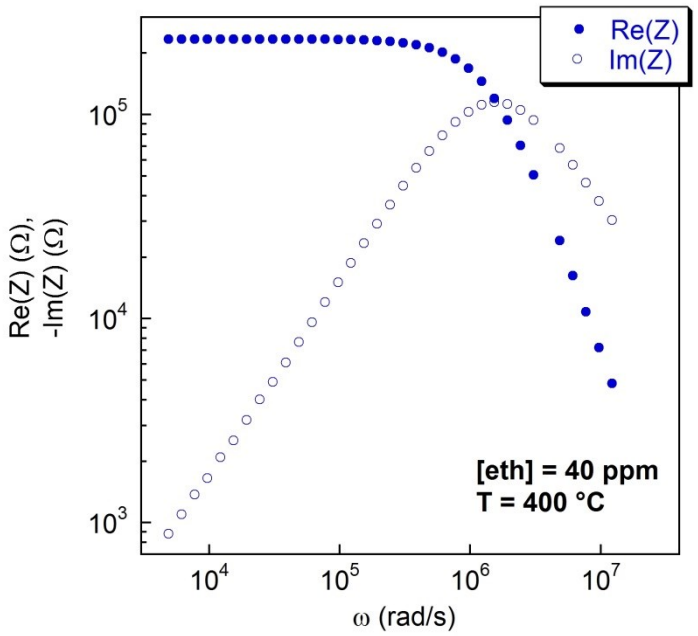

Figure 4.32 Typical impedance spectrum for the nanosheets-based sensor for *T* = 400 °C and [eth] = 40 ppm.

As discussed in section 2.6.5, the impedance spectra were analyzed by finding an empirical equivalent circuit that could provide a good fitting of the both real and imaginary components of the impedance. In this case, the spectrum reported in figure 4.32 is excellently described by an equivalent circuit composed by a resistance, a capacitance and a constant phase element (see paragraph) wired in parallel configuration (figure 4.33).

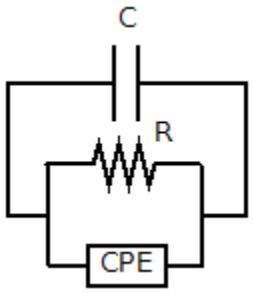

Figure 4.33 Equivalent circuit.

In figure 4.34 the experimental data together with the fitting provided by this equivalent circuit are shown. The estimated parameters of the equivalent circuit are reported in table 4.1.

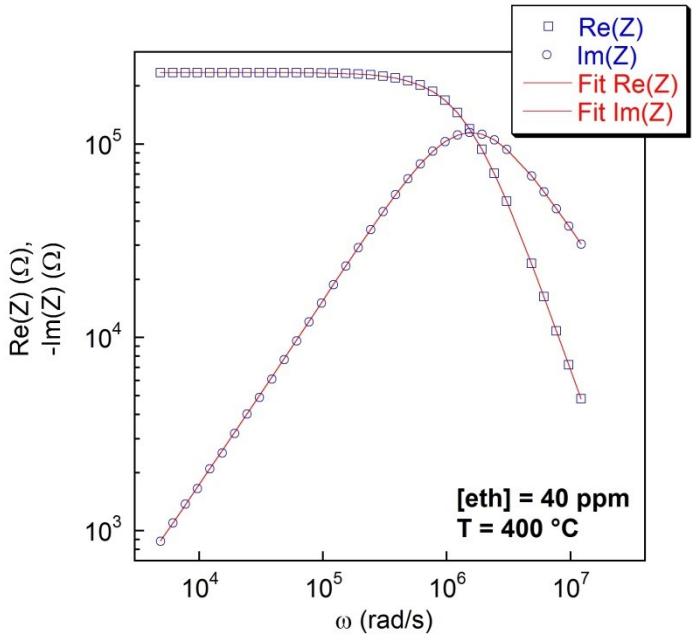

Figure 4.34 Typical impedance spectrum for the nanosheets-based sensor for *T* = 400 °C and [eth] = 40 ppm. Red lines correspond to the best data fitting obtained by the equivalent circuit reported in figure 4.33.

R (kΩ)	234.8
C (pF)	2.34
n	0.81
A (μS · s^n)	$5.29 \cdot 10^{-6}$

Table 4.1 Equivalent circuit parameters obtained from the fitting of the impedance measurement for *T* = 400 °C and [eth] = 40 ppm.

Figure 4.35 shows impedance spectroscopy measurements performed on nanosheets at a fixed ethanol concentration ([eth] = 30 ppm) and different temperatures ranging from 200 to 400 °C. This is the typical temperature range of interest for nanostructured gas sensing devices, as for temperature lower than 200 °C the chemisorption processes are expected to require extremely long times to take place.

The qualitatively features of the impedance spectrum are the same for all the temperatures. When *T* is increased, the real part of *Z* at low frequency shows a strong decrease, indicating that the active layer conductivity has increased. A similar behavior is observed for the imaginary part of *Z*, that is reduced by increasing the sensor temperature. The equivalent circuit represented in figure 4.33 provides an excellent description for all the impedance spectra corresponding to the different ethanol concentrations. The calculated circuital parameters are summarized in table 4.2.

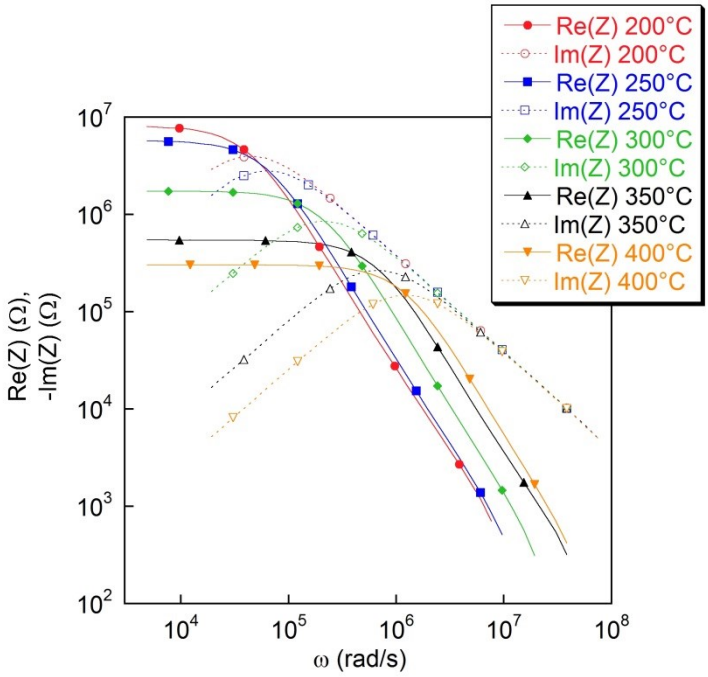

Figure 4.35 Impedance spectra for the nanosheets-based sensor for different temperatures ranging from 200 to 400 °C and fixed [eth] = 30 ppm.

T (°C)	*R* (MΩ)	*C* (pF)	*n*	*A* (μS · s^n)
200	8.081	2.38	0.83	$1.94 \cdot 10^{-6}$
250	5.738	2.45	0.79	$2.41 \cdot 10^{-6}$
300	1.741	2.43	0.84	$2.03 \cdot 10^{-6}$
350	0.547	2.32	0.80	$5.15 \cdot 10^{-6}$
400	0.303	2.50	0.87	$1.81 \cdot 10^{-6}$

Table 4.2 Equivalent circuit parameters obtained from the fitting of the impedance measurements on nanosheets-based sensor for *T* ranging from 200 to 400 C° and [eth] = 30 ppm.

It is worth noting that the values obtained for the capacitance *C* are not significantly affected by temperature variations. A comparable value of *C* was found when performing an impedance spectroscopy measurement on the bare substrate with no nanosheets deposited between the contacts. Therefore, it is possible to assign a physical interpretation to this element of the equivalent circuit, specifically the stray capacitance due to the wiring, the interconnections and the Au contacts on the alumina substrates.

The contribution to the total impedance of the device corresponding to the resistance *R* and the constant phase element at different temperature is represented in figure 4.36. *Z* of the resistance is barely the calculated R value, while for the CPE the modulus of *Z* is calculated as (see equation 2.2)

$$|Z_{\mathrm{CPE}}| = \frac{1}{A\omega^n} \tag{4.10}$$

where A and n have been obtained from the fitting and the value $\omega = 6.28 \cdot 10^5$ rad/s, corresponding to a frequency v = 100 kHz has been taken as reference.

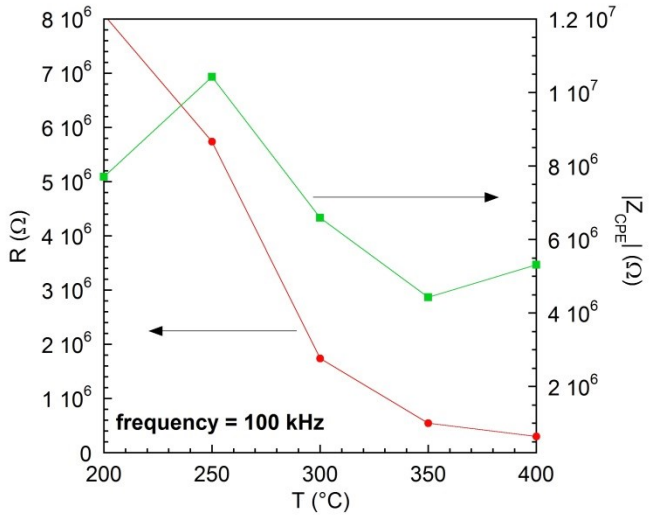

Figure 4.36 Calculated R and $|Z_{CPE}|$ values for different temperatures for the nanosheets-based sensor.

The effect of the variation of the temperature applies on R, that shows a strong decrease when T is increased. It is not possible to identify a trend for the calculated $|Z_{CPE}|$ values. Indeed, values corresponding to different T are scattered, ranging from approximatively $4.4 \cdot 10^6$ to $1.1 \cdot 10^7$ Ω. A similar undefined behavior of $|Z_{CPE}|$ was observed when considering the impedance of the sensor for different ethanol concentrations, as well as the impedance of the nanotetrapods-based sensor for different T and [eth]. It is worth noting that in the fitting procedure leading to the values of table 4.2 all the circuit parameters, that is R, C, n and A are considered as quantities to be refined by the iterative calculation. In particular, the value of the capacitance C is left free to be refined, although it is possible to identify this component with the fixed stray capacitance. This can result in meaningless variations of the obtained C values that affect also the obtained values for n and A, since the capacitance and the constant phase element appear in parallel configuration in the equivalent circuit shown in figure 4.33. Vice versa, if the stray capacitance value is fixed at the average of the C values calculated for different temperatures (table 4.2), that is C = 2.42 pF, mostly monotonic trends for $|Z_{CPE}|$ are obtained. Therefore, considering that the substrate and the wiring configuration is the same for all the considered devices, we decided to fix the C value at 2.42 pF for all the impedance spectra acquired. Under this assumption, the recalculated parameters for the spectra reported in figure 4.35 are:

T (°C)	R (MΩ)	C (pF)	n	A (μS · s^n)
200	8.089	2.42	0.85	$2.00 \cdot 10^{-6}$
250	5.699	2.42	0.92	$0.78 \cdot 10^{-6}$
300	1.726	2.42	0.91	$1.02 \cdot 10^{-6}$
350	0.545	2.42	0.88	$1.97 \cdot 10^{-6}$
400	0.303	2.42	0.90	$1.47 \cdot 10^{-6}$

Table 4.3 Equivalent circuit parameters obtained from the fitting of the impedance measurements on nanosheets-based sensor for T ranging from 200 to 400 C° and [eth] = 30 ppm assuming C = 2.42 pF.

The assumption of a fixed stray capacitance C = 2.42 pF leads to a better defined behavior of $|Z_{CPE}|$ that, similarly to the resistance, is decreased when the temperature is increased (figure 4.37). It is worth noting that the found values for n ranges from 0.85 to 0.92 (table 4.3), indicating that the CPE has a strongly capacitive nature and can be presumptively considered as a non-ideal capacitor[104].

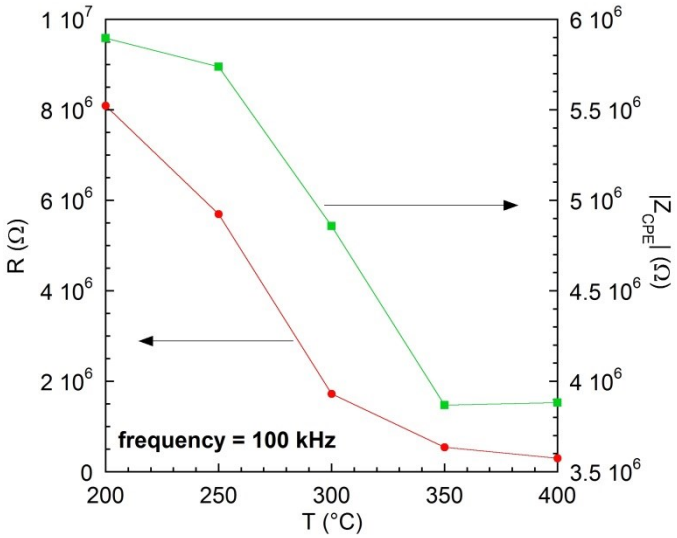

Figure 4.37 Calculated R and $|Z_{CPE}|$ values for different temperatures for the nanosheets-based sensor assuming C = 2.42 pF.

Figure 4.38 shows impedance spectroscopy measurements performed on nanosheets for a fixed temperature (T = 400 °C) and different ethanol concentrations ranging from 0 to 60 ppm.

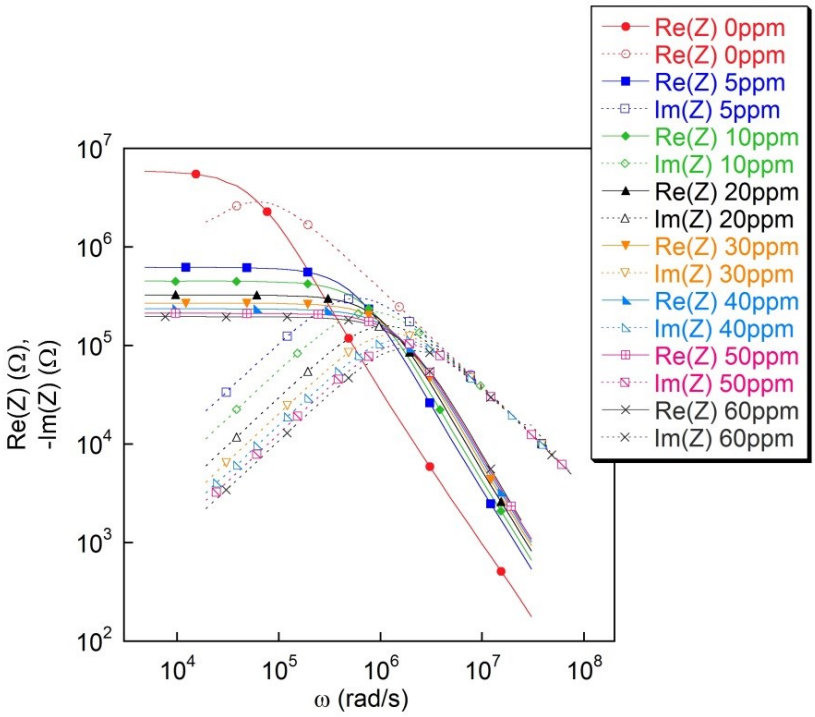

Figure 4.38 Impedance spectra for the nanosheets-based sensor for different ethanol concentrations ranging from 0 to 60 ppm. The sensor was kept at the constant T = 400 °C.

As expected, when [eth] is varied from 0 to 5 ppm, that is when the sensor is initially exposed to ethanol, the real part of *Z* at low frequency shows a strong decrease, indicating that the active layer conductivity has significantly increased. By further enhancing [eth], Re (*Z*) at low ω is more slightly decreased. A similar behavior is observed for the imaginary part of *Z*, that is strongly decreased when the sensor is exposed to ethanol and further reduced by increasing the gas concentration.

The equivalent circuit represented in figure 4.33 provides an excellent description for all the impedance spectra corresponding to the different ethanol concentrations. The obtained values for *R* and $|Z_{CPE}|$ are reported in figure 4.39, under the assumption of fixed *C* = 2.42 pF.

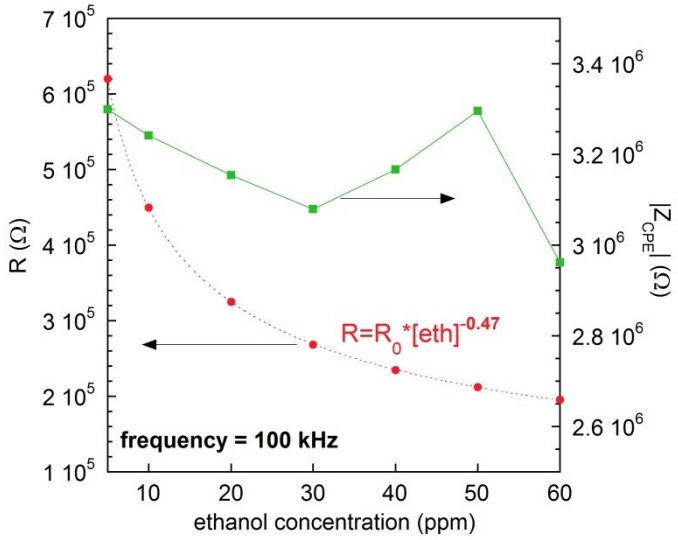

Figure 4.39 Calculated *R* and $|Z_{CPE}|$ values for different ethanol concentrations for the nanosheets-based sensor assuming *C* = 2.42 pF. The red dashed line corresponds to the power-

As the ethanol concentration is increased, *R* shows a reduction that is well described by the power law

$$R = R_0 \cdot [\text{eht}]^{-b} \tag{4.11}$$

where the calculated exponent is *b* = 0.47. It is worth noting that this value is different from those derived from the sensitivity values reported in figure 4.31 (*b* = 0.56). This difference is likely related to the different procedures followed to carry out the two different measurements. While performing impedance spectroscopy measurements, we waited approximatively one hour after setting each [eth] value to allow the sample to reach a complete stability in the new atmosphere. Vice versa, the sensitivity values reported in figure 4.31 are derived from a dynamic response measurement, where the sample is exposed to each ethanol concentrations only for few minutes. Therefore, it is possible that the *S* values reported in figure 4.31 are slightly affected by the inability of the nanosheets layer to reach a stable conductivity value in a short time.

The dependence of $|Z_{CPE}|$ on ethanol concentration is not well defined, anyway it is worth noting that the overall variation in the whole [eth] range is approximatively 10%. Indeed, the maximum $|Z_{CPE}|$ value ($3.30 \cdot 10^6\,\Omega$) is observed for [eth] = 5 ppm and [eth] = 50 ppm, while the minimum value ($2.96 \cdot 10^6\,\Omega$) is observed for [eth] = 60 ppm.

An analogous impedance spectroscopy characterization was performed on nanotetrapods-based gas sensors, aiming to point out the similarities and the differences between the two different systems. In figure 4.40 the impedance spectra achieved at different temperatures (fixed [eth] = 30 ppm) are reported. The effect of the modification of the temperature on the conduction in the nanotetrapods active layer is qualitatively similar to those observed for nanosheets. Remarkably, all the impedance spectra reported in figure 4.40 are excellently fitted by the same equivalent circuit used to describe the impedance of the nanosheets (figure 4.33). The obtained values for R and $|Z_{CPE}|$, under the assumption of fixed C = 2.42 pF, are reported in table 4.4 and in figure 4.41.

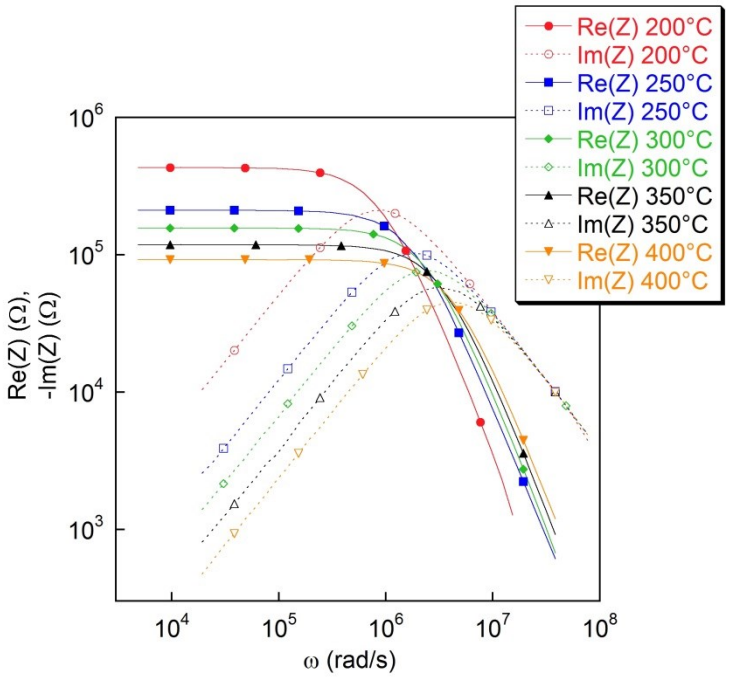

Figure 4.40 Impedance spectra for the nanotetrapods-based sensor for different temperatures ranging from 200 to 400 °C and fixed [eth] = 30 ppm.

T (°C)	R (kΩ)	C (pF)	n	A (μS · s^n)
200	431.2	2.42	0.81	$2.61 \cdot 10^{-6}$
250	210.2	2.42	0.77	$4.54 \cdot 10^{-6}$
300	156.3	2.42	0.77	$3.81 \cdot 10^{-6}$
350	118.0	2.42	0.75	$5.24 \cdot 10^{-6}$
400	91.9	2.42	0.73	$6.65 \cdot 10^{-6}$

Table 4.4 Equivalent circuit parameters obtained from the fitting of the impedance measurements on nanotetrapods-based sensor for T ranging from 200 to 400 °C and [eth] = 30 ppm, assuming C = 2.42 pF.

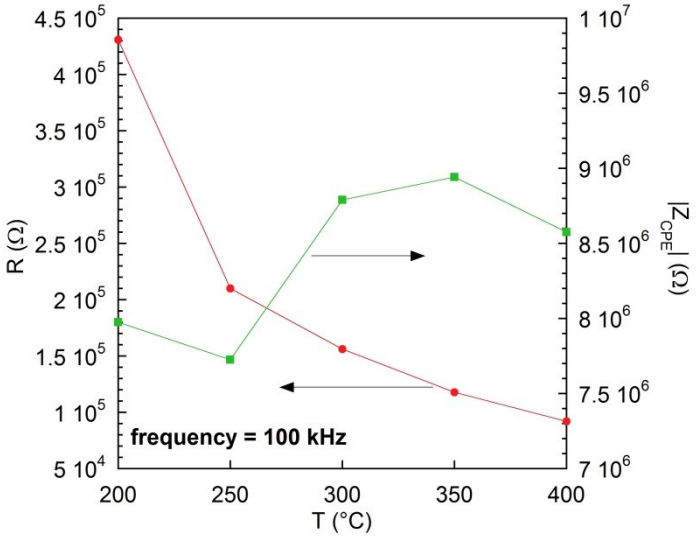

Figure 4.41 Calculated R and $|Z_{CPE}|$ values for different temperatures for the nanotetrapods-based sensor assuming C = 2.42 pF.

Similarly to what observed for the nanosheets, the resistance shows a strong decrease when the temperature is increased, passing from a value of 431.2 kΩ at 200 °C to a value of 91.9 kΩ at 400 °C. The dependence on temperature of $|Z_{CPE}|$ is less defined, however is worth noting that the overall variation in the whole T range is approximatively 15%, with a maximum value of $8.94 \cdot 10^6$ Ω reached at 350 °C and a minimum value of $7.72 \cdot 10^6$ Ω reached at 250 °C. This points out a difference with respect to the nanosheets-based sensor, where $|Z_{CPE}|$ decreases monotonically when the temperature is increased (figure 4.37). The found n value for the tetrapods, ranging from 0.73 to 0.81 (table 4.4) are slightly smaller than those obtained for the nanosheets (table 4.3); anyway, for both nanostructures the n values suggest that the CPE can be considered as a non-ideal capacitor[104].

Figure 4.42 shows the impedance spectra achieved at different ethanol concentrations (fixed T = 400 °C). Similarly to the nanosheets, the nanotetrapods impedance is strongly influenced by the introduction of ethanol in the test cell and then further decreased as the gas concentration is increased. All the spectra reported in figure 4.42 are excellently fitted by the equivalent circuit in figure 4.33, that therefore provides a good description of all the impedance spectra acquired both for nanosheets and nanotetrapods. The obtained values for R and $|Z_{CPE}|$ are reported in figure 4.43, under the assumption of fixed C = 2.42 pF.

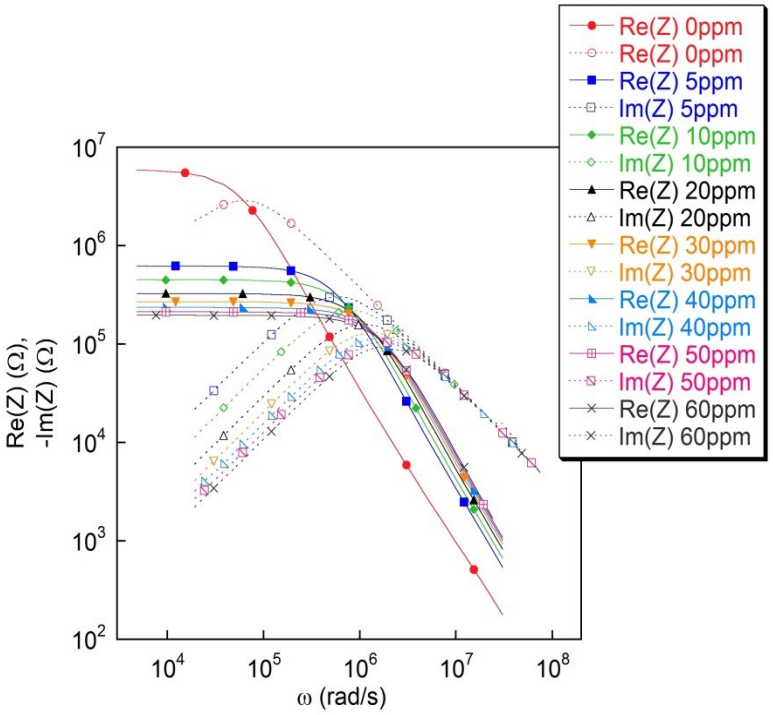

Figure 4.42 Impedance spectra for the nanotetrapods-based sensor for different ethanol concentrations ranging from 0 to 60 ppm. The sensor was kept at the constant T = 400 °C.

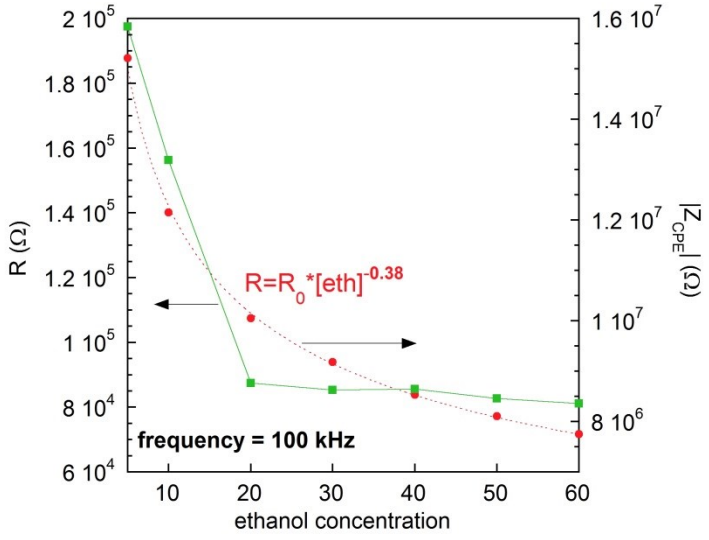

Figure 4.43 Calculated R and $|Z_{CPE}|$ values for different ethanol concentrations for the nanotetrapods-based sensor assuming C = 2.42 pF.

Similarly to the nanosheets, the increase of the ethanol concentrations results in a strong decrease of the resistance, whose trend is well described by the power law 4.11 for b = 0.38. Also for nanotetrapods-based sensors, this value differs from those derived from the sensitivity values

reported in figure 4.31 (b = 0.51), likely for the same reason discussed for the nanosheets-based devices. The comparison between the b exponents derived from impedance measurements for nanosheets and nanotetrapods (0.47 and 0.38, respectively) suggest that the conductivity of the active layer is only slightly less influenced by [eth] in the case of nanotetrapods.

The values calculated for $|Z_{CPE}|$ (figure 4.43) shows that the impedance contribution of the constant phase element is reduced by almost a factor of two when [eth] is varied from 5 to 20 ppm, and then is only influenced to a minor extent by further enhancement of the ethanol concentration. This behavior is different from those observed for the nanosheets (figure 4.39), where the CPE shows a less defined dependence on ethanol concentration in the whole 5-60 ppm range.

The observed behavior of the equivalent circuit parameters when the ethanol concentrations and the temperature are varied suggests some preliminary considerations concerning the charge transport in these systems. The good description that can be obtained by the same equivalent circuit both for nanosheets and nanotetrapods highlights that likely the same mechanisms are related to gas absorption the two systems. Nevertheless, the physical interpretation of the equivalent circuit and the identification of the different contributions to the transport is not trivial. The conduction in nanostructured sensing active layer is sometimes described by equivalent circuits were the contributions of both grains and grain boundaries are clearly distinguished[108,110,185] (as an example, the equivalent circuit proposed by Al-Hardan et al[108] is showed in figure 4.44). Typically, such equivalent circuits considered are composed by two or more elements wired in series configuration representing the impedance of the grains and, the impedance of the grain boundaries; in some cases, the contribution of the electrode-grains interface is also considered[108].

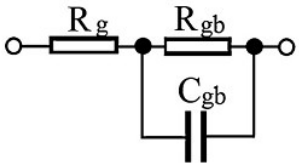

Figure 4.44 Equivalent circuit proposed by Al-Hardan et al to describe the impedance of porous ZnO films. R_g is the resistance associated with grains, while R_{gb} and C_{gb} are the resistance and the capacitance associated with the grain boundaries, respectitely. From [S6].

This circuit doesn't provide a good fitting of the impedance spectra acquired for nanosheets and nanotetrapods, unless the contribution to the total impedance of R_g is negligible with respect to the parallel R_{gb}-C_{gb}. In such a case, the equivalent circuit that describes our impedance spectra (figure 4.33) would be comparable to this one, the main difference being the presence of a non-ideal capacitive element (the CPE) instead of the capacitance C_{gb}, and the transport would be mainly determined by the contact regions between adjacent nanostructures. Anyway, further investigation is required in order to verify this hypothesis. An equivalent circuit comparable to ours has been proposed by Siemons et al to describe the conduction in undoped and La-doped nanocrystalline $CoTiO_3$ employed as sensor for reducing gases as ethanol and propylene[109]; in all the considered atmospheres, the impedance of the active layer has been modeled with a R-CPE parallel circuit, with large n values (n > 0.9) found for the CPE. It is worth noting that the considered nanocrystalline $CoTiO_3$ film is composed by nanoparticles with sizes ranging from 30 to 70 nm, and then possess an

high porosity with pores having dimensions of some tens of nm, similarly to what is observed in our nanosheets (figure 4.27).

To better understand the mechanisms related to charge transport and gas sensing, impedance spectroscopy measurements in CO atmosphere are in progress. According to Kolmakov et al[186], in metal oxides CO reacts with pre-absorbed oxygen species to form carbon dioxide, according to the reaction

$$\mathrm{CO(ads)} + \mathrm{O^-(ads)} \rightarrow \mathrm{CO_2} + \mathrm{e^-} \tag{4.12}$$

Similarly to ethanol sensing mechanism (equation 4.8), CO absorption releases electrons and thus increases the conductivity of the material. It is worth noting that the CO sensing mechanism does not involve the formation of water molecules that instead are produced by ethanol chemisorption. Therefore, the comparison between the measurements carried out in the two different atmospheres (i. e. ethanol and CO) could also give some information about the role of the humidity in the conduction. Figure 4.45 shows preliminary measurements carried out on nanotetrapods in different CO concentrations (fixed *T* = 400 °C).

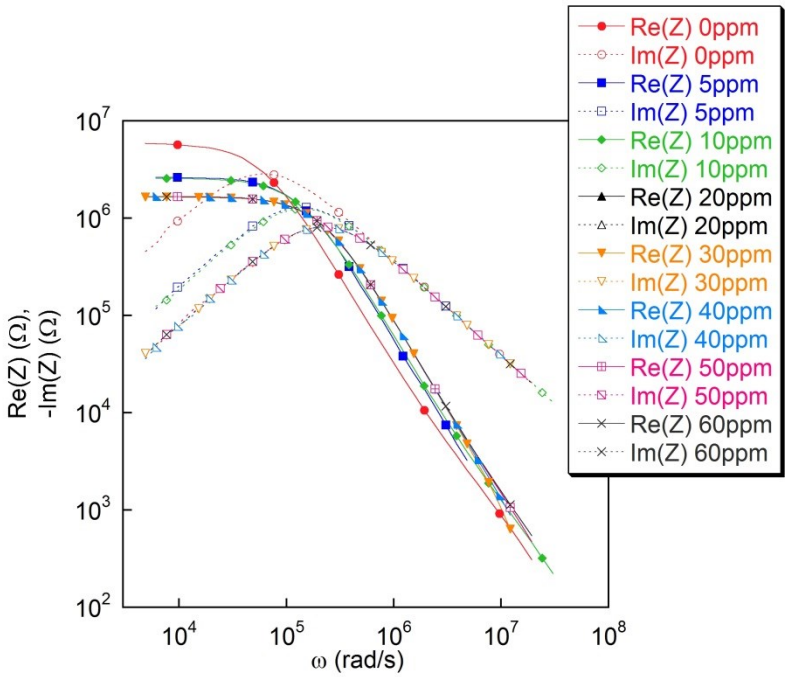

Figure 4.45 Impedance spectra for the nanotetrapods-based sensor for different CO concentrations ranging from 0 to 60 ppm. The sensor was kept at the constant *T* = 400 °C.

The equivalent circuit in figure 4.33 provides an excellent description of the impedance spectra acquired in CO atmosphere. The resulting *R* values are shown in figure 4.46. The resistance is initially decreased as CO concentration is increased up to 30 ppm and then remains almost unchanged when the concentration is further increased. This behavior is significantly different from those observed for nanotetrapods in ethanol atmosphere, where the resistance is monotonically decreased by increasing gas concentration in the whole range 0-60 ppm (figure 4.43).

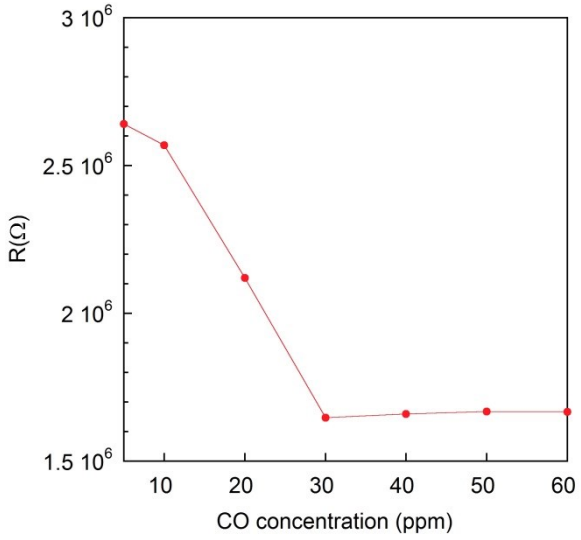

Figure 4.46 Calculated *R* values for different CO concentrations for the nanotetrapods-based sensor assuming *C* = 2.42 pF.

The reasons of this dissimilarity is still under investigation, however the different behavior observed in ethanol and in CO atmosphere could be related to the formation of water molecules resulting from the ethanol absorption mechanism described by equation 4.8. According to Barsan et al[98], at temperatures between 100 and 500 °C the interaction of a metal oxide surface with water vapor leads to molecular water and hydroxyl groups adsorption. The absorption of molecular water is observed for temperatures lower than 200 °C, while for higher temperature the water dissociation in hydrogen (H^+) and hydroxide (OH^-) ions occurs. Different mechanisms have been proposed to describe interaction of H^+ and OH^- with the metal oxide, all of them predicting an increase of the material conductivity, in agreement with the experimental evidences[98]. Therefore, the observed resistance decrease when increasing ethanol concentration (figure 4.43) could result not only from the ethanol absorption itself, but also from the interaction with the water molecules formed in the absorption process. On the contrary, the observed stabilization of the resistance for CO concentrations higher than 30 ppm could be related to the missing water contribution to the conduction, since no water is formed in the absorption process described by equation 4.12. Anyway, the influence of the water on the observed behaviors is still under investigation, and currently impedance spectroscopy measurements in mixed humid air/CO atmosphere are ongoing.

CHAPTER 5
CONCLUSIONS

The activity discussed in this thesis aimed at studying the synthesis procedures and their influence on the properties of two classes of materials, namely $MAPbX_3$ (X = I, Br, Cl) hybrid organic-inorganic perovskites for photovoltaic application and ZnO mesoporous nanostructures for photovoltaics and gas sensing.

The activity on perovskites was devoted to methylammonium lead tri-iodide ($MAPbI_3$) and mixed halide perovskites $MAPbI_{3-x}Y_x$ (Y = Br, Cl).

At first, $MAPbI_3$ perovskite films on glass substrates were obtained following either a single step solution process, but using different solvents (DMF or GBL), or a two-step dipping procedure. It was observed that the synthesis procedure and solvent used do not affect the crystal structure and optical bandgap of the material, whilst dramatically influence the morphology, that is very inhomogeneous for the single step solution-processed films and fairly uniform when films are obtained by the two-step process. Besides, a PbI_2 impurity phase was occasionally observed when the material was prepared in ambient air by single step process from stoichiometric precursor solutions, while the PbI_2 formation was systematically avoided when a slightly MAI-rich precursor solution was used.

The influence of the baking time on structural and optical properties was then investigated preparing $MAPbI_3$ films in air and in inert atmosphere from both stoichiometric and MAI-rich precursor solutions. While the crystal structure and bandgap were found to be nearly unaffected by the annealing conditions and methylammonium excess, the films prepared in inert atmosphere from stoichiometric precursor solution were found to show the highest light absorbance. Preliminary experiments were performed aiming at sensitizing by $MAPbI_3$ mesoporous ZnO nanosheets to be used for photoanode fabrication. Obtained results pointed out that sensitization was likely achieved, even if the process must still be optimized to obtain a complete perovskite infiltration into the nanostructure layer.

Mixed $MAPbI_{3-x}Br_x$ films with Br content varying in the whole $0 \leq x \leq 3$ range were synthetized in ambient air by properly mixing $MAPbI_3$ and $MAPbBr_3$ precursor solution. Structural analysis confirmed that a solid solution can be formed in the whole $0 \leq x \leq 3$ range, pointing out that the

tetragonal crystalline structure of $MAPbI_3$ turns into a cubic structure for $x > 0.57$. The dependence of the bandgap on the bromide content was found to deviate slightly from the linear behavior with a bowing parameter, which points out that composition disorder is low even if samples were prepared in ambient air. The Urbach energy was found to increase with x, reach its maximum of ≈ 85 meV for $x = 1.89$, and then decrease to the 34 meV value of the pure tri-bromide perovskite. Comparing the dependence on x of the Urbach energy and the grain size domain deduced from the XRD patterns we pointed out that in these materials the sub-bandgap absorption is likely due to defect states localized at the grain boundaries.

The influence of the baking parameters on the structural and optical properties of the materials was studied by using I/Br mixed-halide perovskites prepared from two different precursor solutions, the former nearly stoichiometric and the latter highly non stoichiometric. Taking advantage of the obtained $E_g(x)$ dependence, it was found that only the nearly-stoichiometric precursor solution results in perovskites whose composition depends to a minor extent on the annealing procedures, which makes the synthetic process more reproducible and more promising for large scale solar cell production.

Mixed $MAPbI_{3-x}Cl_x$ perovskites pointed out a completely different behavior with respect $MAPbI_{3-x}Br_x$ compound. The structural and optical characterizations with the help of DFT calculations allowed us to demonstrate that, regardless of the components ratio in the precursor solution, Cl incorporation in an iodide-based structure is possible only at relatively low concentrations (3-4%) so that the material that in the literature was initially addressed as $MAPbI_2Cl$ must be actually considered as Cl-doped $MAPbI_3$. By studying the characteristics of ss-DSSCs based on such perovskite we showed that such chloride doping dramatically improves the charge transport within the perovskite layer, which explains the outstanding performances of meso-superstructured solar cells based on this material.

The second part of the activity was focused to the preparation and characterization of mesoporous zinc oxide (ZnO) nanostructures. In particular, we prepared highly porous ZnO nanobelts by thermally decomposing $ZnS(en)_{0.5}$ hybrid parent nanostructures synthesized through a solvothermal route on Zn substrates, the Zn layer acting as both support and Zn source during the growth. The $ZnS(en)_{0.5} \rightarrow ZnS \rightarrow ZnO$ conversion was studied at the nanoscale by transmission and scanning electron microscopy analyses, showing that that hybrid decomposition by thermal annealing of $ZnS(en)_{0.5}$ at 400 °C results in porous ZnS nanobelts, that are gradually transformed into ZnO by an exchange reaction between oxygen and sulfur. This reaction starts at the crystal edges through the formation of ZnO grains and is completed by further annealing the nanobelts at 600 °C. Pores form in the whole nanostructures due to the strong lattice contraction associated with the $ZnS \rightarrow ZnO$ transformation. Obtained ZnO porous nanobelts are single crystal.

Control of the ZnO nanobelts distributions was achieved by patterning the Zn metallization on alumina substrates as a consequence of the parent hybrid nanobelts patterned growth. The presence of nanobelts on alumina in a ≈ 100 μm wide region between Zn stripes allowed the fabrication of two contacts devices where contact pads were electrically connected through a ZnO porous nanobelts entanglement. Such devices were used for the electrical characterization of the ZnO nanobelts. The comparison between cathodoluminescence spectra and electrical measurements suggested the presence of a residual sulfur doping that was confirmed by means of EDX analysis.

In order to get deeper insights about the charge transport mechanisms in ZnO nanostructure entanglements, ZnO mesoporous nanosheets and nanotetrapods were used as active layer in gas sensing devices, that were characterized in different atmospheres by means of impedance spectroscopy. The same equivalent circuit was found to provide a good description of the impedance spectra of both nanostructures in the presence of ethanol (CH_3CH_2OH) and carbon monoxide (CO) at different temperatures and gas concentrations. Even if deeper investigation is needed to better clarify the transport mechanisms, we tentatively suggest that the transport in the active layers is mainly determined by contact regions between adjacent nanostructures. As for the gas sensing mechanisms, we observed a saturation of the sensor response to dry carbon monoxide for high gas concentrations, while no saturation was observed in ethanol. We tentatively explained these different behaviors considering that the water molecules produced during ethanol sensing affect the sensor conductivity. To verify this hypothesis, impedance spectroscopy measurements are ongoing in the presence of both humidity and CO.

REFERENCES

[1] H.-S. Kim, C.-R. Lee, J.-H. Im, K.-B. Lee, T. Moehl, A. Marchioro, S.-J. Moon, R. Humphry-Baker, J.-H. Yum, J. E. Moser, M. Grätzel, N.-G. Park, *Sci. Rep.* **2012**, *2*, 591.

[2] "NREL efficiencies chart," can be found under http://www.nrel.gov/ncpv/images/efficiency_chart.jpg, **2015**.

[3] J. Jang, C. Yu, S. Choi, S. Ji, E. Kim, J. Lee, *J. Catal.* **2008**, *254*, 144.

[4] L. Zhang, H. Yang, L. Li, R. Zhang, R. Liu, J. Ma, X. Xie, *Inorg. Chem.* **2008**, *47*, 11950.

[5] J. Liu, Z. Guo, F. Meng, T. Luo, M. Li, J. Liu, *Nanotechnology* **2009**, *20*, 125501.

[6] J. W. Liu, G. Chen, Z. H. Li, Z. G. Zhang, *J. Solid State Chem.* **2006**, *179*, 3704.

[7] Y. Shi, Y. Guo, S. Yu, M. Arai, A. Belik, A. Sato, K. Yamaura, E. Takayama-Muromachi, H. Tian, H. Yang, J. Li, T. Varga, J. Mitchell, S. Okamoto, *Phys. Rev. B* **2009**, *80*, 161104(R).

[8] T. Okuda, K. Nakanishi, S. Miyasaka, Y. Tokura, *Phys. Rev. B* **2001**, *63*, 113104.

[9] J. W. Fergus, *Sensors Actuators B Chem.* **2007**, *123*, 1169.

[10] V. Primo-Martín, M. Jansen, *J. Solid State Chem.* **2001**, *157*, 76.

[11] A. P. Mackenzie, Y. Maeno, *Rev. Mod. Phys.* **2003**, *75*, 657.

[12] I. O. Troyanchuk, D. V. Karpinsky, M. V. Bushinsky, V. A. Khomchenko, G. N. Kakazei, J. P. Araujo, M. Tovar, V. Sikolenko, V. Efimov, A. L. Kholkin, *Phys. Rev. B* **2011**, *83*, 054109.

[13] L. Armelao, D. Barreca, G. Bottaro, C. Maragno, E. Tondello, A. Caneschi, C. Sangregorio, S. Gialanella, *J. Nanosci. Nanotechnol.* **2006**, *6*, 1060.

[14] A. Kojima, K. Teshima, Y. Shirai, T. Miyasaka, *J. Am. Chem. Soc.* **2009**, *131*, 6050.

[15] J.-H. Im, J. Chung, S.-J. Kim, N.-G. Park, *Nanoscale Res. Lett.* **2012**, *7*, 353.

[16] K. Fütterer, W. Depmeier, V. Petrícek, *Acta Crystallogr. B.* **1995**, *B51*, 768.

[17] D. B. Mitzi, *J. Chem. Soc. Dalt. Trans.* **2001**, 1.

[18] M. Szafrański, K. Ståhlb, *J. Solid State Chem.* **2007**, *180*, 2209.

[19] D. B. Mitzi, *Chem. Mater.* **1996**, *8*, 791.

[20] Z. Xu, D. B. Mitzi, *Inorg. Chem.* **2003**, *42*, 6589.

[21] C. R. Kagan, D. B. Mitzi, C. D. Dimitrakopoulos, *Science* **1999**, *286*, 945.

[22] D. B. Mitzi, C. D. Dimitrakopoulos, L. L. Kosbar, *Chem. Mater.* **2001**, *13*, 3728.

[23] D. B. Mitzi, K. Chondroudis, C. R. Kagan, *Inorg. Chem.* **1999**, *38*, 6246.

[24] Q. Xue, Z. Hu, C. Sun, Z. Chen, F. Huang, H. Yip, *RSC Adv.* **2014**, *5*, 775.

[25] S. Sun, T. Salim, N. Mathews, M. Duchamp, C. Boothroyd, G. Xing, T. C. Sum, Y. M. Lam, *Energy Environ. Sci.* **2014**, *7*, 399.

[26] G. C. Papavassiliou, G. Pagona, N. Karousis, G. A. Mousdis, I. Koutselas, A. Vassilakopoulou, *J. Mater. Chem.* **2012**, *22*, 8271.

[27] J.-H. Im, C.-R. Lee, J.-W. Lee, S.-W. Park, N.-G. Park, *Nanoscale* **2011**, *3*, 4088.

[28] M. M. Lee, J. Teuscher, T. Miyasaka, T. N. Murakami, H. J. Snaith, *Science* **2012**, *338*, 643.

[29] Q. Chen, H. Zhou, Z. Hong, S. Luo, H. Duan, H. Wang, Y. Liu, G. Li, Y. Yang, *J. Am. Chem. Soc.* **2014**, *106*, 622.

[30] B. O'Regan, M. Grätzel, *Nature* **1991**, *353*, 737.

[31] A. Yella, H. W. Lee, H. N. Tsao, C. Yi, A. K. Chandiran, M. K. Nazeeruddin, E. W. G. Diau, C. Y. Yeh, S. M. Zakeeruddin, M. Grätzel, *Science* **2011**, *334*, 629.

[32] D. Weber, *Zeitschrift Fur Naturforsch. Sect. B J. Chem. Sci.* **1978**, *33*, 1443.

[33] J. Burschka, A. Dualeh, F. Kessler, E. Baranoff, N.-L. Cevey-Ha, C. Yi, M. K. Nazeeruddin, M. Grätzel, *J. Am. Chem. Soc.* **2011**, *133*, 18042.

[34] H. J. Snaith, L. Schmidt-Mende, *Adv. Mater.* **2007**, *19*, 3187.

[35] H. J. Snaith, *J. Phys. Chem. Lett.* **2013**, *4*, 3623.

[36] L. Etgar, P. Gao, Z. Xue, Q. Peng, A. K. Chandiran, B. Liu, *J. Am. Chem. Soc.* **2012**, *134*, 17396.

[37] J. H. Noh, S. H. Im, J. H. Heo, T. N. Mandal, S. I. Seok, *Nano Lett.* **2013**, *13*, 1764.

[38] J. Burschka, N. Pellet, S.-J. Moon, R. Humphry-Baker, P. Gao, M. K. Nazeeruddin, M. Grätzel, *Nature* **2013**, *499*, 316.

[39] T. M. Koh, K. Fu, Y. Fang, S. Chen, T. C. Sum, N. Mathews, S. G. Mhaisalkar, P. P. Boix, T. Baikie, *J. Phys. Chem. C* **2014**, *118*, 16458.

[40] H. Zhou, Q. Chen, G. Li, S. Luo, T.-B. Song, H.-S. Duan, Z. Hong, J. You, Y. Liu, Y. Yang, *Science* **2014**, *345*, 542.

[41] M. Liu, M. B. Johnston, H. J. Snaith, *Nature* **2013**, *501*, 395.

[42] C. Bi, Y. Yuan, Y. Fang, N. Huang, *Adv. Energy Mater.* **2014**, 1401616.

[43] F. Hao, C. C. Stoumpos, D. H. Cao, R. P. H. Chang, M. G. Kanatzidis, *Nat. Photonics* **2014**, *8*, 489.

[44] G. Hodes, *Science* **2013**, *342*, 317.

[45] D. Liu, T. L. Kelly, *Nat. Photonics* **2014**, *8*, 133.

[46] A. Mei, X. Li, L. Liu, Z. Ku, T. Liu, Y. Rong, M. Xu, M. Hu, J. Chen, Y. Yang, M. Grätzel, H. Han, *Sci.* **2014**, *345* , 295.

[47] J.-H. Im, I.-H. Jang, N. Pellet, M. Grätzel, N.-G. Park, *Nat. Nanotechnol.* **2014**, *9*, 927.

[48] S. Colella, E. Mosconi, P. Fedeli, A. Listorti, F. Gazza, F. Orlandi, P. Ferro, T. Besagni, A. Rizzo, G. Calestani, G. Gigli, F. De Angelis, R. Mosca, *Chem. Mater.* **2013**, *25*, 4613.

[49] N. J. Jeon, J. H. Noh, W. S. Yang, Y. C. Kim, S. Ryu, J. Seo, S. I. Seok, *Nature* **2015**, *517*, 476.

[50] A. Sadhanala, F. Deschler, T. H. Thomas, E. Dutton, K. C. Goedel, F. C. Hanusch, M. L. Lai, U. Steiner, T. Bein, P. Docampo, D. Cahen, R. H. Friend, *J. Phys. Chem. Lett.* **2014**, *5*, 2501.

[51] J. Qiu, Y. Qiu, K. Yan, M. Zhong, C. Mu, H. Yan, S. Yang, *Nanoscale* **2013**, *5*, 3245.

[52] M. Zhang, M. Lyu, H. Yu, J.-H. Yun, Q. Wang, L. Wang, *Chem. A Eur. J.* **2015**, *21*, 434.

[53] B. Suarez, V. Gonzalez-Pedro, T. S. Ripolles, R. S. Sanchez, L. Otero, I. Mora-Sero, *J. Phys. Chem. Lett.* **2014**, *5*, 1628.

[54] C. W. Bunn, *Proc. Phys. Soc. London* **1935**, *47*, 835.

[55] H. Braekken, C. Jore, *Det Nor. Vidensk. Skr.* **1935**, *1*, NR8.

[56] H. Morkoç, Ü. Özgür, *Zinc Oxide. Fundamentals, Materials and Device Technology.*, Weinheim, **2009**.

[57] Z. L. Wang, *J. Phys. Condens. Matter* **2004**, *16*, R829.

[58] T. Minami, *Semicond. Sci. Technol.* **2005**, *50*, S35.

[59] U. Özgür, Y. I. Alivov, C. Liu, A. Teke, M. A. Reshchikov, S. Doğan, V. Avrutin, S.-J. Cho, H. Morkoç, *J. Appl. Phys.* **2005**, *98*, 041301.

[60] K. Iwata, P. Fons, S. Niki, A. Yamada, K. Matsubara, K. Nakahara, H. Takasu, *Phys. Status Solidi* **2000**, *180*, 287.

[61] K. Maeda, M. Sato, I. Niikura, T. Fukuda, *Semicond. Sci. Technol.* **2005**, *20*, S49.

[62] Z. L. Wang, *Mater. Today* **2004**, *7*, 26.

[63] W. I. Park, D. H. Kim, S. W. Jung, G.-C. Yi, *Appl. Phys. Lett.* **2002**, *80*, 4232.

[64] S. P. Anthony, J. I. Lee, J. K. Kim, *Appl. Phys. Lett.* **2007**, *90*, 103107.

[65] X. Wang, C. J. Summers, Z. L. Wang, *Nano Lett.* **2004**, *4*, 423.

[66] I. Gonzalez-Valls, M. Lira-Cantu, *Energy Environ. Sci.* **2009**, *2*, 19.

[67] W. Lee, S. K. Min, V. Dhas, S. B. Ogale, S. H. Han, *Electrochem. commun.* **2009**, *11*, 103.

[68] D. Calestani, M. Zha, R. Mosca, A. Zappettini, M. C. Carotta, V. Di Natale, L. Zanotti, *Sensors Actuators B. Chem.* **2010**, *144*, 472.

[69] H. Li, M. Zheng, L. Ma, C. Zhu, S. Luc, *Mater. Res. Bull.* **2013**, *48*, 25.

[70] F. Lu, W. Cai, Y. Zhang, *Adv. Funct. Mater.* **2008**, *18*, 1047.

[71] L. Nasi, D. Calestani, F. Fabbri, P. Ferro, T. Besagni, P. Fedeli, F. Licci, R. Mosca, *Nanoscale* **2013**, *5*, 1060.

[72] L. Nasi, D. Calestani, T. Besagni, P. Ferro, F. Fabbri, F. Licci, R. Mosca, *J. Phys. Chem. C* **2012**, *116*, 6960.

[73] Q. Zhang, C. S. Dandeneau, X. Zhou, G. Cao, *Adv. Mater.* **2009**, *21*, 4087.

[74] K. Jacobi, G. Zwicker, A. Gutmann, *Surf. Sci.* **1984**, *141*, 109.

[75] K. Mahmood, H. W. Kang, S. B. Park, H. J. Sung, *Appl. Mater. Interfaces* **2013**, *5*, 3075.

[76] L. Spanhel, M. A. Anderson, *J. Am. Chem. Soc.* **1991**, *113*, 2826.

[77] G. Redmond, D. Fitzmaurice, M. Grätzel, *Chem. Mater.* **1994**, *6*, 686.

[78] X. Sheng, Y. Zhao, J. Zhai, L. Jiang, D. Zhu, *Appl. Phys. A* **2007**, *87*, 715.

[79] A. E. Suliman, Y. W. Tang, L. Xu, *Energy Mater. Sol. Cells* **2007**, *91*, 1658.

[80] C. F. Lin, H. Lin, J. B. Li, X. Li, *J. Alloys Compd.* **2008**, *462*, 175.

[81] W. Chen, H. F. Zhang, I. M. Hsing, S. H. Yang, *Electrochem. commun.* **2009**, *11*, 1057.

[82] D.-Y. Son, J.-H. Im, H.-S. Kim, N.-G. Park, *J. Phys. Chem. C* **2014**, *118*, 16567.

[83] D. Bi, L. Yang, G. Boschloo, A. Hagfeldt, E. M. J. Johansson, *J. Phys. Chem. Lett.* **2013**, *4*, 1532.

[84] X. L. Cheng, H. Zhao, L. H. Huo, S. Gao, J. G. Zhao, *Sensors Actuators B. Chem.* **2004**, *102*, 248.

[85] Y. Chen, C. L. Zhu, G. Xiao, *Nanotechnology* **2006**, *17*, 4537.

[86] L. Bie, X. Yan, J. Yin, Y. Duan, Z. Yuan, *Sensors Actuators B. Chem.* **2007**, *126*, 604.

[87] C. C. Li, Z. F. Du, L. M. Li, H. C. Yu, Q. Wan, *Appl. Phys. Lett.* **2007**, *91*, 032101.

[88] G. D. Khuspe, R. D. Sakhare, S. T. Navale, M. A. Chougule, Y. D. Kolekar, R. N. Mulik, *Ceram. Int.* **2013**, *39*, 8673.

[89] Z. Yang, L.-M. Li, Q. Wan, Q.-H. Liu, T.-H. Wang, *Sensors Actuators B. Chem.* **2008**, *135*, 57.

[90] E. K. Heidari, E. Marzbanrad, C. Zamani, B. Raissi, *Nanoscale Res. Lett.* **2010**, *5*, 370.

[91] A. Giberti, M. C. Carotta, C. Malagù, C. M. Aldao, M. S. Castro, M. A. Ponce, R. Parra, *Phys. Status Solidi* **2011**, *208*, 118.

[92] T. Seiyama, A. Kato, K. Fujiishi, M. Nagatani, *Anal. Chem.* **1962**, *34*, 1502.

[93] Y. Zeng, T. Zhang, L. Qiao, *Mater. Lett.* **2009**, *63*, 843.

[94] T. T. Trinh, N. H. Tu, H. H. Le, K. Y. Ryu, K. B. Le, K. Pillai, J. Yi, *Sensors Actuators B. Chem.* **2011**, *152*, 73.

[95] P. Cao, D. X. Zhao, J. Y. Zhang, D. Z. Shen, Y. M. Lu, B. Yao, B. H. Li, Y. Bai, X. W. Fan, *Appl. Surf. Sci.* **2008**, *254*, 2900.

[96] M. C. Carotta, C. Dallara, G. Martinelli, L. Passari, A. Camanzi, *Sensors Actuators B. Chem.* **1991**, *3*, 191.

[97] C. Malagù, V. Guidi, M. Stefancich, M. C. Carotta, G. Martinelli, *J. Appl. Phys.* **2002**, *91*, 808.

[98] N. Barsan, U. Weimar, *J. Electroceramics* **2002**, *7*, 143.

[99] N. Barsan, U. Weimar, *J. Phys. Condens. Matter* **2003**, *15*, 813.

[100] S. M. Sze, *Physics of Semiconductor Devices*, Hoboken, **1981**.

[101] A. Many, Y. Goldstein, N. B. Grover, *Semiconductor Surfaces*, New York, **1965**.

[102] R. Mosca, P. Ferro, D. Calestani, L. Nasi, T. Besagni, F. Licci, *Cryst. Res. Technol.* **2011**, *46*, 818.

[103] X. Huang, J. Li, Y. Zhang, A. Mascarenhas, *J. Am. Chem. Soc.* **2003**, *125*, 7049.

[104] J. R. McDonald, E. Barsoukov, *Impedance Spectroscopy Theory, Experiment, and Applications*, Hoboken, **2005**.

[105] A. K. Jonscher, R. Holloway, B. N. College, S. T. W. Oex, *Electrochim. Acta* **1990**, *35*, 1595.

[106] T. Z. Fahidy, V. Modi, K. Krischer, A. K. Vijh, A. Lasia, A. C. West, M. C. Lefebvre, J. D. Yang, *Modern Aspects of Electrochemisty N. 32*, New York, **2002**.

[107] M. E. Orazem, B. Tribollet, *Electrochemical Impedance Spectroscopy*, Hoboken, **2008**.

[108] N. Al-Hardan, M. J. Abdullah, A. A. Aziz, *Appl. Surf. Sci.* **2011**, *257*, 8993.

[109] M. Siemons, U. Simon, *Sensors Actuators B. Chem.* **2006**, *120*, 110.

[110] M. Kashif, E. Ali, S. M. U. Ali, U. Hashim, S. Bee, A. Hamid, *Nanoscale Res. Lett.* **2013**, *8*, 68.

[111] M. Quinten, *Optical Properties of Nanoparticle System*, Weinheim, **2011**.

[112] P. Kubelka, F. Munk, *Zeitschrift für Tech. Phys.* **1931**, *12*, 593.

[113] A. B. Murphy, *Sol. Energy Mater. Sol. Cells* **2007**, *91*, 1326.

[114] Z. C. Orel, M. K. Gunde, *Sol. Energy Mater. Sol. Cells* **2000**, *61*, 445.

[115] A. B. Murphy, *J. Phys. D. Appl. Phys.* **2006**, *39*, 3571.

[116] E. L. Simmons, *Appl. Opt.* **1975**, *14*, 1380.

[117] S. P. Tandon, J. P. Gupta, *Phys. Status Solidi* **1970**, *2*, 257.

[118] P. Y. Yu, M. Cardona, *Fundamentals of Semiconductors. Physics and Materials Properties*, New York, **2010**.

[119] A. N. Pikhtin, H. H. Hegazy, *Semiconductors* **2009**, *43*, 1259.

[120] M. Kumar, G. Baldissera, C. Persson, D. G. F. David, M. V. S. da Silva, J. A. Freitas, J. G. Tischler, J. F. D. Chubaci, M. Matsuoka, A. Ferreira da Silva, *J. Cryst. Growth* **2014**, *403*, 124.

[121] M. Bronzoni, M. Stefancich, S. Rampino, *Thin Solid Films* **2012**, *520*, 7054.

[122] C. Men, Z. Tian, Q. Shao, H. Zhang, Z. An, *Appl. Surf. Sci.* **2012**, *258*, 10195.

[123] V. Celli, A. A. Maradudin, A. M. Marvin, A. M. McGurn, *J. Opt. Soc. Am. A* **1985**, *2*, 2225.

[124] F. Urbach, *Phys. Rev.* **1953**, *92*, 1324.

[125] H. W. Martienssen, *J. Phys. Chem. Solids* **1957**, *2*, 257.

[126] I. Studenyak, M. Kranj, M. Kurik, *Int. J. Opt. Appl.* **2014**, *4*, 76.

[127] H. Sumi, A. Sumi, *J. Phys. Soc. Japan* **1987**, *56*, 2211.

[128] A. Skumamch, A. Frova, N. M. Amer, *Solid State Commun.* **1985**, *54*, 597.

[129] G. D. Cody, *J. Non. Cryst. Solids* **1992**, *141*, 3.

[130] C. Rincón, S. M. Wasim, G. Marín, R. Márquez, L. Nieves, G. Sánchez Pérez, E. Medina, *J. Appl. Phys.* **2001**, *90*, 4423.

[131] S. De Wolf, J. Holovsky, S.-J. Moon, P. Löper, B. Niesen, M. Ledinsky, F.-J. Haug, J.-H. Yum, C. Ballif, *J. Phys. Chem. Lett.* **2014**, *5*, 1035.

[132] Y. Kawamura, H. Mashiyama, K. Hasebe, *J. Phys. Soc. Japan* **2002**, *7*, 1694.

[133] A. Poglitsch, D. Weber, *J. Chem. Phys.* **1987**, *87*, 6373.

[134] A. Dal Corso, A. Conte Mosca, *Phys. Rev. B* **2005**, *71*, 115106.

[135] T. Baikie, Y. Fang, J. M. Kadro, M. Schreyer, F. Wei, S. G. Mhaisalkar, M. Grätzel, T. J. White, *J. Mater. Chem. A* **2013**, *1*, 5628.

[136] O. Malinkiewicz, C. Roldán-Carmona, A. Soriano, E. Bandiello, L. Camacho, M. K. Nazeeruddin, H. J. Bolink, *Adv. Energy Mater.* **2014**, 1400345.

[137] E. Mosconi, A. Amat, K. Nazeeruddin, M. Grätzel, F. De Angelis, *J. Phys. Chem. B* **2013**, *117*, 13902.

[138] W. Shockley, H. J. Queisser, *J. Appl. Phys.* **1961**, *32*, 510.

[139] Q. Chen, H. Zhou, Z. Hong, S. Luo, H.-S. Duan, H.-H. Wang, Y. Liu, G. Li, Y. Yang, *J. Am. Chem. Soc.* **2014**, *136*, 622.

[140] K. Liang, D. B. Mitzi, M. T. Prikas, *Chem. Mater.* **1998**, *10*, 403.

[141] T. Kollek, D. Gruber, J. Gehring, E. Zimmermann, L. Schmidt-Mende, S. Polarz, *Angew. Chem. Int. Ed. Engl.* **2014**, *54*, 1341.

[142] E. L. Unger, A. R. Bowring, C. J. Tassone, V. L. Pool, A. Gold-parker, R. Cheacharoen, K. H. Stone, E. T. Hoke, M. F. Toney, M. D. Mcgehee, *Chem. Mater.* **2014**, *26*, 7158.

[143] F. K. Aldibaja, L. Badia, E. Mas-Marzá, R. S. Sánchez, E. M. Barea, I. Mora-Sero, *J. Mater. Chem. A* **2015**, DOI: 10.1039/C4TA06198E.

[144] G. E. Eperon, V. M. Burlakov, P. Docampo, A. Goriely, H. J. Snaith, *Adv. Funct. Mater.* **2014**, *24*, 151.

[145] C. Wehrenfennig, G. E. Eperon, M. B. Johnston, H. J. Snaith, L. M. Herz, *Adv. Mater.* **2014**, *26*, 1584.

[146] H.-S. Kim, J.-W. Lee, N. Yantara, P. P. Boix, S. A. Kulkarni, S. Mhaisalkar, M. Grätzel, N.-G. Park, *Nano Lett.* **2013**, *13*, 2412.

[147] S. A. Kulkarni, T. Baikie, P. P. Boix, N. Yantara, N. Mathews, S. Mhaisalkar, *J. Mater. Chem. A* **2014**, *2*, 9221.

[148] A. R. Denton, N. W. Ashcroft, *Phys. Rev. A* **1991**, *43*, 3161.

[149] S. Boldish, W. White, *Am. Mineral.* **1998**, *83*, 865.

[150] J. A. Van Vechten, T. K. Bergstresser, *Phys. Rev. B* **1970**, *1*, 3351.

[151] Y. Yamada, T. Nakamura, M. Endo, A. Wakamiya, Y. Kanemitsu, *Appl. Phys. Express* **2014**, *7*, 032302.

[152] E. Edri, S. Kirmayer, D. Cahen, G. Hodes, *J. Phys. Chem. Lett.* **2013**, *4*, 897.

[153] Z. Xiao, Q. Dong, C. Bi, Y. Shao, Y. Yuan, J. Huang, *Adv. Mater.* **2014**, *26*, 6503.

[154] M. M. Lee, J. Teuscher, T. Miyasaka, T. N. Murakami, H. J. Snaith, **2012**, 1.

[155] Y. Zhao, K. Zhu, *J. Am. Chem. Soc.* **2014**, *136*, 12241.

[156] M. Yang, R. Guo, K. Kadel, Y. Liu, K. O'Shea, R. Bone, X. Wang, J. He, W. Li, *J. Mater. Chem. A* **2014**, *2*, 19616.

[157] A. Dualeh, N. Tétreault, T. Moehl, P. Gao, M. K. Nazeeruddin, M. Grätzel, *Adv. Funct. Mater.* **2014**, *24*, 3250.

[158] Y. Zhao, K. Zhu, *J. Phys. Chem. C* **2014**, *118*, 9412.

[159] J. M. Ball, M. M. Lee, A. Hey, H. J. Snaith, *Energy Environ. Sci.* **2013**, *6*, 1739.

[160] K. Yamada, K. Nakada, Y. Takeuch, K. Nawa, Y. Yamane, *Bull. Chem. Soc. Jpn.* **2011**, *932*, 926.

[161] R. D. Shannon, *Acta Crystallogr. B.* **1976**, *A32*, 751.

[162] N. Kitazawa, Y. Watanabe, Y. Nakamura, *J. Mater. Sci.* **2002**, *7*, 3585.

[163] B. Qi, J. Wang, *Phys. Chem. Chem. Phys.* **2013**, *15*, 8972.

[164] J. D. Servaites, S. Yeganeh, T. J. Marks, M. A. Ratner, *Adv. Funct. Mater.* **2010**, *20*, 97.

[165] S. D. Stranks, G. E. Eperon, G. Grancini, C. Menelaou, M. J. P. Alcocer, T. Leijtens, L. M. Herz, A. Petrozza, H. J. Snaith, *Science* **2013**, *342*, 341.

[166] G. Xing, N. Mathews, S. Sun, S. S. Lim, Y. M. Lam, M. Grätzel, S. Mhaisalkar, T. C. Sum, *Science* **2013**, *342*, 344.

[167] X. Ouyang, T. Tsai, D. Chen, Q. Huang, W. Cheng, R. Purdue, A. January, *Chem. Commun. (Camb).* **2003**, 886.

[168] H. Y. Lu, S. Y. Chu, S. S. Tan, *J. Cryst. Growth* **2004**, *269*, 385.

[169] G. Shen, J. H. Cho, S. I. Jung, C. J. Lee, *Chem. Phys. Lett.* **2005**, *401*, 529.

[170] M. J. Zheng, L. D. Zhang, G. H. Li, W. Z. Shen, *Chem. Phys. Lett.* **2002**, *363*, 123.

[171] F. Fabbri, M. Villani, A. Catellani, A. Calzolari, G. Cicero, D. Calestani, G. Calestani, A. Zappettini, B. Dierre, T. Sekiguchi, G. Salviati, *Sci. Rep.* **2014**, *4*, 1.

[172] T.-J. Kuo, C.-N. Lin, C.-L. Kuo, M. H. Huang, *Chem. Mater.* **2007**, *19*, 5143.

[173] B. Liu, L. Hub, C. Tang, L. Liu, S. Li, J. Qi, Y. Liu, *J. Lumin.* **2011**, *131*, 1095.

[174] J. Cao, J. Yang, Y. Zhang, L. Yang, D. Wang, M. Wei, Y. Wang, Y. Liu, M. Gao, X. Liu, *J. Phys. D. Appl. Phys.* **2010**, *43*, 075403.

[175] C. H. Liang, Y. Shimizu, T. Sasaki, H. Umehara, N. Koshizaki, *J. Phys. Chem. B* **2004**, *108*, 9728.

[176] K. Moazzami, T. E. Murphy, J. D. Phillips, M. C.-K. Cheung, A. N. Cartwright, *Semicond. Sci. Technol.* **2006**, *21*, 717.

[177] A. Catellani, **2014**, Private communication.

[178] Y.-Z. Yoo, Z. Jin, T. Chikyow, T. Fukumura, M. Kawasaki, H. Koinuma, *Appl. Phys. Lett.* **2010**, *81*, 3798.

[179] L. Zhang, J. Zhao, H. Lu, L. Li, J. Zheng, H. Li, Z. Zhu, *Sensors Actuators B. Chem.* **2012**, *161*, 209.

[180] T. Hsueh, C. Hsu, S. Chang, I. Chen, *Sensors Actuators B. Chem.* **2007**, *126*, 473.

[181] B. L. Zhu, C. S. Xie, A. H. Wang, D. W. Zeng, W. L. Song, X. Z. Zhao, *Mater. Lett.* **2005**, *59*, 1004.

[182] C. Xiangfeng, Y. H. Leung, *Chem. Phys. Lett.* **2005**, *401*, 426.

[183] N. Hongsith, E. Wongrat, T. Kerdcharoen, S. Choopun, *Sensors Actuators B. Chem.* **2010**, *144*, 67.

[184] N. Barsan, D. Koziej, U. Weimar, *Sensors Actuators B. Chem.* **2007**, *121*, 18.

[185] K. Aguir, A. Labidia, *IEEE Sensors* **2006**, 267.

[186] A. Kolmakov, Y. Zhang, G. Cheng, M. Moskovits, *Adv. Mater.* **2003**, *15*, 997.

[187] S. Luo, W. A. Daoud, *J. Mater. Chem. A* **2015**, Advance Article.

[188] S. Mandal, R. K. Singha, a. Dhar, S. K. Ray, *Mater. Res. Bull.* **2008**, *43*, 244.